

STAR FORMATION ACROSS COSMIC TIME

Jennifer C. Sieben

Submitted to the faculty of the University Graduate School
in partial fulfillment of the requirements
for the degree
Doctor of Philosophy
in the Department of Astronomy
Indiana University
December 2022

Accepted by the Graduate Faculty, Indiana University, in partial fulfillment of the requirements for the degree of Doctor of Philosophy.

Doctoral Committee

John J. Salzer, Ph.D.

Katherine Rhode, Ph.D.

Samir Salim, Ph.D.

Enrico Vesperini, Ph.D.

13 June 2022

© 2022
Jennifer C. Sieben

†

To everyone who listened while I info-dumped about astronomy

ACKNOWLEDGEMENTS:

I could probably dedicate every galaxy in this thesis to a different person who has helped me and supported me along the way. And as you'll see, that's a lot of galaxies. I can't thank that many people here, but know that in my heart there is a galaxy named for you.

Adler Planetarium will always be my first astronomy home. That was the best place to foster my love of outer space from a very young age. Thank you to the astronomers in SVL who answered my questions about string theory when I was too young to understand most of it. Thank you to the astronomers who later welcomed me as an intern and taught me how astronomy works. Special thanks to Tom, Dario, Fred, and Paul for teaching me how to do telescope outreach, and to Larry for pushing me to be the one who presented and answered questions in SVL. Because of you all, I gained the confidence to call myself an astronomer.

The physics department at IWU was invaluable in giving me foundational knowledge I needed in order to make this PhD possible. Thank you for the open door policies, the fun lab experiences, and for finally teaching cosmology my last semester. Thank you to Julia for being a study buddy and a great friend. I wouldn't have made it through without you. Special thanks go to Dr French for taking me out of the country on two occasions: once to Cerro Tololo to teach me how to observe with a research class telescope, and once for an unforgettable semester abroad in London. Your mentorship was more valuable than I can say, and certainly I would not be the observer I am without those two weeks in Chile.

None of the data in this thesis would exist without the amazing support staff at WIYN. Especially all the operators who troubleshooted with us, put up with our strange requests, checked if the clouds were gone for the umpteenth time, and just chatted to help the night pass. I will miss observing with you.

I love having friends online from around the world, but I have loved having them even more during grad school. You kept me awake through long observing nights and talked with me while I walked home in the morning. You kept me sane when the whole world was in lockdown. I love hanging out with you all and I'm so glad you let me share pretty pictures of galaxies. Thanks go especially to Amanda who introduced me to the best software for organizing papers, commiserated about grad school, and became my pen pal. And to Shivani who kept me sane in her own special way as we traded stories, brainstormed together, and went from occasional editors to

friends. I'm so proud of both the stories we have created.

My time at IU would've been so much more isolating if I had not joined SciU. It has been a joy to hang out with my SciU friends and compare our grad school experiences. I'm so proud of all the articles I've written for the blog. It has been an honor to be your Editor-at-Large.

I would not have finished this degree without the other grad students in the astronomy department at IU. Whether it was homework help, code debugging, D&D games, movie nights, or just being a friend, I'm so glad to have met you and I hope to see you again at future conferences. All of this is doubly true for my office mates Nick, David, and later Laurin. Thank you for putting up with my need to have music playing and for letting me get you hooked on "Get It On".

Of course, this degree would also be impossible without the support of others in the astronomy department. Emily, Paige, Bob, you all keep this department running so smoothly and really make it feel like home. All of the professors are also so generous with their open door policy and I will miss walking into your offices to talk about astronomy.

Neither this thesis, nor this survey would exist without my advisor: John. Thank you for welcoming a first year student who wanted to study high redshifts and for convincing me that I didn't need $z=10$ to do fun science. Thank you for being patient when I had many, many questions. And thank you for our Friday lunch afternoons where our research family got to bond. I look forward to seeing this survey project grow in the future.

Thank you to my best friend Fiona for so many things, but especially for our Monday night Skype dates. It's never as fun as hanging out in person, but without these we never would've discovered so many fun buildings in the world or improved our crossword skills so much. I'm so glad our paths crossed and we became friends.

Thank you to my Cedar Island family for supporting me, stargazing on the pier, and trusting me to be their source of astronomy news. Even when I give you sarcastic answers. But really, just look up.

Last, but absolutely not least, thank you to my family. You've taken me to museums, conferences, and random astronomy talks all throughout my life, doing everything to support this wild dream of mine. More importantly, you've listened to me talk about astronomy, learning alongside me to stay engaged with what I care about. Stephanie

and Christina, you're the best sisters I could ask for and I'm so lucky to have you both keeping me grounded. Also no one else is on the same sarcasm wavelength as the three of us. I love you all more than I can say.

Jennifer C. Sieben

Star Formation Across Cosmic Time

SFACT (Star Formation Across Cosmic Time) is a novel large-scale narrow-band survey designed to detect emission-line galaxies in a range of redshift windows. These data can be used to study star-formation rates at multiple epochs simultaneously. Using the WIYN 3.5m telescope, this survey detects thousands of emission-line galaxies at nine distinct redshift windows up to $z=1$. It does this by targeting the H α ($\lambda 6563$), [O III] ($\lambda 5007$), and [O II] ($\lambda 3727$) emission lines with three custom narrow-band filters. Images are also taken with g, r, and i broad-band filters; all six filter images are combined to create deep images of each survey field. A custom pipeline has been developed to identify and measure objects of interest, resulting in a uniform selection of candidates across all narrow-band filters. Spectroscopic follow-up is also performed to confirm detections as emission-line galaxies. SFACT has detected objects ranging from H II regions in nearby galaxies to distant compact galaxies and quasars. A total of 12 fields spanning $\sim 6 \text{ deg}^2$ are used in this study, for a total of 1134 targets with both imaging and spectroscopic data. Of these, 940 are star-forming galaxies discovered via one of our three primary emission lines and are used for star-formation rate density analysis.

My dissertation work includes analysis of the SFACT data in order to study star-formation rate densities of galaxies at $z < 1$. This includes the processing of the images, the target selection, and the photometric measurements. A parallel project using previous star-formation studies is also analysed in order to more completely understand the observational biases inherent in emission-line surveys. Together, these two projects provide a valuable examination of the star-formation rate density of emission-line-selected galaxies at a wide range of lookback times.

John J. Salzer, Ph.D.

Katherine Rhode, Ph.D.

Samir Salim, Ph.D.

Enrico Vesperini, Ph.D.

Table of Contents

Chapter 1 An Introduction to Star-Formation Rate Surveys	1
1.1 Using Star Formation Rates to Understand the Universe	1
1.1.1 A History of Star-Formation Rate Studies	1
1.1.2 Determination of SFR Measurements	2
1.1.3 Modern SFR Studies	4
1.2 Designing a Narrow-Band Survey	5
1.3 SFACT and Thesis Outline	8
1.4 References	9
Chapter 2 Introduction to the SFACT Survey	13
2.1 Survey Motivation	13
2.2 Survey Design	15
2.2.1 WIYN Telescope	15
2.2.2 Narrow-Band Filters	17
2.2.3 Target Fields	18
2.3 Applications of SFACT Survey	21
2.4 Samples in this Thesis	22
2.5 References	23
Chapter 3 SFACT Imaging	27
3.1 Introduction	27
3.2 Observations & Data Processing	28

3.2.1	Observations	28
3.2.2	Data Processing	33
3.3	SFACT Target Selection	36
3.3.1	Identifying SFACT Candidates	36
3.3.2	Photometry	41
3.4	Results	45
3.4.1	SFACT Survey Catalogs	45
3.4.2	Example Objects	84
3.4.3	Photometric Properties of SFACT Targets	90
3.4.4	Connecting Selection Parameters to NB Flux	95
3.5	Summary and Conclusions	99
3.6	References	100
Chapter 4	Spectroscopy of the SFACT Pilot-Study Fields	103
4.1	Introduction	103
4.2	Observations with Hydra	104
4.2.1	Instrumentation	104
4.2.2	Observations	105
4.3	Spectral Processing and Measurement	107
4.4	Pilot-Study Spectroscopy Results	109
4.4.1	Redshift Distribution	109
4.4.2	Example Object Spectra	111
4.4.3	Diagnostic Diagram	115
4.4.4	Derived Quantities	117
4.5	Beyond the Pilot-Study Fields	121
4.6	References	121

Chapter 5 Computing Star-Formation Rate Densities using Emission-Line-Selected Galaxy Samples	123
5.1 Introduction	123
5.2 Emission-Line Galaxy Samples	125
5.2.1 KISS	125
5.2.2 ALFALFA H α	127
5.3 Luminosity Function Construction	128
5.4 Results	130
5.4.1 R Band Luminosity Functions	132
5.4.2 Emission-Line Luminosity Functions	135
5.4.3 KISS Blue Comparison	140
5.5 Discussion	141
5.5.1 Different Populations	141
5.5.2 Star-Formation Rate Density Comparisons	142
5.5.3 Scaling Relationships	143
5.6 Future Work	145
5.6.1 Improvements	145
5.6.2 Connection to SFACT	146
5.7 References	146
Chapter 6 Star-Formation Rates with SFACT	150
6.1 Introduction	150
6.2 Flux Corrections	151
6.2.1 Nearby Line Corrections	151
6.2.2 Filter Transmission Correction	153
6.2.3 Dust Correction	154
6.3 Survey Depth Correction	155
6.4 Star-Formation Rate Calculations	158

6.4.1	H α Star-Formation Rates	159
6.4.2	[O III] Star-Formation Rates	159
6.4.3	[O II] Star-Formation Rates	160
6.4.4	Completeness Correction	160
6.5	Results	160
6.5.1	Star-Formation Rates	161
6.5.2	Preliminary Star-Formation Rate Densities	162
6.5.3	Comparison with Literature	165
6.6	Improvements	169
6.7	Conclusion	170
6.8	References	170
Chapter 7	Summary and Future Work	173
7.1	Summary	173
7.2	Future Work	174
7.2.1	Current Catalog	174
7.2.2	Next Steps	177
7.3	Acknowledgements	178
7.4	References	179
Chapter Appendix A	Software Written for the SFACT Project	181
A.1	Field Processing	181
A.2	Target Selection	182
A.3	Photometry	183
A.4	Spectroscopy	185
A.5	Star-Formation Rate Density	185

Curriculum Vitae

List of Tables

2.1	Properties of the SFACT Narrow-Band Filters	17
3.1	Observation Dates	30
4.1	Hydra Pointings	106
5.1	R-band Luminosity Functions	131
5.2	Narrow-Band Luminosity Functions	131
5.3	Comparison of Total Luminosity	144
6.1	SFRD Literature Comparison	166
7.1	Fall SFACT Fields Catalog	175
7.2	Spring SFACT Fields Catalog	176

List of Figures

2.1 Redshift Windows	19
3.1 NB Filter Transmission Curves	32
3.2 SFF01 Diagnostic Plot	39
3.3 H α Candidates	85
3.4 [O III] Candidates	87
3.5 [O II] Candidates	89
3.6 QSO Candidate	90
3.7 Composite Flux Histograms	92
3.8 Composite Filter Histograms	93
3.9 R Magnitude Comparison	94
3.10 Δm vs. NB Flux	95
3.11 Δm vs. EW	97
3.12 Ratio vs. NB Flux	98
4.1 Pilot-Study Fields Redshift Distribution	110
4.2 H α Spectra	112
4.3 [O III] Spectra	114
4.4 [O II] Spectra	116
4.5 QSO Spectrum	117
4.6 Diagnostic Diagram	118
4.7 Absolute Magnitude Distribution	120

5.1	R Band Luminosity Functions	132
5.2	H α Luminosity Function Comparison	136
5.3	H α Luminosity Functions	138
5.4	KISS Blue Luminosity Functions	140
6.1	Correction Effects on SFRD	157
6.2	Emission Line SFR Histogram	161
6.3	Redshift Windows SFR Histogram	163
6.4	Star Formation Rate Densities	164
6.5	Star Formation Rate Density Comparison	168

Chapter 1

An Introduction to Star-Formation Rate Surveys

1.1 Using Star Formation Rates to Understand the Universe

Star formation is one of the principal mechanisms through which galaxies evolve. Episodes of star formation grow the stellar population of a galaxy either in bursts or in a steady production of stars. As such, looking at rates of star formation as a function of lookback time allows us to probe the evolution of galaxy populations. Understanding how galaxy populations evolve over time via star-formation rate density (SFRD) studies helps us understand the history of our universe.

1.1.1 A History of Star-Formation Rate Studies

There have been many studies dedicated to understanding the SFRD at different epochs using different methods of study. Local studies often use optical wavelengths (e.g., Tresse & Maddox 1998; Gallego et al. 2002; Brinchmann et al. 2004; Ly et al. 2007; Westra et al. 2010) to measure the star-formation rate (SFR) of galaxies. To reach higher redshifts, IR studies (e.g., Pettini et al. 1998; Sanders et al. 2003; Daddi et al. 2007; Villar et al. 2008; Vaccari et al. 2010; Ellis et al. 2013) and UV studies (e.g., Lilly et al. 1996; Sullivan et al. 2000) become necessary. Looking at all of these different studies together, they form a consistent picture: the SFRD of the universe started low, then grew to a peak in activity at $z \sim 2$. Since then, the SFRD has been falling. Yet it is not as simple as it may sound. The exact time of peak activity

is somewhere between $z = 1.5$ and $z = 3$ depending on which observational method is used to measure the SFRD. Even at $z < 1$, the range of values in the measured SFRD reported in published studies is nearly a factor of 10 (Hopkins & Beacom 2006; Gunawardhana et al. 2013; Van Sistine et al. 2016). Much of this spread is borne from the probe used to measure SFRs. Robust local measurements are key to anchoring the understanding of the evolution of SFRD from the early universe to today.

1.1.2 Determination of SFR Measurements

There are many different methods of measuring SFRs which probe different timescales of galactic evolution. Nearly all observational tracers measure the rate of massive star formation since most of the energy emitted from a young stellar population originates in massive stars. But different tracers of star formation are sensitive to different stellar masses and thus probe different ranges of the time since the start of the star-forming event. Each of these methods also have their own unique uncertainties and possible biases in the selection method.

UV studies are able to probe young, massive stars with spectral types O, B, and A. These studies trace the formation rates of massive stars and see fluctuations on timescales longer than a 10^8 years. The UV luminosity output is also dependent on its metallicity and dust obscuration. Both of these effects can be corrected for, but these dependencies have led to different conversion factors between UV luminosity and SFR.

The UV energy absorbed by dust is re-radiated in IR wavelengths, making IR studies another common way to study SFRs. Dust extinction of the IR emission is considered negligible in most cases and the IR luminosity is usually directly proportional to the amount of star-formation energy which was absorbed by dust. IR studies are ideally carried out in conjunction with dust emission models fit to the observations, but in practice a local template is often applied to all data, leading to

significant uncertainties in the derived SFRs.

In the optical regime, nebular emission lines are often used to probe star formation. Measuring the flux from the H α recombination line is a very common method of SFR measurements (e.g., Gunawardhana et al. 2013; Coughlin et al. 2018; Kewley et al. 2019; Ramón-Pérez et al. 2019). High energy O and B stars produce many hydrogen-ionizing photons, resulting in many free electrons. As these electrons recombine with hydrogen ions, photons will be emitted as recombination lines. H α recombination lines are one of the best understood SFR indicators because the H α luminosity is directly proportional to the ionizing radiation from massive ($> 10M_{\odot}$) stars, and therefore provides an almost “instantaneous” (< 10 Myr) measure of SFR. This measurement method also has very little dependence on the physical conditions in the surrounding ionizing gas (Kennicutt 1998). However, these lines are only observable from the ground in the optical range at $z \lesssim 0.4$. In order to reach higher redshifts in ground-based optical surveys, many surveys turn to oxygen lines.

Although not directly proportional to SFR, nebular emission lines from heavier elements such as oxygen are also popular lines to use in optical studies (e.g., Moustakas et al. 2006; Suzuki et al. 2016; Guo et al. 2019; Zhai et al. 2019). The two most commonly used star-formation tracers are [O III] $\lambda 5007$ and [O II] $\lambda 3727$. [O II] in particular is a strong line, allowing it to be measured even when the signal-to-noise of the data is less than desirable. However, the strength of these lines have a more complex dependence on metallicity and excitation state of the surrounding gas. [O II] luminosity is highly dependent on the excitation state and chemical abundance of the ionized gas. On top of this, [O II] and [O III] lines are more affected by dust extinction than H α lines. Converting these collisionally-excited line fluxes to SFRs requires careful calibration, either empirically or theoretically.

Although NB flux may be affected by dust extinction and can only be observed optically in limited redshift windows, emission-line flux is one of the best ways to

measure SFRs. For these reasons, narrow-band studies are an increasingly common way to study cosmic SFRD.

1.1.3 Modern SFR Studies

In an effort to better understand SFRs, many studies have used more than one method to measure SFRs. Khostovan et al. (2015) used H β + [O III] emission as well as [O II] emission to study SFRs at $z \sim 2$. They provided the groundwork for using the combined H β + [O III] emission to study SFRD, which Fonseca & Camera (2020) also used. Kennicutt et al. (2009) also recommended using IR measurements to further improve the reliability of both H α and [O II] SFR measurements. This would allow for survey-specific dust-attenuation corrections, rather than relying on models.

Other studies (e.g., Mehta et al. 2015) have focused on putting results from [O III] and [O II] emission lines on the same scale as H α and learning how to properly calibrate SFR results. They propose that [O III] and H α results are directly related and, with some accounting for scatter, can be easily substituted for one another.

However, theoretical studies like Wilkins et al. (2019) have cast doubt on the current conversion factors used to compute SFR from different wavelength regimes (i.e., optical emission lines, UV, and IR) and studies which combine results from more than one method. They specifically see new tension between results borne from UV and IR observations when compared to H α . They suggest that this might not be properly resolved until the James Webb Space Telescope comes online.

Other studies have used different selection methods, many choosing to use narrow-band (NB) and broad-band (BB) filters in combination, instead of only getting emission-line flux in follow-up observations. This changes the selection function of the survey and places greater dependence on the emission lines. Newer projects such as Kellar et al. (2012), Sobral et al. (2013), Coughlin et al. (2018), and Khostovan et al. (2020) detect emission-line galaxies (ELGs) via emission lines directly, subtracting

continuum emission to better pick up faint line emission in NB images.

While all these studies represent steps towards a greater understanding of star-formation rate history, there are still weaknesses in survey methodology and calibration uncertainties to consider when designing a new survey.

1.2 Designing a Narrow-Band Survey

Regardless of the observational technique used in a study, it is important to understand the biases. NB filters used in imaging surveys allow for the discovery of compact sources of emission-line flux which may not otherwise be noticeable in BB surveys. However, using images alone will introduce uncertainty in the redshift of the galaxy. Depending on the wavelength of the NB filter, the source of this line emission could be one of many optical emission lines. If the galaxy is nearby, H α emission lines are the most common cause, but a strong [O III] line, or even [O II] line may also lead to a galaxy being discovered in this way. Furthermore, the overall color of a galaxy is not a robust indicator of either distance or activity.

Even when there is a clear source in the BB image, a strong emission line can lead to unexpected colors, setting it apart from a more typical galaxy at the same redshift. For example, strong [O III] emission in the Sloan Digital Sky Survey BB filters create the appearance of compact green galaxies, later termed Green Pea galaxies (Cardamone et al. 2009). Similar galaxies at a higher redshift appear purple in the Sloan Digital Sky Survey color mapping (Brunker et al. 2020). Green Pea galaxies are a new type of star forming galaxy and their existence is changing the way we understand galactic evolution. The discovery of these unique, compact ELGs underscore the need to understand how to study star-formation history via ELGs.

A NB survey allows for less dependence on strong continuum luminosity than that required by a typical optical survey. A galaxy which is too faint to stand out in a BB study may be detected via strong line emission which is only noticed in an NB survey.

Furthermore, by using a range of NB filters, one can probe a wide range of redshifts using the same core methodology. This allows for better comparison across a larger redshift range, while also reducing the need for many different instruments to be used in the service of the same project. All of these factors were major considerations in the design of the Star Formation Across Cosmic Time (SFACT) survey.

NB surveys tend to take one of two paths. Either they are deep, or they are wide. Deep surveys often make use of well-studied fields (e.g., Hubble Ultra Deep Field (Hogg et al. 1998), GOODS (Bayliss et al. 2011), COSMOS (Coughlin et al. 2018)) and obtain new observations to complement existing data. Deep surveys use long exposure times in order to see faint, and often small, galaxies. This is very valuable, especially for high-z studies. One downside of these very deep surveys, is that they tend to cover a small region on the sky. They suffer from line of sight clustering effects, and can be subject to density variations along the line of sight (also known as cosmic variance). For example, if this small region includes a galaxy cluster within the line of sight, then the region will appear densely populated. If this is the only region of the universe surveyed, biases will be introduced. Any conclusions drawn about the universe as a whole may be flawed because the survey region is only looking at an overdensity. These types of surveys are impacted by cosmic variance and do not provide a broad picture of the universe.

Other surveys choose to lessen the effects of cosmic variance by performing wide studies of many fields spread across the sky. Unfortunately, these surveys are usually shallow, sacrificing depth for spatial coverage. These wide surveys typically only survey galaxies via one emission line. As a recent example, Cook et al. (2019) search for H α galaxies out to 200 Mpc and confirm them using spectroscopy. This study has found hundreds of new ELGs not found by previous emission-line studies, but does not reach to cosmologically interesting distances.

As discussed in Madau & Dickinson (2014), there is a need for a NB survey which

is both deep and wide. This would allow for a wide range of redshift coverage, while also accounting for cosmic variance. This is why the SFACT survey is important. Our survey aims to cover 25-30 deg^2 – across the Fall and Spring sky – to a distance of $z=1$. However, it will also discover sources based on non-optical emission lines which push our redshift coverage further and grow our potential even more. Between the quality of the instrumentation and the quantity of sources, SFACT will provide robust measurements for future studies of the SFRD evolution.

To search this depth, we primarily utilize the $H\alpha$, [O III], and [O II] emission lines. By using the same survey methodology for all three lines (see Chapter 3) we aim to create a coherent sample which is equally robust across our redshift range.

Yet, it is not enough to have a deep and wide imaging survey. The success of SFACT relies on both the imaging and the follow-up spectroscopy. Every target will have both imaging data (in BB and NB filters) as well as a spectrum. This allows us four key advantages.

By obtaining photometric measurements of the NB flux from our images, we include all of the light from a galaxy in our NB filter, no matter how large the angular size of the galaxy is. Although we will have spectroscopic data, flux measurements acquired from spectra may be inaccurate. Measuring emission-line flux via spectroscopic fibers would limit how much flux of a galaxy can actually be measured (only light contained within the radius of the fiber is measured).

However, by using spectra of the SFACT galaxies to complement the imaging data, we can achieve higher accuracy derivations of the total emission-line luminosity for each source.. Having spectra allows us to measure the Balmer decrement with $H\alpha/H\beta$ ratios for all $H\alpha$ -detected galaxies, and with $H\gamma/H\beta$ ratio for many of the [O III] galaxies. This is crucial for reliable absorption corrections. This correction, on an individual basis, was shown by Salim & Lee (2012) to significantly impact the high-luminosity end of the luminosity function. Performing an accurate accounting

of the effects of dust on a source’s narrow-band luminosity is necessary to accurately derive SFRs. Follow-up spectroscopy also allows us to accurately measure and correct for the influence of nearby emission lines such as [N II], which often blends with H α emission (see Chapter 6). Not over-estimating the amount of line emission flux is also key to deriving the correct SFR.

Having spectra of each source allows us to accurately measure the redshift for the object. A precise redshift and distance measurement means we can more precisely determine the absolute properties of a galaxy, and have more accurate determinations of the SFR.

Line ratios from the spectra also allow us to identify many of the active galactic nuclei which otherwise could contaminate the catalog of star-forming galaxies (see Chapter 4). While we cannot wholly count on these line ratios to identify all contaminants, understanding a limit on the influence of other ionizing sources in our sample is valuable.

1.3 SFACT and Thesis Outline

The SFACT project is a team project. It would be impossible to complete without collaboration between multiple people. However, since it was always known that the work would form the basis of multiple theses, there has been a division of labor. I was primarily in charge of the imaging observations, the processing of the images, and the photometric results. These represent the major components to achieve the goal of measuring the SFRD of the local universe.

In Chapter 2, we introduce the SFACT survey. We discuss the survey motivation, survey design, and the current scope of the project. We also discuss the other applications of the survey, beyond just SFRD studies. Chapter 3 describes the processing of the survey images. This includes the observation details, the selection of the SFACT targets, and the photometric process. This chapter discusses all this through the

lens of the three pilot-study fields. This focus on the pilot-study fields is also true of Chapter 4 which presents the spectroscopic side of SFACT. Although not the primary domain of my thesis work, the results borne of the spectroscopic follow-up are crucial for the determination of the SFRs of the SFACT galaxies. Chapter 5 steps away from the main SFACT project in order to discuss a smaller cross-calibration project. This work uses existing surveys to examine emission-line selected galaxy samples and construct NB luminosity functions. This provides a scaffolding for doing the same type of analysis with SFACT galaxies in the future. Combining these two projects, Chapter 6 presents a preliminary examination of the SFRD of the current SFACT catalog. The culmination of the thesis is shown in the H α , [O III], and [O II] SFRs within our nine redshift windows. Finally, Chapter 7 summarizes our work and discusses the future plans for the SFACT survey.

References

- Bayliss, K. D., McMahon, R. G., Venemans, B. P., et al. 2011, MNRAS, 413, 2883.
doi:10.1111/j.1365-2966.2011.18360.x
- Brinchmann, J., Charlot, S., White, S. D. M., et al. 2004, MNRAS, 351, 1151.
doi:10.1111/j.1365-2966.2004.07881.x
- Brunker, S. W., Salzer, J. J., Janowiecki, S., et al. 2020, ApJ, 898, 68.
doi:10.3847/1538-4357/ab9ec0
- Cardamone, C., Schawinski, K., Sarzi, M., et al. 2009, MNRAS, 399, 1191.
doi:10.1111/j.1365-2966.2009.15383.x
- Cook, D. O., Kasliwal, M. M., Van Sistine, A., et al. 2019, ApJ, 880, 7.
doi:10.3847/1538-4357/ab2131
- Coughlin, A., Rhoads, J. E., Malhotra, S., et al. 2018, ApJ, 858, 96. doi:10.3847/1538-4357/aab620
- Daddi, E., Dickinson, M., Morrison, G., et al. 2007, ApJ, 670, 156. doi:10.1086/521818
- Ellis, R. S., McLure, R. J., Dunlop, J. S., et al. 2013, ApJ, 763, L7. doi:10.1088/2041-8205/763/1/L7
- Fonseca, J. & Camera, S. 2020, MNRAS, 495, 1340. doi:10.1093/mnras/staa1136
- Gallego, J., García-Dabó, C. E., Zamorano, J., et al. 2002, ApJ, 570, L1.
doi:10.1086/340830
- Gunawardhana, M. L. P., Hopkins, A. M., Bland-Hawthorn, J., et al. 2013, MNRAS, 433, 2764. doi:10.1093/mnras/stt890
- Guo, H., Yang, X., Raichoor, A., et al. 2019, ApJ, 871, 147. doi:10.3847/1538-4357/aaf9ad

- Hogg, D. W., Cohen, J. G., Blandford, R., et al. 1998, ApJ, 504, 622.
doi:10.1086/306122
- Hopkins, A. M. & Beacom, J. F. 2006, ApJ, 651, 142. doi:10.1086/506610
- Kellar, J. A., Salzer, J. J., Wegner, G., et al. 2012, AJ, 143, 145. doi:10.1088/0004-6256/143/6/145
- Kennicutt, R. C., Hao, C.-N., Calzetti, D., et al. 2009, ApJ, 703, 1672.
doi:10.1088/0004-637X/703/2/1672
- Kennicutt, R. C. 1998, ARA&A, 36, 189. doi:10.1146/annurev.astro.36.1.189
- Kewley, L. J., Nicholls, D. C., & Sutherland, R. S. 2019, ARA&A, 57, 511.
doi:10.1146/annurev-astro-081817-051832
- Khostovan, A. A., Sobral, D., Mobasher, B., et al. 2015, MNRAS, 452, 3948.
doi:10.1093/mnras/stv1474
- Khostovan, A. A., Malhotra, S., Rhoads, J. E., et al. 2020, MNRAS, 493, 3966.
doi:10.1093/mnras/staa175
- Lilly, S. J., Le Fevre, O., Hammer, F., et al. 1996, ApJ, 460, L1. doi:10.1086/309975
- Ly, C., Malkan, M. A., Kashikawa, N., et al. 2007, ApJ, 657, 738. doi:10.1086/510828
- Madau, P. & Dickinson, M. 2014, ARA&A, 52, 415. doi:10.1146/annurev-astro-081811-125615
- Mehta, V., Scarlata, C., Colbert, J. W., et al. 2015, ApJ, 811, 141. doi:10.1088/0004-637X/811/2/141
- Moustakas, J., Kennicutt, R. C., & Tremonti, C. A. 2006, ApJ, 642, 775.
doi:10.1086/500964
- Pettini, M., Kellogg, M., Steidel, C. C., et al. 1998, ApJ, 508, 539. doi:10.1086/306431
- Ramón-Pérez, M., Bongiovanni, Á., Pérez García, A. M., et al. 2019, A&A, 631, A10.
doi:10.1051/0004-6361/201833295
- Salim, S. & Lee, J. C. 2012, ApJ, 758, 134. doi:10.1088/0004-637X/758/2/134

- Sanders, D. B., Mazzarella, J. M., Kim, D.-C., et al. 2003, AJ, 126, 1607.
doi:10.1086/376841
- Sobral, D., Smail, I., Best, P. N., et al. 2013, MNRAS, 428, 1128.
doi:10.1093/mnras/sts096
- Sullivan, M., Treyer, M. A., Ellis, R. S., et al. 2000, MNRAS, 312, 442.
doi:10.1046/j.1365-8711.2000.03140.x
- Suzuki, T. L., Kodama, T., Sobral, D., et al. 2016, MNRAS, 462, 181.
doi:10.1093/mnras/stw1655
- Tresse, L. & Maddox, S. J. 1998, ApJ, 495, 691. doi:10.1086/305331
- Vaccari, M., Marchetti, L., Franceschini, A., et al. 2010, A&A, 518, L20.
doi:10.1051/0004-6361/201014694
- Van Sistine, A., Salzer, J. J., Sugden, A., et al. 2016, ApJ, 824, 25
- Villar, V., Gallego, J., Pérez-González, P. G., et al. 2008, ApJ, 677, 169.
doi:10.1086/528942
- Westra, E., Geller, M. J., Kurtz, M. J., et al. 2010, ApJ, 708, 534. doi:10.1088/0004-637X/708/1/534
- Wilkins, S. M., Lovell, C. C., & Stanway, E. R. 2019, MNRAS, 490, 5359.
doi:10.1093/mnras/stz2894
- Zhai, Z., Benson, A., Wang, Y., et al. 2019, MNRAS, 490, 3667.
doi:10.1093/mnras/stz2844

Chapter 2

Introduction to the SFACT Survey

2.1 Survey Motivation

The majority of my thesis centers on initiating and carrying out the Star Formation Across Cosmic Time (SFACT) survey. This narrow-band survey utilizes the strengths of WIYN² to create a large, diverse catalog of star-forming galaxies at $z < 1$.

Surveys designed to discover emission-line galaxies (ELGs) are not new. Early work used objective-prism spectroscopy in order to select their candidates (e.g., Smith 1975; MacAlpine et al. 1977; MacAlpine & Williams 1981; Sanduleak & Pesch 1982; Pesch & Sanduleak 1983; Wasilewski 1983; Markarian & Stepanian 1983; Zamorano et al. 1994, 1996; Hopp et al. 2000; Salzer et al. 2000, 2001, 2002) and later surveys used narrow-band imaging data (e.g., Boroson et al. 1993; Ryan-Weber et al. 2004; Kakazu et al. 2007; Werk et al. 2010; Ly et al. 2011; Kellar et al. 2012; Cook et al. 2019; Salzer et al. 2020; Watkins et al. 2021). Extreme star-forming objects such as Green Peas (Cardamone et al. 2009; Brunker et al. 2020) and Blueberries (Yang et al. 2017) have even been found in broad-band surveys due to their high equivalent widths (Rosenwasser et al. 2022). Very recently, the HETDEX survey (Gebhardt et

¹This chapter is based on the paper Salzer, J. J., Carr, D. J., Sieben, J., Hirschauer, A. S. 2022,; I contributed significantly to this team effort, primarily by taking the observations and performing image processing.

²The WIYN Observatory is a joint facility of the University of Wisconsin–Madison, Indiana University, NSF’s NOIRLab, the Pennsylvania State University, Purdue University, and the University of California, Irvine.

al. 2021) has conducted a non-targeted, wide-area, blind spectroscopic ELG survey utilizing multiple integral field units.

SFACT builds on all of these previous surveys. This survey uses a narrow-band imaging technique which employs custom filters, allowing the survey to reach to high redshifts. However, the value of the imaging technique is enhanced by the WIYN telescope and instrument combination.

Working at Indiana University has allowed us access to the WIYN 3.5m telescope and the wide field One Degree Imager (ODI) camera. Together, we have the tools to carry out a deep and wide imaging survey. Furthermore, the Hydra bench spectrograph allows us to conduct efficient follow-up spectroscopy. As described in the next section, all of these pieces come together to build a survey which is accurate, reliable, and multi-purpose.

The survey was also motivated by a wide variety of possible science applications. SFACT can be used as the basis of population studies for rare objects such as Green Peas (Cardamone et al. 2009; Brunker et al. 2020), AGN, or extremely metal-poor dwarf galaxies (McQuinn et al. 2020). We expect to discover numerous examples of these objects, allowing for investigations into the environments and evolution of rare galaxies. Our survey design also allows us to gather the data necessary for studying the evolution of metal abundances with redshift. Most importantly for my thesis, SFACT allows for the study of the star-formation history of galaxies up to $z = 1$. This is expanded upon in Chapter 6.

The SFACT survey is built upon the success of the earlier H α Dots survey (Kellar et al. 2012; Watkins et al. 2021). H α Dots were surprise discoveries found in narrow-band (NB) images obtained for an entirely different purpose. The ALFALFA H α (AHA) project (Van Sistine et al. 2016) utilized source lists derived from the Arecibo Fast Legacy ALFA (ALFALFA) blind H I survey (Giovanelli et al. 2005; Haynes et al. 2011). AHA was a NB imaging project designed to measure the star-formation

rate density in the local universe with unprecedented precision. In the course of the AHA project, compact ELGs not associated with the target ALFALFA galaxies were discovered and spawned the H α Dots survey.

Two different telescopes were used to collect H α Dot data, forming two independent survey lists. A total of 358 dots were identified with the WIYN 0.9m telescope (Kellar et al. 2012; Salzer et al. 2020) at Kitt Peak. These objects have a median R-band magnitude of 19.97 and a median NB emission-line flux of $1.95 \times 10^{-15} \text{ erg s}^{-1} \text{ cm}^{-2}$. This yielded a surface density of $5.23 \text{ ELG deg}^{-2}$. The second list contains dots found with the KPNO 2.1m telescope (Watkins et al. 2021). With the larger telescope aperture, the median R-band magnitude was 21.59 with a median NB emission-line flux of $4.57 \times 10^{-16} \text{ erg s}^{-1} \text{ cm}^{-2}$. Correspondingly, more objects were found: 454 dots were discovered for a surface density of $29.30 \text{ ELGS deg}^{-2}$. As shown in Watkins et al. (2021), this difference is primarily due to the telescope aperture.

Extrapolating, we then arrive at approximate figures-of-merit for a similar project carried out on a 3.5m telescope. We predict a median R-band magnitude of 22.7, a median narrow-band emission-line flux of $1.55 \times 10^{-16} \text{ erg s}^{-1} \text{ cm}^{-2}$, and $\sim 100\text{-}120$ ELGs per deg 2 . However, SFACT as it stands has three narrow-band filters, which increases our prediction to 300-360 ELGs deg $^{-2}$. These are estimates, but as discussed later, they are very good estimates of reality.

2.2 Survey Design

2.2.1 WIYN Telescope

As alluded to earlier, the SFACT survey was developed to use the full capabilities of the WIYN 3.5m telescope. There were several key factors which drove the survey design.

- i) The large aperture and superior image quality with the WIYN telescope allows us to reach an excellent depth. As proven by early survey results, we are able to regularly detect objects as faint as $r \sim 26$.
- ii) The $f/6.3$ beam of the Nasmyth focus on WIYN is a slow enough beam to use with our narrow-band filters. NB filters are designed to work in collimated beams; when placed in converging beams the wavelength of the center of the bandpass shifts slightly with increasing distance from the optical axis. This effect is particularly problematic when using NB filters in fast beams usually associated with wide-field cameras. The slower convergence of WIYN means that, despite the wide field of view, we have a fairly uniform bandpass across the entire detector.
- iii) The ODI camera has an image scale of $0.11'' \text{ pixel}^{-1}$, which allows it to take advantage of the excellent image quality provided by the WIYN telescope. With a field of view of $48' \times 40'$, we are able to take images covering $\sim 0.53 \text{ deg}^2$, giving us large target fields in which to find emission-line galaxies. The properties of ODI are discussed further in Chapter 3.
- iv) WIYN also has the Hydra multi-fiber positioner which allows for a direct path for acquiring follow-up spectra of our targets. These spectra (discussed further in Chapter 4) are crucial for determining the distance to our targets, determining the type of object detected, and revealing which emission line fell in our NB filter. Because our survey is an emission-line survey with objects detected via their emission line, we are able to use the WIYN telescope for both the imaging and spectroscopic observations.
- v) Finally, we recognized that the photometric depth of WIYN would allow us to detect multiple emission lines, at different redshifts, in the same narrow-band filter. This allows us to probe multiple redshift windows, over a wide redshift range, with a limited number of filters.

Table 2.1. Properties of the SFACT Narrow-Band Filters

Filter (1)	λ_{center} Å (2)	$\Delta\lambda$ Å (3)	z range - H α (4)	z range - [O III] (5)	z range - [O II] (6)
NB659=NB2	6590	81.1	-0.002 - 0.010	0.308 - 0.324	0.757 - 0.779
NB695=NB1	6950	91.0	0.052 - 0.066	0.378 - 0.397	0.852 - 0.877
NB746=NB3	7460	96.7	0.129 - 0.144	0.480 - 0.500	0.988 - 1.015
NB812*	8120	90	0.230 - 0.244	0.613 - 0.631	1.166 - 1.191
NB912*	9120	90	0.383 - 0.397	0.812 - 0.830	1.435 - 1.459

Notes. — *Proposed additional SFACT filters

2.2.2 Narrow-Band Filters

In order to reach these multiple emission lines, custom narrow-band filters needed to be designed. A filter with a central wavelength of 6950 Å with a width of \sim 90 Å was settled on first. Although a smaller bandwidth would've meant a greater sensitivity to fainter emission lines, a larger width corresponds to a wider redshift range over which we can detect objects. Since our primary objective is to discover a large number of ELGs, this larger width was an acceptable compromise between survey goals and design specifications to guarantee a high quality filter. This filter (henceforth NB1) was chosen as the first filter to order and take test observations with.

After a successful test, subsequent filters were ordered. The other NB filters in our current set of filters are centered at 6590 Å(henceforth NB2) and 7460 Å(henceforth NB3). NB2 was chosen so that it could also serve as a zero redshift H α filter for anyone who uses WIYN.

With these filters we are able to cover nine different redshift windows from z=0 to z=1 via our three primary emission lines (H α , [O III], and [O II]) The redshift ranges for these filters, for each line, can be seen in Table 2.1. Although other emission lines fall into our filters and can be used for star-formation rate studies, the majority of

this thesis focuses on these three emission lines.

Two proposed filters for the future are also detailed in this table. Although these filters have not yet been ordered, the hope is that these future filters will complement the existing redshift coverage. Figure 2.1 shows the wavelength coverage of all current and proposed SFACT filters and the corresponding redshift windows. On the right-hand side, a condensed visualization shows the total redshift coverage of SFACT.

The additional two filters would not only allow us to reach to much higher redshifts, but crucially the NB912 filter would overlap an existing redshift window. At $0.383 < z < 0.397$, a combination of the existing NB1 filter and the proposed NB912 filter would allow us to detect galaxies via both their [O III] and H α emission lines, respectively, perhaps allowing us to directly compare derived properties of the same galaxy despite being detected via different lines. While this is a future plan for the SFACT project, we have attempted to lay the groundwork for such studies using KISS data (see Chapter 5).

2.2.3 Target Fields

SFACT is designed to be large enough to draw robust conclusions about the star formation history in the local universe, but we cannot survey the entire sky. Therefore, we sample target fields spread out across the sky in order to form a representative sample and also to serve as a counter for cosmic variance. This is especially important for our survey since our narrow redshift windows mean we might inadvertently survey extremely high density filaments or low density voids without us immediately noticing. We expect to mitigate these density variations by averaging over many widely-spaced fields, thereby mitigating the effects of cosmic variance. The complete SFACT survey is projected to include 50 to 60 fields, or 25 - 30 deg 2 of sky coverage.

SFACT survey fields must meet multiple criteria. Primarily, our fields must fall within the footprint of the Sloan Digital Sky Survey (SDSS; York et al. 2000) in

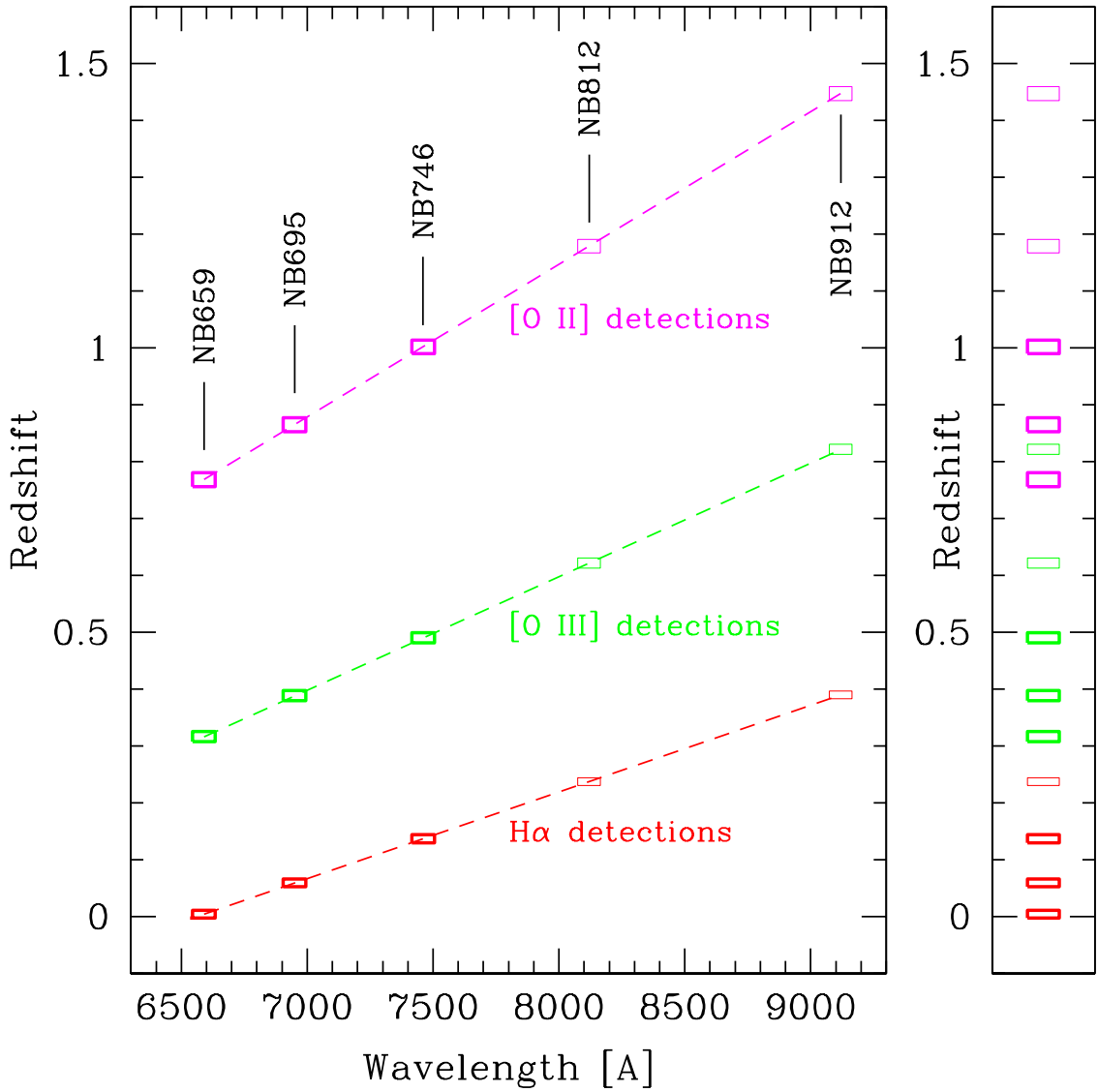


Figure 2.1 Plot showing the wavelength coverage of the SFACT narrow-band filters as well as the redshift ranges associated with the detection of three strong optical nebular emission lines. Each vertical location of a box represents the redshift range for the emission line indicated. The three emission lines shown here are our three primary lines, and the majority of SFACT targets are detected via one of these three lines. We also show the two additional filters we plan to add to the survey. The plot on the right-hand side is a compressed look at the redshift windows to better demonstrate the redshift coverage available through these five filters.

order for our photometric calibrations to be carried out (see Chapter 3). This overlap also allows us to use the SDSS data to help identify image artifacts with ELG-like appearances before we take spectroscopic follow-up observations. Most of our fields are also located at high Galactic latitude to minimize foreground extinction. Most also have declinations between 10° and 50° so that they transit within 20° of the zenith at Kitt Peak. These were the critical criteria for picking target field locations.

Many of our early fields also overlap with previous surveys which have discovered compact ELGs, centering our fields on the ELG in question. These are most commonly Green Pea galaxies (e.g., Cardamone et al. 2009; Brunker et al. 2020). These are extreme star-forming galaxies found in [O III]-detected samples either in the KISS (Salzer et al. 2000, 2001; Gronwall et al. 2004; Jangren et al. 2005) or H α Dot (Kellar et al. 2012; Salzer et al. 2020) surveys. Observing SFACT survey fields at the location of Green Peas fulfills our most important field-selection criteria, while also providing data for future work associated with SFACT data. These fields have been the focus of a pencil-beam redshift survey (Brunker et al. 2022) also using the Hydra multi-fiber positioner on WIYN. This redshift survey will provide a comparison sample for future projects which examine the environment of unique SFACT galaxies. Although the Green Pea galaxy itself is often not at the right redshift to be detected in SFACT, the potential pairing of these data sets is still incredibly valuable.

Field locations for SFACT have also been picked in order to make the best use of the available observing time. When no Green Pea galaxy or H α Dot was available in the right region of the sky, fields were chosen to fill the gap in our coverage such that they met the critical criteria, were widely spaced in comparison with other nearby SFACT fields, and were devoid of bright stars.

All of our fields are given a field designation which we use throughout this thesis. Fall fields are given the nomenclature of SFF##; Spring fields are written as SFS##. The number denotes the order in which the imaging observations are completed, with

the exception of the first fifteen Fall fields. Instead, SFF01 – SFF15 are named in ascending RA order.

2.3 Applications of SFACT Survey

The SFACT survey is a large survey with the potential for many, wide-reaching science applications. Here, we briefly discuss some potential science applications of the SFACT project to convey the scope of the project. This is not intended to be a complete list, as the applications are focused on what the current team members are interested in.

The primary goal of the survey, and of this thesis, is to investigate the evolution of the star-formation rate density (SFRD) to $z=1$ and beyond. In the completed survey, we expect to have large enough samples of star-forming galaxies in each redshift window to provide robust estimates of the SFRD up to $z=1$. As we demonstrate in Chapter 6, we are beginning to achieve this even with a smaller sample.

Another main goal of the survey is the characterization of strong-lined active galactic nuclei (AGN) populations. We have already discovered many AGN in our SFACT fields and are able to use our spectra to study their metallicities. This will be valuable data for studying the evolution of metal abundances beyond the local universe, a subject of recent research (Dors et al. 2019; Carvalho et al. 2020; Flury & Moran 2020).

SFACT will also allow us to study the demographics of dwarf star-forming galaxies out to redshifts of $z\sim 0.5$. These intermediate- and low-luminosity galaxies are detected via $\text{H}\alpha$ and [O III] in substantial quantities. This will allow us to study both the properties and demographics of this group of galaxies, as well as probe for redshift dependencies by using the spectra. This will help increase understanding of the evolution of the dwarf star-forming galaxy population at $z < 0.5$. de los Reyes & Kennicutt (2019) have done recent work looking into deriving SFR surface densities

from dwarf and low-surface-brightness galaxies.

Because SFACT will have an extensive catalog of redshifts, we would also be able to perform environmental studies of star-forming galaxies and AGN out to $z = 0.5$. By studying the galaxy distribution in the vicinity of the SFACT ELGs, we gain insight into the effects the environment has on star-formation and AGN activity. This work has already begun with a study by Brunker et al. (2022) that examined the environment of Green Pea galaxies using data from early SFACT spectra.

With our large spectral catalog we also aim to study the evolution of galaxy abundances out to $z = 0.9$. We expect to measure the abundances of hundreds of galaxies in each redshift window, providing the data to robustly examine the redshift evolution of the luminosity-metallicity and mass-metallicity relations. Similar work has been done with a previous emission-line survey (Hirschauer et al. 2018). Our ability to perform these analyses will grow as we extend our follow-up spectral observations redward.

Like any large survey, SFACT has the potential to discover many rare, and interesting, objects. Already we have identified a cataclysmic variable star (Salzer et al. 2022), many Green Pea Galaxies (Cardamone et al. 2009), and extremely metal-poor dwarf galaxies (see McQuinn et al. 2020 for a recent review of extremely metal-poor galaxies). We also expect to find Blueberries (Yang et al. 2017) which, along with Green Peas, are among the most extreme star-forming galaxies known. For some of these classes of objects we will find large enough quantities to learn more about their global properties and how they change with lookback time. And, we may still be surprised by other unexpected discoveries in our catalog.

2.4 Samples in this Thesis

The SFACT survey is still in progress so the ideal sample of 50 - 60 fields has not yet been realized. The following two chapters focus on the results drawn from our

three pilot-study fields. These are three fields which were the first to have complete imaging data, and the first to have significantly complete follow-up spectroscopy. The bulk of our analysis is based on these pilot-study fields.

However, in order to begin to investigate the star-formation rate density, we needed a larger sample size. We have created an additional subset of our current work which we refer to as the thesis sample. This sample contains 12 Fall fields for which the processed spectroscopy includes at least 40% of the SFACT targets. The results presented in Chapter 6 draw upon this thesis sample.

References

- Boroson, T. A., Salzer, J. J., & Trotter, A. 1993, ApJ, 412, 524. doi:10.1086/172940
- Brunker, S. W., Salzer, J. J., Janowiecki, S., et al. 2020, ApJ, 898, 68. doi:10.3847/1538-4357/ab9ec0
- Brunker, S. W., Salzer, J. J., Kimsey-Miller, B., et al. 2022, ApJ, 926, 131. doi:10.3847/1538-4357/ac469f
- Cardamone, C., Schawinski, K., Sarzi, M., et al. 2009, MNRAS, 399, 1191. doi:10.1111/j.1365-2966.2009.15383.x
- Carvalho, S. P., Dors, O. L., Cardaci, M. V., et al. 2020, MNRAS, 492, 5675. doi:10.1093/mnras/staa193
- Cook, D. O., Kasliwal, M. M., Van Sistine, A., et al. 2019, ApJ, 880, 7. doi:10.3847/1538-4357/ab2131
- de los Reyes, M. A. C. & Kennicutt, R. C. 2019, ApJ, 872, 16. doi:10.3847/1538-4357/aafa82
- Dors, O. L., Monteiro, A. F., Cardaci, M. V., et al. 2019, MNRAS, 486, 5853. doi:10.1093/mnras/stz1242
- Flury, S. R. & Moran, E. C. 2020, MNRAS, 496, 2191. doi:10.1093/mnras/staa1563
- Gebhardt, K., Mentuch Cooper, E., Ciardullo, R., et al. 2021, ApJ, 923, 217. doi:10.3847/1538-4357/ac2e03
- Giovanelli, R., Haynes, M. P., Kent, B. R., et al. 2005, AJ, 130, 2598. doi:10.1086/497431
- Gronwall, C., Jangren, A., Salzer, J. J., et al. 2004, AJ, 128, 644. doi:10.1086/422348
- Haynes, M. P., Giovanelli, R., Martin, A. M., et al. 2011, AJ, 142, 170. doi:10.1088/0004-6256/142/5/170

- Haynes, M. P., Giovanelli, R., Kent, B. R., et al. 2018, ApJ, 861, 49. doi:10.3847/1538-4357/aac956
- Hirschauer, A. S., Salzer, J. J., Janowiecki, S., et al. 2018, AJ, 155, 82. doi:10.3847/1538-3881/aaa4ba
- Hopp, U., Engels, D., Green, R. F., et al. 2000, A&AS, 142, 417.
- Jangren, A., Salzer, J. J., Sarajedini, V. L., et al. 2005, AJ, 130, 2571. doi:10.1086/497071
- Kakazu, Y., Cowie, L. L., & Hu, E. M. 2007, ApJ, 668, 853.
- Kellar, J. A., Salzer, J. J., Wegner, G., et al. 2012, AJ, 143, 145. doi:10.1088/0004-6256/143/6/145
- Ly, C., Lee, J. C., Dale, D. A., et al. 2011, ApJ, 726, 109. doi:10.1088/0004-637X/726/2/109
- MacAlpine, G. M. & Williams, G. A. 1981, ApJS, 45, 113. doi:10.1086/190710
- MacAlpine, G. M., Smith, S. B., & Lewis, D. W. 1977, ApJS, 34, 95. doi:10.1086/190444
- Markarian, B. E. & Stepanian, D. A. 1983, Astrofizika, 19, 639
- McQuinn, K. B. W., Berg, D. A., Skillman, E. D., et al. 2020, ApJ, 891, 181. doi:10.3847/1538-4357/ab7447
- McQuinn, K. B. W., Berg, D. A., Skillman, E. D., et al. 2020, ApJ, 891, 181. doi:10.3847/1538-4357/ab7447
- Pesch, P. & Sanduleak, N. 1983, ApJS, 51, 171. doi:10.1086/190843
- Rosenwasser, B. E., Taylor, A. J., Barger, A. J., et al. 2022, arXiv:2201.10562
- Ryan-Weber, E. V., Meurer, G. R., Freeman, K. C., et al. 2004, AJ, 127, 1431. doi:10.1086/381905
- Salzer, J. J., Gronwall, C., Lipovetsky, V. A., et al. 2000, AJ, 120, 80. doi:10.1086/301418

- Salzer, J. J., Gronwall, C., Lipovetsky, V. A., et al. 2001, AJ, 121, 66.
doi:10.1086/318040
- Salzer, J. J., Gronwall, C., Sarajedini, V. L., et al. 2002, AJ, 123, 1292.
doi:10.1086/339024
- Salzer, J. J., Feddersen, J. R., Derloshon, K., et al. 2020, AJ, 160, 242.
doi:10.3847/1538-3881/abba11
- Salzer, J. J., Carr, D. J., Sieben, J., Hirschauer, A. S. 2022, ApJ (Submitted)
(SFACT1)
- Sanduleak, N. & Pesch, P. 1982, ApJ, 258, L11. doi:10.1086/183821
- Smith, M. G. 1975, ApJ, 202, 591. doi:10.1086/154011
- Van Sistine, A., Salzer, J. J., Sugden, A., et al. 2016, ApJ, 824, 25. doi:10.3847/0004-637X/824/1/25
- Wasilewski, A. J. 1983, ApJ, 272, 68. doi:10.1086/161262
- Watkins, J. D., Salzer, J. J., Van Sistine, A., et al. 2021, ApJS, 253, 39.
doi:10.3847/1538-4365/abdf4b
- Werk, J. K., Putman, M. E., Meurer, G. R., et al. 2010, AJ, 139, 279.
doi:10.1088/0004-6256/139/1/279
- Yang, H., Malhotra, S., Gronke, M., et al. 2017, ApJ, 844, 171. doi:10.3847/1538-4357/aa7d4d
- York, D. G., Adelman, J., Anderson, J. E., et al. 2000, AJ, 120, 1579.
doi:10.1086/301513
- Zamorano, J., Rego, M., Gallego, J. G., et al. 1994, ApJS, 95, 387. doi:10.1086/192103
- Zamorano, J., Gallego, J., Rego, M., et al. 1996, ApJS, 105, 343. doi:10.1086/192317

Chapter 3

SFACT Imaging

3.1 Introduction

The Star Formation Across Cosmic Time (SFACT) survey is an ongoing wide-field imaging and spectroscopic program which targets the detection of large numbers of extragalactic emission-line sources. As a narrow-band (NB) survey, SFACT is able to discover a wealth of new sources that exhibit strong emission lines. The SFACT survey methodology draws upon the rich legacy of previous emission-line galaxy (ELG) surveys (e.g., MacAlpine et al. 1977; Markarian & Stepanian 1983; Salzer et al. 2000; Kakazu et al. 2007; Kellar et al. 2012). SFACT builds on this previous work by using a medium-class telescope with a wide field of view and three custom NB filters. The primary goal is to produce a high quality survey for emission-line objects with a selection function and completeness limits that can be accurately quantified, so that the resulting catalog of ELGs will be useful for a broad range of studies requiring statistically-complete galaxy samples.

The results for our pilot-study fields of SFACT are presented in a series of three papers. The first SFACT paper (Salzer et al. 2022, henceforth referred to as SFACT1) presents the survey goals and motivation. This paper discusses the different types

³The results discussed in this chapter were submitted for publication in Sieben, J., Salzer, J. J., Carr, D. J., Hirschauer, A. S., *The Star Formation Across Cosmic Time (SFACT) Survey. II. The First Catalog of Targets from a New Narrow-Band Survey for Emission-Line Objects*, 2022, ApJS (submitted)

of ELGs which SFACT is designed to discover and explores future applications of such data. Example objects are also shown with both photometric and spectroscopic results. The current chapter (based on the SFACT2 paper) focuses on the imaging portion of the survey. We discuss the observation and processing procedures as well as how targets are selected. This culminates in the presentation of our initial ELG catalogs of the objects in the three pilot-study fields. The third SFACT paper (Carr et al. 2022, henceforth referred to as SFACT3) focuses on the spectroscopic data, discussing the procedures for the observations and processing of the spectroscopic data. These data are used to verify the nature of the targets discovered in the imaging data. Accordingly, SFACT3 presents the spectra corresponding to the example images in SFACT2. This last paper also discusses further implications of the types of ELGs discovered.

In this chapter, we first describe our observation procedures (Section 3.2.1) and our data processing technique (Section 3.2.2). Our method for selecting targets for inclusion in our survey catalogs is detailed in Section 3.3, along with our photometry method and calibration in Section 3.3.2. The results of the pilot study, including the data and example objects, are presented in Section 5.4. For all of the SFACT papers we assume a standard Λ CDM cosmology with $\Omega_m = 0.27$, $\Omega = 0.73$, and $H_0 = 70 \text{ km s}^{-1} \text{ Mpc}^{-1}$.

3.2 Observations & Data Processing

3.2.1 Observations

The fields observed for SFACT were selected to overlap with the Sloan Digital Sky Survey (SDSS, York et al. 2000; Aguado et al. 2019), which we used for photometric calibrations. Two of the fields presented in this pilot study were centered on ELGs found in the previous H α Dots survey (Kellar et al. 2012; Salzer et al. 2020; Watkins

et al. 2021), thus providing a valuable testbed for the current survey methodology. The selection of the SFACT survey fields is discussed in more detail in SFACT1.

The imaging data used for this paper were obtained during three observing seasons. For a full list of observing dates, see Table 3.2.1. In November of 2016, initial test data were acquired for the SFF10 and SFF15 fields in the r-band and first narrow-band filter (NB1). These observations provided the data used to develop our processing and object-selection methods (see Section 3.3). In 2017 we added additional broad-band (BB) observations in g- and i-band plus included an additional field (SFF01). Our data set for the pilot study was then completed upon the subsequent addition of two additional NB filters in 2018.

All survey data were acquired using the One Degree Imager (ODI; Harbeck et al. 2010) on the WIYN⁴ 3.5m telescope sited at Kitt Peak, Arizona. ODI consists of 30 Orthogonal Transfer Array (OTA) CCDs, each of which comprises $64\ 480 \times 494$ pixel cells. The pixel size for the ODI OTAs is 12μ , which yields an image scale of $0.11''\ \text{pixel}^{-1}$. The total field of view of ODI is $40' \times 48'$.

3.2.1.1 Science Observations

After our 2016 observing season, we found that observations with additional BB filters (g and i) were strongly desired for two reasons. First, we discovered that i-filter images were needed to correctly perform our NB1 continuum subtraction as detailed in Section 3.2.2.2. Having three BB filters also allowed us to obtain a wider range of photometric measurements of our targets. Accordingly, we added the two BB filters to our observing procedure. To be considered complete, all survey fields are observed through six filters: three BB filters (gri) and three NB filters. The BB data were obtained through g, r, and i filters $\sim 1500\ \text{\AA}$ in width. The BB bandpasses

⁴The WIYN Observatory is a joint facility of the University of Wisconsin–Madison, Indiana University, NSF’s NOIRLab, the Pennsylvania State University, Purdue University, and the University of California, Irvine.

Table 3.1. Observation Dates

Field	Filter	Observation Date	PSF FWHM	α (J2000)	δ (J2000)
SFF01	r	09/17/2017	0.89''	21:42:42	19:59:28
	i	09/17/2017	0.83''		
	g	09/17/2017	0.76''		
	NB1	09/13/2018	0.93''		
	NB2	09/14/2018	0.78''		
	NB3	09/13/2018	0.96''		
SFF10	r	11/07/2016	0.83''	01:44:20	27:54:13
	i	08/19/2017	0.81''		
	g	08/19/2017	1.23''		
	NB1	11/07/2016	0.85''		
	NB2	09/14/2018	0.85''		
	NB3	09/13/2018	0.69''		
SFF15	r	11/07/2016	0.81''	02:38:52	27:51:43
	i	08/19/2017	0.87''		
	g	08/19/2017	1.17''		
	NB1	11/07/2016	0.72''		
	NB2	09/14/2018	0.70''		
	NB3	09/14/2018	0.66''		

mimic the SDSS filters (York et al. 2000).

The NB data were obtained through three special filters designed for the survey, centered at 6590 Å, 6950 Å, and 7460 Å, each with a width of ~ 90 Å (henceforth NB2, NB1, and NB3, respectively). The exact bandpasses are detailed in SFACT1 as well as the redshift range accessible via four common emission lines. The transmission curves of our NB filters are shown in Figure 3.1. The three NB filters fall within the r or i BB filters and are in a region where the CCD sensitivity is quite high.

All NB and BB images were taken using a nine-point dither pattern. The dither sequence is a carefully-planned sequence of position adjustments in order to move sources off of bad columns, chip gaps, or dead OTA cells on the camera. By moving the telescope such that inactive areas on the camera are not always covering the same region on the sky, we ensured that we were truly covering the full available field of view. In this way, multiple exposures of the same fields increased image depth, allowing for the detection of fainter sources.

Each individual NB exposure was 600 seconds, for a total integration time of 90 minutes for each NB sequence. Because each pixel in the final stacked images is typically illuminated by the sky in only 6-7 images in the dither sequence, the effective exposure time is closer to 60 minutes for each NB image. Each individual BB exposure was 120 seconds, and the final stacked BB images likewise include light from 6-7 images in a given pixel.

Accurate tracking was obtained using a guide star. When using ODI, the guide star tracking occurs using one of the OTA chips, removing this chip from the science image. Before every exposure, a one-second pre-image was taken, from which a suitably-bright source was selected to use as a guide star. With a video exposure time of typically 0.3 seconds, the guiding software of WIYN used this star to remain centered on our target field throughout the exposure. A new guide star was selected for each image in the dither sequence. As the OTA chip used for guiding is lost to the science image, we attempted to use different guide stars to mitigate gaps appearing in the raw image. By using different chips for guiding, we avoided large unusable areas in our final stacked images.

3.2.1.2 Calibration Observations

Following standard observing procedures, bias and dark images were taken each night. This included 10 zero-second bias frames followed by three 600-second dark current images. These are crucial for correcting detector signatures during the initial processing. Spectrophotometric standard star observations were also taken; these are further discussed in section 3.3.2.1.

Flat field images are taken by the WIYN staff approximately once per month through each filter and are applied to the processing of the recently-taken data. A special technique is employed. A slow shutter blade speed is used in order to baffle out internal reflections, and thus eliminate the pupil ghost. The slow shutter technique

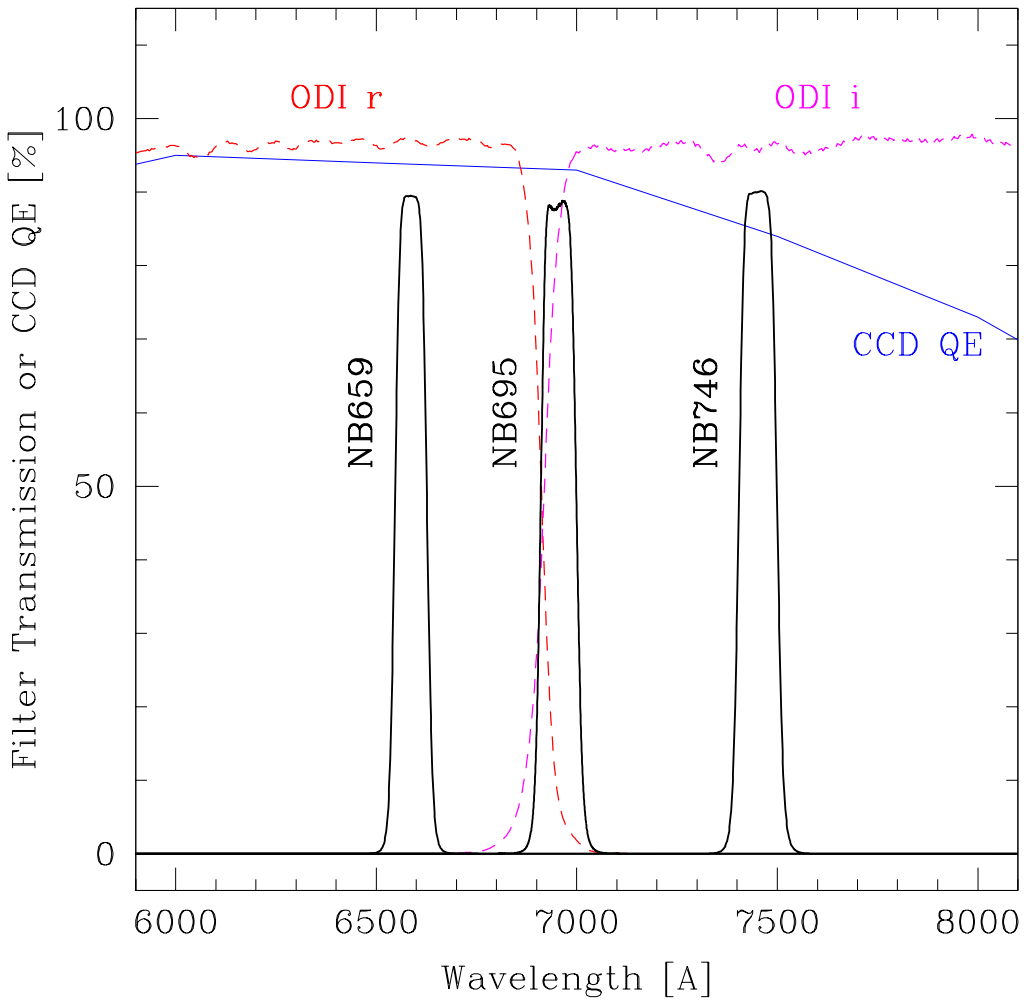


Figure 3.1 The filter transmission curves of our three narrow-band filters: NB659 (NB2), NB695 (NB1), and NB746 (NB3). The dashed lines show part of the transmission curves for the r and i broad-band filters. Overlaid is the efficiency curve of the CCD (solid line), demonstrating that while it does start to drop off around 7000 Å, the sensitivity is still high in i and NB3.

works such that both shutters move at once, with only a small delay between them, effectively creating a slit aperture which moves across the frame. Raw flat field images are acquired with at least two different rotations of the instrument so that any gradients because of non-uniform illumination of the flat field can be smoothed out. The stability of the flats is very good, with variations of less than 1% over many months.

3.2.2 Data Processing

Raw images are processed and analyzed utilizing both the ODI Pipeline, Portal, and Archive (ODI-PPA), as well as custom scripts written in Image Reduction and Analysis Facility (IRAF) and Python⁵. Each of the processing steps are detailed in the following sub-sections.

3.2.2.1 ODI Pipeline, Portal, and Archive

Raw images from ODI are downloaded to the ODI-PPA hosted by Indiana University for initial data reduction steps. Subsequent project-specific processing is accomplished once these preliminary steps are completed.

In the ODI-PPA, the raw data are first run through the `QuickReduce` pipeline (Kotulla 2014), which begins by masking out pixels that are unusable due to persistency, trailing, a defective cell, cross-talk, or a static bad pixel. Overscan levels, bias, and dark levels are determined and subtracted from each of the raw images. A correction based on the flat fields and any known non-linearity between the observed counts and the exposure is then applied. The final step is an astrometric calibration which is performed using Gaia (Gaia Collaboration et al. 2016) as the reference catalog. The output from `QuickReduce` is one complete FITS image for each dither position, properly reduced and ready for further processing.

⁵The field processing scripts are listed in the thesis appendix.

Next, the astrometric mapping software SWarp (Bertin et al. 2002) is run from within the ODI-PPA, which aligns and combines all of our images from each dither sequence to produce one image for each filter for each field. We use a weighted combination mode, an illumination correction, and utilize a surface fit for the background subtraction method, preserving extended objects of at least $3'$. The process also masks bad pixels and removes the OTAs used in guiding. The output image is re-projected with a new pixel scale of $0.125''$ pixel $^{-1}$.

3.2.2.2 SFACT Pre-processing Steps

The reduced and stacked ODI images are retrieved from the ODI-PPA for subsequent processing. The image from each filter is cropped such that all images for one field cover exactly the same area on the sky and are precisely aligned with one another. This ensures that the objects identified in a field have the same positions in each filter later in the processing.

A master image is then created by summing all six individual images together, resulting in a very deep image. Objects as faint as $r \sim 26$ are readily detected in the master image. This depth is used for catalog creation as discussed in Section 3.3. Because this image includes both narrow- and broad-band filters, it allows for the detection of ELGs which have extremely faint continuum flux but strong nebular emission, which would otherwise be missed in a BB-only image.

The average point spread function (PSF) full-width at half-maximum (FWHM) is calculated using roughly a dozen user-selected stars. This measure of the image quality is determined for the master image as well as the individual filter images. A script is then run which allows the user to select an object-free region of the image in order to determine the background noise level of the master image, a crucial parameter used during the object detection stage. All images are then binned 2×2 and possess a resulting image scale of $0.25''$ pixel $^{-1}$, a value chosen because a native resolution

(seeing) better than $0.5''$ pixel $^{-1}$ is only rarely obtained at WIYN. While our objects tend to have small angular sizes, they are almost never undersampled with this choice of pixel scale.

Once the master image is made, we complete the pre-processing of the individual images by scaling the continuum images to the NB images so that the difference image can be created. The fluxes of user-selected stars are also measured so that a flux ratio between the NB image and respective continuum image can be determined. Each of these steps is interactive so that outlier stars may be removed from consideration. The continuum image is then scaled to match the NB image.

In order to create a difference image which leaves behind only emission-line objects, simply subtracting the r image from the NB1 image was insufficient. As seen in Figure 3.1, the NB1 filter falls on the edge of the r filter, so the continuum contained within NB1 is not properly removed when only subtracting the r filter image. In particular, red objects (e.g., M stars and high-redshift early-type galaxies) leave a significant flux excess upon continuum subtraction when only the r filter image is used. This NB flux excess mimics the signature we expect from an ELG. To alleviate this problem, we create a new image that is the sum of the r and i filter images. This summed r+i image is binned and re-scaled like the single-filter BB images before being used in the subtraction. Because the NB2 filter is located closer to the red edge of the r-band filter, our tests indicated that the composite r+i continuum image also yielded better results as the continuum image to be subtracted from NB2 images as well. On the other hand, the i-band image proves adequate for use in the continuum subtraction for NB3. In summary, the r+i image is used as the continuum subtraction image for the NB1 and NB2 images, and the i image is used for the NB3 image.

3.3 SFACT Target Selection

Each target field typically includes on order of 100,000 total objects detected at the sensitivity limit of our master image. Custom scripts were written to identify relevant objects in a fully automated process⁶. Manual verification was performed as a last step. These scripts were implemented to narrow the large number of objects that needed to be evaluated as possible ELG candidates in each field to \sim 200 SFACT targets. We perform the following process on quadrants (designated A-D) of our full-frame images in order to create more manageable data sets for the user. The quadrants were created with 100 pixel overlaps to ensure that objects were not missed along boundaries.

3.3.1 Identifying SFACT Candidates

In order to identify all objects in our images, we perform a series of runs of DAOFIND (Stetson 1987) on the master image. The searches are carried out using multiple image kernel sizes, incremented from 1.25 times the FWHM of the master image to 3.6 times the FWHM, in order to detect objects with a range of light distributions. This allows for the identification of small compact galaxies as well as larger, extended galaxies. The combined six-filter master images provide maximum depth, yielding a greater number of faint objects than would be possible from the individual filter images. All objects identified are recorded in a table, which is used throughout the analysis process.

Because of our multiple DAOFIND searches, we often find a single object multiple times; we remove these duplicates immediately after combining the results of all searches. Then we convert the image positions to sky coordinates, allowing for the identification of cross-matches within the SDSS database. While many of our objects

⁶The target selection scripts are listed in the thesis appendix.

are not identified in SDSS, for those that are we adopt additional information to add to our database, including photometry and SDSS classification (star or galaxy). While this star/galaxy classification is not always accurate, coupled with other data it is a useful piece of additional information for later parts of the process.

After this automatic processing, we visually check the master image for bad regions to mask. This is designed to mitigate problems with sections of the image which, due to the numerous chip gaps and non-functioning OTA cells, do not yield usable data. We mark these regions as a series of boxes and any object within this region is removed from future consideration. The area contained within these masked regions is recorded in the image header and removed from the total area of the field when doing computations involving the survey area.

Once the object detection phase is completed, we carry out photometry on each object in the catalog. In order to do this, we measure the instrumental magnitude from both the NB image before continuum subtraction and the relevant continuum image. We designate these two quantities as m_{NB} and m_{cont} , respectively. These fluxes are measured using small aperture photometry. Light from the entire object is not necessarily included if the object is extended, but for the purposes of identifying objects with a considerable flux difference, this serves our purpose well. We used an aperture with a diameter of three times the FWHM of the PSF of each image. Using these instrumental magnitudes, we then compute the magnitude difference (Δm):

$$\Delta m = m_{NB} - m_{cont}. \quad (3.1)$$

We next perform a fine tuning offset calculation. While the NB and continuum images have already been scaled to each other (see Section 3.2.2.2) this secondary scaling makes use of more stars and is typically only a small adjustment. All stars which have $m_{cont} < -10.5$ and Δm between ± 1 are used to compute an offset such

that the median $\Delta m = 0$ for these stars. This is because stars typically do not have emission lines and thus should not have any emission line flux in our NB filters. Using the median of these offset values, a quadrant-wide offset is determined and applied to all of the objects in the table and this corrected Δm value is used going forward. The scaling offset is typically between 0 and 0.15 magnitudes which, although small, helps ensure that all of the continuum flux is removed in the difference image. Figure 3.2 shows an example of the subset of stars used to compute this scaling offset.

We also measure a pseudo signal-to-noise ratio (henceforth referred to simply as *ratio*) for each object. We use

$$\sigma_{\Delta m} = (\sigma_{NB}^2 + \sigma_{cont}^2)^{\frac{1}{2}} \quad (3.2)$$

$$ratio = \frac{\Delta m}{\sigma_{\Delta m}} \quad (3.3)$$

where σ_{NB}^2 is the uncertainty in m_{NB} and σ_{cont}^2 is the uncertainty in m_{cont} . We use Δm and *ratio* as an indicator of objects with a statistically significant excess of flux in the NB filter. Our goal was to create thresholds to select candidate objects which are as faint as possible, while minimizing the number of false detections. We also intended to use a single set of limits for constructing our catalog of ELGs, rather than varying the limits from field to field. Therefore, we experimented with a range of values for Δm and *ratio*, and ran tests on multiple fields before reaching a decision on what the limits should be (these limits can be seen as gray dashed lines in Figure 3.2). In addition, we used our experience with previous emission-line surveys (e.g., Salzer et al. 2000; Kellar et al. 2012) as a guide for reasonable values for the limits. After some experimentation, we resolved that if an object has a *ratio* of at least 5.0 and a Δm less than -0.4 , this object is considered a possible ELG candidate and moves to the next stage of processing. Based on a NB filter width of ~ 90 Å, our Δm threshold will correspond to an approximate equivalent width selection limit of ~ 40 Å.

In Figure 3.2 we present a diagnostic plot for the SFF01 field. The left plot shows Δm versus the continuum magnitude and the right plot is Δm versus *ratio*. Objects with larger *ratio* and more negative Δm found in the lower right quadrant of the right plot move forward as candidates.

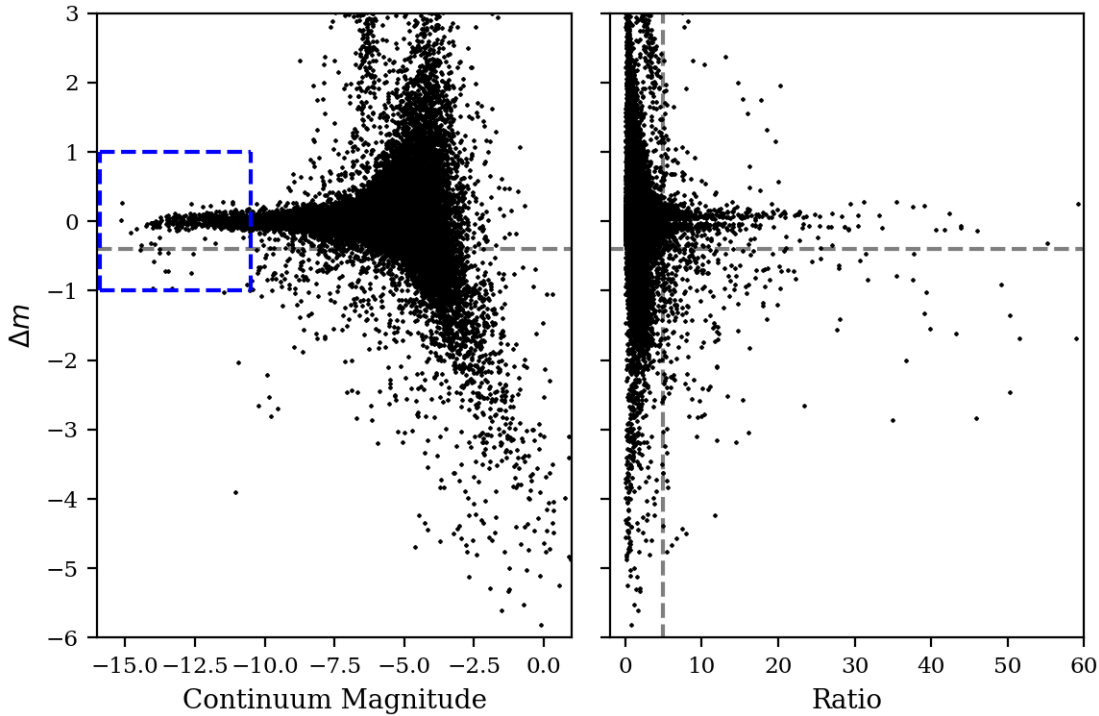


Figure 3.2 An example diagnostic plot for the SFF01 field. On the left we plot Δm against the continuum magnitude. On the right, we plot the Δm against *ratio*. The horizontal line represents our Δm cutoff of -0.4 ; the vertical line represents our *ratio* cutoff of 5.0 . Inside the blue box in the left panel are the stars used to refine the Δm offsets. All objects within the lower right quadrant of the right plot are considered possible targets, subject to further filtering.

Additional scripts identify and filter out false detections. Using data from SDSS, saturated stars are identified as objects with SDSS r-band magnitudes brighter than 13.0 . A radius around each star is defined that scales with their brightness (brighter stars have larger radii). Objects within this radius are considered contaminated by the light from the bright star and are removed from our consideration. We have found that objects within this radius often have inaccurate flux measurements due to

saturated pixels or are actually bleed trails rather than an astronomical object. We also remove objects which exhibit artifact-like signatures. Our criteria for identifying artifacts were developed using early data combined with the SDSS database. Objects were visually inspected (compared against SDSS images and previous proven false detections), and objects within certain Δm and *ratio* regimes were essentially never real objects. Rather, they were image artifacts such as bad pixels (resulting from flaws with ODI) or cosmic rays.

Once the software has selected a list of possible candidates, each member of our team looks at the continuum image, the NB image, and the difference image (see Figures 3.3 – 3.6), along with other information about the object such as the instrumental colors and, for brighter objects, its appearance in the SDSS image database. Each team member makes an independent decision regarding whether or not it is a valid ELG candidate. A candidate should be a real object which exhibits significant flux in the difference image. Many spurious sources are rejected at this stage. These often consist of objects which are bleed spikes from bright stars, cosmic rays, or other image artifacts. In general, these types of artifacts are readily identifiable via visual inspection and are thus easier to remove. We also look at the coordinates in the SDDS image database which helps to confirm if our detection is a true astronomical object. Finally, the list of acceptable candidates from the individual team members are merged, and any object not selected by all members is reviewed. Together, we confirm or reject each selection, and create a final list of candidates.

Typically there are a few hundred objects per field per filter identified as SFACT candidates by our automated software, but approximately three-quarters are rejected as spurious during this manual checking process. Most of these are image artifacts. Our target selection software has been improved since these pilot fields have been processed and is projected to improve further as we better integrate information from our preliminary search efforts. For example, quasars often display properties very

similar to a nearby red star and sometimes even looking at the SDSS image does not help us to distinguish a faint red star from a distant quasar. An under-abundance of quasars in the current catalog has lead us to investigate this possibility in more detail.

The nature of SFACT means that we often detect multiple H II regions in a single spiral galaxy. However, we are primarily concerned with the global properties of a galaxy. As such, we do not retain every single H II region in our catalog. As discussed in SFACT1, we retain only the most prominent H II region as a target for spectroscopic follow-up, and we use the center of the galaxy for carrying out global photometry.

We do err on the side of inclusivity in order to investigate potentially interesting ELG sources in greater detail when the follow-up spectroscopy is complete. We also note that our ability to identify signatures of real detections has improved, especially once we were able to process the early follow-up spectroscopy. The pilot fields presented here were classified at the beginning of our survey program. SFF01 has 132 SFACT targets, SFF10 has 216, and SFF15 has 185. All of these objects are then slated for spectroscopic observation, as discussed in SFACT3.

3.3.2 Photometry

After the target selection is complete, we perform photometry on the images⁷. This includes measuring the fluxes of all SFACT targets using an iterative process to determine the correct aperture. We also measure many of the SDSS stars found in our fields which allow us to calibrate our measurements. Here we discuss our method for performing the calibration of the BB fluxes and the two-step process for correctly putting the NB fluxes on an appropriate flux scale. As part of this, we discuss the measurement of the additional spectrophotometric standard stars.

⁷The photometry scripts are listed in the thesis appendix.

3.3.2.1 Calibration

All SFACT imaging products are calibrated utilizing photometric information from SDSS stars present in our science images. We limit the use of SDSS stars to those with a g-r color within $0.4 - 1.1$ and brighter than $r \sim 20$ to be calibration sources. These are further refined in each filter by an upper limit of the photometric error. This upper limit is based on the average SDSS magnitude errors for the stars in our BB images, and is interactively optimized by the user for each field. There exist sufficient numbers of high-quality sources to ensure robust photometric calibrations. The tabulated SDSS photometry is compared to our instrumental magnitudes, providing a difference value for each calibration star ($\Delta m(\text{SDSS})$). We compute the mean and standard deviation of the $\Delta m(\text{SDSS})$ values for all stars in each filter, retaining those within 3σ , iterating this once to remove outliers to ensure a clean sample. This clean sample contains hundreds of stars in each BB and NB filter. A final mean $\Delta m(\text{SDSS})$ is calculated for this clean sample and used as the zero point constant (ZPC) of the entire field ($\text{ZPC}(\text{SDSS})$).

In order to evaluate the homogeneity of the SDSS-based calibration across our spatially-large images (an average field is $9,000 \times 11,000$ pixels, or $35' \times 45'$), we divide each field into nine sections. Each section of the image typically has several dozen stars per filter. In each section, we compute the mean difference of the stars: a section-specific $\text{ZPC}(\text{SDSS})$. In our three pilot fields, no significant positional differences in the ZPC values across the images have been found.

We also utilize the section-specific $\text{ZPC}(\text{SDSS})$ values to derive an estimate of the uncertainty of the overall $\text{ZPC}(\text{SDSS})$ for each field. This is done because computing a formal uncertainty in the main ZPC by adopting a more traditional σ/\sqrt{N} type error in the mean results in an unphysically small ZPC uncertainty due to the large number of SDSS stars in each field. As an alternative, we determine the standard

deviation of the mean values in each of the nine sections. This standard deviation is used as our estimate of the uncertainty in the ZPC(SDSS) of the entire field. This process is done for each BB filter and each NB filter.

Due to the narrow filter bandwidth, NB photometric calibrations traditionally do not use a color term, a convention followed by this study. For BB photometry, we expected the color terms to be extremely small since the filters utilized are similar to those used by SDSS. We used our photometry from the pilot-study fields to verify that the color terms for the r and i filters are vanishingly small. The color term for g is somewhat larger ($\epsilon_g = 0.105 \pm 0.002$), and we have applied it to our g-band magnitudes.

3.3.2.2 NB Offset Calibration

In the previous section, we described the calibration process performed to place our photometric measurements on the SDSS magnitude scale. This works well for calibrating our BB magnitudes. However, the calibration of our NB flux measurements requires an additional step. This step utilizes observations of spectrophotometric standard stars (e.g., Oke & Gunn 1983; Massey et al. 1988) that were observed through each of our NB filters.

In the NB SFACT science images, we perform the initial calibration using the SDSS stars in the same manner as it is performed on the BB images. This produces a magnitude difference between our SFACT targets and the SDSS stars. Because the magnitudes are measured in the same image, time dependent quantities such as atmospheric extinction are effectively accounted for.

To properly place our NB measurements on an appropriate flux scale, we then perform an additional offset calibration utilizing observations of spectrophotometric standard stars. We repeat the same measurement procedure described above using the spectrophotometric standard stars as the “science target” and the SDSS stars in

the field as the calibration sources. We arrive at a magnitude difference between the SDSS stars and our standard star. Because we employ the same filters for the science images and the calibration images, the ZPC of the SDSS stars will be the same. We can make use of this equivalence to place our NB measurements on an absolute flux scale. This offset calibration is applied on a filter by filter basis to all SFACT targets to complete the NB calibration.

3.3.2.3 Aperture Photometry

We perform photometric measurements on each SFACT target using a range of apertures. Initially, this is performed on the master image in order to determine the proper BB photometric aperture for each object. We carry out a curve-of-growth analysis to determine the optimal aperture to use, looking for either the local maximum of the curve or where the change in instrumental magnitude is insignificant. This is quantified by examining the change in flux and the errors of adjacent fluxes added in quadrature. These thresholds are slightly different between small compact objects and nearby, extended objects. Photometry is then performed on each of the individual filter images using the selected aperture. The ZPC for each filter is added to the instrumental magnitude to determine the calibrated magnitude.

Because many H II regions are located in extended galaxies, appearing as multiple knots of emission, determining the correct aperture to use is a challenge. Moreover, light from the rest of the galaxy will always be conflated with the light from the H II region. For the sake of uniformity, all H II regions are assigned the same aperture of 16 pixels ($4''$). This size has been chosen through visual trial and error since it adequately encapsulates the light from each individual H II region.

If the curve-of-growth analysis in our custom script does not converge on an aperture to use, we examine the object by eye. We display a tiled image of each BB filter image as well as the master image overlaid with the suggested aperture. We use an

interactive process to manually select an aperture which best captures the light from the target. We also confirm the apertures of targets which have other objects nearby.

The process is repeated for the NB images with only minor differences. The curve-of-growth analysis is performed only on the continuum-subtracted NB image corresponding to the NB filter the target was detected in. This ensures that we are only determining an aperture based on the image which actually contains the object and which we want to measure. We use the continuum-subtracted NB image in order to only measure the light which is unique to the NB image, excluding the light already captured in the BB images. Once again, we visually check the aperture of any target where the software does not yield a robust solution.

Once we have instrumental magnitudes in all of the BB filters, we apply the ZPC previously calculated which puts our objects on the same scale as SDSS. For the NB fluxes, we apply the NB ZPC calculated in the same way as the BB ZPC. We then also apply the NB calibration offset described in Section 3.3.2.2 to place our NB measurements on a proper flux scale.

3.4 Results

3.4.1 SFACT Survey Catalogs

We present the full list of our SFACT targets from our pilot-study fields in Tables 3.2 – 3.4. In each table, column (1) is the SFACT ID, the unique identifier by which we refer to any candidate. This ID is made up of the field name (ex: SFF01), the filter designation (ex: NB3), the quadrant in which the object was found (ex: D), and a number which is assigned in the initial object detection stage (ex: 20110). Together this would form the SFACT ID SFF01–NB3–D20110. Columns (2) and (3) give the astrometric positions of the object in J2000 coordinates on the Gaia astrometric system, while columns (4) and (5) are the Δm and *ratio* values used to

select candidates (Section 3.3.1). Column (6) is the type of object, which is assigned during the selection process. Objects are either labelled an H II region (marked as H II), a galaxy center for an object which contains one or more H II regions (marked as GAL), or denoted as an ELG (everything else still deemed to be a viable candidate). Columns (7) through (9) are the broad-band magnitudes. Finally, the flux in the relevant narrow-band filter is tabulated in column (10). The tables are sorted by the RA of the objects within each field.

There are 533 total SFACT targets in these three pilot-study fields. A total of 1.50 deg² on the sky was searched. Counting only unique targets (not double counting the 19 H II regions and the corresponding galaxy centers), this gives us a surface density of 342.7 SFACT targets deg⁻².

Table 3.2 (cont'd)

SFACT ID	$\alpha(J2000)$ H:M:S (2)	$\delta(J2000)$ D:M:S (3)	Δm mag (4)	Ratio (5)	Object Type (6)	m_r mag (7)	m_i mag (8)	m_g mag (9)	$\log(f_{NB})$ erg/s/cm ² (10)
SFF01-NB2-B18506	21:41:36.06	19:56:53.7	-0.81 ± 0.15	5.52	ELG	23.401 ± 0.108	23.098 ± 0.139	23.895 ± 0.109	-15.804 ± 0.050
SFF01-NB3-B18371	21:41:36.92	19:37:34.2	-1.30 ± 0.17	7.60	ELG	23.484 ± 0.119	23.154 ± 0.140	23.773 ± 0.097	-15.574 ± 0.047
SFF01-NB3-B17245	21:41:41.87	19:57:07.7	-1.02 ± 0.14	7.27	ELG	22.817 ± 0.073	22.685 ± 0.108	23.026 ± 0.059	-15.452 ± 0.051
SFF01-NB3-D15415	21:41:42.73	20:12:52.3	-0.68 ± 0.10	6.89	ELG	22.246 ± 0.055	22.249 ± 0.090	22.801 ± 0.067	-15.581 ± 0.058
SFF01-NB2-D15191	21:41:43.48	20:04:48.4	-0.61 ± 0.08	7.47	ELG	21.655 ± 0.049	21.398 ± 0.062	22.468 ± 0.059	-15.466 ± 0.046
SFF01-NB1-B16317	21:41:46.59	19:43:28.3	-0.75 ± 0.11	6.97	ELG	22.463 ± 0.086	22.048 ± 0.097	22.937 ± 0.092	-15.647 ± 0.056
SFF01-NB3-B16011	21:41:48.07	19:57:58.9	-1.10 ± 0.11	10.46	ELG	22.690 ± 0.056	22.609 ± 0.087	23.090 ± 0.057	-15.367 ± 0.038
SFF01-NB3-B15732	21:41:49.54	19:40:38.6	-0.67 ± 0.10	6.99	ELG	22.540 ± 0.070	22.134 ± 0.074	22.964 ± 0.061	-15.548 ± 0.065
SFF01-NB2-B15722	21:41:49.60	19:38:48.3	-0.42 ± 0.07	5.56	ELG	22.185 ± 0.058	21.341 ± 0.044	23.100 ± 0.077	-15.670 ± 0.054
SFF01-NB1-D13076	21:41:50.05	20:07:28.2	-0.96 ± 0.13	7.26	ELG	23.247 ± 0.104	22.684 ± 0.110	23.813 ± 0.113	-15.705 ± 0.053
SFF01-NB1-D12776	21:41:50.91	20:23:41.9	-0.51 ± 0.08	6.04	ELG	22.214 ± 0.085	21.255 ± 0.053	23.202 ± 0.114	-15.577 ± 0.057
SFF01-NB3-B14965	21:41:53.12	19:52:35.0	-0.42 ± 0.03	14.55	ELG	19.891 ± 0.016	19.600 ± 0.019	20.450 ± 0.016	-14.907 ± 0.021
SFF01-NB3-B14799	21:41:53.89	19:52:27.9	-0.62 ± 0.11	5.74	ELG	22.701 ± 0.072	22.138 ± 0.075	22.990 ± 0.066	-15.595 ± 0.059
SFF01-NB3-D11444	21:41:55.02	20:15:11.4	-0.65 ± 0.09	7.22	ELG	22.600 ± 0.050	22.323 ± 0.063	23.051 ± 0.060	-15.619 ± 0.047

Table 3.2 (cont'd)

SFACT ID	α (J2000) H:M:S (2)	δ (J2000) D:M:S (3)	Δm mag (4)	Ratio (5)	Object Type (6)	m_r mag (7)	m_i mag (8)	m_g mag (9)	$\log(f_{NB})$ erg/s/cm ² (10)
SFF01-NB2-B14205	21:41:56.04	19:53:10.0	-0.83 ± 0.08	10.89	ELG	21.993 ± 0.048	21.888 ± 0.069	22.622 ± 0.054	-15.308 ± 0.031
SFF01-NB1-D10796	21:41:57.21	20:15:12.0	-0.92 ± 0.10	9.25	ELG	22.868 ± 0.068	22.466 ± 0.073	25.569 ± 0.509	-15.471 ± 0.044
SFF01-NB3-D10585	21:41:58.04	20:11:00.9	-0.63 ± 0.11	5.67	ELG	22.454 ± 0.057	22.420 ± 0.086	23.031 ± 0.061	-15.674 ± 0.068
SFF01-NB1-B13331	21:41:58.71	19:54:25.2	-1.41 ± 0.11	12.90	ELG	23.042 ± 0.103	22.760 ± 0.138	23.584 ± 0.111	-15.283 ± 0.034
SFF01-NB3-B12548	21:42:01.37	19:51:11.5	-1.11 ± 0.06	19.44	ELG	21.633 ± 0.043	21.406 ± 0.056	22.212 ± 0.045	-14.926 ± 0.021
SFF01-NB3-B12171	21:42:02.68	19:37:05.6	-0.73 ± 0.10	7.44	ELG	22.705 ± 0.123	21.800 ± 0.086	22.771 ± 0.108	-15.176 ± 0.055
SFF01-NB1-D9478	21:42:02.96	20:02:05.7	-1.93 ± 0.35	5.47	ELG	24.907 ± 0.371	24.156 ± 0.327	25.207 ± 0.301	-15.779 ± 0.067
SFF01-NB3-D9164	21:42:04.10	20:13:59.2	-0.44 ± 0.03	15.91	ELG	20.367 ± 0.017	19.920 ± 0.017	21.123 ± 0.021	-14.972 ± 0.019
SFF01-NB1-D9159	21:42:04.16	20:02:44.4	-0.67 ± 0.11	5.98	ELG	22.728 ± 0.068	22.491 ± 0.083	23.490 ± 0.081	-15.694 ± 0.066
SFF01-NB1-D9121	21:42:04.36	20:07:02.8	-1.26 ± 0.19	6.77	ELG	23.708 ± 0.117	23.633 ± 0.183	24.043 ± 0.099	-15.709 ± 0.063
SFF01-NB2-B10467	21:42:07.91	19:52:58.7	-1.67 ± 0.10	16.00	ELG	22.968 ± 0.081	23.051 ± 0.142	23.585 ± 0.099	-15.229 ± 0.024
SFF01-NB2-D8200	21:42:09.03	20:05:41.1	-0.72 ± 0.13	5.62	ELG	22.856 ± 0.072	22.807 ± 0.117	23.509 ± 0.088	-15.710 ± 0.058
SFF01-NB2-B10095	21:42:09.06	19:51:29.3	-0.44 ± 0.04	10.21	ELG	21.019 ± 0.023	20.992 ± 0.030	21.379 ± 0.021	-15.266 ± 0.021
SFF01-NB1-B8574	21:42:13.87	19:54:58.6	-1.04 ± 0.13	7.86	ELG	23.420 ± 0.103	22.915 ± 0.109	23.653 ± 0.086	-15.590 ± 0.053

Table 3.2 (cont'd)

SFACT ID	α (J2000) H:M:S (1)	δ (J2000) D:M:S (2)	Δm mag (4)	Ratio (5)	Object Type (6)	m_r mag (7)	m_i mag (8)	m_g mag (9)	$\log(f_{NB})$ erg/s/cm ² (10)
SFF01-NB2-B7116	21:42:19.20	19:43:49.7	-0.68 ± 0.09	7.82	ELG	22.323 ± 0.067	21.690 ± 0.061	22.940 ± 0.079	-15.548 ± 0.047
SFF01-NB3-B7043	21:42:19.48	19:50:51.5	-0.77 ± 0.12	6.21	ELG	22.741 ± 0.096	22.412 ± 0.118	23.021 ± 0.076	-15.632 ± 0.059
SFF01-NB3-B6897	21:42:20.03	19:52:33.3	-0.65 ± 0.02	34.84	ELG	19.164 ± 0.012	18.843 ± 0.011	19.664 ± 0.011	-14.329 ± 0.011
SFF01-NB3-B6548	21:42:21.25	19:52:29.1	-0.79 ± 0.07	10.91	ELG	21.563 ± 0.046	21.491 ± 0.069	22.044 ± 0.046	-15.304 ± 0.032
SFF01-NB3-B5847	21:42:24.05	19:50:06.3	-0.91 ± 0.09	10.24	ELG	22.668 ± 0.069	22.270 ± 0.078	23.077 ± 0.062	-15.346 ± 0.038
SFF01-NB3-B5577	21:42:24.94	19:40:45.1	-0.86 ± 0.07	12.41	ELG	22.161 ± 0.058	21.551 ± 0.053	22.467 ± 0.055	-15.243 ± 0.029
SFF01-NB3-D4681	21:42:25.48	20:16:30.4	-1.50 ± 0.24	6.22	ELG	24.036 ± 0.189	23.675 ± 0.235	25.017 ± 0.283	15.707 ± 0.050
SFF01-NB2-B5379	21:42:25.57	19:54:24.0	-2.37 ± 0.44	5.36	ELG	24.655 ± 0.271	25.570 ± 1.036	25.352 ± 0.333	-15.754 ± 0.052
SFF01-NB2-B5360	21:42:25.67	19:47:00.9	-0.66 ± 0.11	6.26	ELG	22.896 ± 0.069	22.248 ± 0.066	23.278 ± 0.066	-15.673 ± 0.057
SFF01-NB1-D4500	21:42:26.42	20:12:28.8	-1.21 ± 0.06	20.35	ELG	21.933 ± 0.040	21.715 ± 0.053	22.558 ± 0.045	-14.994 ± 0.020
SFF01-NB3-D4204	21:42:27.98	19:59:59.9	-0.42 ± 0.04	11.81	ELG	20.478 ± 0.017	20.511 ± 0.021	20.961 ± 0.017	-15.156 ± 0.024
SFF01-NB1-D3919	21:42:29.54	20:12:10.2	-0.67 ± 0.08	8.31	ELG	22.625 ± 0.057	21.912 ± 0.049	23.203 ± 0.058	-15.585 ± 0.046
SFF01-NB1-D3646	21:42:30.90	20:07:38.6	-1.58 ± 0.23	6.85	ELG	24.220 ± 0.181	23.870 ± 0.206	24.634 ± 0.167	-15.661 ± 0.055
SFF01-NB1-D3423	21:42:31.97	20:16:44.4	-0.48 ± 0.07	6.52	ELG	21.715 ± 0.049	21.527 ± 0.066	22.802 ± 0.079	-15.549 ± 0.061

Table 3.2 (cont'd)

SFACT ID	$\alpha(J2000)$ H:M:S (2)	$\delta(J2000)$ D:M:S (3)	Δm mag (4)	Ratio (5)	Object Type (6)	m_r mag (7)	m_i mag (8)	m_g mag (9)	$\log(f_{NB})$ erg/s/cm ² (10)
SFF01-NB2-B3665	21:42:32.10	19:52:44.1	-0.64 ± 0.10	6.26	ELG	22.642 ± 0.068	22.530 ± 0.093	23.417 ± 0.085	-15.645 ± 0.053
SFF01-NB1-D2289	21:42:36.08	20:07:12.0	-0.85 ± 0.12	7.20	ELG	23.033 ± 0.099	22.423 ± 0.095	23.653 ± 0.107	-15.497 ± 0.056
SFF01-NB3-D2271	21:42:36.17	20:12:39.4	-0.43 ± 0.04	9.75	ELG	20.965 ± 0.027	20.577 ± 0.028	21.509 ± 0.026	-15.290 ± 0.031
SFF01-NB3-D2175	21:42:36.52	20:00:38.4	-0.58 ± 0.08	7.37	ELG	22.009 ± 0.049	21.677 ± 0.060	22.405 ± 0.049	-15.554 ± 0.046
SFF01-NB1-B2410	21:42:36.70	19:54:45.7	-1.29 ± 0.19	6.74	ELG	23.848 ± 0.159	23.831 ± 0.245	24.668 ± 0.214	-15.693 ± 0.066
SFF01-NB2-B2289	21:42:37.18	19:39:32.5	-1.16 ± 0.07	17.00	ELG	22.114 ± 0.079	21.824 ± 0.097	22.275 ± 0.068	-15.158 ± 0.022
SFF01-NB1-B2204	21:42:37.49	19:55:19.7	-0.79 ± 0.13	6.09	ELG	23.031 ± 0.093	22.642 ± 0.100	23.424 ± 0.088	-15.627 ± 0.062
SFF01-NB1-D1779	21:42:38.13	20:12:26.2	-0.85 ± 0.09	9.75	ELG	22.646 ± 0.065	21.968 ± 0.056	23.136 ± 0.058	-15.446 ± 0.041
SFF01-NB3-B1387	21:42:40.47	19:37:06.8	-1.07 ± 0.14	7.70	ELG	22.747 ± 0.078	22.697 ± 0.130	23.551 ± 0.132	-15.410 ± 0.047
SFF01-NB2-B1287	21:42:40.84	19:49:23.2	-0.71 ± 0.08	9.31	ELG	22.170 ± 0.041	22.133 ± 0.058	22.835 ± 0.048	-15.435 ± 0.034
SFF01-NB1-D1042	21:42:40.95	20:23:25.2	-0.58 ± 0.04	13.37	GAL	19.798 ± 0.030	19.561 ± 0.039	20.163 ± 0.025	-14.828 ± 0.024
SFF01-NB2-A25674	21:42:41.34	19:52:40.9	-0.80 ± 0.15	5.33	ELG	23.033 ± 0.086	23.194 ± 0.169	23.591 ± 0.102	-15.908 ± 0.071
SFF01-NB1-A25436	21:42:42.25	19:41:12.9	-0.50 ± 0.06	8.38	ELG	21.286 ± 0.031	21.107 ± 0.041	21.630 ± 0.029	-15.400 ± 0.042
SFF01-NB1-C58631	21:42:43.30	20:23:46.2	-1.38 ± 0.17	8.34	ELG	23.579 ± 0.171	23.282 ± 0.209	23.187 ± 0.101	-15.541 ± 0.057

Table 3.2 (cont'd)

SFACT ID	$\alpha(J2000)$ H:M:S (1)	$\delta(J2000)$ D:M:S (2)	Δm mag (4)	Ratio (5)	Object Type (6)	m_r mag (7)	m_i mag (8)	m_g mag (9)	$\log(f_{NB})$ erg/s/cm ² (10)
SFF01-NB1-C58611	21:42:43.41	20:05:36.3	-2.08 ± 0.29	7.16	ELG	24.774 ± 0.393	24.365 ± 0.416	25.929 ± 0.668	-15.601 ± 0.049
SFF01-NB2-C58547	21:42:43.75	20:05:45.4	-0.50 ± 0.09	5.23	ELG	22.519 ± 0.063	22.243 ± 0.077	23.233 ± 0.075	-15.830 ± 0.048
SFF01-NB3-A24402	21:42:46.29	19:53:17.2	-0.84 ± 0.05	16.11	ELG	21.492 ± 0.030	21.273 ± 0.039	21.912 ± 0.030	-15.140 ± 0.022
SFF01-NB2-A24110	21:42:47.50	19:58:10.9	-0.40 ± 0.01	28.35	ELG	18.854 ± 0.011	18.511 ± 0.008	19.323 ± 0.008	-14.426 ± 0.011
SFF01-NB1-A23989	21:42:47.96	19:57:27.1	-1.14 ± 0.16	7.24	ELG	23.687 ± 0.160	22.976 ± 0.135	23.913 ± 0.121	-15.658 ± 0.065
SFF01-NB3-C57269	21:42:49.83	20:17:01.5	-0.43 ± 0.06	7.59	ELG	21.267 ± 0.035	21.070 ± 0.042	21.923 ± 0.038	-15.539 ± 0.050
SFF01-NB3-A23274	21:42:50.75	19:51:05.1	-0.76 ± 0.05	14.80	ELG	20.674 ± 0.025	20.373 ± 0.031	21.210 ± 0.025	-15.024 ± 0.026
SFF01-NB1-A22936	21:42:51.99	19:43:03.3	-1.58 ± 0.13	12.00	ELG	23.736 ± 0.126	22.989 ± 0.115	24.158 ± 0.135	-15.386 ± 0.038
SFF01-NB2-C56418	21:42:54.46	20:04:07.5	-1.07 ± 0.07	15.25	ELG	21.967 ± 0.055	21.777 ± 0.078	22.708 ± 0.077	-15.230 ± 0.026
SFF01-NB1-A22149	21:42:54.71	19:53:15.0	-0.99 ± 0.20	5.03	ELG	23.891 ± 0.144	23.622 ± 0.196	24.998 ± 0.222	-15.792 ± 0.074
SFF01-NB2-C56153	21:42:55.78	20:06:06.5	-1.11 ± 0.13	8.38	ELG	23.279 ± 0.085	23.004 ± 0.112	24.036 ± 0.114	-15.664 ± 0.046
SFF01-NB2-A21754	21:42:56.03	19:51:56.4	-0.92 ± 0.18	5.01	ELG	23.641 ± 0.145	23.528 ± 0.200	24.233 ± 0.134	-15.928 ± 0.073
SFF01-NB2-A21681	21:42:56.31	19:42:11.4	-0.82 ± 0.08	9.75	ELG	22.333 ± 0.046	22.165 ± 0.062	22.913 ± 0.057	-15.466 ± 0.039
SFF01-NB1-A20668	21:43:00.03	19:47:45.5	-1.22 ± 0.07	17.95	ELG	22.155 ± 0.050	21.863 ± 0.068	22.519 ± 0.043	-15.052 ± 0.022

Table 3.2 (cont'd)

SFACT ID	$\alpha(J2000)$ H:M:S (2)	$\delta(J2000)$ D:M:S (3)	Δm mag (4)	Ratio (5)	Object Type (6)	m_r mag (7)	m_i mag (8)	m_g mag (9)	$\log(f_{NB})$ erg/s/cm ² (10)
SFF01-NB2-A20446	21:43:00.87	19:53:58.7	-0.60 ± 0.11	5.26	ELG	23.002 ± 0.076	22.392 ± 0.082	23.460 ± 0.076	-15.802 ± 0.065
SFF01-NB1-C54801	21:43:01.87	20:10:18.1	-0.99 ± 0.11	8.90	ELG	23.048 ± 0.074	22.875 ± 0.104	23.711 ± 0.085	-15.513 ± 0.044
SFF01-NB3-A20023	21:43:02.36	19:37:05.4	-1.32 ± 0.21	6.23	ELG	24.970 ± 0.506	23.216 ± 0.193	24.206 ± 0.229	-15.510 ± 0.059
SFF01-NB2-A19891	21:43:02.97	20:00:34.9	-0.68 ± 0.13	5.29	ELG	22.873 ± 0.079	22.914 ± 0.142	23.731 ± 0.101	-15.672 ± 0.063
SFF01-NB2-A19498	21:43:04.75	19:42:29.2	-0.74 ± 0.08	8.92	ELG	22.254 ± 0.052	22.123 ± 0.072	22.910 ± 0.058	-15.444 ± 0.045
SFF01-NB1-C53732	21:43:06.08	20:21:57.5	-0.20 ± 0.03	6.60	GAL	18.190 ± 0.012	17.796 ± 0.011	18.795 ± 0.011	-14.380 ± 0.021
SFF01-NB3-C53049	21:43:08.70	20:19:32.9	-0.48 ± 0.06	8.15	ELG	21.953 ± 0.044	21.275 ± 0.041	22.346 ± 0.044	-15.482 ± 0.046
SFF01-NB2-C52998	21:43:08.85	20:06:58.3	-0.45 ± 0.06	7.75	ELG	21.671 ± 0.039	20.962 ± 0.033	22.357 ± 0.046	-15.524 ± 0.032
SFF01-NB2-A18053	21:43:10.82	19:45:03.2	-0.49 ± 0.09	5.49	ELG	22.323 ± 0.076	21.604 ± 0.067	22.917 ± 0.093	-15.428 ± 0.045
SFF01-NB1-C52442	21:43:11.18	20:09:57.8	-0.88 ± 0.15	5.76	ELG	23.352 ± 0.101	23.031 ± 0.115	24.668 ± 0.193	-15.737 ± 0.072
SFF01-NB2-A17803	21:43:11.74	19:40:42.5	-0.73 ± 0.07	10.26	ELG	21.477 ± 0.052	21.320 ± 0.067	22.345 ± 0.061	-15.277 ± 0.033
SFF01-NB1-C51178	21:43:16.68	20:16:41.8	-0.72 ± 0.07	10.81	ELG	21.677 ± 0.043	21.445 ± 0.053	22.440 ± 0.053	-15.306 ± 0.036
SFF01-NB2-A16509	21:43:17.08	19:38:18.0	-0.71 ± 0.12	6.05	ELG	22.620 ± 0.109	22.030 ± 0.098	23.215 ± 0.115	-15.598 ± 0.058
SFF01-NB1-A16406	21:43:17.52	19:50:06.6	-0.76 ± 0.14	5.63	ELG	22.776 ± 0.090	23.078 ± 0.201	23.900 ± 0.144	-15.762 ± 0.070

Table 3.2 (cont'd)

SFACT ID	$\alpha(J2000)$ H:M:S (2)	$\delta(J2000)$ D:M:S (3)	Δm mag (4)	Ratio (5)	Object Type (6)	m_r mag (7)	m_i mag (8)	m_g mag (9)	$\log(f_{NB})$ erg/s/cm ² (10)
SFF01-NB3-C50192	21:43:21.45	20:03:32.5	-0.28 ± 0.03	9.99	GAL	19.376 ± 0.015	19.058 ± 0.015	19.918 ± 0.013	-14.674 ± 0.019
SFF01-NB3-C50159	21:43:21.59	20:03:33.2	-0.55 ± 0.04	13.39	HII	20.509 ± 0.018	20.157 ± 0.020	20.967 ± 0.018	-15.154 ± 0.029
SFF01-NB2-A15270	21:43:22.04	19:48:56.4	-1.11 ± 0.16	6.80	ELG	23.518 ± 0.132	23.297 ± 0.200	24.418 ± 0.169	-15.743 ± 0.067
SFF01-NB2-C49986	21:43:22.46	20:21:31.6	-0.71 ± 0.10	7.08	ELG	22.297 ± 0.082	22.161 ± 0.150	22.878 ± 0.082	-15.552 ± 0.050
SFF01-NB3-A14952	21:43:23.27	19:46:13.7	-0.67 ± 0.10	6.36	ELG	22.738 ± 0.067	22.322 ± 0.075	23.681 ± 0.096	-15.708 ± 0.061
SFF01-NB2-A14869	21:43:23.71	19:57:33.7	-0.72 ± 0.13	5.46	ELG	23.234 ± 0.092	22.883 ± 0.111	24.192 ± 0.121	-15.874 ± 0.054
SFF01-NB1-A14769	21:43:24.04	19:38:26.3	-0.58 ± 0.07	8.49	ELG	22.155 ± 0.060	20.986 ± 0.038	23.561 ± 0.163	-15.443 ± 0.045
SFF01-NB1-A14492	21:43:25.26	19:44:10.9	-1.12 ± 0.19	5.76	ELG	23.742 ± 0.132	23.447 ± 0.174	24.082 ± 0.120	-15.847 ± 0.074
SFF01-NB1-C47596	21:43:25.61	20:19:24.8	-0.97 ± 0.11	8.72	ELG	22.949 ± 0.084	22.287 ± 0.074	23.306 ± 0.074	-15.527 ± 0.050
SFF01-NB3-A13828	21:43:27.97	19:49:38.1	-0.80 ± 0.14	5.88	ELG	23.031 ± 0.096	22.775 ± 0.125	24.074 ± 0.147	-15.777 ± 0.061
SFF01-NB2-C44923	21:43:27.99	20:02:09.0	-0.60 ± 0.09	6.53	ELG	22.672 ± 0.061	22.162 ± 0.066	23.040 ± 0.056	-15.518 ± 0.043
SFF01-NB3-A13758	21:43:28.26	19:59:25.6	-1.59 ± 0.09	17.99	ELG	23.267 ± 0.106	22.309 ± 0.082	23.655 ± 0.093	-15.054 ± 0.021
SFF01-NB2-A13649	21:43:28.64	19:57:09.8	-0.41 ± 0.05	7.66	ELG	21.384 ± 0.029	21.129 ± 0.035	22.094 ± 0.034	-15.491 ± 0.033
SFF01-NB2-A13518	21:43:29.13	19:57:58.1	-0.76 ± 0.08	9.55	ELG	22.241 ± 0.050	22.365 ± 0.081	23.311 ± 0.078	-15.458 ± 0.037

Table 3.2 (cont'd)

SFACT ID	$\alpha(J2000)$ H:M:S (1)	$\delta(J2000)$ D:M:S (2)	Δm mag (4)	Ratio (5)	Object Type (6)	m_r mag (7)	m_i mag (8)	m_g mag (9)	$\log(f_{NB})$ erg/s/cm ² (10)
SFF01-NB2-C43552	21:43:29.36	20:00:49.6	-0.77 ± 0.15	5.07	ELG	23.349 ± 0.110	22.983 ± 0.130	23.820 ± 0.111	-15.918 ± 0.084
SFF01-NB1-A12901	21:43:30.71	19:45:59.5	-0.53 ± 0.09	6.14	ELG	22.584 ± 0.057	21.750 ± 0.047	23.086 ± 0.059	-15.654 ± 0.057
SFF01-NB3-A12159	21:43:33.58	19:41:59.9	-1.44 ± 0.22	6.60	ELG	23.262 ± 0.070	23.630 ± 0.149	24.128 ± 0.093	-15.485 ± 0.053
SFF01-NB1-A11526	21:43:36.27	19:53:31.1	-0.70 ± 0.13	5.33	ELG	23.473 ± 0.115	22.361 ± 0.069	24.011 ± 0.109	-15.866 ± 0.086
SFF01-NB2-A10946	21:43:38.36	19:55:17.7	-0.75 ± 0.08	9.37	ELG	22.305 ± 0.060	21.827 ± 0.066	22.595 ± 0.049	-15.355 ± 0.036
SFF01-NB3-A10001	21:43:42.84	19:55:03.4	-0.41 ± 0.06	6.86	ELG	21.414 ± 0.033	21.191 ± 0.042	21.807 ± 0.030	-15.404 ± 0.048
SFF01-NB2-A9737	21:43:43.47	19:36:33.6	-1.57 ± 0.25	6.25	ELG	24.230 ± 0.228	23.639 ± 0.255	24.417 ± 0.273	-15.668 ± 0.068
SFF01-NB2-A9531	21:43:43.83	19:46:18.3	-1.31 ± 0.15	8.64	ELG	23.746 ± 0.182	22.991 ± 0.161	24.564 ± 0.256	-15.676 ± 0.046
SFF01-NB1-A9219	21:43:44.84	19:56:47.8	-0.67 ± 0.08	8.41	ELG	22.488 ± 0.052	21.811 ± 0.046	23.088 ± 0.056	-15.533 ± 0.041
SFF01-NB2-A8756	21:43:46.60	19:42:06.6	-0.62 ± 0.07	8.49	ELG	22.045 ± 0.050	21.468 ± 0.051	22.485 ± 0.042	-15.374 ± 0.036
SFF01-NB2-C20022	21:43:46.88	20:03:47.1	-0.59 ± 0.10	6.03	ELG	22.424 ± 0.061	22.339 ± 0.092	22.940 ± 0.059	-15.560 ± 0.056
SFF01-NB1-A7320	21:43:50.65	19:51:02.0	-0.43 ± 0.02	20.76	ELG	19.496 ± 0.013	19.256 ± 0.013	20.131 ± 0.012	-14.661 ± 0.013
SFF01-NB2-A6398	21:43:54.34	19:40:38.8	-0.56 ± 0.10	5.37	ELG	22.548 ± 0.084	21.925 ± 0.079	23.099 ± 0.083	-15.796 ± 0.064
SFF01-NB2-C10523	21:43:54.82	20:01:46.0	-0.64 ± 0.12	5.29	ELG	23.164 ± 0.099	22.328 ± 0.076	23.639 ± 0.090	-15.711 ± 0.075

Table 3.2 (cont'd)

SFACT ID	$\alpha(J2000)$ H:M:S (1)	$\delta(J2000)$ D:M:S (2)	Δm mag (4)	Ratio (5)	Object Type (6)	m_r mag (7)	m_i mag (8)	m_g mag (9)	$\log(f_{NB})$ erg/s/cm ² (10)
SFF01-NB1-A6064	21:43:55.85	19:57:33.0	-0.74 ± 0.07	10.80	ELG	21.929 ± 0.043	21.660 ± 0.053	22.700 ± 0.053	-15.335 ± 0.034
SFF01-NB3-A5741	21:43:56.92	19:40:10.0	-0.87 ± 0.07	13.29	ELG	21.826 ± 0.047	21.442 ± 0.057	22.364 ± 0.044	-15.169 ± 0.033
SFF01-NB1-A4724	21:43:57.95	19:40:36.3	-0.67 ± 0.04	18.60	ELG	20.832 ± 0.022	20.489 ± 0.024	21.335 ± 0.022	-14.891 ± 0.019
SFF01-NB2-A2748	21:44:00.66	19:59:38.4	-0.71 ± 0.07	10.41	HII	21.336 ± 0.032	21.179 ± 0.042	21.940 ± 0.033	-15.321 ± 0.036
SFF01-NB2-A2672	21:44:00.83	19:59:39.5	-0.21 ± 0.05	4.20	GAL	20.157 ± 0.023	19.902 ± 0.027	20.810 ± 0.024	-15.524 ± 0.049
SFF01-NB3-A498	21:44:03.87	19:38:47.8	-1.29 ± 0.20	6.53	ELG	23.174 ± 0.086	23.217 ± 0.156	23.821 ± 0.113	-15.534 ± 0.059

Notes. — SFACT ID is a unique identifier which includes information about the field, quadrant, and filter in which the object was found.

Table 3.3 (cont'd)

SFACT ID	$\alpha(J2000)$ H:M:S (1)	$\delta(J2000)$ D:M:S (2)	Δm mag (4)	Ratio (5)	Object Type (6)	m_r mag (7)	m_i mag (8)	m_g mag (9)	$\log(f_{NB})$ erg/s/cm ² (10)
SFF10-NB1-B7320	1:43:35.76	27:37:39.3	-1.12 ± 0.12	9.54	ELG	23.108 ± 0.111	22.384 ± 0.068	23.502 ± 0.080	-15.344 ± 0.051
SFF10-NB1-B7950	1:43:31.62	27:31:24.1	-1.11 ± 0.18	6.10	ELG	23.845 ± 0.376	22.587 ± 0.128	23.500 ± 0.136	-15.554 ± 0.073
SFF10-NB1-A10261	1:44:43.40	27:49:37.0	-0.48 ± 0.09	5.49	ELG	21.933 ± 0.089	21.387 ± 0.052	22.414 ± 0.053	-15.660 ± 0.053
SFF10-NB1-A11682	1:44:32.14	27:39:56.1	-1.05 ± 0.17	6.30	ELG	23.398 ± 0.181	23.198 ± 0.145	24.128 ± 0.151	-15.733 ± 0.068
SFF10-NB1-B9720	1:43:18.80	27:46:44.7	-0.63 ± 0.11	5.93	ELG	22.612 ± 0.102	22.121 ± 0.067	23.204 ± 0.079	-15.579 ± 0.065
SFF10-NB1-A10098	1:44:44.69	27:46:04.5	-0.78 ± 0.12	6.60	ELG	23.185 ± 0.196	22.190 ± 0.080	23.401 ± 0.093	-15.612 ± 0.051
SFF10-NB1-B9661	1:43:19.30	27:41:12.1	-1.16 ± 0.12	9.82	ELG	23.383 ± 0.156	22.624 ± 0.079	23.534 ± 0.078	-15.496 ± 0.042
SFF10-NB1-B12579	1:43:00.97	27:41:22.1	-0.52 ± 0.08	6.62	ELG	22.108 ± 0.070	21.398 ± 0.040	22.775 ± 0.058	-15.518 ± 0.050
SFF10-NB1-C19975	1:44:40.01	28:02:02.9	-1.19 ± 0.18	6.72	ELG	23.737 ± 0.246	22.762 ± 0.106	24.095 ± 0.142	-15.644 ± 0.072
SFF10-NB1-C19716	1:44:42.01	28:04:00.5	-0.95 ± 0.10	10.00	ELG	22.804 ± 0.092	22.190 ± 0.056	23.062 ± 0.059	-15.440 ± 0.040
SFF10-NB1-A11585	1:44:32.95	27:52:27.5	-0.66 ± 0.13	5.05	ELG	23.260 ± 0.103	22.503 ± 0.062	23.713 ± 0.077	-15.745 ± 0.081
SFF10-NB1-C20074	1:44:39.28	28:05:46.5	-0.91 ± 0.13	6.96	ELG	23.121 ± 0.140	22.567 ± 0.086	23.429 ± 0.079	-15.720 ± 0.063
SFF10-NB1-C20839	1:44:33.56	28:10:01.3	-0.75 ± 0.10	7.44	ELG	22.610 ± 0.087	22.235 ± 0.067	23.070 ± 0.063	-15.448 ± 0.055
SFF10-NB1-C21448	1:44:29.08	27:56:24.3	-0.73 ± 0.06	12.17	ELG	21.694 ± 0.058	21.023 ± 0.032	22.155 ± 0.038	-15.203 ± 0.030

Table 3.3 (cont'd)

SFACT ID	$\alpha(J2000)$ H:M:S (1)	$\delta(J2000)$ D:Mi:S (2)	Δm mag (4)	Ratio (5)	Object Type (6)	m_r mag (7)	m_i mag (8)	m_g mag (9)	$\log(f_{NB})$ erg/s/cm ² (10)
SFF10-NB1-C11325	1:45:25.62	28:04:07.8	-0.48 ± 0.08	6.03	ELG	22.110 ± 0.062	21.637 ± 0.042	23.137 ± 0.064	-15.607 ± 0.052
SFF10-NB1-D11121	1:43:15.23	28:01:25.9	-1.00 ± 0.09	10.82	ELG	22.779 ± 0.089	22.039 ± 0.049	23.280 ± 0.061	-15.322 ± 0.037
SFF10-NB3-B11533	1:43:07.68	27:52:44.6	-0.48 ± 0.09	5.36	ELG	22.565 ± 0.100	22.222 ± 0.077	22.925 ± 0.065	-15.623 ± 0.049
SFF10-NB3-B10141	1:43:16.41	27:44:30.5	-1.28 ± 0.20	6.43	ELG	24.082 ± 0.250	23.518 ± 0.144	24.400 ± 0.137	-15.788 ± 0.062
SFF10-NB3-A4352	1:45:25.73	27:43:32.3	-1.17 ± 0.15	7.76	ELG	24.020 ± 0.277	23.126 ± 0.130	24.592 ± 0.191	-15.618 ± 0.046
SFF10-NB3-B7605	1:43:33.93	27:32:09.8	-0.59 ± 0.08	7.00	ELG	21.929 ± 0.094	21.499 ± 0.069	22.245 ± 0.059	-15.320 ± 0.049
SFF10-NB3-C14676	1:45:14.65	27:54:48.7	-1.02 ± 0.15	6.68	ELG	23.668 ± 0.210	23.074 ± 0.115	23.857 ± 0.103	-15.772 ± 0.063
SFF10-NB3-B12471	1:43:01.74	27:39:28.5	-0.61 ± 0.11	5.39	ELG	23.218 ± 0.123	22.704 ± 0.078	23.700 ± 0.085	-15.722 ± 0.064
SFF10-NB3-B11195	1:43:09.97	27:38:13.9	-0.87 ± 0.13	6.67	ELG	23.137 ± 0.123	22.993 ± 0.103	23.593 ± 0.081	-15.608 ± 0.055
SFF10-NB3-D5399	1:43:47.87	28:05:28.9	-1.31 ± 0.21	6.29	ELG	23.700 ± 0.257	23.491 ± 0.209	24.338 ± 0.197	-15.701 ± 0.074
SFF10-NB3-B1091	1:44:14.77	27:36:54.4	-0.69 ± 0.14	5.01	ELG	23.481 ± 0.155	23.055 ± 0.118	24.190 ± 0.150	-15.799 ± 0.068
SFF10-NB3-B9105	1:43:23.42	27:49:55.3	-1.03 ± 0.15	6.77	ELG	23.667 ± 0.251	23.085 ± 0.140	24.016 ± 0.148	-15.706 ± 0.059
SFF10-NB3-B11870	1:43:06.06	27:44:31.6	-0.75 ± 0.13	5.68	ELG	23.412 ± 0.145	22.970 ± 0.093	24.127 ± 0.116	-15.742 ± 0.064
SFF10-NB3-D4944	1:43:51.43	27:54:47.1	-0.63 ± 0.11	5.94	ELG	22.918 ± 0.131	22.359 ± 0.081	23.176 ± 0.070	-15.730 ± 0.049

Table 3.3 (cont'd)

SFACT ID	$\alpha(J2000)$ H:M:S (1)	$\delta(J2000)$ D:M:S (2)	Δm mag (4)	Ratio (5)	Object Type (6)	m_r mag (7)	m_i mag (8)	m_g mag (9)	$\log(f_{NB})$ erg/s/cm ² (10)
SFF10-NB3-D12024	1:43:08.50	28:11:03.9	-0.64 ± 0.12	5.16	ELG	23.389 ± 0.117	22.811 ± 0.075	24.219 ± 0.106	-15.860 ± 0.063
SFF10-NB1-D803	1:44:18.05	27:58:02.1	-0.43 ± 0.07	5.88	ELG	21.653 ± 0.056	21.191 ± 0.038	22.107 ± 0.040	-15.494 ± 0.053
SFF10-NB1-A1475	1:45:44.32	27:32:08.9	-0.48 ± 0.09	5.09	ELG	22.038 ± 0.073	21.832 ± 0.062	22.894 ± 0.070	-15.527 ± 0.075
SFF10-NB2-A10251	1:44:43.43	27:36:19.6	-1.01 ± 0.15	6.84	ELG	23.079 ± 0.110	23.412 ± 0.151	24.053 ± 0.124	-15.686 ± 0.071
SFF10-NB1-A2772	1:45:36.21	27:38:49.3	-0.74 ± 0.08	9.31	ELG	22.437 ± 0.069	21.597 ± 0.038	23.270 ± 0.064	-15.380 ± 0.042
SFF10-NB3-A2346	1:45:39.18	27:35:27.8	-0.54 ± 0.05	11.77	ELG	21.875 ± 0.045	21.061 ± 0.028	22.406 ± 0.037	-15.177 ± 0.028
SFF10-NB2-C17818	1:44:58.31	28:15:15.5	-0.78 ± 0.12	6.69	ELG	22.579 ± 0.101	22.330 ± 0.074	23.307 ± 0.080	-15.680 ± 0.077
SFF10-NB2-D3614	1:44:00.23	28:00:42.6	-1.64 ± 0.22	7.36	ELG	24.349 ± 0.264	24.224 ± 0.228	25.110 ± 0.211	-15.744 ± 0.056
SFF10-NB2-B5907	1:43:43.63	27:51:01.8	-1.36 ± 0.14	9.68	ELG	23.344 ± 0.137	23.491 ± 0.153	24.166 ± 0.127	-15.552 ± 0.040
SFF10-NB2-D3460	1:44:01.67	28:13:55.7	-2.02 ± 0.35	5.79	ELG	24.177 ± 0.329	25.437 ± 0.952	25.653 ± 0.467	-15.683 ± 0.054
SFF10-NB1-D4520	1:43:54.03	28:01:14.1	-0.96 ± 0.11	8.34	ELG	22.515 ± 0.073	22.853 ± 0.094	23.668 ± 0.098	-15.530 ± 0.046
SFF10-NB1-A6548	1:45:09.38	27:54:18.0	-0.53 ± 0.09	5.94	ELG	22.346 ± 0.054	22.172 ± 0.049	23.084 ± 0.049	-15.658 ± 0.058
SFF10-NB1-C15638	1:45:09.55	27:54:18.7	-0.63 ± 0.06	10.61	ELG	21.577 ± 0.036	21.455 ± 0.033	22.455 ± 0.036	-15.328 ± 0.034
SFF10-NB1-D1045	1:44:16.70	28:15:07.2	-0.78 ± 0.10	8.03	ELG	21.842 ± 0.070	21.711 ± 0.074	22.634 ± 0.072	-15.258 ± 0.053

Table 3.3 (cont'd)

SFACT ID	$\alpha(J2000)$ H:M:S (1)	$\delta(J2000)$ D:M:S (2)	Δm mag (4)	Ratio (5)	Object Type (6)	m_r mag (7)	m_i mag (8)	m_g mag (9)	$\log(f_{NB})$ erg/s/cm ² (10)
SFF10-NB1-A12225	1:44:28.17	27:43:54.6	-0.86 ± 0.07	11.47	ELG	22.049 ± 0.053	21.894 ± 0.046	22.766 ± 0.049	-15.270 ± 0.034
SFF10-NB1-A10666	1:44:40.12	27:46:14.5	-0.60 ± 0.09	6.69	ELG	22.244 ± 0.060	21.915 ± 0.048	22.949 ± 0.051	-15.570 ± 0.054
SFF10-NB1-A12226	1:44:28.16	27:43:52.6	-0.55 ± 0.11	5.03	ELG	22.787 ± 0.077	22.222 ± 0.054	23.555 ± 0.078	-15.698 ± 0.065
SFF10-NB1-A10641	1:44:40.36	27:46:10.6	-0.82 ± 0.09	9.08	ELG	22.297 ± 0.060	22.126 ± 0.054	23.184 ± 0.061	-15.408 ± 0.049
SFF10-NB1-A6522	1:45:09.41	27:36:55.6	-1.12 ± 0.14	8.14	ELG	22.727 ± 0.110	22.751 ± 0.105	23.857 ± 0.128	-15.598 ± 0.058
SFF10-NB1-B1926	1:44:08.21	27:34:46.2	-1.24 ± 0.13	9.51	ELG	23.236 ± 0.115	22.936 ± 0.092	24.130 ± 0.123	-15.492 ± 0.050
SFF10-NB1-C9606	1:45:32.58	28:11:44.2	-1.91 ± 0.19	9.94	ELG	24.205 ± 0.295	23.434 ± 0.161	24.313 ± 0.156	-15.366 ± 0.042
SFF10-NB1-B383	1:44:20.28	27:40:09.6	-1.00 ± 0.13	7.52	ELG	23.063 ± 0.115	22.792 ± 0.081	23.926 ± 0.095	-15.590 ± 0.061
SFF10-NB1-B497	1:44:19.28	27:33:24.4	-0.77 ± 0.15	5.21	ELG	22.590 ± 0.115	22.414 ± 0.102	24.024 ± 0.215	-15.544 ± 0.082
SFF10-NB1-D2562	1:44:08.04	28:11:35.5	-1.41 ± 0.24	5.84	ELG	23.475 ± 0.219	24.254 ± 0.433	25.157 ± 0.414	-15.724 ± 0.087
SFF10-NB1-A5862	1:45:14.51	27:47:02.1	-0.93 ± 0.16	5.72	ELG	23.388 ± 0.144	23.097 ± 0.108	24.197 ± 0.123	-15.750 ± 0.071
SFF10-NB1-A6655	1:45:08.42	27:35:44.7	-0.52 ± 0.04	12.04	ELG	20.484 ± 0.028	20.266 ± 0.024	21.196 ± 0.026	-14.940 ± 0.025
SFF10-NB1-D2096	1:44:10.56	28:10:19.0	-0.44 ± 0.06	7.72	ELG	21.453 ± 0.041	21.223 ± 0.034	22.302 ± 0.039	-15.372 ± 0.038
SFF10-NB1-B4875	1:43:49.23	27:38:25.7	-0.75 ± 0.10	7.49	ELG	22.495 ± 0.095	22.034 ± 0.068	23.285 ± 0.096	-15.502 ± 0.054

Table 3.3 (cont'd)

SFACT ID	$\alpha(J2000)$ H:M:S (2)	$\delta(J2000)$ D:M:S (3)	Δm mag (4)	Ratio (5)	Object Type (6)	m_r mag (7)	m_i mag (8)	m_g mag (9)	$\log(f_{NB})$ erg/s/cm ² (10)
SFF10-NB1-D419	1:44:20.86	28:06:32.2	-1.22 ± 0.08	14.87	ELG	22.371 ± 0.090	22.148 ± 0.073	23.071 ± 0.070	-15.158 ± 0.031
SFF10-NB1-C14348	1:45:16.61	28:08:02.7	-0.76 ± 0.06	13.19	ELG	21.451 ± 0.039	21.144 ± 0.031	21.907 ± 0.030	-15.231 ± 0.026
SFF10-NB1-D3522	1:44:00.98	28:09:43.8	-0.86 ± 0.15	5.82	ELG	23.349 ± 0.155	22.972 ± 0.102	24.272 ± 0.150	-15.600 ± 0.066
SFF10-NB1-C19598	1:44:43.02	28:06:12.1	-0.87 ± 0.13	6.61	ELG	22.879 ± 0.105	22.864 ± 0.099	23.842 ± 0.100	-15.608 ± 0.070
SFF10-NB1-A7938	1:44:59.37	27:39:53.5	-1.40 ± 0.11	12.46	ELG	23.126 ± 0.104	22.793 ± 0.082	23.891 ± 0.105	-15.370 ± 0.033
SFF10-NB1-C18725	1:44:50.18	28:03:51.9	-1.06 ± 0.15	7.02	ELG	23.473 ± 0.137	23.024 ± 0.102	24.141 ± 0.118	-15.581 ± 0.049
SFF10-NB1-D9440	1:43:23.84	28:09:47.9	-1.87 ± 0.14	12.95	ELG	23.758 ± 0.240	23.095 ± 0.134	24.020 ± 0.139	-15.319 ± 0.033
SFF10-NB1-D12909	1:43:02.15	28:11:52.9	-0.45 ± 0.04	10.02	GAL	20.319 ± 0.028	20.137 ± 0.025	21.013 ± 0.025	-14.911 ± 0.026
SFF10-NB1-C12454	1:45:21.46	27:55:01.1	-2.20 ± 0.34	6.53	ELG	25.453 ± 0.543	24.109 ± 0.180	25.157 ± 0.198	-15.660 ± 0.065
SFF10-NB3-C18015	1:44:56.63	27:56:38.7	-1.17 ± 0.22	5.33	ELG	24.685 ± 0.513	23.801 ± 0.236	24.891 ± 0.247	-15.956 ± 0.092
SFF10-NB3-D643	1:44:19.17	27:54:38.5	-1.50 ± 0.10	14.82	ELG	24.049 ± 0.198	22.862 ± 0.077	24.802 ± 0.178	-15.304 ± 0.023
SFF10-NB3-A6346	1:45:10.87	27:47:16.2	-0.74 ± 0.08	9.16	ELG	22.488 ± 0.071	22.162 ± 0.057	23.152 ± 0.058	-15.547 ± 0.033
SFF10-NB3-A8797	1:44:54.08	27:48:10.7	-1.38 ± 0.23	5.90	ELG	24.880 ± 0.336	24.098 ± 0.169	25.821 ± 0.324	-15.827 ± 0.055
SFF10-NB3-A11382	1:44:34.41	27:48:57.9	-0.85 ± 0.14	6.24	ELG	23.265 ± 0.157	23.019 ± 0.119	24.063 ± 0.131	-15.794 ± 0.055

Table 3.3 (cont'd)

SFACT ID	$\alpha(J2000)$ H:M:S (1)	$\delta(J2000)$ D:Mi:S (2)	Δm mag (4)	Ratio (5)	Object Type (6)	m_r mag (7)	m_i mag (8)	m_g mag (9)	$\log(f_{NB})$ erg/s/cm ² (10)
SFF10-NB3-D13569	1:42:58.14	27:57:40.4	-0.72 ± 0.08	8.46	ELG	22.157 ± 0.087	22.058 ± 0.073	23.016 ± 0.074	-15.299 ± 0.038
SFF10-NB3-B9259	1:43:22.47	27:37:13.7	-0.90 ± 0.18	5.10	ELG	24.090 ± 0.227	23.517 ± 0.142	24.963 ± 0.211	-15.839 ± 0.071
SFF10-NB3-A549	1:45:48.36	27:40:54.8	-2.23 ± 0.21	10.40	ELG	24.887 ± 0.595	23.906 ± 0.298	23.740 ± 0.167	-15.181 ± 0.025
SFF10-NB3-A7951	1:44:59.30	27:38:23.6	-0.41 ± 0.07	6.20	ELG	21.765 ± 0.052	21.525 ± 0.042	22.603 ± 0.051	-15.626 ± 0.044
SFF10-NB3-B5549	1:43:45.88	27:40:49.0	-1.01 ± 0.16	6.48	ELG	23.381 ± 0.253	22.916 ± 0.161	24.065 ± 0.192	-15.724 ± 0.054
SFF10-NB3-C17585	1:44:59.91	28:03:43.4	-0.89 ± 0.12	7.66	ELG	22.871 ± 0.086	22.781 ± 0.085	24.066 ± 0.112	-15.697 ± 0.050
SFF10-NB3-C18103	1:44:55.73	28:06:05.0	-1.02 ± 0.08	13.02	ELG	22.682 ± 0.074	22.215 ± 0.053	23.594 ± 0.074	-15.360 ± 0.031
SFF10-NB3-B7845	1:43:32.34	27:42:06.5	-1.23 ± 0.11	11.71	ELG	23.326 ± 0.118	22.818 ± 0.074	24.151 ± 0.099	-15.424 ± 0.028
SFF10-NB3-B2549	1:44:04.04	27:49:59.9	-1.32 ± 0.10	13.49	ELG	22.709 ± 0.128	22.101 ± 0.079	23.573 ± 0.120	-15.304 ± 0.026
SFF10-NB3-B6575	1:43:39.91	27:46:53.2	-0.88 ± 0.14	6.30	ELG	23.407 ± 0.157	22.898 ± 0.093	24.798 ± 0.214	-15.777 ± 0.052
SFF10-NB3-A9340	1:44:50.11	27:37:18.3	-1.43 ± 0.09	16.13	ELG	22.603 ± 0.116	22.312 ± 0.095	23.093 ± 0.077	-15.120 ± 0.026
SFF10-NB3-A12470	1:44:26.38	27:36:42.3	-0.70 ± 0.13	5.57	ELG	22.918 ± 0.089	22.831 ± 0.087	24.488 ± 0.149	-15.710 ± 0.074
SFF10-NB3-B12244	1:43:03.57	27:36:55.2	-1.09 ± 0.13	8.16	ELG	23.287 ± 0.161	23.030 ± 0.124	24.242 ± 0.151	-15.572 ± 0.046
SFF10-NB3-A10752	1:44:39.42	27:33:49.2	-1.51 ± 0.23	6.62	ELG	24.445 ± 0.339	23.904 ± 0.210	25.195 ± 0.294	-15.660 ± 0.050

Table 3.3 (cont'd)

SFACT ID	$\alpha(J2000)$ H:M:S (1)	$\delta(J2000)$ D:M:S (2)	Δm mag (4)	Ratio (5)	Object Type (6)	m_r mag (7)	m_i mag (8)	m_g mag (9)	$\log(f_{NB})$ erg/s/cm ² (10)
SFF10-NB3-A10414	1:44:42.08	27:48:20.6	-0.56 ± 0.11	5.20	ELG	22.858 ± 0.102	22.447 ± 0.069	23.936 ± 0.101	-15.714 ± 0.046
SFF10-NB3-B9471	1:43:20.82	27:35:30.0	-1.06 ± 0.21	5.13	ELG	23.710 ± 0.161	23.677 ± 0.161	24.630 ± 0.177	-15.848 ± 0.067
SFF10-NB3-A5689	1:45:15.79	27:49:43.6	-0.82 ± 0.08	10.17	ELG	22.511 ± 0.094	22.086 ± 0.068	23.220 ± 0.075	-15.474 ± 0.033
SFF10-NB3-A11218	1:44:35.60	27:33:17.0	-1.62 ± 0.19	8.58	ELG	24.389 ± 0.373	23.428 ± 0.183	24.863 ± 0.310	-15.476 ± 0.052
SFF10-NB3-B8309	1:43:29.20	27:35:52.8	-0.49 ± 0.09	5.42	ELG	22.334 ± 0.067	22.082 ± 0.061	23.408 ± 0.091	-15.596 ± 0.050
SFF10-NB3-B6168	1:43:42.49	27:48:51.1	-1.14 ± 0.16	7.14	ELG	23.748 ± 0.203	23.279 ± 0.126	24.194 ± 0.141	-15.658 ± 0.052
SFF10-NB3-C17347	1:45:01.44	27:59:29.2	-1.47 ± 0.06	23.25	ELG	22.415 ± 0.079	21.854 ± 0.048	23.062 ± 0.059	-14.984 ± 0.017
SFF10-NB3-C15851	1:45:08.55	27:55:11.2	-0.61 ± 0.06	9.61	ELG	21.659 ± 0.049	21.366 ± 0.038	22.498 ± 0.046	-15.270 ± 0.035
SFF10-NB3-C21577	1:44:28.15	28:06:40.4	-0.64 ± 0.13	5.08	ELG	22.996 ± 0.131	22.609 ± 0.089	23.831 ± 0.108	-15.876 ± 0.067
SFF10-NB3-B5620	1:43:45.40	27:47:58.1	-1.27 ± 0.25	5.02	ELG	24.070 ± 0.206	24.036 ± 0.193	25.763 ± 0.391	-15.873 ± 0.082
SFF10-NB3-D2650	1:44:07.41	28:01:14.7	-0.78 ± 0.14	5.48	ELG	23.558 ± 0.164	23.203 ± 0.110	24.504 ± 0.153	-15.750 ± 0.063
SFF10-NB3-D11772	1:43:10.63	28:06:41.6	-1.91 ± 0.22	8.82	ELG	24.347 ± 0.311	23.978 ± 0.219	25.479 ± 0.377	-15.512 ± 0.042
SFF10-NB3-D13083	1:43:00.87	28:06:23.8	-1.18 ± 0.10	11.59	ELG	22.741 ± 0.127	22.534 ± 0.099	23.534 ± 0.107	-15.414 ± 0.032
SFF10-NB3-B6311	1:43:41.74	27:32:15.6	-0.61 ± 0.06	9.69	ELG	21.035 ± 0.062	20.877 ± 0.047	22.142 ± 0.071	-15.065 ± 0.032

Table 3.3 (cont'd)

SFACT ID	$\alpha(J2000)$ H:M:S (1)	$\delta(J2000)$ D:Mi:S (2)	Δm mag (4)	Ratio (5)	Object Type (6)	m_r mag (7)	m_i mag (8)	m_g mag (9)	$\log(f_{NB})$ erg/s/cm ² (10)
SFF10-NB3-A11134	1:44:36.31	27:42:18.3	-1.39 ± 0.09	14.69	ELG	23.377 ± 0.154	22.475 ± 0.070	23.535 ± 0.079	-15.285 ± 0.026
SFF10-NB3-B5777	1:43:44.55	27:36:16.8	-0.50 ± 0.09	5.84	ELG	22.352 ± 0.065	22.037 ± 0.051	23.321 ± 0.074	-15.586 ± 0.044
SFF10-NB3-D13755	1:42:56.70	28:16:15.3	-1.72 ± 0.28	6.26	ELG	25.846 ± 0.986	24.064 ± 0.189	25.600 ± 0.370	-15.572 ± 0.053
SFF10-NB3-D11032	1:43:15.47	28:15:21.9	-1.27 ± 0.06	19.98	ELG	21.873 ± 0.070	21.629 ± 0.055	22.787 ± 0.055	-14.941 ± 0.020
SFF10-NB3-D4316	1:43:55.36	28:09:16.6	-0.86 ± 0.09	9.14	ELG	22.904 ± 0.098	22.497 ± 0.070	24.174 ± 0.126	-15.473 ± 0.034
SFF10-NB1-C22247	1:44:23.46	28:07:59.8	-0.10 ± 0.02	5.24	GAL	16.091 ± 0.014	15.847 ± 0.009	16.595 ± 0.010	-13.670 ± 0.012
SFF10-NB1-C20476	1:44:36.42	28:09:24.2	-0.27 ± 0.03	9.97	GAL	17.549 ± 0.015	17.343 ± 0.011	17.912 ± 0.011	-14.169 ± 0.017
SFF10-NB1-C22168	1:44:23.85	28:08:06.4	-0.56 ± 0.04	14.48	HII	19.728 ± 0.027	19.519 ± 0.023	20.092 ± 0.024	-14.740 ± 0.020
SFF10-NB1-C14858	1:45:13.66	28:07:10.1	-0.82 ± 0.03	25.70	HII	19.388 ± 0.029	19.202 ± 0.027	19.819 ± 0.030	-14.358 ± 0.014
SFF10-NB1-C14875	1:45:13.58	28:07:00.5	-0.33 ± 0.01	21.93	GAL	15.596 ± 0.014	15.326 ± 0.009	16.042 ± 0.010	-13.311 ± 0.011
SFF10-NB1-B1564	1:44:10.98	27:51:32.3	-0.08 ± 0.03	2.56	GAL	18.045 ± 0.015	17.711 ± 0.011	18.381 ± 0.011	-14.446 ± 0.020
SFF10-NB1-B1549	1:44:11.10	27:51:30.5	-0.53 ± 0.03	15.41	HII	19.811 ± 0.020	19.556 ± 0.016	20.368 ± 0.017	-14.857 ± 0.021
SFF10-NB1-C15146	1:45:12.14	28:15:48.2	-0.72 ± 0.03	22.80	ELG	20.202 ± 0.027	19.886 ± 0.021	20.523 ± 0.018	-14.722 ± 0.018
SFF10-NB1-D770	1:44:18.33	28:00:24.8	-0.41 ± 0.02	17.95	GAL	17.834 ± 0.016	17.556 ± 0.012	18.198 ± 0.012	-13.986 ± 0.015

Table 3.3 (cont'd)

SFACT ID	$\alpha(J2000)$ H:M:S (2)	$\delta(J2000)$ D:M:S (3)	Δm mag (4)	Ratio (5)	Object Type (6)	m_r mag (7)	m_i mag (8)	m_g mag (9)	$\log(f_{NB})$ erg/s/cm ² (10)
SFF10-NB1-C20523	1:44:36.09	27:59:04.8	-0.48 ± 0.03	18.17	ELG	19.760 ± 0.020	19.456 ± 0.016	20.262 ± 0.016	-14.771 ± 0.017
SFF10-NB1-C10079	1:45:30.90	27:56:30.3	-0.61 ± 0.05	12.32	HII	19.828 ± 0.036	19.524 ± 0.032	20.438 ± 0.036	-14.897 ± 0.030
SFF10-NB1-C10025	1:45:31.13	27:56:30.0	-0.19 ± 0.02	8.14	GAL	17.008 ± 0.015	16.673 ± 0.010	17.595 ± 0.011	-13.851 ± 0.015
SFF10-NB1-C11120	1:45:26.45	28:01:27.0	-0.43 ± 0.04	10.98	ELG	19.148 ± 0.020	18.857 ± 0.014	19.670 ± 0.015	-14.739 ± 0.024
SFF10-NB1-C15185	1:45:11.84	28:00:03.5	-1.44 ± 0.21	6.97	HII	23.914 ± 0.369	23.215 ± 0.202	23.097 ± 0.089	-15.508 ± 0.063
SFF10-NB1-C15092	1:45:12.27	28:00:09.0	-0.31 ± 0.04	7.97	GAL	18.757 ± 0.020	18.519 ± 0.015	19.121 ± 0.014	-14.518 ± 0.037
SFF10-NB1-C8749	1:45:34.44	27:57:16.2	-0.88 ± 0.04	23.65	GAL	19.519 ± 0.029	19.233 ± 0.022	19.861 ± 0.019	-14.491 ± 0.019
SFF10-NB1-C4795	1:45:43.18	28:00:09.3	-0.76 ± 0.07	11.17	ELG	21.780 ± 0.058	21.556 ± 0.047	21.823 ± 0.033	-15.272 ± 0.036
SFF10-NB1-D5000	1:43:51.07	27:55:22.8	-0.20 ± 0.07	3.04	GAL	19.900 ± 0.030	19.718 ± 0.024	20.213 ± 0.019	-15.499 ± 0.065
SFF10-NB1-D5040	1:43:50.78	27:55:20.3	-0.98 ± 0.10	9.80	HII	22.188 ± 0.078	22.027 ± 0.066	22.224 ± 0.041	-15.386 ± 0.051
SFF10-NB1-A4253	1:45:26.21	27:32:02.4	-0.53 ± 0.02	28.91	GAL	17.125 ± 0.015	16.846 ± 0.010	17.704 ± 0.011	-13.692 ± 0.015
SFF10-NB1-C16117	1:45:07.31	28:10:22.2	-0.48 ± 0.02	21.98	ELG	18.929 ± 0.017	18.474 ± 0.012	19.617 ± 0.013	-14.514 ± 0.015
SFF10-NB1-A4212	1:45:26.45	27:36:40.8	-0.38 ± 0.01	28.39	GAL	16.281 ± 0.014	15.862 ± 0.009	17.043 ± 0.010	-13.380 ± 0.011
SFF10-NB1-D9121	1:43:25.65	28:00:57.8	-0.93 ± 0.03	32.35	ELG	20.103 ± 0.023	19.857 ± 0.018	20.379 ± 0.016	-14.491 ± 0.014

Table 3.3 (cont'd)

SFACT ID	$\alpha(J2000)$ H:M:S (1)	$\delta(J2000)$ D:M:S (2)	Δm mag (4)	Ratio (5)	Object Type (6)	m_r mag (7)	m_i mag (8)	m_g mag (9)	$\log(f_{NB})$ erg/s/cm ² (10)
SFF10-NB1-A4290	1:45:26.05	27:36:39.4	-0.85 ± 0.02	46.93	HII	18.743 ± 0.017	18.353 ± 0.013	19.456 ± 0.014	-14.058 ± 0.011
SFF10-NB1-A9679	1:44:47.94	27:46:18.3	-0.50 ± 0.02	23.18	ELG	18.890 ± 0.017	18.581 ± 0.013	19.327 ± 0.013	-14.508 ± 0.014
SFF10-NB1-B10674	1:43:13.32	27:41:24.6	-0.75 ± 0.04	16.69	ELG	21.134 ± 0.038	20.823 ± 0.030	21.463 ± 0.026	-15.008 ± 0.022
SFF10-NB1-D1007	1:44:16.86	28:03:15.4	-0.40 ± 0.03	13.22	ELG	19.755 ± 0.025	19.539 ± 0.019	20.101 ± 0.016	-14.864 ± 0.023
SFF10-NB3-B3914	1:43:55.14	27:50:16.5	-0.41 ± 0.07	5.72	ELG	21.686 ± 0.055	21.316 ± 0.039	22.282 ± 0.040	-15.600 ± 0.048
SFF10-NB3-D9185	1:43:25.37	27:57:00.1	-0.46 ± 0.03	14.18	HII	20.257 ± 0.021	19.904 ± 0.017	20.921 ± 0.019	-14.762 ± 0.015
SFF10-NB3-B4721	1:43:50.19	27:49:17.2	-0.78 ± 0.10	8.07	ELG	22.573 ± 0.115	22.373 ± 0.089	23.079 ± 0.078	-15.536 ± 0.044
SFF10-NB3-B12131	1:43:04.20	27:50:25.1	-0.87 ± 0.04	22.34	ELG	20.993 ± 0.030	20.699 ± 0.025	21.564 ± 0.026	-14.830 ± 0.016
SFF10-NB3-B8279	1:43:29.35	27:40:45.6	-0.89 ± 0.05	18.52	ELG	21.073 ± 0.047	20.879 ± 0.037	21.548 ± 0.031	-15.009 ± 0.022
SFF10-NB3-D10890	1:43:16.09	27:58:45.4	-0.66 ± 0.03	20.21	HII	20.058 ± 0.020	19.625 ± 0.015	20.707 ± 0.018	-14.659 ± 0.015
SFF10-NB3-D5659	1:43:45.84	28:03:43.0	-0.55 ± 0.04	14.37	ELG	20.544 ± 0.027	20.335 ± 0.023	20.985 ± 0.021	-14.887 ± 0.018
SFF10-NB3-B5929	1:43:43.56	27:50:36.2	-0.54 ± 0.07	8.14	ELG	21.844 ± 0.041	21.641 ± 0.036	22.503 ± 0.039	-15.495 ± 0.033
SFF10-NB3-B12081	1:43:04.52	27:50:30.9	-0.59 ± 0.03	18.35	ELG	20.137 ± 0.024	19.879 ± 0.019	20.777 ± 0.021	-14.802 ± 0.015
SFF10-NB3-D5678	1:43:45.73	28:03:42.7	-0.83 ± 0.05	16.32	ELG	22.029 ± 0.039	21.780 ± 0.034	22.554 ± 0.035	-15.117 ± 0.019

Table 3.3 (cont'd)

SFACT ID	$\alpha(J2000)$ H:M:S (1)	$\delta(J2000)$ D:Mi:S (2)	Δm mag (4)	Ratio (5)	Object Type (6)	m_r mag (7)	m_i mag (8)	m_g mag (9)	$\log(f_{NB})$ erg/s/cm ² (10)
SFF10-NB3-D9104	1:43:25.76	27:57:02.1	-0.29 ± 0.02	16.00	GAL	18.201 ± 0.016	17.732 ± 0.011	18.925 ± 0.012	-14.064 ± 0.012
SFF10-NB3-A3001	1:45:34.73	27:48:39.0	-0.78 ± 0.09	8.44	ELG	22.408 ± 0.084	22.086 ± 0.067	22.860 ± 0.058	-15.577 ± 0.043
SFF10-NB3-D10873	1:43:16.14	27:58:43.3	-0.38 ± 0.02	17.35	GAL	19.055 ± 0.019	18.647 ± 0.014	19.803 ± 0.016	-14.418 ± 0.014
SFF10-NB3-A10219	1:44:43.72	27:34:46.7	-0.40 ± 0.03	14.57	ELG	19.934 ± 0.023	19.558 ± 0.018	20.640 ± 0.022	-14.901 ± 0.019
SFF10-NB3-B9844	1:43:17.87	27:49:44.8	-0.63 ± 0.06	10.64	ELG	21.233 ± 0.045	21.128 ± 0.037	21.813 ± 0.032	-15.112 ± 0.029
SFF10-NB3-B1688	1:44:09.96	27:34:28.6	-1.32 ± 0.02	59.17	ELG	19.899 ± 0.020	19.677 ± 0.017	20.413 ± 0.017	-14.142 ± 0.010
SFF10-NB3-B3390	1:43:58.66	27:47:38.7	-0.41 ± 0.06	6.62	ELG	21.718 ± 0.045	21.579 ± 0.044	22.284 ± 0.037	-15.514 ± 0.042
SFF10-NB3-C19702	1:44:42.13	28:02:43.2	-0.62 ± 0.02	34.71	ELG	19.177 ± 0.017	18.781 ± 0.012	19.939 ± 0.014	-14.423 ± 0.011
SFF10-NB3-A4998	1:45:21.19	27:46:21.6	-0.55 ± 0.03	19.75	ELG	20.217 ± 0.025	19.758 ± 0.018	20.809 ± 0.020	-14.728 ± 0.015
SFF10-NB3-B8691	1:43:26.46	27:42:47.2	-0.57 ± 0.06	10.03	ELG	21.492 ± 0.039	21.270 ± 0.032	22.086 ± 0.032	-15.379 ± 0.028
SFF10-NB3-B9693	1:43:19.05	27:42:31.8	-0.66 ± 0.02	29.72	ELG	19.795 ± 0.019	19.495 ± 0.015	20.426 ± 0.016	-14.552 ± 0.012
SFF10-NB3-B8178	1:43:30.10	27:43:40.6	-1.54 ± 0.08	18.36	ELG	22.324 ± 0.082	22.393 ± 0.088	22.878 ± 0.060	-15.107 ± 0.021
SFF10-NB3-D5712	1:43:45.49	28:03:43.6	-0.72 ± 0.03	25.88	ELG	20.327 ± 0.022	20.065 ± 0.018	20.874 ± 0.018	-14.681 ± 0.014
SFF10-NB3-A6834	1:45:07.05	27:43:41.9	-0.89 ± 0.01	73.16	GAL	17.622 ± 0.014	17.218 ± 0.010	18.155 ± 0.011	-13.622 ± 0.009

Table 3.3 (cont'd)

SFACT ID	$\alpha(J2000)$ H:M:S (1)	$\delta(J2000)$ D:M:S (2)	Δm mag (4)	Ratio (5)	Object Type (6)	m_r mag (7)	m_i mag (8)	m_g mag (9)	$\log(f_{NB})$ erg/s/cm ² (10)
SFF10-NB3-A4854	1:45:22.25	27:46:26.5	-0.72 ± 0.07	10.74	ELG	21.691 ± 0.067	21.422 ± 0.048	22.042 ± 0.038	-15.244 ± 0.029
SFF10-NB3-D7061	1:43:37.87	27:58:26.9	-0.36 ± 0.01	27.06	GAL	17.584 ± 0.015	17.144 ± 0.010	18.384 ± 0.012	-13.870 ± 0.012
SFF10-NB3-B8276	1:43:29.32	27:45:37.5	-0.42 ± 0.04	10.06	ELG	20.377 ± 0.026	20.134 ± 0.022	21.048 ± 0.023	-14.993 ± 0.025
SFF10-NB3-B1178	1:44:14.14	27:38:31.2	-0.77 ± 0.12	6.21	ELG	23.303 ± 0.135	22.741 ± 0.086	23.535 ± 0.076	-15.733 ± 0.055
SFF10-NB3-D6776	1:43:39.40	28:07:45.0	-0.70 ± 0.03	23.66	GAL	19.612 ± 0.022	19.313 ± 0.017	19.999 ± 0.016	-14.462 ± 0.013
SFF10-NB3-D5978	1:43:43.80	28:07:24.7	-0.58 ± 0.11	5.40	ELG	22.564 ± 0.089	22.464 ± 0.078	23.049 ± 0.059	-15.694 ± 0.060
SFF10-NB3-D8227	1:43:30.95	28:07:48.5	-0.95 ± 0.05	19.93	GAL	20.626 ± 0.035	20.505 ± 0.029	21.137 ± 0.026	-14.809 ± 0.019
SFF10-NB3-D11938	1:43:09.34	28:03:05.7	-1.41 ± 0.09	16.23	ELG	21.941 ± 0.079	21.785 ± 0.066	22.331 ± 0.051	-15.029 ± 0.032
SFF10-NB3-D6265	1:43:42.19	28:02:06.1	-0.22 ± 0.04	5.73	GAL	19.846 ± 0.023	19.560 ± 0.018	20.375 ± 0.017	-14.931 ± 0.029
SFF10-NB3-C18546	1:44:51.82	28:01:14.0	-0.50 ± 0.03	16.59	ELG	19.884 ± 0.022	19.569 ± 0.017	20.395 ± 0.016	-14.739 ± 0.016
SFF10-NB3-C18449	1:44:52.63	28:07:41.4	-0.31 ± 0.03	8.93	GAL	19.475 ± 0.020	19.167 ± 0.015	20.125 ± 0.016	-14.882 ± 0.023
SFF10-NB3-D5891	1:43:44.36	28:05:15.5	-0.50 ± 0.04	12.34	ELG	20.320 ± 0.031	19.998 ± 0.024	20.874 ± 0.024	-15.043 ± 0.024
SFF10-NB3-D7098	1:43:37.53	28:12:21.4	-1.15 ± 0.08	15.24	ELG	22.209 ± 0.098	22.049 ± 0.069	22.650 ± 0.053	-15.163 ± 0.024
SFF10-NB3-A7072	1:45:05.29	27:48:35.3	-0.41 ± 0.08	5.06	ELG	21.936 ± 0.072	21.518 ± 0.055	22.363 ± 0.049	-15.629 ± 0.059

Table 3.3 (cont'd)

SFACT ID	$\alpha(J2000)$ H:M:S (1)	$\delta(J2000)$ D:Mi:S (2)	Δm mag (4)	Ratio (5)	Object Type (6)	m_r mag (7)	m_i mag (8)	m_g mag (9)	$\log(f_{NB})$ erg/s/cm ² (10)
SFF10-NB3-C17713	1:44:58.97	28:02:40.8	-0.77 ± 0.12	6.39	ELG	23.096 ± 0.123	22.671 ± 0.085	23.538 ± 0.086	-15.770 ± 0.057
SFF10-NB3-A11166	1:44:36.07	27:38:42.3	-0.46 ± 0.09	5.01	ELG	22.594 ± 0.076	22.210 ± 0.061	23.267 ± 0.070	-15.762 ± 0.067
SFF10-NB3-A1927	1:45:41.90	27:34:19.3	-0.19 ± 0.02	7.93	GAL	18.264 ± 0.017	17.946 ± 0.012	18.975 ± 0.013	-14.277 ± 0.018
SFF10-NB3-D12508	1:43:05.18	27:56:32.9	-0.70 ± 0.12	5.66	ELG	23.594 ± 0.281	22.564 ± 0.111	23.403 ± 0.099	-15.670 ± 0.073
SFF10-NB3-A11714	1:44:31.98	27:36:11.6	-0.99 ± 0.15	6.76	ELG	23.693 ± 0.132	23.256 ± 0.094	25.043 ± 0.205	-15.724 ± 0.050
SFF10-NB1-A3582	1:45:30.76	27:39:23.5	-0.68 ± 0.12	5.52	ELG	22.775 ± 0.093	22.445 ± 0.071	23.333 ± 0.066	-15.694 ± 0.057
SFF10-NB2-B1674	1:44:10.07	27:50:52.1	-0.68 ± 0.04	16.42	ELG	21.002 ± 0.033	20.836 ± 0.029	21.414 ± 0.025	-15.082 ± 0.019
SFF10-NB3-C15701	1:45:09.40	28:11:50.4	-0.49 ± 0.05	9.93	ELG	21.115 ± 0.036	20.927 ± 0.032	21.623 ± 0.028	-15.350 ± 0.032
SFF10-NB3-C21661	1:44:27.45	28:02:22.1	-0.50 ± 0.10	5.02	ELG	22.568 ± 0.091	22.193 ± 0.067	23.616 ± 0.103	-15.728 ± 0.080
SFF10-NB2-B12225	1:43:03.75	27:37:44.4	-1.04 ± 0.12	8.91	ELG	22.974 ± 0.150	22.436 ± 0.089	23.445 ± 0.094	-15.520 ± 0.043
SFF10-NB1-B12096	1:43:04.64	27:34:18.2	-0.59 ± 0.09	6.66	ELG	22.348 ± 0.087	21.572 ± 0.046	22.721 ± 0.054	-15.453 ± 0.057
SFF10-NB2-A2322	1:45:39.44	27:46:17.8	-0.88 ± 0.15	5.78	ELG	23.551 ± 0.159	22.916 ± 0.090	23.899 ± 0.096	-15.858 ± 0.063
SFF10-NB3-D11925	1:43:09.51	27:54:34.0	-0.47 ± 0.09	5.42	ELG	22.771 ± 0.137	21.581 ± 0.046	22.482 ± 0.045	-15.727 ± 0.057
SFF10-NB1-A12945	1:44:22.55	27:34:02.2	-1.74 ± 0.30	5.75	ELG	24.502 ± 0.391	24.084 ± 0.262	25.057 ± 0.268	-15.681 ± 0.089

Table 3.3 (cont'd)

SFACT ID	$\alpha(J2000)$ H:M:S (1)	$\delta(J2000)$ D:M:S (2)	Δm mag (4)	Ratio (5)	Object Type (6)	m_r mag (7)	m_i mag (8)	m_g mag (9)	$\log(f_{NB})$ erg/s/cm ² (10)
SFF10-NB2-A2783	1:45:36.16	27:39:14.4	-0.48 ± 0.04	12.91	ELG	20.612 ± 0.028	20.508 ± 0.024	20.790 ± 0.018	-15.102 ± 0.022
SFF10-NB1-B10986	1:43:11.40	27:33:00.7	-1.21 ± 0.12	9.93	ELG	23.077 ± 0.135	22.663 ± 0.083	23.339 ± 0.069	-15.392 ± 0.039
SFF10-NB3-C18332	1:44:53.69	28:07:53.4	-0.81 ± 0.13	6.30	ELG	22.853 ± 0.103	22.815 ± 0.103	23.359 ± 0.076	-15.788 ± 0.062
SFF10-NB3-A5857	1:45:14.56	27:45:17.0	-1.39 ± 0.26	5.27	ELG	24.856 ± 0.414	24.189 ± 0.239	25.805 ± 0.388	-15.894 ± 0.064
SFF10-NB3-B6212	1:43:42.27	27:49:54.4	-0.58 ± 0.11	5.32	ELG	24.144 ± 0.398	22.674 ± 0.092	25.424 ± 0.449	-15.732 ± 0.065
SFF10-NB3-A6044	1:45:13.30	27:48:43.8	-0.83 ± 0.15	5.36	ELG	23.805 ± 0.230	23.141 ± 0.131	24.358 ± 0.157	-15.832 ± 0.069
SFF10-NB3-B12772	1:42:59.69	27:40:52.3	-0.52 ± 0.09	5.57	ELG	22.981 ± 0.126	22.067 ± 0.063	24.509 ± 0.216	-15.558 ± 0.063
SFF10-NB3-B8425	1:43:28.35	27:40:47.4	-0.58 ± 0.09	6.41	ELG	22.488 ± 0.079	22.246 ± 0.062	23.067 ± 0.056	-15.550 ± 0.052
SFF10-NB3-B9621	1:43:19.61	27:42:43.0	-0.48 ± 0.09	5.45	ELG	22.676 ± 0.087	22.241 ± 0.059	23.413 ± 0.072	-15.542 ± 0.054
SFF10-NB2-B9526	1:43:20.42	27:33:41.2	-0.65 ± 0.12	5.41	ELG	22.676 ± 0.130	22.291 ± 0.088	24.266 ± 0.233	-15.786 ± 0.047
SFF10-NB2-A6330	1:45:10.90	27:36:34.5	-0.98 ± 0.16	6.22	ELG	22.799 ± 0.086	...	23.518 ± 0.074	-15.784 ± 0.071
SFF10-NB2-A4747	1:45:22.96	27:44:25.2	-0.43 ± 0.07	6.07	ELG	21.863 ± 0.061	21.657 ± 0.051	22.728 ± 0.056	-15.580 ± 0.054
SFF10-NB3-C19014	1:44:47.73	28:14:05.2	-0.50 ± 0.09	5.87	ELG	22.279 ± 0.091	21.779 ± 0.054	22.878 ± 0.063	-15.556 ± 0.063
SFF10-NB3-A5089	1:45:20.37	27:34:58.0	-1.02 ± 0.10	10.29	ELG	22.614 ± 0.134	22.285 ± 0.089	23.275 ± 0.095	-15.501 ± 0.035

Table 3.3 (cont'd)

SFACT ID	$\alpha(J2000)$ H:M:S (1)	$\delta(J2000)$ D:M:S (2)	Δm mag (4)	Ratio (5)	Object Type (6)	m_r mag (7)	m_i mag (8)	m_g mag (9)	$\log(f_{NB})$ erg/s/cm ² (10)
SFF10-NB1-C18567	1:44:51.68	28:12:16.2	-1.20 ± 0.24	5.07	ELG	23.974 ± 0.232	23.591 ± 0.144	25.130 ± 0.245	-15.853 ± 0.106
SFF10-NB2-B10675	1:43:13.39	27:33:56.3	-0.47 ± 0.06	7.38	ELG	21.985 ± 0.054	21.429 ± 0.035	22.719 ± 0.046	-15.493 ± 0.041
SFF10-NB1-A6784	1:45:07.51	27:48:47.2	-0.76 ± 0.13	5.63	ELG	23.093 ± 0.107	22.781 ± 0.083	24.265 ± 0.127	-15.688 ± 0.068
SFF10-NB3-B7077	1:43:36.93	27:46:15.4	-0.57 ± 0.09	6.27	ELG	22.715 ± 0.102	22.203 ± 0.068	24.202 ± 0.166	-15.672 ± 0.049
SFF10-NB2-A8466	1:44:56.30	27:46:58.5	-0.74 ± 0.02	32.27	ELG	19.710 ± 0.019	19.887 ± 0.018	19.942 ± 0.013	-14.548 ± 0.012
SFF10-NB1-C16113	1:45:07.33	28:09:12.4	-0.62 ± 0.09	6.57	ELG	22.450 ± 0.124	21.655 ± 0.060	22.875 ± 0.077	-15.621 ± 0.065

Notes. — SFACT ID is a unique identifier which includes information about the field, quadrant, and filter in which the object was found. Non-real magnitude measurements are removed from the catalog.

Table 3.4 (cont'd)

SFACT ID	$\alpha(J2000)$ H:M:S (1)	$\delta(J2000)$ D:Mi:S (2)	Δm mag (4)	Ratio (5)	Object Type (6)	m_r mag (7)	m_i mag (8)	m_g mag (9)	$\log(f_{NB})$ erg/s/cm ² (10)
SFF15-NB2-B12874	2:37:40.34	27:29:39.9	-1.17 ± 0.09	13.00	ELG	22.549 ± 0.070	22.583 ± 0.078	23.556 ± 0.078	-15.367 ± 0.029
SFF15-NB2-B12729	2:37:41.60	27:29:59.4	-1.70 ± 0.14	11.94	ELG	22.939 ± 0.159	23.720 ± 0.345	23.682 ± 0.161	-15.291 ± 0.033
SFF15-NB2-D19839	2:37:41.93	28:10:35.0	-0.63 ± 0.12	5.11	ELG	22.770 ± 0.097	22.906 ± 0.142	23.573 ± 0.105	-15.757 ± 0.066
SFF15-NB1-B12675	2:37:42.16	27:29:38.9	-0.74 ± 0.13	5.60	ELG	22.927 ± 0.100	22.736 ± 0.083	23.988 ± 0.114	-15.662 ± 0.071
SFF15-NB3-B12608	2:37:42.63	27:46:16.0	-0.51 ± 0.09	5.56	ELG	22.604 ± 0.058	22.288 ± 0.049	23.408 ± 0.065	-15.707 ± 0.054
SFF15-NB3-B12427	2:37:44.04	27:45:33.7	-0.63 ± 0.05	12.28	ELG	21.254 ± 0.034	21.076 ± 0.029	22.009 ± 0.032	-15.248 ± 0.024
SFF15-NB3-D18788	2:37:44.26	28:13:30.5	-0.54 ± 0.08	7.05	ELG	22.009 ± 0.051	21.968 ± 0.055	22.806 ± 0.054	-15.391 ± 0.046
SFF15-NB2-B12371	2:37:44.60	27:34:41.2	-0.60 ± 0.06	9.79	GAL	21.934 ± 0.045	21.494 ± 0.035	22.767 ± 0.045	-15.335 ± 0.030
SFF15-NB1-D18539	2:37:44.78	28:13:40.3	-1.37 ± 0.10	13.44	ELG	21.511 ± 0.033	21.295 ± 0.030	23.178 ± 0.083	-15.386 ± 0.033
SFF15-NB3-B12212	2:37:45.92	27:39:18.5	-0.77 ± 0.09	8.86	ELG	22.657 ± 0.075	22.226 ± 0.056	23.561 ± 0.078	-15.525 ± 0.030
SFF15-NB3-D17352	2:37:46.87	28:04:21.5	-0.71 ± 0.11	6.15	ELG	24.036 ± 0.220	22.660 ± 0.069	26.150 ± 0.717	-15.750 ± 0.061
SFF15-NB3-B11965	2:37:47.82	27:48:51.5	-0.75 ± 0.10	7.21	ELG	22.912 ± 0.115	22.340 ± 0.069	23.403 ± 0.075	-15.570 ± 0.057
SFF15-NB1-D15218	2:37:48.24	28:15:11.6	-0.53 ± 0.10	5.22	ELG	21.954 ± 0.109	21.542 ± 0.083	23.025 ± 0.165	-15.326 ± 0.067
SFF15-NB1-D14190	2:37:49.21	28:09:02.6	-0.73 ± 0.14	5.01	ELG	22.798 ± 0.126	22.347 ± 0.109	23.184 ± 0.100	-15.754 ± 0.081

Table 3.4 (cont'd)

SFACT ID	$\alpha(J2000)$ H:M:S (1)	$\delta(J2000)$ D:Mi:S (2)	Δm mag (4)	Ratio (5)	Object Type (6)	m_r mag (7)	m_i mag (8)	m_g mag (9)	$\log(f_{NB})$ erg/s/cm ² (10)
SFF15-NB2-B11684	2:37:50.76	27:28:58.2	-1.91 ± 0.17	11.41	ELG	23.082 ± 0.127	24.305 ± 0.440	24.916 ± 0.315	-15.383 ± 0.035
SFF15-NB3-D13288	2:37:51.99	27:53:46.3	-0.65 ± 0.07	8.78	ELG	22.373 ± 0.070	21.789 ± 0.044	23.281 ± 0.072	-15.364 ± 0.042
SFF15-NB2-B11359	2:37:53.59	27:43:08.3	-0.43 ± 0.06	7.21	ELG	21.694 ± 0.050	21.309 ± 0.037	21.401 ± 0.022	-15.597 ± 0.033
SFF15-NB3-D12301	2:37:53.67	27:53:11.6	-0.75 ± 0.14	5.26	ELG	23.759 ± 0.150	23.132 ± 0.096	24.945 ± 0.233	-15.881 ± 0.076
SFF15-NB3-D11976	2:37:53.92	28:09:33.0	-0.44 ± 0.07	5.89	ELG	21.436 ± 0.050	21.524 ± 0.067	22.221 ± 0.050	-15.542 ± 0.055
SFF15-NB2-B11181	2:37:55.25	27:42:04.6	-0.49 ± 0.07	7.52	ELG	21.665 ± 0.055	21.477 ± 0.046	22.515 ± 0.054	-15.571 ± 0.039
SFF15-NB3-D11324	2:37:55.50	28:03:48.3	-0.80 ± 0.14	5.91	ELG	24.726 ± 0.378	22.968 ± 0.079	26.249 ± 0.650	15.641 ± 0.064
SFF15-NB2-B10976	2:37:57.10	27:37:01.2	-0.62 ± 0.12	5.12	ELG	22.938 ± 0.077	23.059 ± 0.099	23.841 ± 0.085	-15.851 ± 0.072
SFF15-NB3-D10140	2:37:57.31	28:14:42.7	-1.30 ± 0.13	9.86	ELG	21.935 ± 0.052	21.660 ± 0.039	23.263 ± 0.070	-15.598 ± 0.049
SFF15-NB3-D9467	2:37:58.29	28:13:13.8	-1.06 ± 0.06	17.61	ELG	21.120 ± 0.025	21.043 ± 0.026	22.592 ± 0.047	-15.211 ± 0.023
SFF15-NB3-B10613	2:38:00.59	27:42:46.2	-0.44 ± 0.08	5.62	ELG	22.209 ± 0.050	22.107 ± 0.047	23.010 ± 0.048	-15.523 ± 0.036
SFF15-NB1-B10541	2:38:01.24	27:36:52.3	-0.86 ± 0.14	6.23	ELG	23.167 ± 0.134	22.791 ± 0.103	23.850 ± 0.114	-15.607 ± 0.069
SFF15-NB3-B10532	2:38:01.32	27:36:47.0	-0.67 ± 0.13	5.21	ELG	23.024 ± 0.138	22.664 ± 0.107	23.931 ± 0.132	-15.766 ± 0.058
SFF15-NB2-D8167	2:38:01.85	27:53:05.2	-0.93 ± 0.12	7.64	ELG	22.876 ± 0.131	22.761 ± 0.137	23.822 ± 0.159	-15.639 ± 0.051

Table 3.4 (cont'd)

SFACT ID	$\alpha(12000)$ H:M:S (1)	$\delta(12000)$ D:M:S (2)	Δm mag (4)	Ratio (5)	Object Type (6)	m_r mag (7)	m_i mag (8)	m_g mag (9)	$\log(f_{NB})$ erg/s/cm ² (10)
SFF15-NB1-D7156	2:38:04.44	27:59:29.8	-0.43 ± 0.09	5.05	ELG	21.896 ± 0.058	21.601 ± 0.044	22.944 ± 0.065	-15.459 ± 0.064
SFF15-NB1-D6852	2:38:05.98	28:14:04.0	-0.41 ± 0.08	5.21	ELG	21.758 ± 0.065	21.344 ± 0.051	22.871 ± 0.075	-15.530 ± 0.067
SFF15-NB2-B9363	2:38:09.33	27:37:02.7	-1.36 ± 0.07	18.67	ELG	22.214 ± 0.067	22.222 ± 0.083	22.799 ± 0.061	-15.089 ± 0.022
SFF15-NB2-B9265	2:38:09.92	27:36:42.4	-0.50 ± 0.08	6.04	ELG	22.181 ± 0.066	21.635 ± 0.045	23.061 ± 0.075	-15.631 ± 0.060
SFF15-NB1-B9057	2:38:11.20	27:42:51.1	-1.00 ± 0.13	7.50	ELG	22.939 ± 0.114	23.041 ± 0.131	23.909 ± 0.121	-15.646 ± 0.047
SFF15-NB1-B8797	2:38:12.91	27:38:50.2	-0.93 ± 0.19	5.04	ELG	23.716 ± 0.173	23.136 ± 0.110	24.430 ± 0.149	-15.874 ± 0.066
SFF15-NB2-B8478	2:38:14.71	27:36:12.1	-0.71 ± 0.09	8.27	ELG	21.985 ± 0.064	22.191 ± 0.082	22.636 ± 0.062	-15.477 ± 0.057
SFF15-NB1-B8408	2:38:14.86	27:45:31.8	-1.17 ± 0.08	15.44	ELG	22.242 ± 0.061	22.043 ± 0.053	23.078 ± 0.060	-15.198 ± 0.025
SFF15-NB3-D5611	2:38:16.22	28:02:41.4	-1.11 ± 0.17	6.50	ELG	23.369 ± 0.152	23.524 ± 0.177	24.578 ± 0.240	-15.748 ± 0.064
SFF15-NB2-B7986	2:38:16.55	27:47:47.3	-0.66 ± 0.08	8.35	ELG	22.261 ± 0.073	21.823 ± 0.050	23.134 ± 0.075	-15.583 ± 0.038
SFF15-NB1-D5555	2:38:16.65	28:08:01.4	-0.73 ± 0.08	9.07	ELG	22.033 ± 0.060	21.844 ± 0.048	23.076 ± 0.065	-15.368 ± 0.044
SFF15-NB1-D5493	2:38:17.21	28:07:57.3	-1.31 ± 0.11	12.11	ELG	23.159 ± 0.106	22.493 ± 0.061	23.598 ± 0.072	-15.322 ± 0.036
SFF15-NB3-D5449	2:38:17.61	27:57:37.2	-0.67 ± 0.12	5.72	ELG	22.693 ± 0.101	22.321 ± 0.080	23.453 ± 0.107	-15.806 ± 0.055
SFF15-NB2-B7773	2:38:17.65	27:45:00.0	-0.63 ± 0.09	6.64	ELG	22.315 ± 0.089	22.203 ± 0.085	23.375 ± 0.121	-15.771 ± 0.045

Table 3.4 (cont'd)

SFACT ID	$\alpha(12000)$ H:M:S (1)	$\delta(12000)$ D:M:S (2)	Δm mag (4)	Ratio (5)	Object Type (6)	m_r mag (7)	m_i mag (8)	m_g mag (9)	$\log(f_{NB})$ erg/s/cm ² (10)
SFF15-NB1-B7603	2:38:18.80	27:34:21.4	-0.57 ± 0.05	11.29	ELG	20.000 ± 0.054	19.656 ± 0.042	20.544 ± 0.042	-15.242 ± 0.052
SFF15-NB2-B7530	2:38:19.21	27:36:10.5	-0.99 ± 0.16	6.03	ELG	23.048 ± 0.154	23.048 ± 0.173	23.761 ± 0.142	-15.716 ± 0.079
SFF15-NB1-D5258	2:38:19.36	27:58:25.5	-0.45 ± 0.05	9.74	GAL	19.771 ± 0.026	19.431 ± 0.017	20.223 ± 0.017	-15.014 ± 0.025
SFF15-NB1-D5059	2:38:20.90	28:03:54.5	-0.64 ± 0.07	9.85	ELG	21.704 ± 0.043	21.703 ± 0.045	22.772 ± 0.051	-15.329 ± 0.028
SFF15-NB3-B6889	2:38:22.12	27:31:23.2	-0.55 ± 0.11	5.12	ELG	21.859 ± 0.079	22.264 ± 0.131	22.583 ± 0.093	-15.577 ± 0.100
SFF15-NB3-B6717	2:38:23.24	27:38:00.0	-1.39 ± 0.20	6.86	ELG	24.181 ± 0.232	23.598 ± 0.161	24.915 ± 0.212	-15.677 ± 0.058
SFF15-NB1-B6693	2:38:23.38	27:39:24.4	-0.71 ± 0.05	13.67	ELG	21.213 ± 0.041	20.768 ± 0.029	21.734 ± 0.030	-15.102 ± 0.024
SFF15-NB1-B6638	2:38:23.65	27:46:23.0	-0.95 ± 0.09	10.35	ELG	21.316 ± 0.054	21.114 ± 0.047	21.936 ± 0.046	-15.328 ± 0.048
SFF15-NB3-D4633	2:38:24.53	28:13:50.0	-0.87 ± 0.11	8.19	ELG	22.741 ± 0.112	22.431 ± 0.086	23.547 ± 0.113	-15.562 ± 0.044
SFF15-NB2-B6385	2:38:25.00	27:48:37.0	-0.87 ± 0.13	6.66	ELG	23.254 ± 0.134	22.955 ± 0.101	24.043 ± 0.130	-15.813 ± 0.057
SFF15-NB2-B6273	2:38:25.56	27:41:40.6	-1.57 ± 0.31	5.00	ELG	24.700 ± 0.319	24.581 ± 0.301	25.967 ± 0.461	-15.997 ± 0.079
SFF15-NB3-B6188	2:38:25.99	27:34:30.5	-0.93 ± 0.05	18.69	ELG	21.694 ± 0.034	21.347 ± 0.030	22.481 ± 0.037	-15.019 ± 0.019
SFF15-NB2-B6016	2:38:26.74	27:38:55.6	-0.63 ± 0.12	5.42	ELG	22.888 ± 0.096	22.507 ± 0.080	23.647 ± 0.099	-15.787 ± 0.056
SFF15-NB2-D4061	2:38:29.24	27:59:44.8	-1.75 ± 0.31	5.56	ELG	24.050 ± 0.220	25.062 ± 0.522	26.231 ± 0.732	-15.950 ± 0.075

Table 3.4 (cont'd)

SFACT ID	$\alpha(12000)$ H:M:S (1)	$\delta(12000)$ D:M:S (2)	Δm mag (4)	Ratio (5)	Object Type (6)	m_r mag (7)	m_i mag (8)	m_g mag (9)	$\log(f_{NB})$ erg/s/cm ² (10)
SFF15-NB2-B5240	2:38:29.28	27:48:45.4	-0.68 ± 0.11	6.36	ELG	22.530 ± 0.098	22.156 ± 0.069	23.536 ± 0.109	-15.704 ± 0.059
SFF15-NB2-D3744	2:38:32.08	27:55:34.2	-1.03 ± 0.10	9.82	ELG	22.866 ± 0.095	22.723 ± 0.090	23.634 ± 0.086	-15.610 ± 0.035
SFF15-NB1-D3723	2:38:32.12	28:14:59.5	-0.40 ± 0.08	5.02	ELG	21.805 ± 0.063	21.389 ± 0.047	22.620 ± 0.065	-15.624 ± 0.063
SFF15-NB2-D3331	2:38:34.15	27:56:24.9	-0.64 ± 0.05	13.84	ELG	21.141 ± 0.026	21.319 ± 0.029	21.871 ± 0.025	-15.225 ± 0.024
SFF15-NB1-B3575	2:38:34.57	27:41:13.2	-0.97 ± 0.04	26.79	ELG	20.622 ± 0.023	20.336 ± 0.017	21.068 ± 0.017	-14.685 ± 0.015
SFF15-NB2-B3475	2:38:34.86	27:50:20.0	-1.55 ± 0.25	6.14	ELG	23.709 ± 0.198	24.858 ± 0.569	25.712 ± 0.528	-15.736 ± 0.073
SFF15-NB3-B3231	2:38:36.12	27:31:50.4	-0.48 ± 0.09	5.10	ELG	22.691 ± 0.142	21.935 ± 0.081	23.064 ± 0.109	-15.306 ± 0.049
SFF15-NB1-B2993	2:38:37.47	27:35:30.7	-0.41 ± 0.08	5.13	ELG	21.551 ± 0.053	21.237 ± 0.045	22.916 ± 0.093	-15.318 ± 0.052
SFF15-NB1-B2957	2:38:37.64	27:34:20.9	-0.79 ± 0.10	8.06	ELG	22.297 ± 0.078	22.130 ± 0.075	22.916 ± 0.072	-15.439 ± 0.052
SFF15-NB2-D2938	2:38:38.26	27:59:15.0	-1.88 ± 0.16	11.39	ELG	23.688 ± 0.142	24.035 ± 0.205	24.982 ± 0.225	-15.487 ± 0.035
SFF15-NB1-B2821	2:38:38.38	27:31:31.2	-0.43 ± 0.07	5.93	ELG	21.462 ± 0.048	21.042 ± 0.039	22.433 ± 0.061	-15.382 ± 0.055
SFF15-NB2-B2790	2:38:38.56	27:43:19.8	-0.62 ± 0.10	6.06	ELG	22.729 ± 0.093	22.171 ± 0.060	23.579 ± 0.091	-15.765 ± 0.055
SFF15-NB3-D2859	2:38:38.91	28:14:08.7	-1.10 ± 0.18	5.97	ELG	23.927 ± 0.307	23.451 ± 0.198	24.361 ± 0.234	-15.724 ± 0.054
SFF15-NB1-B2663	2:38:39.26	27:38:13.8	-0.82 ± 0.15	5.54	ELG	23.456 ± 0.156	22.705 ± 0.091	23.680 ± 0.111	-15.710 ± 0.059

Table 3.4 (cont'd)

SFACT ID	$\alpha(J2000)$ H:M:S (2)	$\delta(J2000)$ D:M:S (3)	Δm mag (4)	Ratio (5)	Object Type (6)	m_r mag (7)	m_i mag (8)	m_g mag (9)	$\log(f_{NB})$ erg/s/cm ² (10)
SFF15-NB3-B2431	2:38:40.79	27:40:07.9	-0.83 ± 0.09	8.78	ELG	22.977 ± 0.116	22.253 ± 0.068	23.334 ± 0.079	-15.540 ± 0.039
SFF15-NB3-D2537	2:38:41.63	27:56:56.7	-1.25 ± 0.17	7.55	ELG	23.805 ± 0.166	23.472 ± 0.122	24.952 ± 0.212	-15.656 ± 0.044
SFF15-NB1-D2243	2:38:43.66	27:53:14.4	-0.57 ± 0.10	5.62	ELG	21.984 ± 0.067	21.828 ± 0.062	22.607 ± 0.057	-15.563 ± 0.065
SFF15-NB1-D1894	2:38:45.93	28:10:35.0	-0.48 ± 0.08	6.23	ELG	21.788 ± 0.046	21.659 ± 0.040	22.784 ± 0.048	-15.548 ± 0.049
SFF15-NB2-D1721	2:38:46.82	27:53:35.8	-0.91 ± 0.06	15.22	ELG	21.827 ± 0.044	21.740 ± 0.041	22.635 ± 0.042	-15.163 ± 0.022
SFF15-NB2-B1429	2:38:48.44	27:51:46.3	-1.54 ± 0.18	8.82	ELG	23.616 ± 0.194	23.452 ± 0.156	24.753 ± 0.235	-15.655 ± 0.051
SFF15-NB2-D1081	2:38:50.34	28:14:56.9	-0.61 ± 0.06	9.80	ELG	21.704 ± 0.063	21.326 ± 0.046	22.301 ± 0.052	-15.403 ± 0.034
SFF15-NB1-B945	2:38:51.16	27:36:59.8	-0.99 ± 0.18	5.61	ELG	23.702 ± 0.175	22.979 ± 0.108	24.659 ± 0.220	-15.718 ± 0.077
SFF15-NB1-B777	2:38:51.99	27:44:30.2	-0.73 ± 0.01	54.04	ELG	17.733 ± 0.014	17.181 ± 0.006	18.685 ± 0.009	-13.941 ± 0.012
SFF15-NB1-B752	2:38:52.14	27:32:15.1	-0.53 ± 0.05	9.94	ELG	21.406 ± 0.029	21.098 ± 0.024	21.947 ± 0.027	-15.240 ± 0.027
SFF15-NB1-A11868	2:38:53.43	27:45:25.1	-1.29 ± 0.04	30.89	HII	20.188 ± 0.033	19.723 ± 0.026	20.609 ± 0.028	-14.470 ± 0.015
SFF15-NB1-A11851	2:38:53.52	27:45:27.1	-0.32 ± 0.03	9.49	GAL	17.662 ± 0.014	17.321 ± 0.007	18.171 ± 0.008	-13.910 ± 0.014
SFF15-NB1-A11802	2:38:53.75	27:49:15.4	-0.88 ± 0.14	6.52	ELG	23.202 ± 0.161	22.021 ± 0.060	23.673 ± 0.115	-15.687 ± 0.073
SFF15-NB2-B334	2:38:54.45	27:32:53.3	-1.18 ± 0.13	8.81	ELG	22.984 ± 0.131	22.746 ± 0.098	23.762 ± 0.110	-15.599 ± 0.049

Table 3.4 (cont'd)

SFACT ID	$\alpha(J2000)$ H:M:S (2)	$\delta(J2000)$ D:M:S (3)	Δm mag (4)	Ratio (5)	Object Type (6)	m_r mag (7)	m_i mag (8)	m_g mag (9)	$\log(f_{NB})$ erg/s/cm ² (10)
SFF15-NB2-C21339	2:38:59.79	28:06:01.1	-0.75 ± 0.11	6.55	ELG	22.819 ± 0.088	22.741 ± 0.088	23.798 ± 0.106	-15.803 ± 0.054
SFF15-NB1-C21190	2:39:01.18	28:03:15.3	-0.96 ± 0.13	7.36	ELG	22.949 ± 0.110	22.767 ± 0.091	24.009 ± 0.121	-15.591 ± 0.058
SFF15-NB2-C21160	2:39:01.42	27:56:55.6	-0.47 ± 0.09	5.20	ELG	22.186 ± 0.075	22.195 ± 0.077	23.257 ± 0.094	-15.867 ± 0.051
SFF15-NB3-A10777	2:39:01.44	27:35:44.2	-0.94 ± 0.16	5.99	ELG	25.286 ± 0.997	22.980 ± 0.138	24.675 ± 0.293	-15.761 ± 0.062
SFF15-NB1-C20871	2:39:03.93	28:02:58.5	-0.65 ± 0.05	12.97	ELG	20.052 ± 0.026	19.732 ± 0.019	20.652 ± 0.021	-14.988 ± 0.028
SFF15-NB2-C20849	2:39:04.08	27:52:35.4	-1.42 ± 0.02	66.09	ELG	19.697 ± 0.020	19.368 ± 0.014	21.168 ± 0.026	-14.167 ± 0.011
SFF15-NB3-C20822	2:39:04.26	28:00:38.8	-0.90 ± 0.17	5.38	ELG	23.887 ± 0.179	23.310 ± 0.111	25.061 ± 0.243	-15.819 ± 0.072
SFF15-NB2-A10320	2:39:04.77	27:49:29.6	-1.08 ± 0.20	5.32	ELG	23.979 ± 0.211	23.984 ± 0.216	24.592 ± 0.161	-15.759 ± 0.059
SFF15-NB1-A10251	2:39:05.25	27:44:23.1	-0.61 ± 0.01	53.63	GAL	16.470 ± 0.013	16.035 ± 0.005	17.211 ± 0.007	-13.409 ± 0.010
SFF15-NB3-A9877	2:39:08.39	27:38:38.2	-0.96 ± 0.09	10.45	ELG	22.777 ± 0.097	22.430 ± 0.076	23.762 ± 0.107	-15.486 ± 0.031
SFF15-NB1-C20349	2:39:08.43	28:07:01.3	-0.50 ± 0.09	5.47	ELG	22.537 ± 0.108	21.410 ± 0.044	23.605 ± 0.128	-15.696 ± 0.052
SFF15-NB3-C20216	2:39:09.56	28:12:24.9	-0.98 ± 0.18	5.45	ELG	23.935 ± 0.257	23.365 ± 0.159	24.949 ± 0.283	-15.769 ± 0.080
SFF15-NB1-A9721	2:39:09.60	27:37:20.2	-0.42 ± 0.01	39.84	GAL	17.031 ± 0.013	16.477 ± 0.005	17.860 ± 0.007	-13.783 ± 0.011
SFF15-NB3-C20126	2:39:10.31	28:10:26.2	-0.48 ± 0.09	5.24	ELG	22.645 ± 0.081	22.028 ± 0.054	23.389 ± 0.083	-15.786 ± 0.064

Table 3.4 (cont'd)

SFACT ID	$\alpha(J2000)$ H:M:S (2)	$\delta(J2000)$ D:M:S (3)	Δm mag (4)	Ratio (5)	Object Type (6)	m_r mag (7)	m_i mag (8)	m_g mag (9)	$\log(f_{NB})$ erg/s/cm ² (10)
SFF15-NB2-C19961	2:39:11.64	28:09:56.7	-0.72 ± 0.10	7.20	ELG	22.577 ± 0.073	22.271 ± 0.060	23.430 ± 0.074	-15.706 ± 0.046
SFF15-NB2-C19927	2:39:11.79	27:52:58.6	-1.47 ± 0.17	8.67	ELG	23.642 ± 0.161	23.521 ± 0.151	24.536 ± 0.172	-15.619 ± 0.046
SFF15-NB2-C19852	2:39:12.41	27:52:01.5	-0.61 ± 0.06	10.75	ELG	21.343 ± 0.042	21.372 ± 0.045	22.150 ± 0.047	-15.428 ± 0.028
SFF15-NB1-C19841	2:39:12.49	27:53:33.2	-0.55 ± 0.05	10.88	ELG	21.040 ± 0.037	20.854 ± 0.031	22.004 ± 0.039	-15.209 ± 0.032
SFF15-NB2-A9253	2:39:13.46	27:41:14.5	-1.27 ± 0.20	6.44	ELG	23.673 ± 0.249	23.628 ± 0.263	25.219 ± 0.502	-15.781 ± 0.066
SFF15-NB2-A9203	2:39:13.80	27:46:36.2	-0.99 ± 0.09	11.03	ELG	22.389 ± 0.084	22.118 ± 0.071	23.226 ± 0.083	-15.453 ± 0.035
SFF15-NB1-A9145	2:39:14.12	27:35:19.3	-0.81 ± 0.15	5.27	ELG	23.274 ± 0.131	22.833 ± 0.095	23.344 ± 0.071	-15.760 ± 0.080
SFF15-NB1-C19187	2:39:17.96	27:57:35.5	-1.31 ± 0.05	23.96	ELG	20.043 ± 0.034	19.817 ± 0.030	20.504 ± 0.026	-14.858 ± 0.021
SFF15-NB3-C19116	2:39:18.60	28:14:15.7	-0.56 ± 0.09	6.36	ELG	22.157 ± 0.071	21.845 ± 0.058	23.269 ± 0.092	-15.643 ± 0.054
SFF15-NB1-C18438	2:39:24.04	28:12:58.4	-1.25 ± 0.18	7.00	ELG	23.837 ± 0.282	22.862 ± 0.119	23.957 ± 0.129	-15.536 ± 0.078
SFF15-NB1-A7599	2:39:25.04	27:35:56.2	-0.45 ± 0.05	9.04	HII	20.308 ± 0.025	21.274 ± 0.055	22.155 ± 0.055	-15.106 ± 0.036
SFF15-NB1-A7554	2:39:25.37	27:35:53.1	0.10 ± 0.04	2.36	GAL	18.074 ± 0.016	17.897 ± 0.010	18.933 ± 0.012	-15.231 ± 0.162
SFF15-NB1-A7296	2:39:27.32	27:41:44.0	-0.79 ± 0.14	5.71	ELG	23.436 ± 0.132	22.564 ± 0.071	24.068 ± 0.139	-15.711 ± 0.074
SFF15-NB1-C17851	2:39:28.09	28:14:03.8	-2.27 ± 0.36	6.38	ELG	24.917 ± 0.435	24.531 ± 0.317	25.680 ± 0.421	-15.674 ± 0.069

Table 3.4 (cont'd)

SFACT ID	$\alpha(J2000)$ H:M:S (2)	$\delta(J2000)$ D:M:S (3)	Δm mag (4)	Ratio (5)	Object Type (6)	m_r mag (7)	m_i mag (8)	m_g mag (9)	$\log(f_{NB})$ erg/s/cm ² (10)
SFF15-NB2-C17583	2:39:30.08	27:54:21.9	-0.73 ± 0.14	5.38	ELG	22.974 ± 0.093	23.070 ± 0.103	24.075 ± 0.114	-15.925 ± 0.063
SFF15-NB1-A6426	2:39:33.64	27:35:51.0	-0.59 ± 0.11	5.36	ELG	22.608 ± 0.093	21.786 ± 0.048	23.468 ± 0.107	-15.606 ± 0.071
SFF15-NB3-A6370	2:39:33.97	27:32:20.8	-0.42 ± 0.04	10.02	ELG	20.980 ± 0.032	20.520 ± 0.023	21.861 ± 0.037	-15.206 ± 0.027
SFF15-NB1-A6342	2:39:34.21	27:36:56.8	-0.86 ± 0.11	7.57	ELG	23.018 ± 0.101	22.264 ± 0.060	23.792 ± 0.102	-15.577 ± 0.066
SFF15-NB2-A6234	2:39:35.33	27:44:59.7	-0.78 ± 0.10	7.39	ELG	22.584 ± 0.064	22.855 ± 0.088	23.521 ± 0.071	-15.661 ± 0.046
SFF15-NB2-C16966	2:39:35.51	28:14:35.2	-1.49 ± 0.08	17.76	ELG	22.404 ± 0.087	22.281 ± 0.073	23.310 ± 0.089	-15.106 ± 0.024
SFF15-NB2-C16947	2:39:35.59	28:08:32.2	-1.47 ± 0.11	13.05	ELG	23.017 ± 0.097	22.946 ± 0.102	24.109 ± 0.151	-15.427 ± 0.031
SFF15-NB2-C16911	2:39:35.87	27:56:03.3	-1.22 ± 0.15	7.88	ELG	23.566 ± 0.155	23.428 ± 0.154	24.069 ± 0.129	-15.670 ± 0.052
SFF15-NB2-C16848	2:39:36.30	27:56:10.9	-0.66 ± 0.08	8.60	ELG	22.054 ± 0.061	21.824 ± 0.054	22.942 ± 0.068	-15.568 ± 0.038
SFF15-NB2-A5900	2:39:37.89	27:44:32.9	-0.57 ± 0.11	5.10	ELG	22.371 ± 0.079	22.236 ± 0.064	23.539 ± 0.095	-15.722 ± 0.067
SFF15-NB3-C16449	2:39:38.97	28:09:04.8	-0.41 ± 0.07	5.59	ELG	23.303 ± 0.133	21.858 ± 0.043	24.622 ± 0.190	-15.710 ± 0.041
SFF15-NB1-C16037	2:39:41.96	28:11:19.0	-1.22 ± 0.23	5.40	ELG	24.422 ± 0.318	23.347 ± 0.134	24.627 ± 0.201	-15.865 ± 0.099
SFF15-NB2-A5401	2:39:42.11	27:34:16.8	-0.44 ± 0.09	5.00	ELG	22.219 ± 0.069	21.373 ± 0.038	23.315 ± 0.091	-15.653 ± 0.066
SFF15-NB3-A5357	2:39:42.63	27:39:27.5	-0.97 ± 0.17	5.78	ELG	23.391 ± 0.135	23.288 ± 0.126	24.925 ± 0.224	-15.828 ± 0.071

Table 3.4 (cont'd)

SFACT ID	$\alpha(J2000)$ H:M:S (1)	$\delta(J2000)$ D:M:S (2)	Δm mag (4)	Ratio (5)	Object Type (6)	m_r mag (7)	m_i mag (8)	m_g mag (9)	$\log(f_{NB})$ erg/s/cm ² (10)
SFF15-NB1-C15891	2:39:43.14	28:08:15.8	-1.33 ± 0.25	5.22	ELG	24.552 ± 0.312	23.730 ± 0.163	26.184 ± 0.604	-15.914 ± 0.093
SFF15-NB1-C15708	2:39:44.53	28:12:18.6	-0.57 ± 0.04	16.10	ELG	20.256 ± 0.024	19.850 ± 0.017	21.044 ± 0.023	-14.944 ± 0.020
SFF15-NB2-A5122	2:39:44.90	27:45:28.9	-0.76 ± 0.15	5.01	ELG	23.366 ± 0.122	23.032 ± 0.094	24.341 ± 0.136	-15.945 ± 0.070
SFF15-NB1-A5083	2:39:45.22	27:39:44.6	-0.98 ± 0.13	7.82	ELG	22.821 ± 0.130	22.385 ± 0.089	23.447 ± 0.104	-15.517 ± 0.059
SFF15-NB2-C15565	2:39:45.66	28:11:36.4	-0.57 ± 0.10	5.53	ELG	22.512 ± 0.091	22.021 ± 0.064	23.555 ± 0.102	-15.577 ± 0.062
SFF15-NB2-A5017	2:39:45.97	27:49:24.4	-0.68 ± 0.08	9.01	ELG	21.842 ± 0.055	21.532 ± 0.045	22.537 ± 0.048	-15.462 ± 0.038
SFF15-NB1-A4836	2:39:47.52	27:30:27.3	-0.66 ± 0.10	6.94	ELG	22.370 ± 0.097	21.664 ± 0.059	23.321 ± 0.123	-15.599 ± 0.058
SFF15-NB3-A4797	2:39:47.99	27:50:38.8	-0.63 ± 0.11	5.63	ELG	22.753 ± 0.115	22.282 ± 0.080	23.463 ± 0.093	-15.632 ± 0.057
SFF15-NB1-C14876	2:39:49.39	28:02:43.7	-0.68 ± 0.11	6.21	ELG	23.092 ± 0.091	22.439 ± 0.058	23.552 ± 0.069	-15.693 ± 0.044
SFF15-NB2-A4443	2:39:50.63	27:30:40.0	-0.70 ± 0.05	13.20	ELG	21.255 ± 0.041	21.136 ± 0.038	21.974 ± 0.038	-15.187 ± 0.025
SFF15-NB1-A4444	2:39:50.71	27:40:37.4	-0.76 ± 0.13	5.71	ELG	23.334 ± 0.122	22.387 ± 0.060	23.993 ± 0.105	-15.757 ± 0.068
SFF15-NB3-C13945	2:39:52.18	27:55:12.3	-0.93 ± 0.15	6.17	ELG	23.846 ± 0.205	22.982 ± 0.102	24.333 ± 0.143	-15.739 ± 0.063
SFF15-NB3-A4265	2:39:52.29	27:32:44.4	-1.56 ± 0.28	5.54	ELG	23.885 ± 0.191	24.020 ± 0.216	24.755 ± 0.176	-15.757 ± 0.070
SFF15-NB3-C13789	2:39:52.70	28:00:18.6	-0.89 ± 0.15	5.82	ELG	23.663 ± 0.172	23.223 ± 0.127	24.341 ± 0.149	-15.813 ± 0.060

Table 3.4 (cont'd)

SFACT ID	$\alpha(J2000)$ H:M:S (2)	$\delta(J2000)$ D:M:S (3)	Δm mag (4)	Ratio (5)	Object Type (6)	m_r mag (7)	m_i mag (8)	m_g mag (9)	$\log(f_{NB})$ erg/s/cm ² (10)
SFF15-NB3-A4188	2:39:52.92	27:33:04.6	-1.34 ± 0.26	5.14	ELG	24.327 ± 0.340	24.022 ± 0.293	25.154 ± 0.350	-15.647 ± 0.057
SFF15-NB2-A4189	2:39:52.94	27:36:56.3	-0.45 ± 0.06	7.60	ELG	21.557 ± 0.040	21.291 ± 0.034	22.484 ± 0.042	-15.477 ± 0.035
SFF15-NB2-C13705	2:39:53.13	28:11:43.1	-0.81 ± 0.10	8.45	ELG	22.018 ± 0.086	22.525 ± 0.159	21.897 ± 0.052	-15.508 ± 0.056
SFF15-NB2-A4153	2:39:53.19	27:30:32.3	-0.98 ± 0.09	10.33	ELG	22.548 ± 0.073	22.475 ± 0.074	23.374 ± 0.075	-15.480 ± 0.037
SFF15-NB1-C12736	2:39:55.99	28:07:15.5	-0.75 ± 0.15	5.01	ELG	23.099 ± 0.131	23.078 ± 0.134	23.520 ± 0.091	-15.680 ± 0.081
SFF15-NB1-A3657	2:39:57.90	27:39:48.2	-0.77 ± 0.12	6.20	ELG	23.092 ± 0.116	22.402 ± 0.071	23.645 ± 0.090	-15.630 ± 0.073
SFF15-NB2-A3355	2:40:00.47	27:46:46.3	-1.82 ± 0.11	17.25	ELG	22.976 ± 0.080	23.437 ± 0.131	24.219 ± 0.120	-15.214 ± 0.023
SFF15-NB3-C10926	2:40:01.45	28:01:54.8	-0.55 ± 0.06	9.63	ELG	22.012 ± 0.086	21.392 ± 0.050	22.860 ± 0.080	-15.314 ± 0.024
SFF15-NB3-A3094	2:40:02.68	27:49:27.1	-0.83 ± 0.10	7.92	ELG	22.855 ± 0.072	22.595 ± 0.064	24.025 ± 0.103	-15.608 ± 0.047
SFF15-NB3-C10241	2:40:03.06	28:02:38.8	-0.91 ± 0.08	11.24	ELG	22.791 ± 0.079	22.251 ± 0.055	23.432 ± 0.074	-15.433 ± 0.032
SFF15-NB3-A2676	2:40:05.89	27:46:42.4	-0.45 ± 0.08	5.43	ELG	22.214 ± 0.074	21.823 ± 0.055	23.249 ± 0.078	-15.691 ± 0.049
SFF15-NB1-A2606	2:40:06.26	27:33:13.6	-0.91 ± 0.03	28.15	HII	19.500 ± 0.031	19.115 ± 0.025	19.929 ± 0.024	-14.296 ± 0.012
SFF15-NB1-A2574	2:40:06.50	27:33:11.5	-0.31 ± 0.02	16.20	GAL	16.625 ± 0.013	16.295 ± 0.005	17.158 ± 0.007	-13.626 ± 0.011
SFF15-NB1-A2519	2:40:07.00	27:42:14.1	-0.50 ± 0.10	5.05	ELG	22.411 ± 0.059	22.354 ± 0.061	24.066 ± 0.118	-15.675 ± 0.079

Table 3.4 (cont'd)

SFACT ID	$\alpha(12000)$ H:M:S (1)	$\delta(12000)$ D:M:S (2)	Δm mag (4)	Ratio (5)	Object Type (6)	m_r mag (7)	m_i mag (8)	m_g mag (9)	$\log(f_{NB})$ erg/s/cm ² (10)
SFF15-NB1-C8670	2:40:07.32	27:58:41.9	-0.74 ± 0.05	13.91	ELG	19.910 ± 0.045	19.649 ± 0.033	20.315 ± 0.029	-14.956 ± 0.038
SFF15-NB2-C8616	2:40:07.44	27:53:36.2	-0.64 ± 0.12	5.38	ELG	22.797 ± 0.085	22.836 ± 0.089	23.774 ± 0.107	-15.827 ± 0.055
SFF15-NB2-C8523	2:40:07.78	27:55:08.7	-0.71 ± 0.09	7.90	ELG	22.143 ± 0.079	21.944 ± 0.067	22.950 ± 0.075	-15.628 ± 0.047
SFF15-NB1-C8250	2:40:08.51	27:58:15.0	-0.19 ± 0.02	10.28	GAL	17.005 ± 0.013	16.632 ± 0.006	17.639 ± 0.007	-13.822 ± 0.014
SFF15-NB1-C8190	2:40:08.63	27:58:06.7	-1.20 ± 0.10	12.12	HII	21.919 ± 0.081	21.549 ± 0.068	22.189 ± 0.054	-15.092 ± 0.033
SFF15-NB3-A2157	2:40:09.97	27:49:40.6	-0.68 ± 0.10	6.90	ELG	22.629 ± 0.119	22.159 ± 0.088	23.042 ± 0.080	-15.569 ± 0.047
SFF15-NB2-A2035	2:40:10.64	27:32:54.5	-1.13 ± 0.22	5.05	ELG	23.641 ± 0.151	24.753 ± 0.447	24.801 ± 0.198	-15.990 ± 0.068
SFF15-NB2-C7045	2:40:11.49	28:07:06.7	-1.29 ± 0.11	12.01	ELG	21.803 ± 0.080	22.064 ± 0.100	22.505 ± 0.070	-15.353 ± 0.038
SFF15-NB2-C6598	2:40:12.22	27:51:58.9	-1.94 ± 0.07	27.07	ELG	21.986 ± 0.065	22.291 ± 0.084	22.780 ± 0.055	-14.817 ± 0.019
SFF15-NB2-A1747	2:40:12.99	27:44:20.6	-0.99 ± 0.04	26.89	ELG	20.684 ± 0.031	20.581 ± 0.028	21.391 ± 0.027	-14.757 ± 0.017
SFF15-NB2-A1673	2:40:13.56	27:42:11.7	-0.77 ± 0.12	6.42	ELG	23.163 ± 0.120	22.430 ± 0.066	23.774 ± 0.098	-15.713 ± 0.062
SFF15-NB2-A1625	2:40:13.93	27:44:14.2	-0.75 ± 0.03	22.96	ELG	20.177 ± 0.023	20.076 ± 0.020	20.834 ± 0.018	-14.732 ± 0.017
SFF15-NB1-A1544	2:40:14.38	27:34:34.0	-1.07 ± 0.01	82.18	GAL	17.317 ± 0.013	16.989 ± 0.006	17.566 ± 0.007	-13.483 ± 0.010
SFF15-NB1-A1530	2:40:14.44	27:34:29.7	-0.99 ± 0.03	34.24	HII	19.431 ± 0.018	19.136 ± 0.014	19.654 ± 0.013	-14.310 ± 0.012

Table 3.4 (cont'd)

SFACT ID (1)	α (J2000) H:M:S (2)	δ (J2000) D:M:S (3)	Δm mag (4)	Ratio Type (5)	Object Type (6)	m_r mag (7)	m_i mag (8)	m_g mag (9)	$\log(f_{NB})$ erg/s/cm ² (10)
SFF15-NB1-A1465	2:40:14.71	27:34:08.2	-1.20 ± 0.05	26.45	HII	20.818 ± 0.049	20.348 ± 0.040	21.000 ± 0.038	-14.504 ± 0.014
SFF15-NB1-A1439	2:40:14.79	27:34:15.0	-0.51 ± 0.02	24.91	GAL	16.829 ± 0.013	16.465 ± 0.006	17.241 ± 0.007	-13.476 ± 0.011
SFF15-NB2-C4662	2:40:15.62	27:53:45.8	-0.67 ± 0.06	11.68	ELG	21.411 ± 0.038	21.333 ± 0.037	22.099 ± 0.038	-15.221 ± 0.031

Notes. — SFACT ID is a unique identifier which includes information about the field, quadrant, and filter in which the object was found.

3.4.2 Example Objects

We illustrate the types of objects detected in our survey by showing ten examples of SFACT targets. These are all objects which were selected for follow-up spectroscopy and have been confirmed to be genuine emission-line galaxies. We have chosen examples which demonstrate the variety of objects found in the SFACT catalog and the depth of our images. The example objects have been grouped by their detected line. For each object, the redshift and type of object is derived from spectral analysis. This is discussed in SFACT3 where the corresponding spectra for these example objects can be found.

The following figures are the images produced by our software and are used during ELG candidate evaluations and checking. Each figure is comprised of three $50'' \times 50''$ cutouts of the same object from different images. The leftmost image is the relevant continuum image; this is r+i when the NB image is NB1 or NB2 and i when the NB image is NB3. The middle image is the NB image before continuum subtraction. The rightmost image is the NB continuum-subtracted image (the difference image). In each cutout, the objects are marked with crosshairs to guide the eye.

3.4.2.1 H α Detections

The first three SFACT example targets, shown in Figure 3.3, were all detected via their H α emission line. SFF01-NB2-B19198 at the top of Figure 3.3 is one of our closest targets at $z = 0.0034$. The specific target is not actually the galaxy center, but an H II region near the center. As discussed in section 3.3.2.3, the H II region remains in our catalog, but the photometric properties measured are those for the galaxy as a whole. Here it is visually clear that the H II region is a large knot of emission in an otherwise quiescent dwarf galaxy. In a more traditional BB only survey this may not have stood out as a source of emission. This galaxy has a g-band magnitude of 19.00 and a narrow-band flux of 2.24×10^{-15} erg s $^{-1}$ cm $^{-2}$.

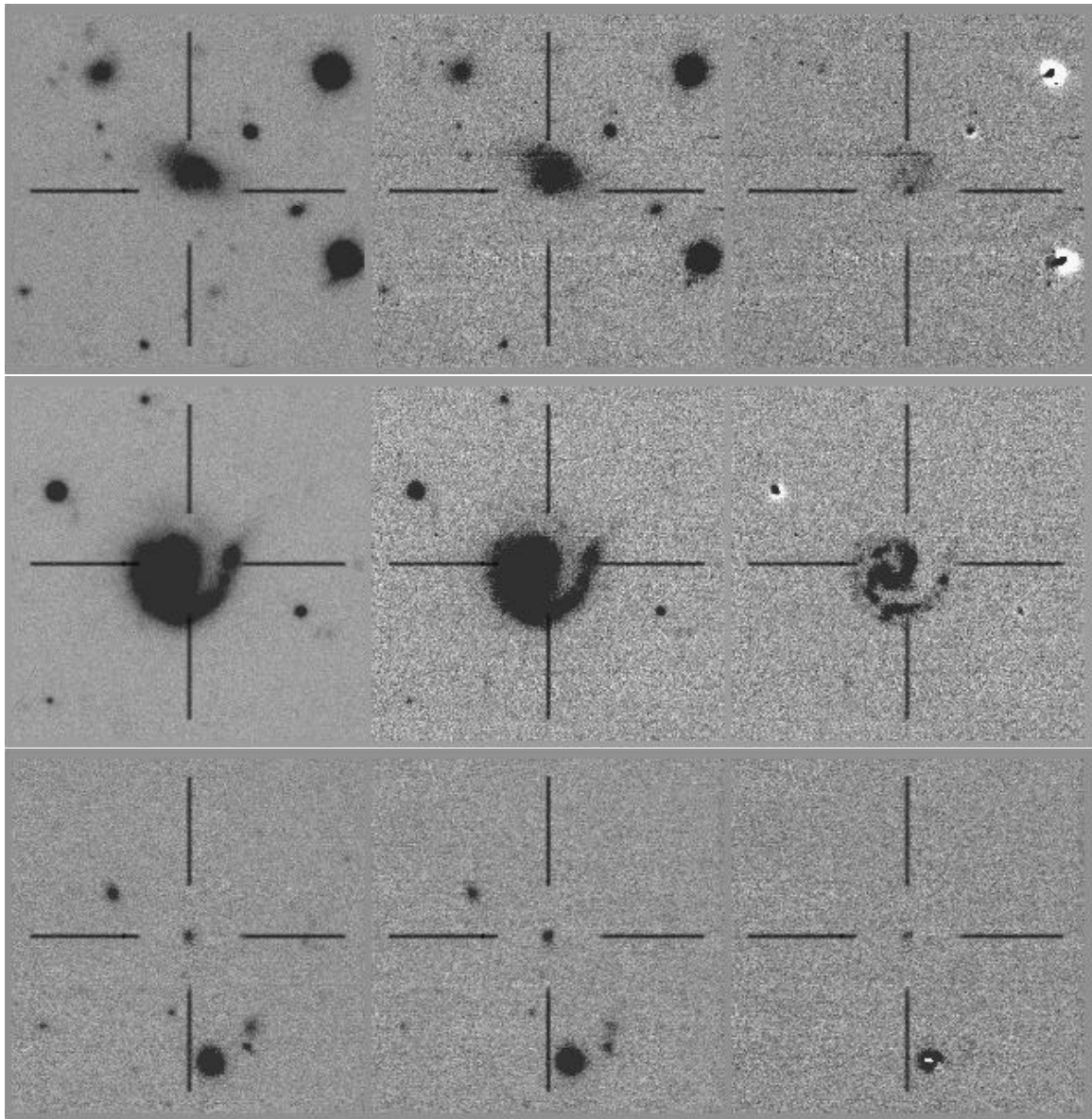


Figure 3.3 Three of our H α -detected objects. The H α detections span $0.0 < z < 0.15$ and include all of our spiral galaxies. Top: SFF01-NB2-B19198 was detected in our NB2 filter and is a faint dwarf galaxy. Middle: SFF15-NB1-A2606 was detected in our NB1 filter via many of its H II regions. Bottom: SFF01-NB3-D2175 was detected in our NB3 filter.

The middle galaxy is SFF15-NB1-A2606 and was detected in our NB1 filter. Again, this is an H II region in a larger galaxy. The galaxy has an BB aperture radius of 100 pixels ($25''$) and a NB aperture of 72 pixels. This spiral galaxy is found at $z = 0.0643$ with a g-band magnitude of 17.16 and an integrated narrow-band flux of 2.36×10^{-14} erg s $^{-1}$ cm $^{-2}$. Both of these first two galaxies demonstrate the ability of SFACT to find H II regions in extended sources, the former of which is discussed in more detail in SFACT1.

The last of this set is a more typical SFACT target. SFF01-NB3-D2175 is a compact object which is visible in the continuum image and appears slightly brighter in the NB image. This particular target has a g-band magnitude of 22.41, a NB flux of 2.80×10^{-16} erg s $^{-1}$ cm $^{-2}$, and is found at $z = 0.1374$. Unlike the previous two galaxies, the aperture for this object was successfully determined using our curve-of-growth analysis. This is the case for most objects which appear as compact dots like SFF01-NB3-D2175.

3.4.2.2 [O III] Detections

The next three examples, shown in Figure 3.4, are each [O III] detections. In the top set of images is SFF15-NB2-C20849. This galaxy has very strong line emission. In our nearest [O III] redshift window, this object is at $z = 0.3228$ with a g-band magnitude of 21.17 and narrow-band flux of 6.81×10^{-15} erg s $^{-1}$ cm $^{-2}$, making it the object with the second strongest flux in this example set, and the strongest of those which are not large spiral galaxies. Follow-up analysis (discussed in SFACT3) has confirmed that this object is a Seyfert 2.

The middle set of images shows SFF01-NB1-D4500 which has a g-band magnitude of 22.56. This object is found at $z = 0.3906$ and has a NB flux of 1.01×10^{-15} erg s $^{-1}$ cm $^{-2}$. This galaxy's aperture needed to be checked by eye due to the other object nearby.

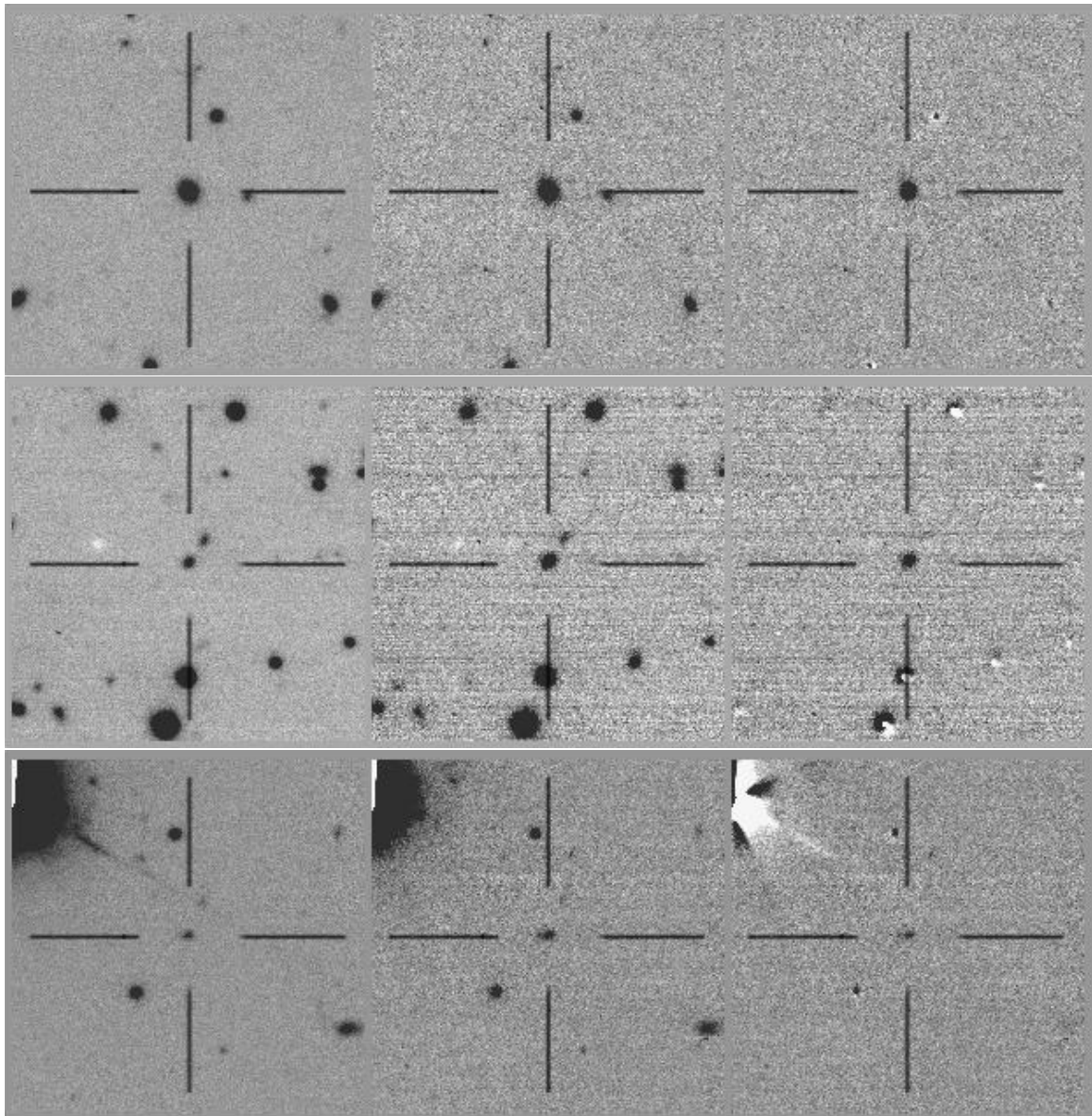


Figure 3.4 Three of our [O III]-detected objects. The [O III] detections span $0.31 < z < 0.50$ and are typically compact sources like these. Top: SFF15-NB2-C20849 was detected in our NB2 filter. Middle: SFF01-NB1-D4500 was detected in our NB1 filter. Bottom: SFF10-NB3-D13569 was detected in our NB3 filter.

Rounding out the [O III]-detected set is SFF10-NB3-D13569 at the bottom of Figure 3.4. This target is at a redshift of $z = 0.4829$ with a g-band magnitude of 23.02 and a narrow-band flux of 5.03×10^{-16} erg s $^{-1}$ cm $^{-2}$. This object is representative of many SFACT targets which are very compact but have only moderately strong emission in the NB filter. Nonetheless, the nebular emission is strong enough to allow us to detect it.

3.4.2.3 [O II] Detections

The final set of three targets is shown in Figure 3.5 and each candidate was detected by its [O II] line. SFF10-NB2-A8098 is shown in the top row of Figure 3.5 and is one of our fainter sources at a g-band magnitude of 23.78, falling over half a magnitude below the median g-band magnitude of the pilot-study targets. The r- and i-band magnitudes are similarly faint at 23.12 and 23.54, respectively. This demonstrates the sensitivity of SFACT. The galaxy in the NB image before continuum subtraction (the middle cutout) looks brighter than it does in the continuum image on the left, demonstrating the visually strong emission line. It is at a distance of $z = 0.7670$ and has a narrow-band flux of 2.04×10^{-16} erg s $^{-1}$ cm $^{-2}$.

Shown in the middle row of Figure 3.5 is SFF10-NB1-C19716. This target is at $z = 0.8694$; at such a distance it is understandably very compact in our images. This object has a g-band magnitude of 23.06 and a narrow-band flux of 3.63×10^{-16} erg s $^{-1}$ cm $^{-2}$.

One of the most distant galaxies in our primary redshift windows is SFF01-NB3-B5847 at $z = 1.0023$. It has a g-band magnitude of 23.08 and a narrow-band flux of 4.51×10^{-16} erg s $^{-1}$ cm $^{-2}$. This was another object which required us to check the suggested photometry aperture since there is another faint object identified nearby.

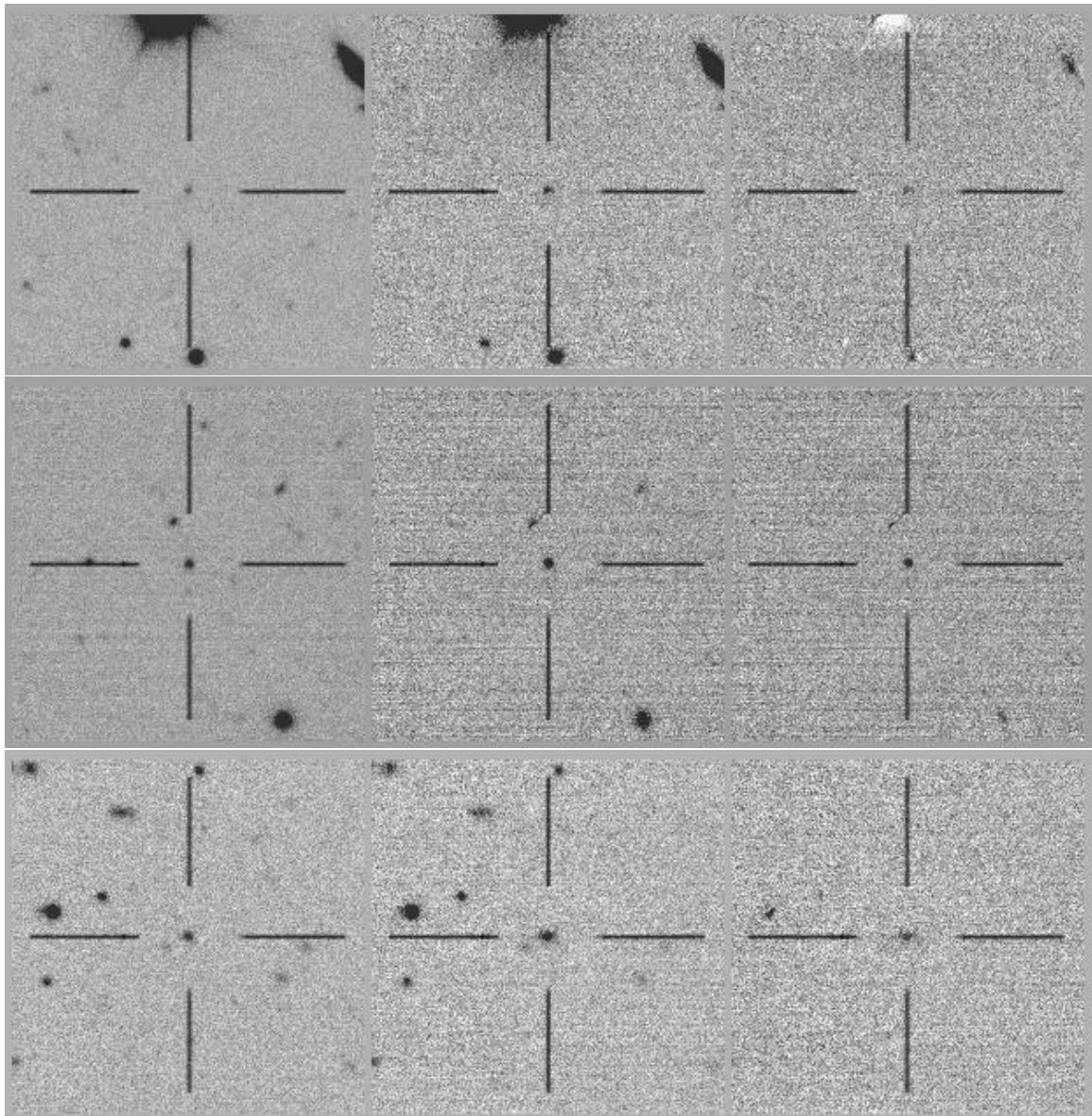


Figure 3.5 Three of our [O II]-detected objects. The [O II] detections span $0.78 < z < 1.0$ and are typically small dots like these. Top: SFF10-NB2-A8098 was detected in our NB2 filter. Middle: SFF10-NB1-C19716 was detected in our NB1 filter. Bottom: SFF01-NB3-B5847 was detected in our NB3 filter.

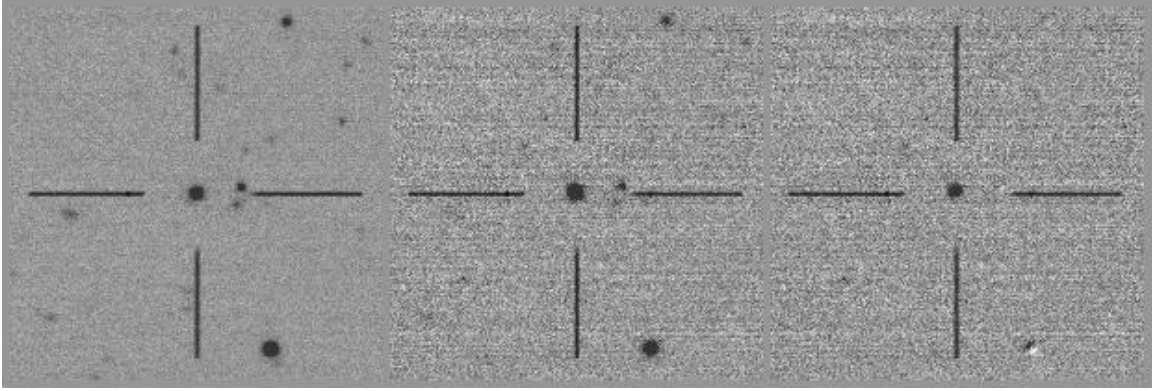


Figure 3.6 SFF10-NB2-C21205: This target was detected in our NB2 filter by a strong line at 1908Å. It has been determined to be a quasar.

3.4.2.4 Other Detections

SFACT detects objects outside of our primary redshift windows, including numerous QSOs. The last example object, shown in Figure 3.6, is one such QSO. An emission line at 1908 Å fell into our NB2 filter, allowing us to detect it. As can be seen from Figure 3.6, it is a bright target, with a g-band magnitude of 20.95. It exhibits a moderate line flux of 7.94×10^{-16} erg s⁻¹ cm⁻² yet its large redshift, $z = 2.4643$, demonstrates SFACT’s ability to detect objects well beyond $z = 1$. There are ~ 10 other objects in this pilot study at redshifts greater than our primary redshift windows, all of which are QSOs.

For all of the example SFACT targets shown here, the corresponding spectra can be found in SFACT3.

3.4.3 Photometric Properties of SFACT Targets

In this section we examine the photometric properties of the SFACT targets. We also investigate our photometric uncertainties in relation to SDSS to provide context for our results. SFACT1 (Figure 2)⁸ presents a set of composite histograms showing the range of BB apparent magnitudes for the full sample of pilot-study candidates,

⁸See also Figure 4.7 of this thesis.

demonstrating the depth of our sample. It is worthwhile to compare the distributions of BB magnitude and NB line flux across the three pilot-study fields as well as across the three narrow-band filters.

Figure 3.7 shows the distribution of r-band magnitude and NB flux for each pilot-study field separately. While there are variations between the fields, the broad characteristics are remarkably similar. The r-band magnitude medians are 22.53, 22.50 and 22.51, demonstrating a consistent depth between the fields. This figure also demonstrates the range of brightness in our catalog. We see targets which have an r-band magnitude as bright as 16 and as faint as 25. The NB flux distributions on the right hand side of Figure 3.7 also exhibit strong similarities with each other. The median log NB flux is seen to be very stable across the three fields: -15.51 , -15.50 , and -15.57 $\text{erg s}^{-1} \text{ cm}^{-2}$.

Figure 2 of SFACT1 also presents a composite g-r histogram (see also Figure 4.7). Like the BB magnitudes, there is a broad range of colors represented in the sample. The median g-r color of 0.65 is consistent with early-type spiral galaxies, but the bulk of the sample have colors between $0.2 < g - r < 1.2$ and include many red systems. As discussed in SFACT1, this is due in part to our selection method. Strong emission lines are present in many of our targets, and these strong lines can influence the overall color of the galaxy, leading to an actively star-forming system appearing redder than expected. These strong emission lines can be seen as part of a wide range of emission line flux strengths in Figure 3.7. This figure highlights SFACT's sensitivity. The strong peak in $\log(f_{NB})$ between -15.50 and -15.75 implies that our survey is complete to approximately this level.

As another way of viewing the distribution, Figure 3.8 shows a similar set of histograms, this time broken down according to which NB filter the object was detected in. While there is a slightly greater spread in the medians, there is still strong consistency across the data set. The most striking difference is the extended bright end

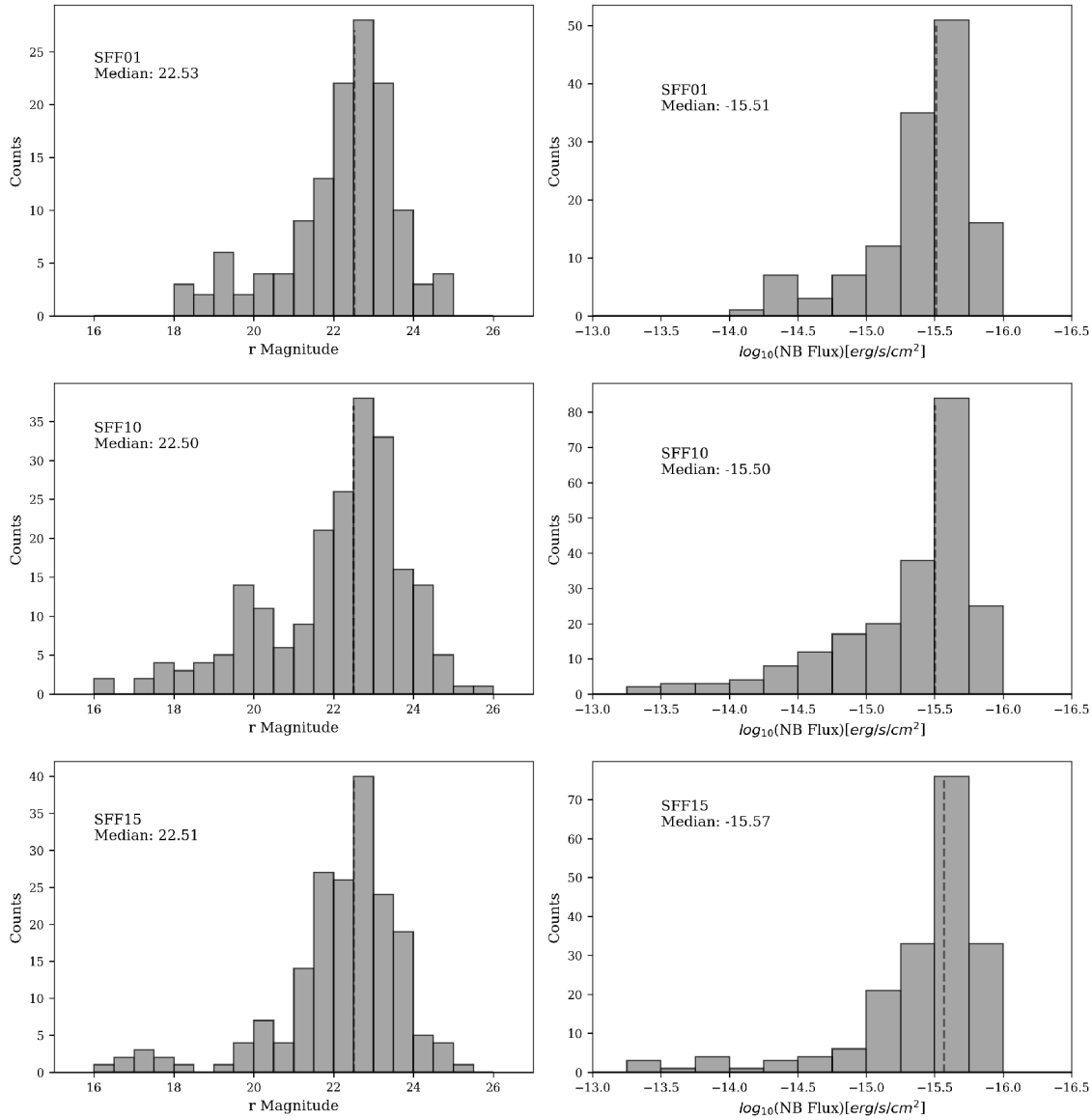


Figure 3.7 Distributions of r magnitude and NB flux broken down by field. The left column shows the r magnitude distributions for each of the pilot-study fields while the right shows the NB flux distributions. From top to bottom is SFF01, SFF10, then SFF15. The vertical dashed lines mark the median of each distribution. The distributions are seen to be very similar from field to field.

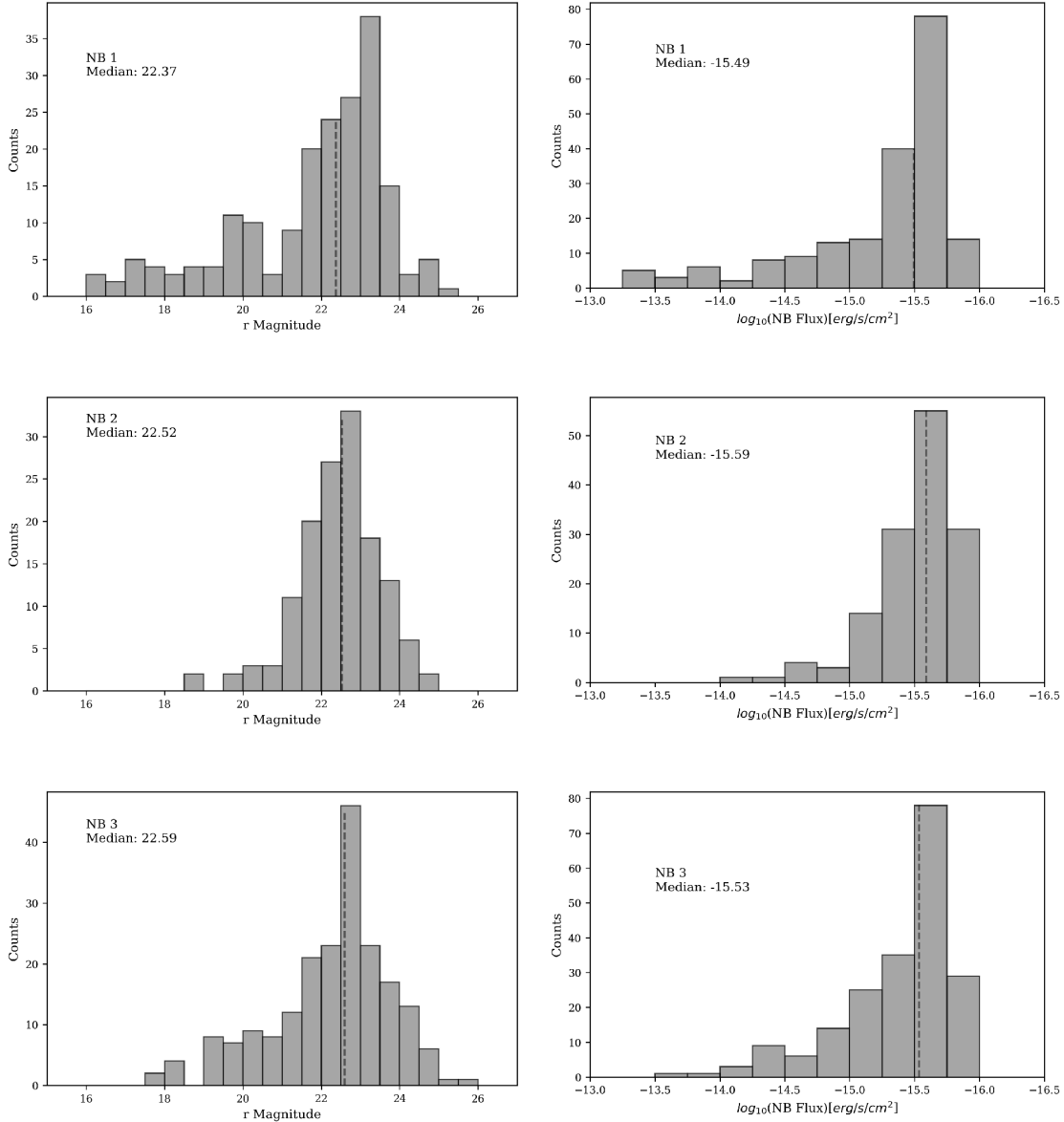


Figure 3.8 Distributions of r magnitude and NB flux broken down by NB filter. The left column shows the r magnitude distributions for each of the pilot-study fields while the right shows the NB flux distributions. From top to bottom is NB1, NB2, then NB3. The vertical dashed lines mark the median of each distribution. Again, there is a strong similarity between the distributions from the different filters, but with a few notable differences.

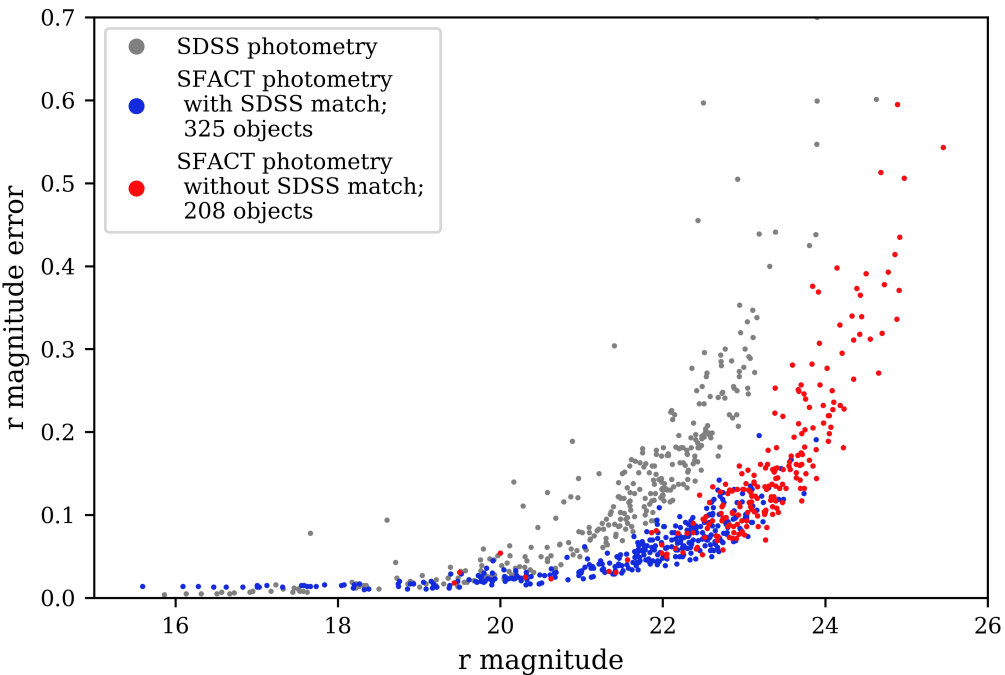


Figure 3.9 A comparison of the r-band photometry between SFACT and SDSS. SDSS photometry is shown in gray. Objects for which there is no corresponding SDSS data are marked in red, while all other SFACT photometry is blue.

of the distributions in NB1 and the deficit of brighter sources in NB2. The latter is presumably caused by the almost complete lack of H α detections in NB2. This is expected, due to the limited volume over which any H α sources could be found within the NB2 filter. Conversely, NB1 finds more H α -detected galaxies that are bright.

Figure 3.9 compares our SFACT photometry to SDSS photometry in the r-band for objects in both catalogs. SDSS photometry is denoted as gray dots while SFACT photometry is given as red or blue. One of the most important conclusions to be drawn from this plot is the clear trend that while photometric errors are low for objects brighter than 20th magnitude in both catalogs, as we move toward fainter objects the uncertainties are increasing at different rates. The errors in the SDSS photometry grow much faster while the SFACT errors for the same magnitude are consistently smaller. Because our BB filters are a near match to the SDSS filters,

there is good agreement in the measured r magnitude value across both catalogs.

Marked in red are SFACT objects for which there was no corresponding SDSS photometry. While most of these targets could be seen visually in the online SDSS images, they were too faint to be included in the SDSS catalogs. The reduced photometric errors at fainter magnitudes for the SFACT data come as no surprise, since our data are obtained with a larger telescope and our integration times for our BB images are longer than the effective integration times for SDSS.

3.4.4 Connecting Selection Parameters to NB Flux

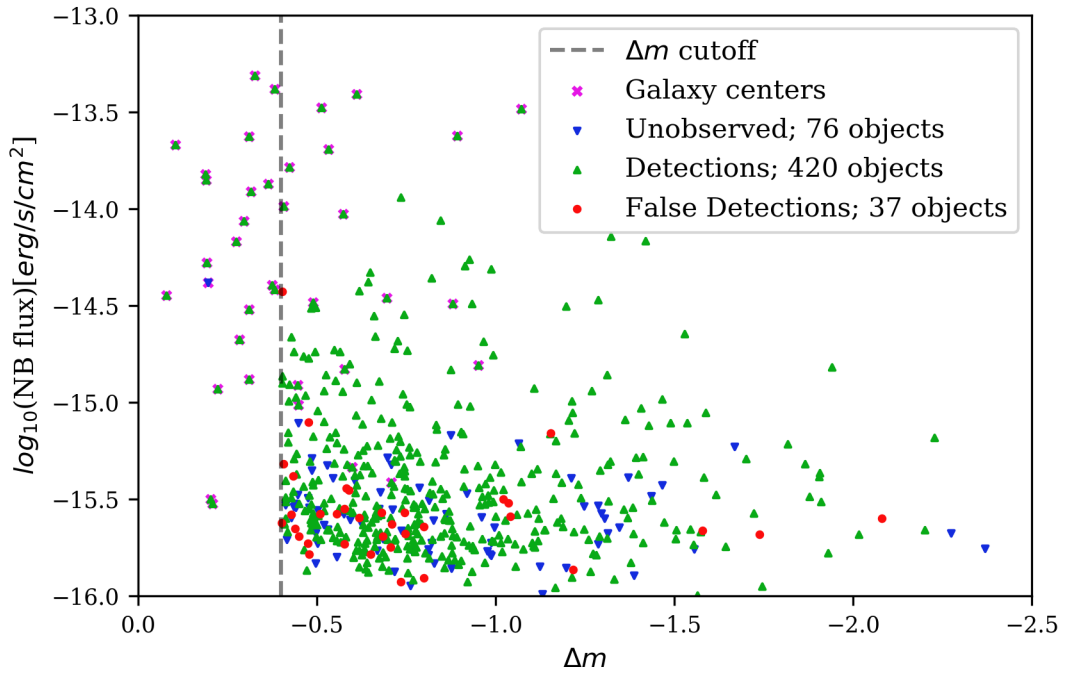


Figure 3.10 Shown here are the SFACT targets comparing their Δm against their measured NB flux. The dashed vertical line shows the cutoff of objects which proceed to the next step of target selection. Objects marked as pink crosses are galaxy centers. Blue downward triangles are targets which do not yet have follow-up spectroscopy. Green upward triangles have been confirmed as ELGs and red circles denote objects which are confirmed to be false detections. The sample size of each is indicated in the legend.

In this section we investigate the result of the automatic target selection we presented earlier in Figure 3.2. In Figure 3.10 we show the Δm values and the corresponding NB flux for each object. Because of our follow-up spectroscopy (discussed in SFACT3) we are able to denote confirmed emission-line objects (green upward triangles) and false detections (red circles) while also marking those which have yet to be observed (blue downward triangles). The dashed line marks the Δm cutoff of -0.4 as one of our selection criteria to identify ELG candidates. Anything to the left of this line is a galaxy center which corresponds to an H II region located somewhere to the right of the cutoff line. There is no strong correlation between Δm and the strength of the emission line. This is expected since Δm is a flux ratio which should not scale with an absolute flux.

Instead, we expect the strongest correlation to be between Δm and the emission-line equivalent width (EW). Since Δm is a measure of excess flux in the difference image, we expect that a larger excess flux (and thus a smaller Δm) is driven by stronger line emission (with a larger EW). However, as explained in SFACT3, our EW measurements are not all reliable. This is due to the sky-subtraction procedure followed for our multi-fiber spectra and the faint nature of our objects. Our sky subtraction often over-subtracts the continuum, leading to a negative continuum measurement and indeterminate — or even negative — EWs. Even when the continuum is positive, this effect can result in unphysically large EWs (e.g., $\text{EW}_{5007} > 5000\text{\AA}$). While the majority of our EWs appear to be reliably measured, the outliers render our EWs dubious and undependable.

Despite this limitation, we can see the expected correlation between Δm and EW in Figure 3.11. There is a tendency for a larger Δm to correlate with larger emission-line EW. This trend is true regardless of which emission line was detected in our NB filter. The figure indicates that there might be a tendency for the objects detected via $\lambda 3757$ to have smaller EWs, but this could also be due to more distant and fainter

objects having noisier spectra, and therefore a less well-determined continuum level. Further investigation will be conducted and addressed in future papers with a larger catalog.

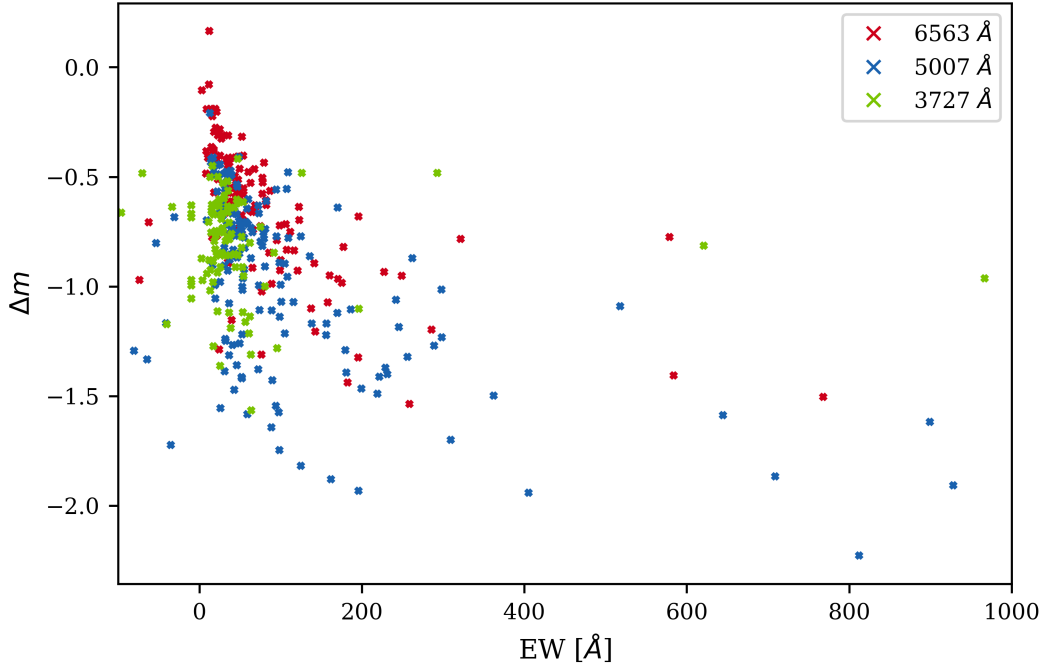


Figure 3.11 Shown here is the correlation between Δm and the emission-line equivalent widths. Upward red triangles are objects detected via their H α emission line, objects depicted as a blue downward triangle were detected via their [O III] emission line, and the green squares are all objects detected via their [O II] emission line. The equivalent widths are highly uncertain, though the expected trend is still visible.

Referring back to Figure 3.2, our selection criteria is based on Δm and *ratio*. We examine the relationship between the NB flux and the *ratio* in Figure 3.12. The two plots both show the *ratio* values of our targets and their corresponding NB flux values. The bottom plot is zoomed in to smaller values of *ratio* in order to focus on where the majority of the targets are. Again, most of the false detections are near the cutoff line, with 80% of the false detections below *ratio* = 8. Here there is a clearer correlation between one of our target selection limits and the measured NB flux. As

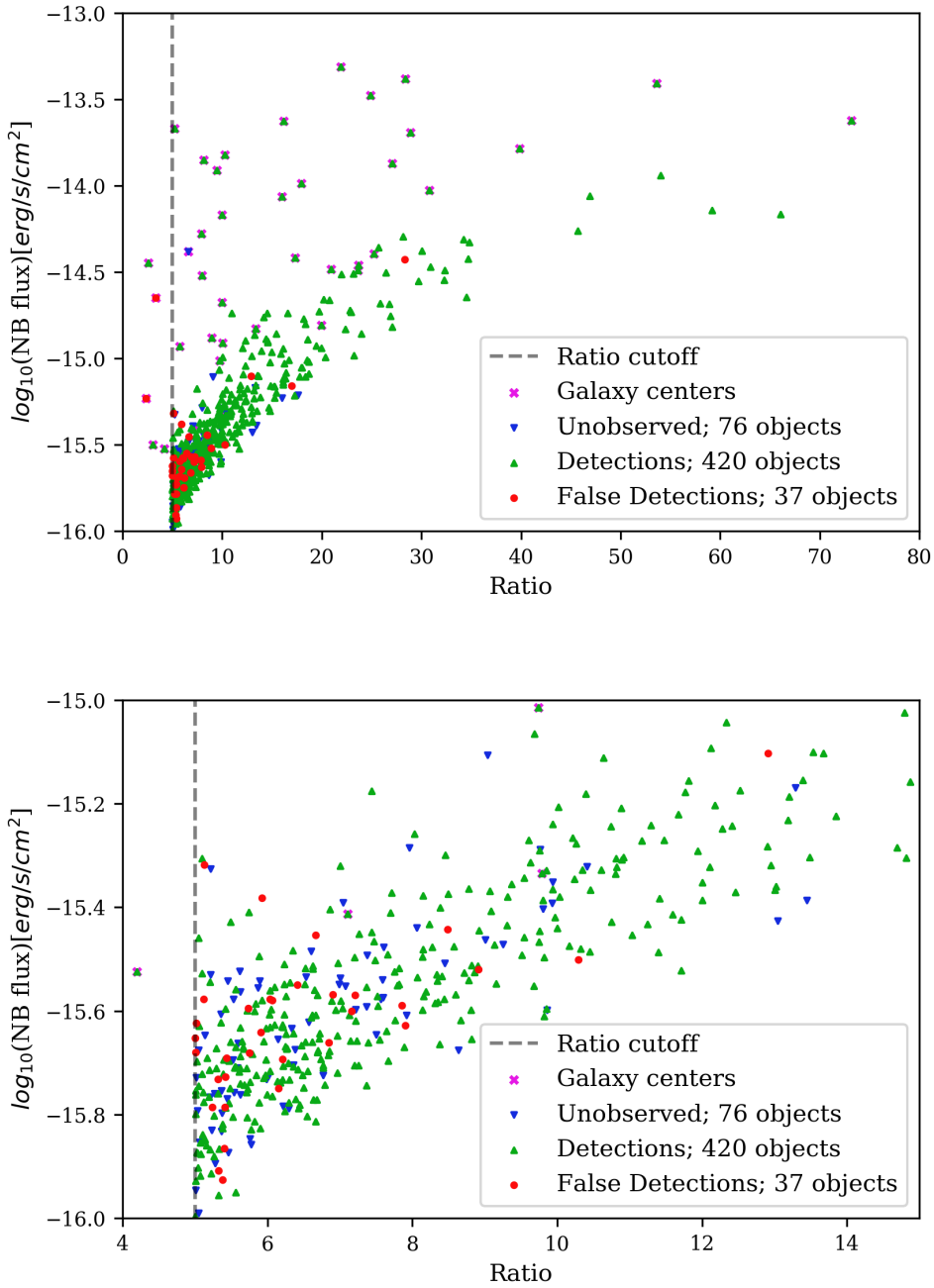


Figure 3.12 Shown here are the SFACT targets comparing their *ratio* values against their measured NB flux. The dashed vertical line shows the cutoff of objects which proceed to the next step of filtering. Objects marked as pink crosses are galaxy centers. Blue downward triangles are targets which do not yet have follow-up spectroscopy. Green upward triangles have been confirmed as ELGs and red circles denote objects which are confirmed to be false detections. The sample size of each is indicated in the legend. The bottom plot is a zoomed in version focusing on the location of the false detections.

mentioned previously, our *ratio* is a pseudo signal-to-noise measurement, so a strong signal (larger flux) means a higher value of *ratio*.

3.5 Summary and Conclusions

In this paper, we present our initial survey lists from the SFACT pilot-study fields. We also describe in detail how the imaging portion of the survey was carried out.

By using the WIYN 3.5m telescope and ODI camera, we make good use of the wide field of view to create science fields with robust image quality across the full field of the camera. WIYN also regularly achieves sub-arcsecond seeing and has an excellent light grasp, allowing us to detect faint objects. We create a stacked master image of the three custom NB filters and the three SDSS-like BB filters. This master image gives us the depth to detect very faint objects.

We outline our procedure used to detect potential ELGs. We search for objects using the six-filter, deep master image and then use preliminary photometry to identify those candidates which have an excess of NB flux. Our software detects candidates with visually-significant flux in the difference image. These candidates are visually inspected in order to remove the image artifacts which have ELG-like signatures. Those remaining are considered SFACT targets.

Aperture photometry is performed on all SFACT targets in both the BB and NB filters. SDSS stars in our images are used to calibrate the BB magnitudes and spectrophotometric stars are used to put the NB fluxes on an appropriate NB flux scale. We also demonstrate that, due to the depth of our images and the resolution of our camera, we are able to achieve reliable photometry to fairly faint magnitudes.

The 533 SFACT targets and their properties are tabulated. In these three fields, we find a surface density of 355 emission-line objects deg⁻², offering significant improvement over previous emission-line surveys. Example candidates are shown for each of the primary emission lines ($\text{H}\alpha$, $[\text{O III}]\lambda 5007$, and $[\text{O II}]\lambda 3727$) as detected in

each of our NB filters. We also present one QSO at $z > 1$ which was detected via its C III] λ 1908 line (SFF10-NB2-C21205 in Figure 3.6). These demonstrate the wide range of objects in the SFACT catalog. Our study is dominated by faint compact objects such as SFF10-NB2-A8098 seen in Figure 3.5, yet SFACT also able to detect luminous QSOs. In the local universe, SFACT also detects numerous H II regions in large extended spirals like SFF15-NB1-A2606 in Figure 3.3.

Our three survey fields also demonstrate good stability. We detect objects as faint as an r-band magnitude of 25 in each of our fields and, as Figures 3.7 and 3.8 demonstrate, this is achieved in all fields and in each filter. SFACT is able to detect objects with a wide range of properties, all with robust photometry.

This paper focused on the photometric results of the SFACT pilot-study fields. The corresponding spectroscopic confirmation results are discussed in greater detail in SFACT3.

We currently have an additional 35 SFACT survey fields processed, many of which already have partially-complete spectroscopic follow-up observations. These fields have the benefit of improvements to the process based on the pilot study. With thousands of additional SFACT targets in hand, future papers will begin to analyze global properties of the growing catalog.

References

- Aguado, D. S., Ahumada, R., Almeida, A., et al. 2019, ApJS, 240, 23. doi:10.3847/1538-4365/aaf651
- Bertin, E., Mellier, Y., Radovich, M., et al. 2002, Astronomical Data Analysis Software and Systems XI, 281, 228
- Carr, D. J., Sieben, J., Salzer, J. J., Brunker, S. W., Cousins, B. 2022, ApJS (Submitted) (SFACT3)
- Gaia Collaboration, Brown, A. G. A., Vallenari, A., et al. 2016, A&A, 595, A2. doi:10.1051/0004-6361/201629512
- Gaia Collaboration, Prusti, T., de Bruijne, J. H. J., et al. 2016, A&A, 595, A1. doi:10.1051/0004-6361/201629272
- Harbeck, D. R., Martin, P., Cavin, J., et al. 2010, Proc. SPIE, 7735, 77350G. doi:10.1117/12.857149
- Jangren, A., Salzer, J. J., Sarajedini, V. L., et al. 2005, AJ, 130, 2571. doi:10.1086/497071
- Kakazu, Y., Cowie, L. L., & Hu, E. M. 2007, ApJ, 668, 853. doi:10.1086/521333
- Kellar, J. A., Salzer, J. J., Wegner, G., et al. 2012, AJ, 143, 145. doi:10.1088/0004-6256/143/6/145
- Kotulla, R. 2014, Astronomical Data Analysis Software and Systems XXIII, 485, 375
- MacAlpine, G. M., Smith, S. B., & Lewis, D. W. 1977, ApJS, 34, 95. doi:10.1086/190444
- Markarian, B. E. & Stepanian, D. A. 1983, Astrofizika, 19, 639
- Massey, P., Strobel, K., Barnes, J. V., et al. 1988, ApJ, 328, 315. doi:10.1086/166294

- Oke, J. B. & Gunn, J. E. 1983, ApJ, 266, 713. doi:10.1086/160817
- Salzer, J. J., Gronwall, C., Lipovetsky, V. A., et al. 2000, AJ, 120, 80.
doi:10.1086/301418
- Salzer, J. J., Gronwall, C., Lipovetsky, V. A., et al. 2001, AJ, 121, 66.
doi:10.1086/318040
- Salzer, J. J., Feddersen, J. R., Derloshon, K., et al. 2020, AJ, 160, 242.
doi:10.3847/1538-3881/abba11
- Salzer, J. J., Carr, D. J., Sieben, J., Hirschauer, A. S. 2022, ApJ (Submitted)
(SFACT1)
- Sieben, J., Salzer, J. J., Carr, D. J., Hirschauer, A. S. 2022, ApJS (Submitted)
(SFACT2)
- Stetson, P. B. 1987, PASP, 99, 191. doi:10.1086/131977
- Van Sistine, A., Salzer, J. J., Sugden, A., et al. 2016, ApJ, 824, 25
- Watkins, J. D., Salzer, J. J., Van Sistine, A., et al. 2021, ApJS, 253, 39.
doi:10.3847/1538-4365/abdf4b
- York, D. G., Adelman, J., Anderson, J. E., et al. 2000, AJ, 120, 1579.
doi:10.1086/301513

Chapter 4

Spectroscopy of the SFACT Pilot-Study Fields

4.1 Introduction

This is a summary of the follow-up spectroscopy portion of SFACT. Much of this was previously published in Carr et al. (2022) and has been re-contextualized here. We focus on the results which are necessary for the later parts of my thesis. The data discussed here also pertain to only the three pilot-study fields included in the previous chapter. The methods for processing the spectra are, of course, applicable to all of the SFACT target fields which are discussed in later chapters.

Although this is the primary domain of my collaborator, the spectroscopic results are crucial for the confirmation of the targets discovered in the imaging portion of the survey. Without the spectroscopy, we also would not know the emission line which was found by our detection software, or the distance to each object, both of which are needed in order to determine the star formation rate density.

In this chapter, we provide an overview of the spectroscopic portion of SFACT. This includes the observational techniques (Section 4.2) and the processing of the spectral images (Section 4.3). We also discuss some overall results of the pilot-study field spectroscopy in Section 4.4. This includes the spectra of the example objects

⁹The results discussed in this chapter were submitted for publication in Carr, D. J., Sieben, J., Salzer, J. J., Brunker, S. W., & Cousins, B. 2022, The Star Formation Across Cosmic Time (SFACT) Survey. III. Spectroscopy of the Initial Catalog of Emission-Line Objects, ApJS (submitted). I contributed significantly to the data collection and the early observation preparation necessary for the content of the paper.

which we have shown in Section 3.4.2. We conclude with a brief overview of the current status of the spectroscopic follow-up for the SFACT survey.

4.2 Observations with Hydra

4.2.1 Instrumentation

Spectroscopic data was taken with Hydra and the Bench Spectrograph using the WIYN 3.5m telescope. Hydra is a multi-fiber positioner with a one degree field of view which provides a good match for the field of view of the One Degree Imager (ODI) camera. It is able to position \sim 60 fibers per configuration. This allows us to efficiently gather follow-up spectra for all SFACT targets identified in the imaging process.

In order to obtain spectra of SFACT targets, regardless of which narrow-band (NB) filter they were detected in, we have chosen a wavelength range of roughly 4760 – 7580 Å, with a central wavelength of 6175 Å. SFACT makes use of the red fibers on Hydra since these have a nearly constant transmission across our wavelength range. Each fiber subtends 2'' on the sky, encapsulating the entire galaxy for our high redshift, compact objects. On the end of each fiber is a small right angle prism which is then attached to a magnet. A mechanical gripper positions each fiber and the magnet holds it in place on the focal plate.

Light from our targets is transmitted through the fibers to the Bench Spectrograph. For SFACT, we use the 600 @ 10.1 grating because it has the highest efficiency across our wavelength range. With 600 grooves/mm, we obtain a spectral resolution of 3.35 Å, and a dispersion of 1.4 Å/pixel. Like our imaging data, the spectral images are binned 2×2 . This increases our signal-to-noise without losing any resolution.

4.2.2 Observations

Hydra requires more preparation than ODI. Pointing files need to be created from the list of SFACT targets selected by the imaging process. The pointing file instructs the mechanical gripper to place each of the Hydra fibers in the correct location on the focal plate. Targets selected for follow-up spectroscopy were given initial fiber assignments using `whydra` and then edited by hand in the Hydra simulator in order to maximize the efficiency of each observational set up, or pointing.

Each SFACT field has multiple pointings observed over multiple nights. Each pointing typically includes 20 – 60 SFACT targets in addition to 10 – 30 sky fibers and 3 – 7 field orientation probes (FOPs). The FOPs are positioned on stars with g magnitudes between 10.5 and 14.0 in the Sloan Digital Sky Survey (SDSS), with a preference toward stars around 12.5 magnitudes. These are used to guide the telescope and keep it locked on our targets over the course of the long exposures. Any extra fibers not used to observe an SFACT target or a sky position were assigned to SDSS galaxies to obtain spectra for potential environmental studies.

A single pointing is observed for three 30 minute exposures. This exposure time was determined via test observations and found to yield spectra of sufficient quality for our survey. Multiple exposures allow us to remove cosmic rays and other artifacts when the images are combined. The exception to this is when there is poor weather. If conditions still allow for observations, we will add an additional exposure or two in order to achieve as much depth as possible in the final image. Calibration images are also taken even night. These include bias images, dome flats, dark images, images of a CuAr comparison lamp, and observations of spectrophotometric standard stars.

Table 4.1 shows the observation dates for the spectroscopic follow-up of the pilot-study fields, as well as how many different pointings were observed in that observing run. Each field has many pointings, observed over many observing runs. This is due

Table 4.1. Hydra Pointings

Field	Observing Run	Pointings
SFF01	10/2018	3
	08/2019	1
	10/2019	1
	10/2021	1
SFF10	11/2017	2
	10/2018	3
	08/2019	1
	10/2021	2
SFF15	11/2017	3
	10/2018	3
	08/2019	2
	10/2021	1

to both the high density of SFACT targets, and the need to re-observe some targets. Although there are many fibers available on Hydra, there are still limitations on where each fiber can be placed. In particular, the fibers cannot be placed on two objects if the positions on the sky are separated by less than $\sim 40''$. Many fields required multiple fiber configurations in order to observe every target. This was especially true in fields with H II regions; at least two pointings were needed to obtain a spectrum of both the H II region and the host galaxy center.

Re-observations were also carried out to verify false detections after a development in the photometry process called into doubt the quality of some early spectra. These two factors mean that the total number of spectra per field is higher than the total number of SFACT targets in the field. Our process for identifying targets has improved since these early pilot-study fields and more recent fields have a much closer match between number of spectra and number of targets.

Recalling the observation dates for the imaging of the pilot-study fields (Table 3.2.1), it should be clear that the follow-up spectroscopy lags behind the imaging observations. Ideally, the fastest turnaround is one year, giving the team time to process the images and determine a list of targets before the fields are in an optimal

area of the sky to observe again. However, this is further complicated by the limited number of fibers and the proximity of objects in a crowded field. This means that more pointings will be needed to observe every object in a field, which necessitates more telescope time. As with any ground-based observational project, poor weather conditions also interfere in the efficiency of our follow-up spectroscopy program. We do not have complete spectroscopic coverage for our pilot-study fields, but we have enough spectra to form a representative sample of the fields and demonstrate the breadth of objects discovered in SFACT.

4.3 Spectral Processing and Measurement

The first phase of processing is carried out using IRAF¹⁰. In this phase, the overscan level is measured and removed from each image. Then we average the biases, darks, and flats, and subtract the biases and darks from the data. The multiple exposures for each pointing are then median scaled based on the amount of flux in a region free of sky lines in a bright object’s spectrum. This ensures that each image is on the same scale before median combining all exposures from a pointing to remove cosmic rays and artifacts.

Next, we make use of IRAF’s HYDRA package and the DOHYDRA task (Valdes et al. 1995). DOHYDRA identifies the multiple spectra in each image, then traces each spectrum and fits a function to the positions. The scattered light is measured and subtracted. The flat field spectrum are also fit and used to correct for any sensitivity differences across the CCD. The wavelength calibration is also created based on the comparison lamp spectrum. Emission lines in one aperture of the comparison lamp are identified by the user across the wavelength range. Using these lines, a preliminary fit is created. From this, the rest of the emission lines in the CuAr lamps are then identified automatically. The user trims saturated and poorly fit lines before a

¹⁰The spectroscopy scripts are listed in the thesis appendix.

final calibration fit is created. This is then used to automatically fit the remaining apertures. Sky spectra are examined for possible outliers—spectra which actually display properties of a star or galaxy. The remaining sky spectra are averaged with cosmic ray rejection and subtracted from each science spectra.

Flux calibrations are performed using the spectrophotometric standard stars observed each night. These observations are used to create a nightly sensitivity function which is then applied to all observations from that night as additional calibration. A well-exposed standard star spectrum is also used to create a template for the telluric absorption lines. Finally, regions around bright sky lines are masked to avoid contaminating the spectra of our faint targets. These masked lines include [O I] λ 5577, λ 6300, and λ 6363.

Line identification and measurement is conducted in **WRALF** (WRapped Automated Line Fitting; Cousins 2019), a python wrapper based on **ALFA** (Wesson 2016). The user identifies a single emission line and the software uses this line to estimate the redshift and then predict the positions of other lines in the spectrum. Gaussian functions are fit at the predicted locations of other lines which are expected to be visible in the wavelength range of the spectrum. Any lines with a signal-to-noise ratio greater than three are considered real lines. A fit to the continuum is also automatically performed. The user is able to verify the final solution. Once a solution is determined, redshifts measured from individual lines with a signal-to-noise ratio greater than or equal to five are averaged and used to derive a final redshift measurement.

Unfortunately, **ALFA** is not optimized for broad lines and as such it often struggles to identify broad emission lines in QSOs and Seyfert 1 active galactic nuclei (AGN). It also often misses lines in low quality spectra or spectra which contain very weak lines. Objects with spectra that fit these categories are re-examined by hand using an auxiliary code to allow the user to identify and measure the features missed by **ALFA**. While these measurements may not be of the same quality, it often allows us

to set limits on the properties of measured lines, which is still a valuable diagnostic tool.

4.4 Pilot-Study Spectroscopy Results

To provide an idea of the potential scope of SFACT, here we present the spectroscopic results from the three pilot-study fields. Of the 533 targets identified in the imaging reduction, 457 targets have spectroscopic follow-up observations. Of these, 420 are confirmed to be emission-line galaxies (ELGs). This is a 91.9% success rate for identifying ELGs in our pilot-study fields! As mentioned in Chapter 3, we have been more inclusive in our target selection during the pilot study, therefore we expect our success rate to increase for the larger sample.

The complete listing of the spectroscopic results for the pilot-study fields can be found in Carr et al. 2022. This includes the type of object (e.g., star-forming galaxy, AGN, QSO, false detection), the redshift of the object, and which emission line was in our filter. The flux of the detected line is also listed in the table, along with any other prominent emission lines which are seen in the wavelength range of our spectra.

4.4.1 Redshift Distribution

In Figure 4.1 we present a redshift distribution plot for the galaxies in the pilot study which also have follow-up spectroscopy. Only objects detected via a strong optical nebular line are included; higher redshift QSOs are not shown. The plot is formatted as a histogram, however the bin sizes are not equal. Rather they change to match the changing size of the redshift windows; these bins get wider with increasing redshift. The redshift range of each bin is based on the objects accessible within the half-height width of the relevant filter and corresponds to the values in Table 2.1.

There are three primary groups in Figure 4.1, corresponding to our three primary emission lines ($\text{H}\alpha$, [O III], and [O II]). The objects in Figures 3.3 - 3.5 all fall within

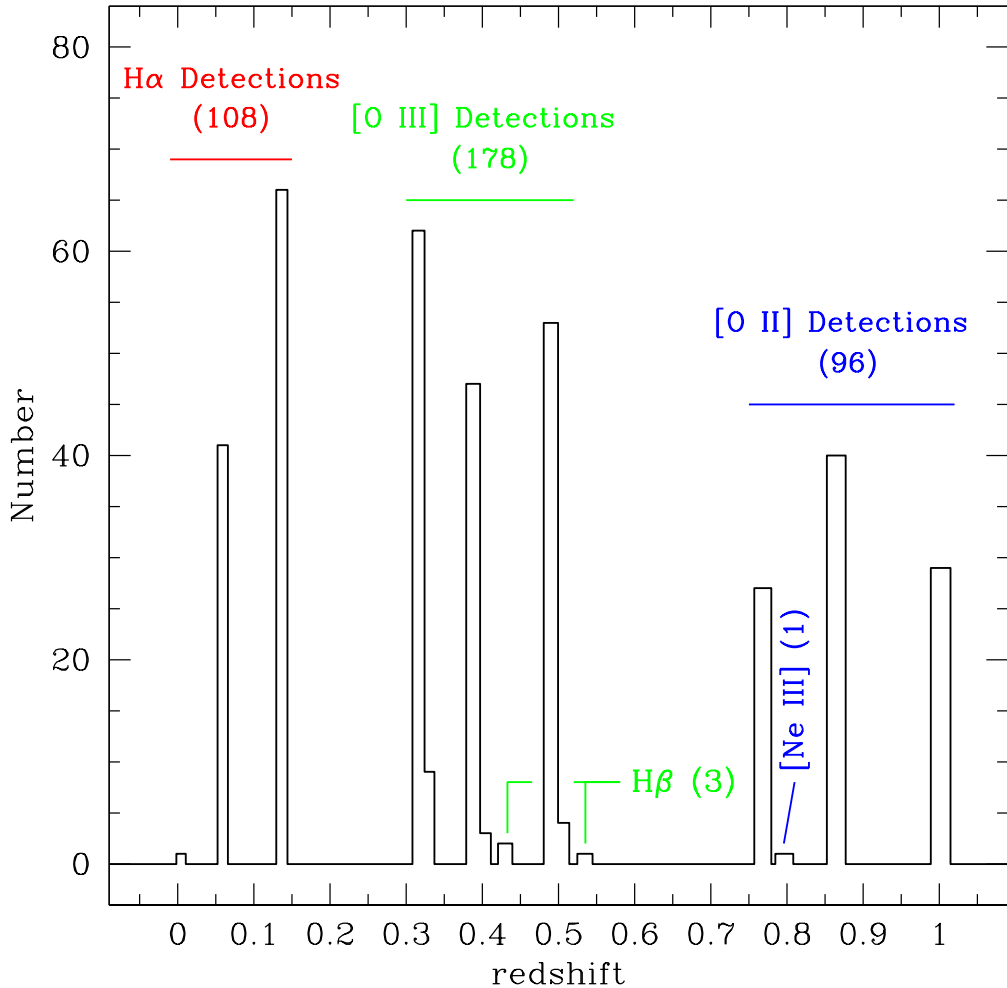


Figure 4.1 Histogram showing the redshift distribution of the SFACT ELGs. Only galaxies detected via their $\text{H}\alpha$, $[\text{O III}]$, $\text{H}\beta$, $[\text{N III}]$, and $[\text{O II}]$ lines are included in the figure; higher redshift QSOs are excluded.

these bins and their corresponding spectra are seen in Figures 4.2 - 4.4. For each of the three groups in this figure, we present three example spectra to facilitate discussion of what is included in our different redshift windows.

4.4.2 Example Object Spectra

In the following subsections, we present the spectra for the candidates shown in Section 3.4.2. These figures demonstrate the variety of emission-line sources discovered in SFACT, and the varying quality of the spectra. In the subsequent figures, the red-dashed vertical lines mark the location of the NB filter in which the object was detected. The redshift is written on each plot along with an object type classification when available. For each primary emission line, we discuss the general properties and present example spectra.

4.4.2.1 H α Spectra

The 106 objects detected via their H α emission are in the lowest redshift group ($0.00 < z < 0.15$). Many of these are large, extended galaxies with multiple H II regions in their disks. All three of the spectra shown in Figure 4.2 display the prominent emission line we expect in a nearby ELG detected by SFACT. The top object (SFF01-NB2-B19198) is an H II region in a dwarf irregular galaxy. This H II region and the host galaxy are the only two objects in the lowest redshift window seen in Figure 4.1. This small population was expected since we search over a very limited volume at that redshift.

The middle object (SFF15-NB1-A2606) demonstrates SFACT’s ability to detect other emission lines. Here, the [S II] doublet, [N II] $\lambda\lambda 6583, 6548$, [O III] $\lambda\lambda 5007$, and H β lines are all clearly visible.

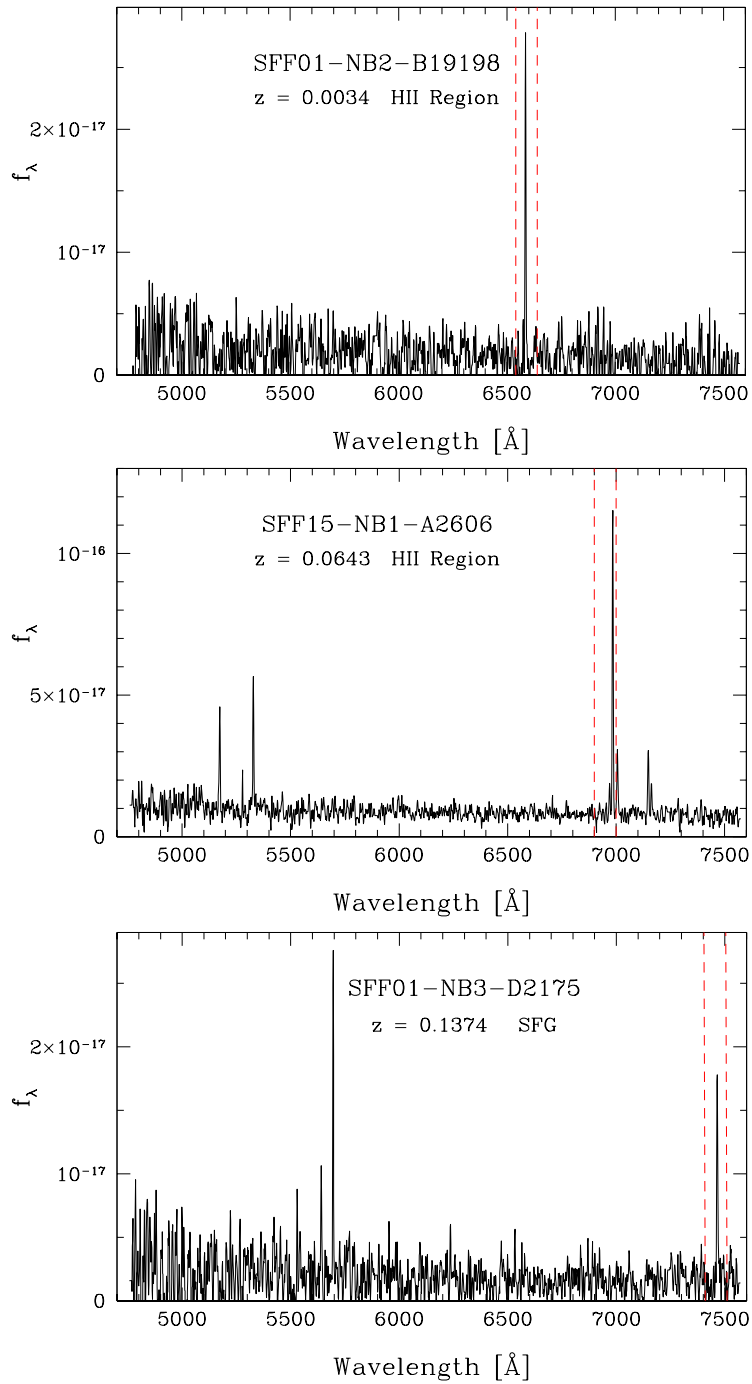


Figure 4.2 Three of our H α -detected objects. The red-dashed vertical lines denote the wavelength range covered by the NB filter in which the object was detected. The H α detections span $0.0 < z < 0.15$ and include all of our spiral galaxies. Top: SFF01-NB2-B19198 was detected in our NB2 filter and is an H II region in a faint dwarf galaxy. Middle: SFF15-NB1-A2606 was detected in our NB1 filter and is one of many H II regions in this galaxy. Bottom: SFF01-NB3-D2175 was detected in our NB3 filter.

4.4.2.2 [O III] Spectra

The most populous group of SFACT detections include the 178 objects detected via their [O III] emission and span $0.31 < z < 0.50$. The specific emission line which fell in our filter is often the $\lambda 5007$ line, but sometimes the $\lambda 4959$ line was the the one we picked up on despite being a weaker line. These latter objects are seen in Figure 4.1 as the small “bumps” next to the tall boxes in the middle grouping. The objects in Figure 3.4 are all represented in this group and their corresponding spectra can be seen in Figure 4.3.

The top object in Figure 4.3 (SFF15-NB2-C20849) is a Seyfert 2 galaxy. Unlike the previous spectra, the lines are visibly broad and the line ratios indicate a non-stellar ionizing source. The other two [O III] detections shown here are both star forming galaxies. Many of the [O III]-detected galaxies also have useful diagnostic lines in their spectra like $H\beta$ or the [O II] doublet.

4.4.2.3 [O II] Spectra

The last group are the [O II] detections. All of these objects are at a high enough redshift ($0.75 < z < 1.02$) that they are unresolved in our images, as seen in Figure 3.5. While we are searching over a large volume in these redshift windows, because of their distance, we are likely missing galaxies with lower luminosities (see Figure 4.7). Hence, we expect this group to have a depressed number of detections. Their corresponding spectra are shown here in Figure 4.4.

For most of the galaxies detected via the [O II] doublet, there are a limited number of other available lines which one could use to determine the nature of the object. As such, none of these three example spectra in Figure 4.4 have a confirmed classification. While some other lines such as [Ne III] are visible in the top two spectra, additional observations covering a redder part of the spectra are needed. A wider spectral range would allow us to measure their $H\alpha$ or [O III] lines. Taking additional spectra using

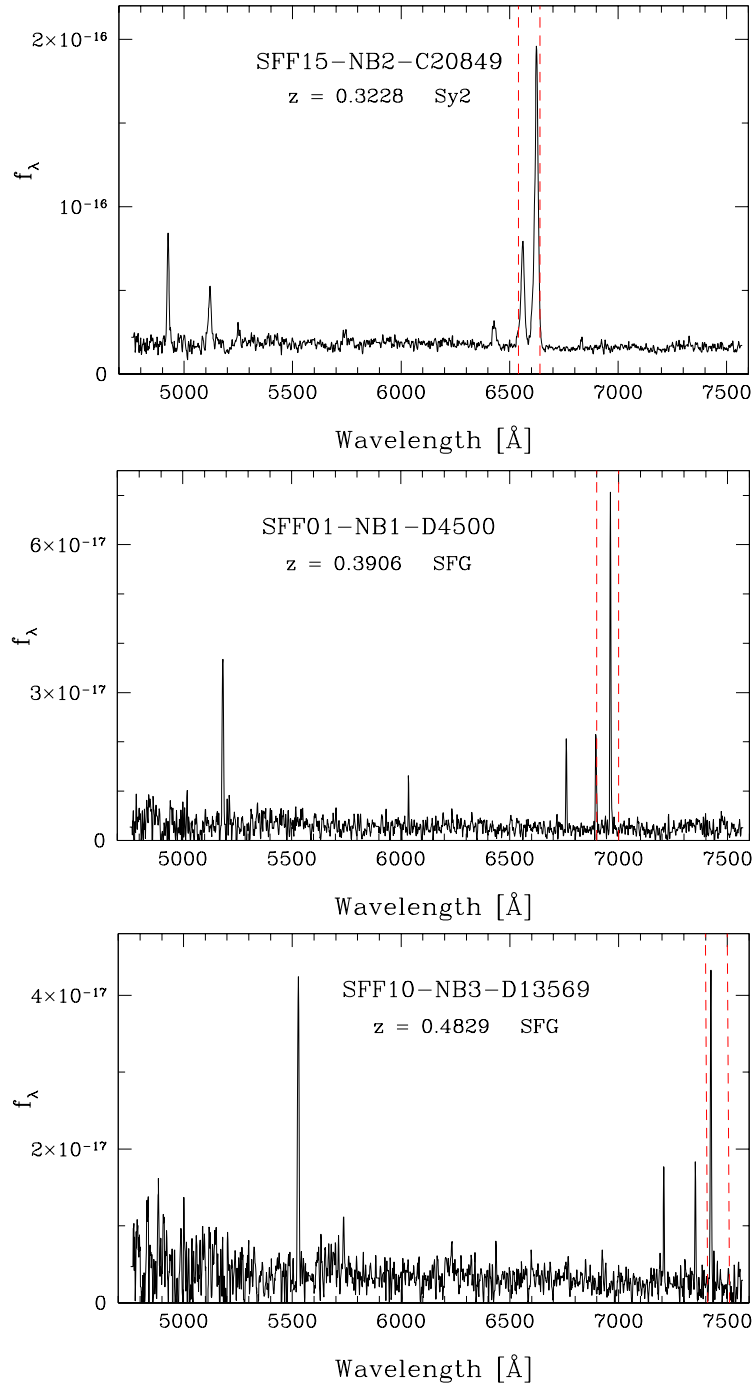


Figure 4.3 Three of our [O III]-detected objects. The red-dashed vertical lines denote the wavelength range covered by the NB filter in which the object was detected. The [O III] detections span $0.31 < z < 0.50$. Top: SFF15-NB2-C20849 was detected in our NB2 filter. Middle: SFF01-NB1-D4500 was detected in our NB1 filter. Bottom: SFF10-NB3-D13569 was detected in our NB3 filter.

a different wavelength range for objects like this are part of the future plan for the SFACT survey.

4.4.2.4 QSO Spectrum

Although not included in Figure 4.1, we also want to highlight one object at $z > 1$. SFF10-NB2-C21205 is seen in Figure 3.6 and the spectrum is in Figure 4.5. This QSO was detected via its C III] $\lambda 1908$ line, and the C IV] $\lambda 1549$ emission is also evident. At $z=2.4643$, this is one of the highest redshift objects in the pilot-study fields.

4.4.3 Diagnostic Diagram

As alluded to earlier, we are able to use diagnostic diagrams to discover the ionization sources of many of our galaxies. However, this is limited by the availability of different lines in the spectra, depending on the redshift of the object. Here, we briefly present one of the diagnostic diagrams which we have used in order to separate the star-forming galaxies from the AGN.

The Baldwin, Phillips, Terlevich (BPT) diagram (Baldwin et al. 1981) uses the [O III]/H β ratio vs. the [N II]/H α ratio to identify AGN among a population of ELGs. Because of the spectral range of SFACT, not every target has all four emission lines available for measurement. This means that not every object is able to be plotted on a BPT diagram. While there are other diagnostic diagrams we have made use of, we focus on the most common here to serve as an example.

Whenever possible, emission-line ratios are first corrected for underlying Balmer absorption and reddening. These corrected ratios are also presented in Carr et al. (2022). There are 56 objects for which WRALF was able to automatically measure all four necessary lines. We have re-examined many of the spectra where we expect to see a line just below the signal-to-noise threshold of WRALF. For many of these, we were able to measure the line flux by hand and still achieve an acceptable result; this

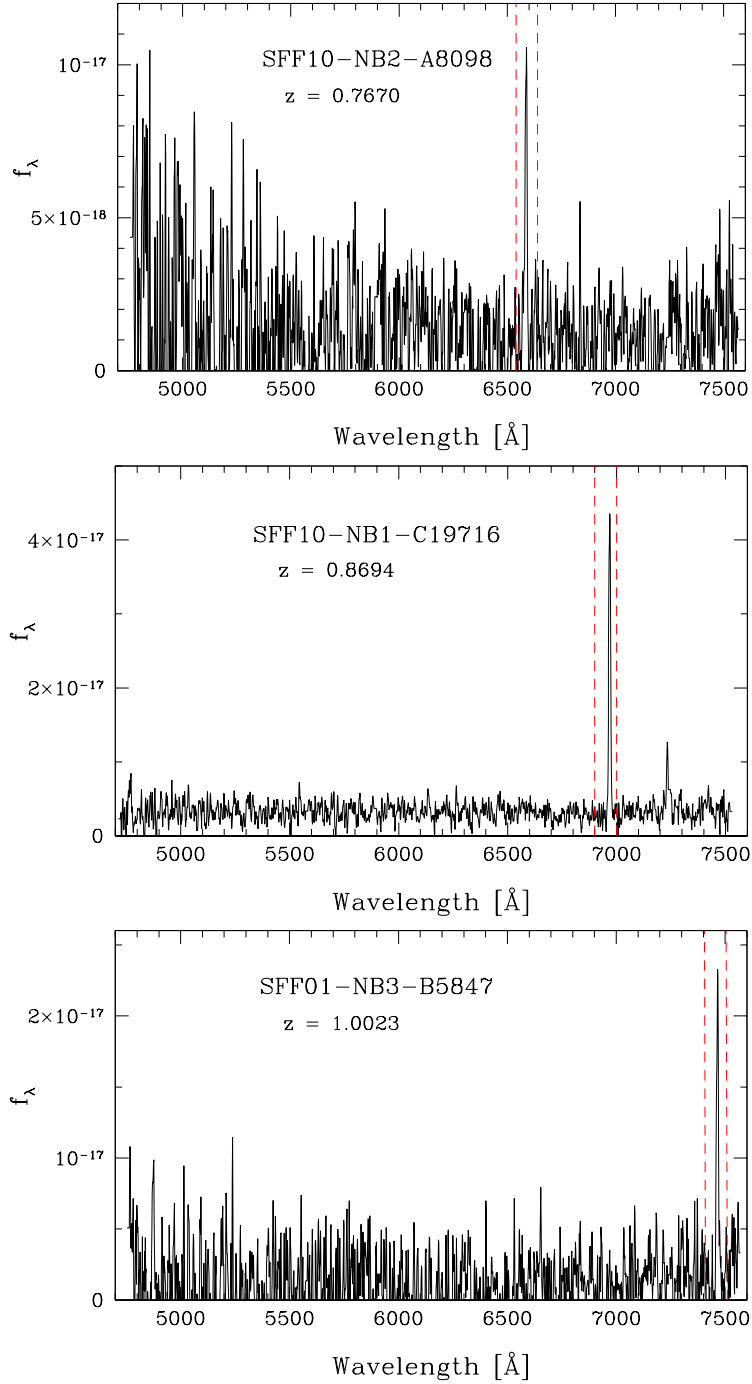


Figure 4.4 Three of our [O II]-detected objects. The red-dashed vertical lines denote the wavelength range covered by the NB filter in which the object was detected. The [O II] detections span $0.78 < z < 1.02$ and typically have noisier spectra like these. Top: SFF10-NB2-A8098 was detected in our NB2 filter. Middle: SFF10-NB1-C19716 was detected in our NB1 filter. Bottom: SFF01-NB3-B5847 was detected in our NB3 filter.

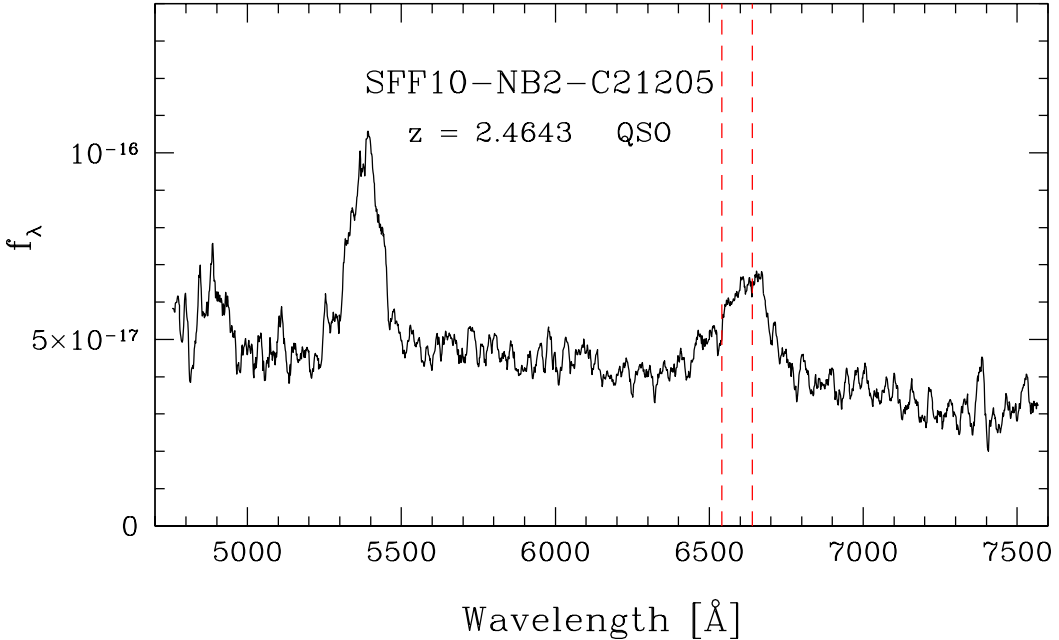


Figure 4.5 SFF10-NB2-C21205: This target was detected in our NB2 filter via a strong $\text{C III}\lambda 1908$ line. In addition, the spectrum exhibits the $\text{C IV}\lambda 1549$ line (seen at $\sim 5400 \text{ \AA}$.) The red-dashed vertical lines denote the wavelength range covered by the NB2 filter. It has been determined to be a quasar.

added 52 objects to our analysis.

In Figure 4.6 we plot all 108 galaxies with reliable line ratios on the traditional BPT diagram. The empirical Kauffmann et al. 2003 line is shown as a dashed line. Objects below this curve are star-forming galaxies without a significant AGN component. These are the galaxies which we use for later star-formation rate (SFR) measurements.

4.4.4 Derived Quantities

We can use the distances derived from the spectra to compute the absolute magnitudes of the pilot-study sample. In Figure 4.7 we look at the g-band absolute magnitudes and the distributions divided according to the emission line which was redshifted into our NB filter. Each panel also shows the luminosity distribution of the full sample as a black-lined histogram. We exclude H II regions from this figure, instead showing

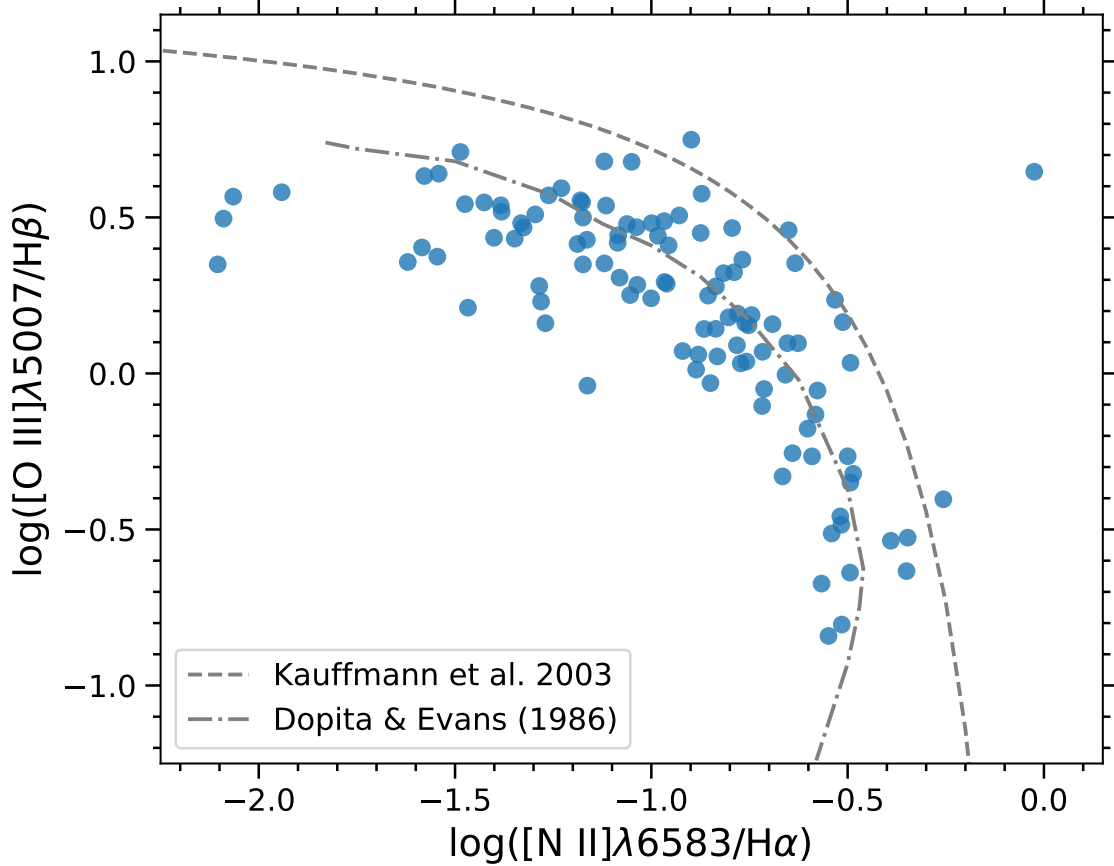


Figure 4.6 A BPT diagram for the pilot-study sample. The dashed line is from Kauffmann et al. (2003) and is an empirical delimiter between the star-forming galaxies and AGN. The dashed-dotted line is from Dopita & Evans (1986) and is derived from stellar photo-ionization models.

the luminosity of the galaxy in which they reside.

The overall distribution of absolute magnitudes is very broad, with $-16 > M_g > -21$ exhibiting a fairly flat array of values. This is a common signature of emission-line-selected galaxy samples (e.g., Salzer et al. 1989, 2020). Such surveys are more likely to detect lower-luminosity ELGs, in contrast to traditional magnitude-limited surveys which have strongly peaked distributions. This demonstrates what we alluded to in Chapter 2: SFACT is sensitive to low-luminosity dwarf systems, especially at low to intermediate redshifts.

The top panel of Figure 4.7 shows the M_g distribution of the galaxies detected via H α emission. These detections are all in the lowest redshift windows (see Figure 4.1) and are the most diverse subset of galaxies in our redshift windows. Many luminous galaxies are large spirals and irregulars with multiple detected H II regions. The lower luminosity galaxies are typically compact star-forming galaxies like blue compact dwarfs.

Our [O III]-detected galaxies are shown in the middle panel of Figure 4.7. This distribution is very symmetric with a median M_g of -18.1 , close to the overall median of the sample. We note that since [O III] emission lines are stronger in lower metallicity systems, the strength of the [O III] doublet peaks in galaxies with metal abundances of $\sim 10\%$ solar. These same galaxies typically have absolute magnitudes of $-16 > M_g > -19$, exactly where the bulk of our [O III]-detected galaxies are. The slight tail of higher luminosity galaxies includes some Seyfert 2 galaxies.

Presented in the bottom panel of Figure 4.7 are the [O II]-detected galaxies. This subsample of galaxies is strongly skewed toward the the high-luminosity end of the luminosity distribution. With its stronger peak, this subsample is more reminiscent of magnitude-limited samples. The observed luminosity distribution is caused by a combination of the [O II] doublet not exhibiting a strong metallicity dependence, and the fact that all of these galaxies are at a greater distance than those in the other

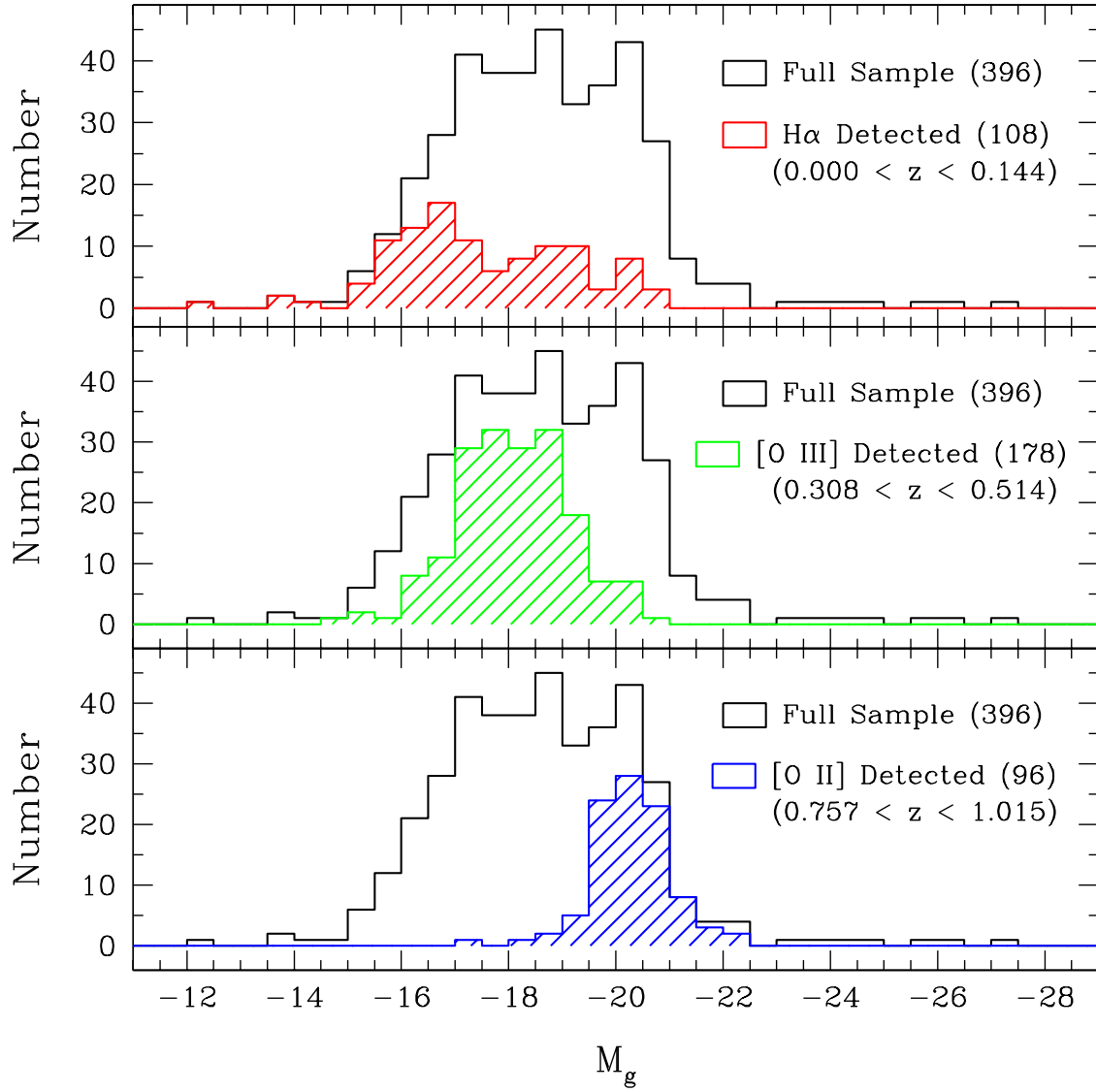


Figure 4.7 Histograms showing the g-band absolute magnitude distributions for the SFACT objects located in our pilot-study fields. The upper panel shows the M_g distribution for the lower-redshift $\text{H}\alpha$ -detected galaxies, while the middle and lower panels show the same distributions for the intermediate-redshift $[\text{O III}]$ -selected galaxies and the $[\text{O II}]$ -selected galaxies, respectively. In all three panels the black-lined histogram plots the luminosity distribution for the full sample. The latter includes the higher-luminosity QSOs.

subsamples.

4.5 Beyond the Pilot-Study Fields

The spectroscopic data have allowed us to glimpse the full potential of SFACT. Although we target our nine primary redshift windows at $z < 1$, we have also detected emission-line sources at higher redshifts via different emission lines. And in the very nearby universe, we have detected a cataclysmic variable star (Salzer et al. 2022). It had been previously suspected to be a cataclysmic variable star, but our spectrum was able to confirm this classification. While these are not pertinent to the present analysis, it speaks volumes about the potential projects which can be done in the future with the full SFACT catalog.

The spectroscopic results of SFACT are crucial for confirming that our target selection is selecting primarily ELGs. We also rely on the spectra to determine which redshift window each object falls in so that we know which emission line we are seeing in our NB filter image, and how far away each object is. All of these measurements are essential for computing the star-formation rate density of our SFACT sample.

This chapter focused on the three pilot-study fields. The present SFACT spectroscopic catalog includes 20 fields for which the spectroscopic follow-up observations are at least 40% complete. Of these, we focus on the Fall fields and use a total of 12 fields in the thesis sample. The results from these 12 fields will be the relevant sample for the rest of this thesis.

References

- Baldwin, J. A., Phillips, M. M., & Terlevich, R. 1981, PASP, 93, 5. doi:10.1086/130766
- Carr, D. J., Sieben, J., Salzer, J. J., Brunker, S. W., Cousins, B. 2022, ApJS (Submitted) (SFACT3)
- Cousins, B. S. 2019, Senior Honors Thesis, Indiana University, Department of Astronomy
- Dopita, M. A. & Evans, I. N. 1986, ApJ, 307, 431. doi:10.1086/164432
- Kauffmann, G., Heckman, T. M., Tremonti, C., et al. 2003, MNRAS, 346, 1055. doi:10.1111/j.1365-2966.2003.07154.x
- Salzer, J. J., MacAlpine, G. M., & Boroson, T. A. 1989, ApJS, 70, 479. doi:10.1086/191346
- Salzer, J. J., Feddersen, J. R., Derloshon, K., et al. 2020, AJ, 160, 242. doi:10.3847/1538-3881/abba11
- Salzer, J. J., Carr, D. J., Sieben, J., Hirschauer, A. S. 2022, ApJ (Submitted) (SFACT1)
- Valdes, F. G., Campusano, L. E., Velasquez, J. D., et al. 1995, PASP, 107, 1119. doi:10.1086/133667
- Veilleux, S. & Osterbrock, D. E. 1987, ApJS, 63, 295. doi:10.1086/191166
- Wesson, R. 2016, MNRAS, 456, 3774. doi:10.1093/mnras/stv2946

Chapter 5

Computing Star-Formation Rate Densities using Emission-Line-Selected Galaxy Samples

5.1 Introduction

Understanding the star-formation history of galaxies is crucial to understanding the history of our universe. Luminosity functions (LFs) are key tools in determining the star formation rate density (SFRD) of a survey. Historically, LFs are created using broad-band (BB) fluxes. (e.g., Schechter 1976; Binggeli et al. 1988; Ellis et al. 1996 (B band); Lin et al. 1996 (R band)). More recently, narrow-band (NB) surveys have begun to compile LFs using the directly measured NB fluxes (Gallego et al. 1995). The most commonly constructed is an H α LF. These have proven invaluable for creating a more direct measure of the star-formation density of the survey sample (Ly et al. 2007; Dale et al. 2010; Westra et al. 2010). However, H α is not the only possible indicator of star formation.

Oxygen emission lines can also be used to measure star-formation rate, but this method comes with additional difficulties. The main difficulty is that oxygen line strengths are more dependent on the metallicity of the galaxy being measured (Kennicutt 1992; Kewley et al. 2019). Despite this, [O III] and [O II] are still common emission lines measured in star-formation surveys since they are observable in the optical regime from the ground (Gallego et al. 1995; Hogg et al. 1998; Hicks et al. 2002; Hippelein et al. 2003; Teplitz et al. 2003; Drozdovsky et al. 2005; Khstovan et

al. 2020).

Because these three star-formation-indicating emission lines are all available from the ground via optical surveys, there is a strong potential for calibrating between these three measurements in order to provide more robust measurements of the SFRD. This is not a new idea. Ly et al. (2007) have compiled multiple surveys across multiple wavelengths and investigated how the resultant LF changes. They found that there is a steep evolution in the number density, and a flattening of the faint-end slope as the redshift increases. Other studies have done similar comparisons, some within the same survey (Dale et al. 2010; Khostovan et al. 2020; Lim et al. 2020). While these are important first steps, we choose to approach this problem from a different angle.

Instead of simply measuring NB lines, we use them as our selection method. By doing this, we are changing the LFs are constructed to focus on galaxies that have medium to strong emission lines, and thus are more likely to be actively forming stars. With this change, we will investigate the resultant change in the LF. Because we will be looking at galaxies selected via different lines, we will be able to more robustly compare the shape of the LF that results from different selection methods. Understanding these differences will be crucial as future studies rely more heavily on measures other than H α to determine star-formation rates and the history of the universe. This work also provides groundwork for better interpretation of the results of the SFACT survey.

In Section 5.2 we present the data we used for our analysis. Section 5.3 describes the methodology used to create the LFs we present in 5.4 and discuss in 5.5. All of the calculation in this chapter were carried out using a cosmology of $H_0 = 70 \text{ km s}^{-1} \text{ Mpc}^{-1}$ and $\Omega_m = 0.3$.

5.2 Emission-Line Galaxy Samples

We use galaxies detected from three emission-line selected surveys to construct our LFs. This allows us to determine how the selection function impacts the resultant LFs. We have chosen to use data from KISS Red ($\text{H}\alpha$ -selected galaxies), KISS Blue ($[\text{O III}]$ -selected galaxies), and the AHA project (H I -selected galaxies). In this section we describe relevant details of each of these surveys.

5.2.1 KISS

The KPNO International Spectroscopic Survey (KISS; Salzer et al. 2000) is a wide-field survey designed to observe the properties of nearby, actively star-forming galaxies. To do this, KISS used an objective prism to find nearby emission-line galaxies (ELGs). KISS was also the first digital objective-prism survey, utilising the larger dynamical range of CCDs to detect bright galaxies while also extending approximately two magnitudes fainter than previous photographic line-selected surveys. The survey observations were conducted with the Burrell Schmidt 0.61m telescope at KPNO.

KISS was carried out in two wavelengths: KISS Red and KISS Blue. Both surveys detected galaxies out to $z \sim 0.095$. KISS Red targeted $\text{H}\alpha$ emission using a custom filter that restricted the wavelength range of the objective-prism spectra to be between 6400 Å and 7200 Å. Similarly, KISS Blue targeted $[\text{O III}]$ emission by using a filter that covered 4800 Å to 5500 Å. Due to these wavelength ranges, galaxies found in KISS Blue via $[\text{O III}]$ emission may also be detected in KISS Red via their $\text{H}\alpha$ emission when the same area on the sky was observed. In the current project, we limit our analysis to galaxies with distances greater than 35 Mpc. The large peculiar velocities that nearby galaxies can have leads to large uncertainties in their distances; this in turn makes them unsuitable for use in constructing reliable LFs.

The redshift limit imposed by the filters means that KISS is volume limited as

well as emission-line-flux limited. Galaxies were confirmed as ELGs during a follow-up spectroscopy program (Wegner et al. 2003; Gronwall et al. 2004; Jangren et al. 2005; Salzer et al. 2005; see also Hirschauer et al. 2018). This allowed for confirmation of which emission line fell in the filter and dominated the flux, and whether the galaxy was star-forming or had an active nucleus. KISS is well suited for the construction of reliable LFs due to the statistically complete nature of the survey.

The KISS Red data analyzed in the current study covers a total of 128 deg^2 split into two 1° -wide survey strips. The first strip is centered at a declination of 30° and spans $12^h15^m < R.A. < 17^h0^m$ (hereafter the 30° strip; Salzer et al. 2001), while the second strip is located at a declination of 43° and extends from $11^h55^m < R.A. < 16^h15^m$ (hereafter the 43° strip; Gronwall et al. 2004). Due to observing time limitations, there is a gap in the continuous strip of fields in the 30° strip from 14^h30^m to 14^h45^m ; this affects the total overlap area between KISS Red and KISS Blue. A third sub-survey of KISS Red was also carried out (Jangren et al. 2005), but the current project only utilizes data from the first two KISS Red survey catalogs. In total, 2157 ELG candidates were identified in the first two catalogs, 1739 of which are star-forming galaxies.

KISS Blue covered 117 deg^2 centered at a declination of 30° , spanning $8^h30^m < R.A. < 17^h0^m$ (Salzer et al. 2002), and identified 223 ELG candidates, 170 of which are star-forming galaxies. Due to the substantial overlap of the KISS Red 30° strip and KISS Blue, many of the star-forming galaxies were detected in both surveys, allowing the overlap galaxies to have robust measurements of their H α and [O III] line emission. KISS Red only covered a subset of the KISS Blue area, but of the 125 KISS Blue galaxies in this overlap region, 90% were detected in both surveys.

5.2.2 ALFALFA H α

The Arecibo Legacy Fast ALFA (ALFALFA) survey is a blind 21-cm drift-scan survey designed to provide a representative sample of nearby, gas-bearing galaxies out to $z \sim 0.06$. Because the survey detects galaxies based on their H I content, it catalogs galaxies with the raw materials necessary for making stars. Hence it is the perfect survey for studying star formation in the local universe. ALFALFA has detected galaxies with H I masses as low as $10^6 M_\odot$ and includes galaxies that are historically under-represented in optical surveys, such as low-surface brightness galaxies. Observations were conducted with the Arecibo 305m telescope and covered 7000 deg 2 . Since ALFALFA targeted fields at high Galactic latitude, there is a Spring and Fall subsample. The survey and observation details can be found in Giovanelli et al. (2005). The α .40 data release (Haynes et al. 2011) contains all of the galaxies used in the current project, however the full catalog of ALFALFA sources can be found in Haynes et al. (2018).

The ALFALFA H α (AHA) project (Van Sistine et al. 2016) observed a volume-limited subsample of 1555 H I-detected galaxies with narrow-band imaging in order to measure H α fluxes and derive their star formation rates (SFRs). Observations were carried out with the WIYN 0.9m and NOAO 2.1m telescopes at KPNO. As with ALFALFA, this project was split into a Spring sample of 990 ELGs ($10^\circ < decl. < 16^\circ$, $7^h30^m < R.A. < 16^h30^m$) and a Fall sample of 565 ELGs ($24^\circ < decl. < 29^\circ$, $22^h00^m < R.A. < 3^h04^m$). The project had a minimum redshift limit of 1460 km s $^{-1}$ and outer limits of 7600 km s $^{-1}$ and 7200 km s $^{-1}$ for the Fall and Spring samples, respectively. The Spring sample also excluded the Virgo cluster region. In total, H α emission was detected in 1450 ALFALFA sources (93.5% of the total sample) over 1070 deg 2 . Details of the observations and data analysis are given in Van Sistine et al. (2016), who used the data to derive a very precise value of the local

star-formation rate density.

5.3 Luminosity Function Construction

We use these three surveys to construct seven luminosity functions. We focus on H α LFs, creating both familiar broad-band LFs and LFs based on emission-line fluxes. We also use KISS Blue galaxies to construct an [O III] LF to illustrate the distinct non-Schechter shape of the distribution. All of these together lay out a picture of how the selection function of a sample impacts the luminosity function.

We adopt a methodology to construct our LFs which is similar to most flux- or magnitude-limited surveys. We use this methodology when constructing each of our seven LFs for each ELG sample. The data from each survey must be corrected to account for low luminosity galaxies that are undetected and binned before any LF can be plotted. Then we use one of two functions to fit the data.

Due to AHA and KISS being emission-line-selected samples, there are two volume limits (the maximum volume within which a galaxy could be detected by the survey) that must be considered. One is due to the flux detection limit, while the other is set by the filter redshift limit. The flux limit of the survey is the same as most surveys. Low luminosity galaxies are more difficult to detect because there is a limit imposed by the capabilities of the telescope being used. This informs the flux sensitivity limits of the surveys, which can be found in Gronwall et al. (2004) for KISS and Haynes et al. (2011) for ALFALFA. However, there is also a strict redshift limit imposed by the spectral range of the observations. For example, a galaxy may have a very strong H α line, yet will not be detected by KISS Red if the redshift is outside the redshift range imposed by the KISS Red filter. These two volumes are not the same. For each galaxy, both of these volume limits are calculated and the smaller of the two is used as V_{max} for the construction of the luminosity function. Once a corrected V_{max} is determined, the volume density can be found by $\phi = \sum \frac{1}{V_{max,i}}$ where i is each galaxy

in a given luminosity bin. Together the volume densities in these bins make up our LFs.

Bin sizes used in the AHA LFs were chosen by the the original author and we have used similar bin sizes to match. An exception is made for larger bin sizes when limited by the data; fewer galaxies necessitate larger bins in order to yield reliable results. For the R band LFs, each of our LFs used a bin size of one magnitude for each set of survey data, centered on the half magnitude. For the emission-line LFs, different bin widths were used. KISS Blue data were binned every 0.4 dex in log luminosity space, a rough equivalent to bins of one magnitude in width. Because AHA and KISS Red are larger surveys with many more galaxies, we could utilize smaller bin widths of 0.25 and 0.2 dex, respectively. The differences in bin width were accounted for with a normalization factor to scale to the bin width of KISS Blue. This factor was applied to the volume density of each survey's LF.

The error on the LFs is dominated by Poisson uncertainty, $\sigma_\phi = \frac{1}{\sqrt{N}} \sum \frac{1}{V_{max}}$, where N is the number of galaxies in the bin. The bins with the fewest galaxy counts therefore have the largest Poisson error. The Poisson uncertainties are used to weight the data in the least squares fitting methods.

The subsamples within KISS Red (the 30° and 43° strips) and AHA (the Fall and Spring samples) also have unique volume limits based on the sky coverage. For this reason, a different V_{max} , associated with the volume-limited portion of each survey, is used for each subsample. Independent LFs are created for the two subsamples. Then, a weighted average between the corresponding bins in each LF is found and used to make a LF which represents the full survey. These final weighted-averaged, completeness-corrected, normalized volume densities are used as the average magnitude or luminosity in each bin to set the x-position in each LF plot.

For each of our LFs, we have used Scipy's (Virtanen et al. 2020) curve fitting function to perform a non-linear least squares fit to the data and determine the best-

fitting parameters. We have used either the traditional Schechter function (Schechter 1976) in the form presented by Felten (1977):

$$\phi(M)dM = \frac{2}{5}\phi^* \ln 10 \left[\text{dex} \frac{2}{5}(M^* - M) \right]^{\alpha+1} \times \exp \left[-\text{dex} \frac{2}{5}(M^* - M) \right] dM \quad (5.1)$$

or a double power law (DPL) as presented by Stevans et al. (2018) in the form:

$$\phi(M) = \frac{\phi^*}{10^{0.4(\alpha+1)(M-M^*)} + 10^{0.4(\beta+1)(M-M^*)}}. \quad (5.2)$$

In both functions, ϕ^* is the overall normalization, M is the absolute magnitude, and M^* is the “knee” of the function or the characteristic absolute magnitude. The Schechter function parameterizes the low luminosity end slope α , while the DPL parameterizes a low luminosity end slope, α , and a high luminosity end slope, β . The choice between these two functions will be explored in Section 5.4.2.1.

5.4 Results

Here we present our LFs constructed using the methods in the previous sections. In Section 5.4.1 we present our R band LFs, Section 5.4.2 our H α LFs, and Section 5.4.3 presents an [O III] LF for KISS Blue and compares it with the corresponding H α LF. In each following LF plots, data from the AHA project will be rendered in green, data from KISS Red will be rendered in red, and data from KISS Blue will be rendered in blue (excepting Figure 5.4 where it is in both blue and purple). The parameters for all the fitted functions have been tabulated and can be found in Table 5.1 for the R band LFs and in Table 5.2 for all of the emission-line LFs.

Table 5.1. R-band Luminosity Functions

Survey (1)	Detection Method (2)	Measured Flux (3)	$\log(\phi^*)$ Mpc^{-3} (4)	α (5)	L^* $erg s^{-1}$ (6)
AHA	H I	R	-2.44 ± 0.43	-1.34 ± 0.04	-21.72 ± 0.15
KISS Red	H α	R	-2.33 ± 0.43	-0.78 ± 0.12	-20.77 ± 0.19
KISS Blue	[O III]	R	-2.44 ± 0.43	-0.18 ± 1.02	-18.16 ± 0.74

Notes. — The parameters from the Schechter fit for our R band LFs.

Table 5.2. Narrow-Band Luminosity Functions

Survey (1)	Detection Method (2)	Measured Flux (3)	$\log(\phi^*)$ Mpc^{-3} (4)	α (5)	L^* $erg s^{-1}$ (6)	β (7)
AHA	H I	H α	-2.42 ± 0.43	-1.254 ± 0.001	41.68 ± 0.07	
			-2.16 ± 0.43	-3.653 ± 0.188	41.65 ± -0.18	-1.312 ± 0.039
KISS Red	H α	H α	-3.20 ± 0.43	-1.161 ± 0.050	41.99 ± -0.07	
			-3.21 ± 0.43	-2.702 ± 0.317	41.80 ± -0.10	-1.151 ± 0.062
KISS Blue	[O III]	H α	-3.83 ± 0.43	-1.426 ± 0.254	41.65 ± -0.42	
			-2.69 ± 0.43	0.210 ± 1.48	39.85 ± -1.23	-1.910 ± 0.260
KISS Blue	[O III]	[O III]	-2.95 ± 0.43	-0.819 ± 0.352	40.91 ± -0.17	
			-2.70 ± 0.43	0.058 ± 0.643	40.22 ± -0.32	-2.191 ± 0.226

Notes. — The first row of each survey displays the parameters from the Schechter fit with the second row displaying the double power law fit parameters.

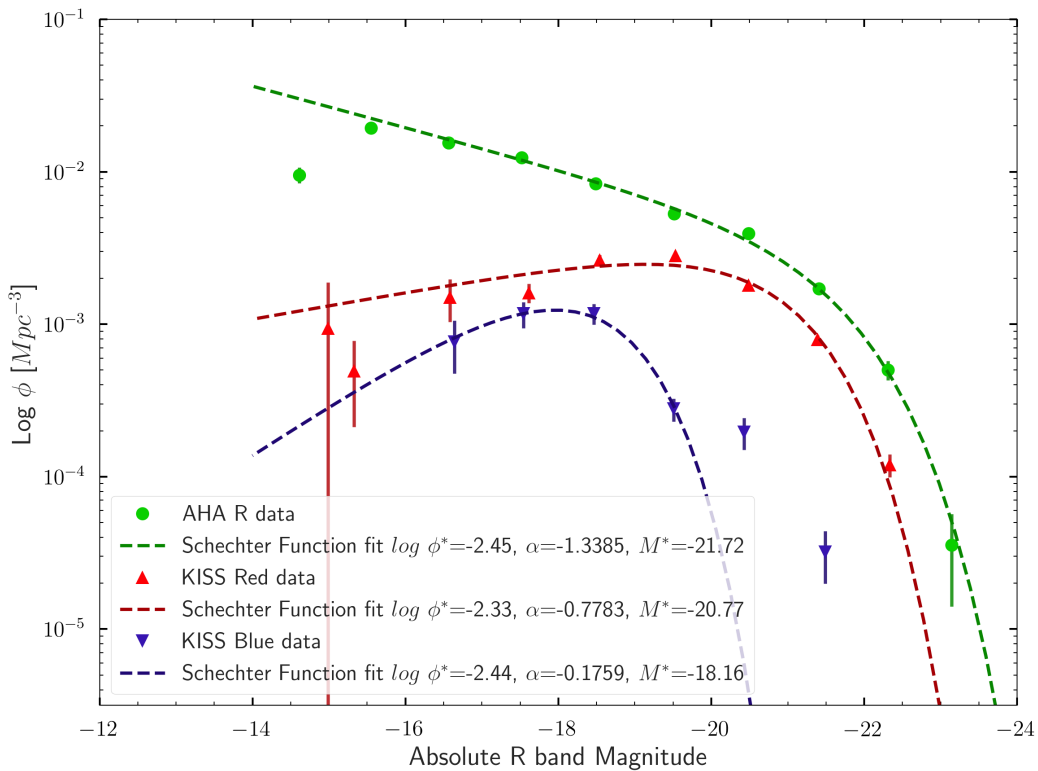


Figure 5.1 Presented here are three R band luminosity functions, each with a fitted Schechter function. The topmost line shows galaxies from the AHA survey as green circles with $M^* = -21.72 \pm 0.15$. The middle line shows H α -detected ELGs from KISS Red as red triangles with $M^* = -20.77 \pm 0.19$. The bottom data are the [O III]-detected galaxies from KISS Blue as blue triangles with $M^* = -18.16 \pm 0.74$.

5.4.1 R Band Luminosity Functions

Although our galaxies are all selected via their emission-line flux and this project is primarily focused on emission-line flux, we choose to start with the more traditionally constructed broad-band LF to allow the reader to directly visualize the impact of the selection function on the resulting LF.

Due to the sensitivity of ALFALFA, the AHA data represent a fairly comprehensive R band LF for the galaxies in the local universe with H I gas. This is evident in Figure 5.1. The KISS LFs are both lower than the AHA LF since KISS detects a subsample of all galaxies found by AHA. For this reason, we will treat the AHA LF as representative of the overall population of gas bearing galaxies in the local universe

that are capable of forming stars.

As is typically the case with broad-band LFs, the AHA R band LF is well fit by a Schechter function. The volume density of galaxies slowly increases from the characteristic magnitude to the low luminosity end, and there is a steep drop on the high luminosity end as the density of luminous, rare galaxies falls toward zero.

The slope of the linear portion, on the low luminosity side, is a fairly steep slope of $\alpha = -1.34 \pm 0.04$. The characteristic absolute magnitude is $M^* = -21.72 \pm 0.15$, representing the “knee” of the Schechter function. A relevant comparison LF is that of the Century Survey (Geller et al. 1997). The Century Survey is a local, red-selected survey that is complete to $m_R = 16.13$ and contains ~ 1700 galaxies, including both early- and late-type galaxies. This survey found a slope of $\alpha = -1.17 \pm 0.19$ and (after converting to the cosmology used in this project) $M^* = -21.50_{-0.39}^{+0.37}$. Both of these values are consistent with our AHA LF. The fact that the low luminosity end has a slope steeper than that of the AHA sample is perhaps no surprise. The sensitivity of the AHA survey as well as its low-redshift-only design should result in a more robust measurement of the low-luminosity portion of the LF than the strictly magnitude limited Century Survey.

It is also relevant to mention the shape of the H I mass function of the ALFALFA data (Jones et al. 2018). Although it plots mass, rather than absolute magnitude, the slope of the linear portion is expected to be similar. Indeed the H I mass function slope of $\alpha = -1.2 \pm 0.1$ is consistent with our R band slope.

The KISS Red LF is also reasonably well fit by a Schechter function, although the low luminosity end looks different from that of the AHA LF. The volume density actually rises toward the knee of the function with a slope of $\alpha = -0.78 \pm 0.12$. This is mainly due to survey design. KISS relied on a galaxy having a strong emission line in contrast to the continuum flux. This meant that galaxies with weaker H II regions and minimal H α flux were less likely to be detected. KISS was biased toward

galaxies with strong knot of emission while ALFALFA found all galaxies with H I gas. Accordingly, KISS Red is deficient at the low luminosity end, relative to the AHA LF. Lower luminosity, dwarf galaxies are less likely to have a concentrated knot of star formation with ultra-strong emission lines of the type that KISS Red is sensitive to.

At the high luminosity end, KISS is quite effective. Looking at Figure 5.1, we can see the shape of the KISS LF nearly matches with AHA at $M_R < -20$, demonstrating that the difference in survey designs has less of an impact when sampling high luminosity galaxies. These high luminosity galaxies tend to have both strong nuclear emission and also star formation in the disk, increasing the chances that the galaxy will be detected by both AHA and KISS. At $M_R \approx -21.4$, for example, KISS Red accounts for 47% of AHA's LF.

By integrating over the low luminosity end, $-15 < M_R < -18$, and the high luminosity end, $-20 < M_R < -22$, we can more directly compare the overlap of the samples. At the low luminosity end, KISS Red is only detecting 10.4% of the AHA sample, whereas at the high luminosity end it detects 51.0% of AHA.

The KISS Blue LF is noticeably different from the other two LFs illustrated in Figure 5.1. The LF is practically unrecognisable and certainly bears little resemblance to a Schechter function. The LF rises toward the knee of the function, similar to the KISS Red LF. Like KISS Red, KISS Blue was also dependent on a strong contrast between the emission line and the continuum flux. However, the characteristic magnitude is more than two magnitudes fainter than the other LFs. The largest volume density of KISS Blue sources is around $M_R = -17$, right where [O III] line tends to be strongest in star forming galaxies. The LF then falls again at the high luminosity end. While KISS Blue has the same general methodology as KISS Red, KISS Blue is also strongly affected by the metallicity of the galaxies because it selects by the [O III] line. Luminous, metal-rich galaxies have weaker [O III] emission lines,

which decreases their chances of being detected by KISS Blue. The reverse is also true. Galaxies with strong [O III] emission and low metallicity are more likely to be detected, making KISS Blue biased against metal-rich galaxies. This selection bias becomes more clear when we turn to the emission-line LFs.

5.4.2 Emission-Line Luminosity Functions

In this section we present emission-line LFs derived from our three emission-line surveys. We have constructed an H α LF from each of the three surveys and an [O III] LF from KISS Blue. In order to carry this out, we replace the broad-band magnitudes with emission-line luminosities, re-binning the data by the line luminosity. The selection function and derivation of V_{max} remain the same; only the luminosity and the bin sizes change in the methodology.

5.4.2.1 Double Power Law vs Schechter Function

Although Schechter functions are most commonly used for broad-band LFs, this is not the case for all LFs. We suspected that our emission-line LFs would not be well described by a traditional Schechter function. As Salim & Lee (2012) pointed out, there are two fundamental types of LFs. There are “mass” LFs, which use broad-band optical and near-IR data to trace older stellar populations; these are well fit by a Schechter function. There are also “SFR” LFs, which use UV, mid- and far-IR, and narrow-band data to trace younger stellar populations; these are typically not well fit by a Schechter function. The latter are characterized as having a shallower decline at the high luminosity end and are especially distinct when dust correction is performed on a galaxy-by-galaxy basis. Many IR and radio surveys use a single or double power law (Prescott et al. 2016; Matthee et al. 2017; Symeonidis & Page 2019), and Salim & Lee (2012) suggest that many dust-corrected UV surveys are better fit by a Saunders function (Saunders et al. 1990).

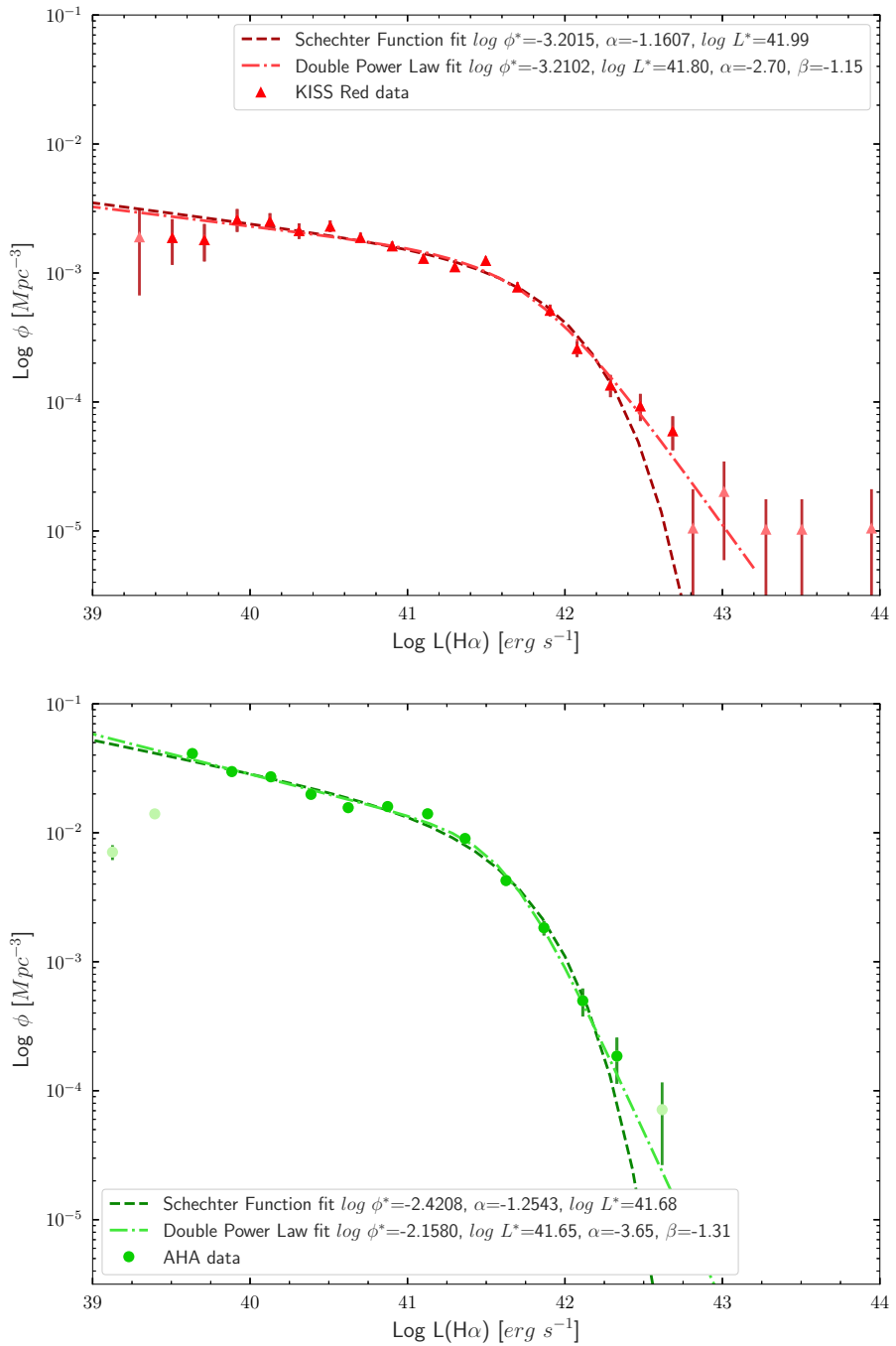


Figure 5.2 The H α luminosity function for KISS Red (top) and the AHA project (bottom). Data which have not been included in the fitting are shown as a lighter color. The Schechter function fit is shown as a dashed line with the DPL fit as a dot-dash line. The two fit functions most clearly deviate at the high luminosity end with the DPL more closely following the data.

Our data clearly shows this discrepancy. To highlight this, we look at two of our H α LFs in Figure 5.2. Both surveys' LFs have been fit by a Schechter function and a DPL (Equation 5.2). Although at first glance the data both seem to be Schechter-like, at the ends of the function there are deviations. The two models are nearly identical at the low luminosity end. However, at the high luminosity end the Schechter function has a much steeper decline than the observed LF, which is much better fit by the DPL. The DPL even encompasses the bins which were not included in the fit (the fainter points in the figure). For this reason, we have chosen to use double power laws only to fit our emission-line data. The parameters for all emission-line LFs can be found in Table 5.2.

5.4.2.2 H α Luminosity Functions

We present our H α LFs in Figure 5.3. The AHA LF again has a larger volume density than the KISS LFs. The characteristic luminosity of the function is $L_{H\alpha}^* = 41.65 \pm 0.18 \text{ erg s}^{-1}$ and the density at that point is $\log(\phi^*) = -2.16 \pm 0.43 \text{ Mpc}^{-3}$. Once again, the extreme sensitivity of Arecibo is seen as the AHA project contains nearly every local galaxy with H I gas and H α emission within the survey volume. At the low luminosity end, the AHA LF dominates the plot, but it intersects with the KISS Red LF at the high luminosity end.

KISS Red has a very shallow, upward slope away from the characteristic luminosity toward the low luminosity end, $\alpha = -2.70 \pm 0.32$ and $L_{H\alpha}^* = 41.80 \pm 0.10 \text{ erg s}^{-1}$, respectively. This is different than the trend of the slope in the R band LF.

There are a couple reasons why the AHA and KISS LFs differ at the high-luminosity end. Although AHA is a more comprehensive survey, KISS extends to a higher redshift and thus encompasses a much larger volume over which to detect the rarer, more luminous galaxies. This will boost the high-luminosity end. The surveys also have different selection functions. KISS is primarily sensitive to higher-

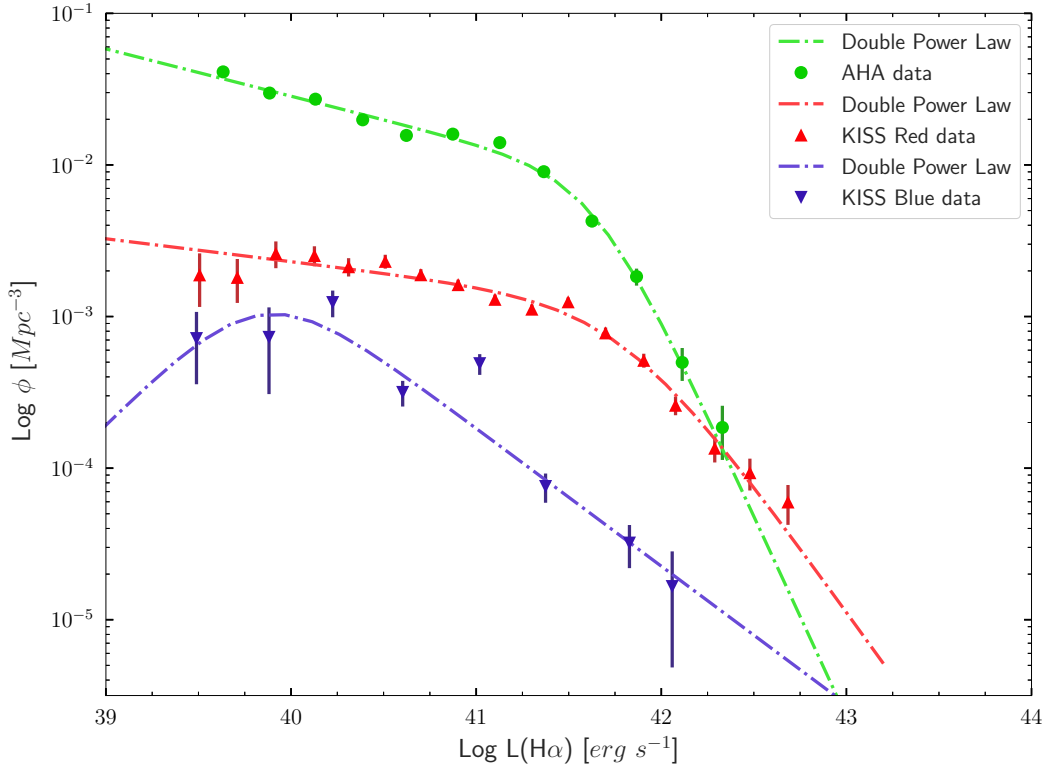


Figure 5.3 Presented here are three H α LFs, each with a fitted double power law function. The topmost line shows galaxies from the AHA survey as green circles. The middle line shows H α -detected ELGs from KISS Red as red triangles. The bottom data are the [O III]-detected galaxies from KISS Blue. Parameters for all functions can be found in Table 5.2. AHA and KISS Red have similar low luminosity slopes, but KISS Red has a shallower drop-off. KISS Blue is strikingly different with most of the function being a decreasing density as you move toward the high luminosity end.

luminosity star-forming galaxies with strong emission lines, giving a boost to their density at the high luminosity end. For these reasons, KISS Red has a higher volume density of star-forming galaxies at the high luminosity end.

Another example of an H α -selected galaxy sample from the local universe is the Wyoming Survey. Their lowest redshift bin was $z = 0.16$ (Dale et al. 2010) which is slightly higher than our KISS Red survey, but still a good comparison point for the KISS Red Schechter function. Although not plotted here, the fit is defined by $\alpha = -1.16 \pm 0.05$, $\log L_{H\alpha}^* = 41.99 \pm 0.07 \text{ erg s}^{-1}$, and $\log(\phi^*) = -3.20 \pm 0.43 \text{ Mpc}^{-3}$. Dale et al. (2010) only fit to a Schechter function and found $\alpha = 1.36 \pm 0.06$, $\log L_{H\alpha}^* = 42.0 \pm 0.2 \text{ erg s}^{-1}$, and $\log(\phi^*) = -3.05 \pm 0.11 \text{ Mpc}^{-3}$. Although our slope value is not consistent with their findings, this is not surprising as Dale et al. (2010) says that they had difficulty identifying the low luminosity end slope. This may be due to [O II] and [O III] contamination which is difficult to detect without spectra. Our survey also extends toward lower luminosity galaxies because we are using a lower redshift window which allows us to determine a more robust low luminosity slope.

Once again, the KISS Blue LF is strikingly dissimilar. While the characteristic luminosity of AHA and KISS Red are both close to $\log L_{H\alpha}^* = 41.7 \text{ erg s}^{-1}$, the characteristic luminosity of KISS Blue is closer to $\log L_{H\alpha}^* = 39.9 \text{ erg s}^{-1}$, and even there, it is hard to tell if that is the true peak. The fit shows a clear peak, however the data hint at the possibility of a more flat curve at lower luminosities. With the limited data, it is difficult to draw firm conclusions about the low luminosity end. Still, there is a clear shallow decline in volume density from $\log L_{H\alpha} = 40 \text{ erg s}^{-1}$ to $\log L_{H\alpha} = 42 \text{ erg s}^{-1}$, with a slope of $\beta = -1.91 \pm 0.26$. This difference in the shape of the LF is dominated by metallicity effects. Since KISS Blue selected galaxies by their oxygen lines, high metallicity galaxies were less likely to be found. This contributes primarily to the shift in the peak of the KISS Blue LF.

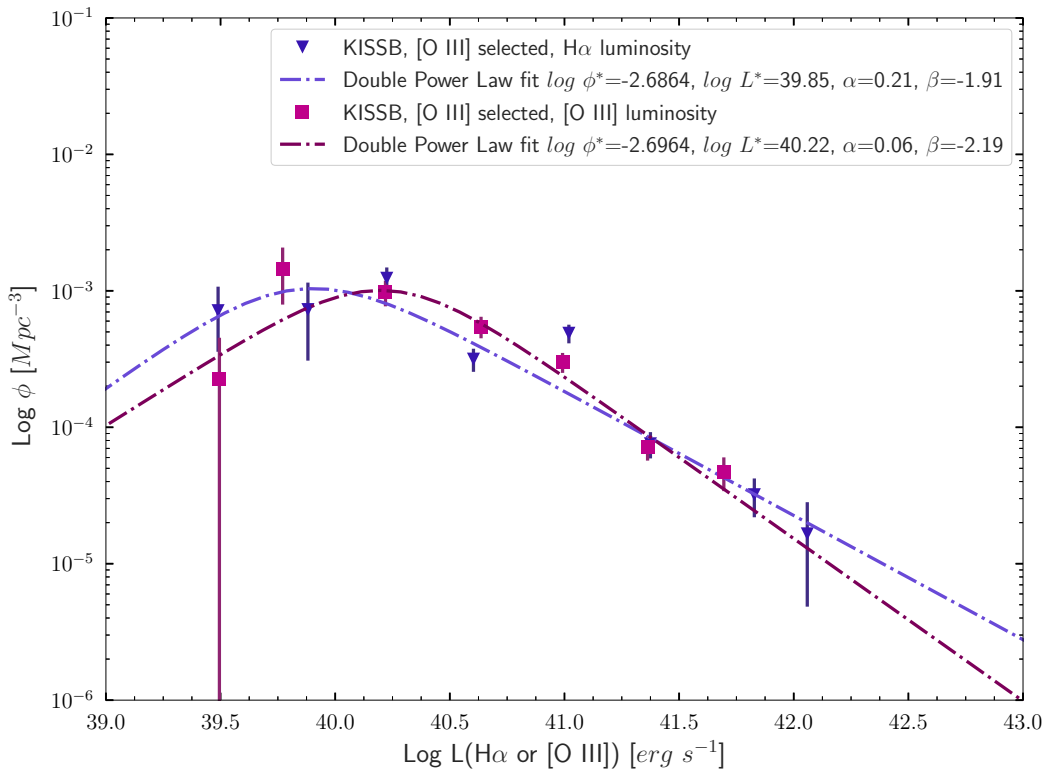


Figure 5.4 Both [O III]-selected LFs from the KISS Blue survey are shown here with the H α LF represented by blue triangles and the [O III] LF represented by purple squares. While there are slight differences, the overall shape of the LFs are similar.

5.4.3 KISS Blue Comparison

We present our [O III] LF in Figure 5.4. The KISS Blue galaxies were selected via their [O III] emission lines and those same lines were subsequently measured. The resultant luminosity function is shown as purple squares. The data are well fit by a DPL peaking at $\log L_{[OIII]} = 40.22 \text{ erg s}^{-1}$. This seems to be consistent with Khostovan et al. (2020). Each of the [O III] LFs decrease toward the high-luminosity end, however, none of their data extend far enough into the low-luminosity end to directly compare with our peak location. Ly et al. (2007) does extend far enough. They use a Schechter fit, but examination of the data points indicates signs of a peak in their function around $\log L_{[OIII]} = 40.25 \text{ erg s}^{-1}$.

KISS Blue allows us the opportunity to compare an H α and [O III] LF, which have

the same selection function and include the same galaxies. Since the only difference is the plotted LF, this provides a way to examine how one might translate from [O III] measurements to H α measurements.

To make a direct comparison, we overplot the [O III]-selected, H α LF from Figure 5.3, shown as blue triangles. Both LFs peak around $\log L_X = 40 \text{ erg s}^{-1}$, with a clearly decreasing slope away toward both ends. The DPLs for each LF match each other remarkably well. This close alignment is promising when it comes to future attempts to translate between the two LFs. It means that the selection function is the main cause of the difference between the KISS Red LF and the KISS Blue LF in Figure 5.3. This will aid in creating more robust star-formation rate density (SFRD) measurements at high redshifts. We will discuss this more in the following section.

5.5 Discussion

5.5.1 Different Populations

Even across three surveys, there are clear differences between our broad-band LFs, Figure 5.1, and our H α LFs, Figure 5.3. While broad-band fluxes measure light from the entire galaxy, these emission-line fluxes specifically probe the light from a young population of stars.

Not only are different functions used to best describe the LFs in each plot, but there are different shapes in relationship to the other surveys. In the H α LF, KISS Red has a higher density of galaxies than AHA at the highest luminosity bins, but KISS Red densities never exceed AHA densities in the R band LF. As mentioned earlier, KISS Red extends to a deeper redshift, and thus a larger volume, which means KISS Red is more likely to detect rare, extremely luminous galaxies. While AHA is designed to detect galaxies with the gas content possible for star formation, KISS Red is biased toward strongly star-forming galaxies, those which are likely to

have strong H α emission. Both of these factors boost the high luminosity end of KISS Red’s LF in Figure 5.3 without a significant boost in the bright end of the R band LF.

The relative positions of the LF “knee” between each survey is the same in each band: AHA and KISS Red have similar relative positions while KISS Blue is at a less luminous position. As expected, missing luminosity is more pronounced in the H α LFs. This is expected due to our selection effects. For galaxies with a high luminosity ($L_{H\alpha} \sim 42$) and a high metallicity, the apparent strength of the [O III] emission lines will be weakened, while the H α emission lines are unaffected. Hence when we select via the [O III] line emission, there will be fewer high luminosity galaxies detected, and a bias toward low luminosity galaxies. This leads to the “knee” of the [O III] LF being offset from the other LFs, as we see in Figure 5.3.

It is also interesting to note that in Figure 5.1 the bright-end slopes of KISS Red and AHA appear to match while in Figure 5.3 it is the low-luminosity end slopes of those same surveys that appear to match. The similar low-luminosity slopes may be due to the H α emission being directly related to star formation. KISS Red galaxies are sampling galaxies with recent bursts of star formation, which are also likely to have H I gas and thus have been detected by AHA.

5.5.2 Star-Formation Rate Density Comparisons

We have integrated each of these luminosity functions in order to derive a rough SFRD of each sample. The total luminosities of each luminosity function and the log(SFRD) are listed in Table 5.3. In this section, we discuss the total integrated luminosities and the SFRD measurements derived from the full sample. We also compare between surveys using a more limited data range. For all of these values, we have used a Riemann sum to better reflect the data since the KISS Blue H α sample is not well fit by either a Schechter or DPL function.

The full H α AHA sample has a $\log(\text{SFRD})$ of $-1.64 \text{ M}_\odot \text{ yr}^{-1} \text{ Mpc}^{-3}$, which is close to the Van Sistine et al. (2016) measurement of $\log(\text{SFRD}[\text{M}_\odot \text{ yr}^{-1} \text{ Mpc}^{-3}]) = -1.747 \pm 0.018$ (random) ± 0.05 (systematic). We expect this to be slightly different since we are using both Fall and Spring data, while the SFRD published in Van Sistine et al. (2016) only includes Fall data.

The integrated SFRDs of the KISS Red and KISS Blue H α samples are lower than the AHA sample. We have found $\log(\text{SFRD})$ values of -2.11 and $-3.25 \text{ M}_\odot \text{ yr}^{-1} \text{ Mpc}^{-3}$, respectively. These lower values reflect the “lower” curves seen in Figure 5.3, emphasizing the differences created by the selection function of the sample.

Looking again at Figure 5.4, we can now compare the H α -derived SFRD and the [O III]-derived SFRD, both samples selected via their [O III] emission. We find an H α $\log(\text{SFRD})$ of -3.25 and an [O III] $\log(\text{SFRD})$ of $-3.00 \text{ M}_\odot \text{ yr}^{-1} \text{ Mpc}^{-3}$, respectively. As expected, these computed SFRD values are very similar, even though they have slightly different numbers of galaxies.

Because the SFRD is calculated differently for [O III] luminosity and H α luminosity, we can also directly compare the total luminosity for each curve. When we do so, we find a ratio of only 0.524. Although small, this is an important value to be able to translate [O III] LFs to H α LFs, and thus to correctly compare the SFRD of different samples detected via different methods. This is important because in order to study the SFRD at different redshifts, different selection functions are required. By being able to put all measurements on an H α system, we would be able to use the robust conversion between H α luminosity and SFR.

5.5.3 Scaling Relationships

With all of these luminosity functions integrated, we can now return to the main purpose of the project: cross calibration of samples. As mentioned previously, the AHA sample can be used as an approximation for the universe. By virtue of using an

Table 5.3. Comparison of Total Luminosity

Survey	Detection Method	Measured Flux	L _{tot} (Full)	L _{tot} (Limited)	log(SFRD)	Fraction of AHA sample
			erg s ⁻¹	erg s ⁻¹	erg s ⁻¹	
AHA	H I	H α	2.91×10^{39}	2.49×10^{39}	-1.638	1.000
KISSR	H α	H α	9.76×10^{38}	3.18×10^{38}	-2.113	0.127
KISSB	[O III]	H α	7.12×10^{37}	6.03×10^{37}	-3.250	0.024
KISSB	[O III]	[O III]	1.36×10^{38}	5.53×10^{37}	-3.001	0.022

Notes. — The full L_{tot} comprises the full range of data for each survey. The limited L_{tot} includes bins which fall within $39 < \log(L_X) < 42.5$. The SFRD values are based on the full L_{tot} value.

H I selection function, this survey should have detected any galaxies with the potential for star formation in the nearby universe. This means that by comparing the total luminosity of each KISS survey to the AHA H α total luminosity, we can approximate how much of the universe each KISS survey misses due to the selection function. For the purposes of direct comparison, we integrate over $39 < \log(L_X) < 42.5$. Within this range, each survey is well populated. While this does not include some of the most extreme galaxies, it limits the integration range to where most of the galaxies are, and thus is a better value for comparison with other surveys. This is our “limited” sample indicated in Table 5.3.

When we compare the KISS Red total H α luminosity to the AHA total H α luminosity, we find that the KISS Red survey includes 13% of the total H α luminosity. This means that surveys which look for star-forming galaxies by their H α emission lines, are potentially missing 87% of the luminosity from star-forming galaxies in their survey volume. While this number is based only on the comparison between KISS Red and AHA, this difference is something which all emission-line selected surveys should be aware of and account for in some way. Looking at Figure 5.3 we can see that this discrepancy is going to be especially apparent at lower-luminosities. It is not surprising that a survey that selects galaxies via their line emission might miss

less active galaxies without strong emission lines.

We also find that the KISS Blue survey misses 97.6% of the H α luminosity measured by AHA. Likewise, this gives us a comparison for how much luminosity a survey might miss if it only selects via the [O III] emission line.

However, this second connection only applies to surveys which perform [O III] selection and then measure the H α flux. A more common methodology is to find galaxies based on their [O III] emission, and then use that same emission to calculate SFR. Since the KISS Blue survey did both, we can use this scaling to put the [O III]-selected, [O III] flux on an H I-selected, H α flux scale. When we do this, we find that the KISS Blue [O III] subsample missed 97.8% of the total luminosity. While this is not a terribly precise comparison, it provides valuable context for understanding the results of emission-line selected galaxy surveys.

5.6 Future Work

5.6.1 Improvements

At the time of this writing, we have only computed rough SFRDs and we would like to more accurately measure these values. This would involve using our fit functions of the data to integrate over a wider luminosity range, allowing us to extrapolate to include luminosity bins which are under-represented in our data sample.

There is a danger that the ratio between the [O III] and H α luminosity bins in the emission-line LFs might change with redshift. If it differs from what we have seen, it would likely be the result of changing metallicity in the galaxies. However, we believe this to be a small, and correctable effect. Understanding this relationship opens up the possibility of directly comparing surveys which have used these different selection methods. This would be a more robust method than simply using average line ratios since there are many selection effects involved which change the shape of

the luminosity function and thus affect the final SFRD determination.

5.6.2 Connection to SFACT

All of the work in this chapter is done in the local universe, $z < 0.1$. While we hope that the relationship between these types of LFs remain steady, performing this same study at a higher redshift would be beneficial. With the future planned SFACT NB filter NB912 (Chapter 2), it will be possible to compare the same galaxies selected via both H α and [O III] lines at $0.383 < z < 0.397$. Even without this confirmation, we hope to use this KISS-based calibration to back up our SFACT SFRD measurements.

While these ratios can be applied to any emission-line survey which selects galaxies based on either H α or [O III] emission lines, the most obvious survey this could be applied to is the SFACT survey. As an emission-line survey, SFACT has similar limitations to KISS in terms of which galaxies are detected. These ratios can be used to scale up the results of the [O III] and H α -selected luminosities to better approximate the total SFRD.

References

- Binggeli, B., Sandage, A., & Tammann, G. A. 1988, *ARA&A*, 26, 509.
doi:10.1146/annurev.aa.26.090188.002453
- Dale, D. A., Barlow, R. J., Cohen, S. A., et al. 2010, *ApJ*, 712, L189
- Drozdovsky, I., Yan, L., Chen, H.-W., et al. 2005, *AJ*, 130, 1324. doi:10.1086/430884
- Ellis, R. S., Colless, M., Broadhurst, T., et al. 1996, *MNRAS*, 280, 235.
doi:10.1093/mnras/280.1.235
- Felten, J. E. 1977, *AJ*, 82, 861
- Gallego, J., Zamorano, J., Aragon-Salamanca, A., et al. 1995, *ApJ*, 455, L1.
doi:10.1086/309804
- Geller, M. J., Kurtz, M. J., Wegner, G., et al. 1997, *AJ*, 114, 2205
- Giovanelli, R., Haynes, M. P., Kent, B. R., et al. 2005, *AJ*, 130, 2598
- Gronwall, C., Salzer, J. J., Sarajedini, V. L., et al. 2004, *AJ*, 127, 1943
- Gronwall, C., Jangren, A., Salzer, J. J., et al. 2004, *AJ*, 128, 644
- Haynes, M. P., Giovanelli, R., Martin, A. M., et al. 2011, *AJ*, 142, 170
- Haynes, M. P., Giovanelli, R., Kent, B. R., et al. 2018, *ApJ*, 861, 49
- Hicks, E. K. S., Malkan, M. A., Teplitz, H. I., et al. 2002, *ApJ*, 581, 205.
doi:10.1086/344224
- Hippelein, H., Maier, C., Meisenheimer, K., et al. 2003, *A&A*, 402, 65.
doi:10.1051/0004-6361:20021898
- Hirschauer, A. S., Salzer, J. J., Janowiecki, S., et al. 2018, *AJ*, 155, 82.
doi:10.3847/1538-3881/aaa4ba

- Hogg, D. W., Cohen, J. G., Blandford, R., et al. 1998, ApJ, 504, 622.
doi:10.1086/306122
- Jangren, A., Salzer, J. J., Sarajedini, V. L., et al. 2005, AJ, 130, 2571
- Jangren, A., Wegner, G., Salzer, J. J., et al. 2005, AJ, 130, 496
- Jones, M. G., Haynes, M. P., Giovanelli, R., et al. 2018, MNRAS, 477, 2
- Kennicutt, R. C. 1992, ApJ, 388, 310. doi:10.1086/171154
- Kewley, L. J., Nicholls, D. C., & Sutherland, R. S. 2019, ARA&A, 57, 511.
doi:10.1146/annurev-astro-081817-051832
- Khostovan, A. A., Malhotra, S., Rhoads, J. E., et al. 2020, MNRAS, 493, 3966.
doi:10.1093/mnras/staa175
- Lim, C.-F., Wang, W.-H., Smail, I., et al. 2020, ApJ, 889, 80. doi:10.3847/1538-4357/ab607f
- Lin, H., Kirshner, R. P., Shectman, S. A., et al. 1996, ApJ, 464, 60.
doi:10.1086/177300
- Ly, C., Malkan, M. A., Kashikawa, N., et al. 2007, ApJ, 657, 738. doi:10.1086/510828
- Matthee, J., Sobral, D., Best, P., et al. 2017, MNRAS, 471, 629
- Prescott, M., Mauch, T., Jarvis, M. J., et al. 2016, MNRAS, 457, 730
- Salim, S., & Lee, J. C. 2012, ApJ, 758, 134
- Salzer, J. J., Gronwall, C., Lipovetsky, V. A., et al. 2000, AJ, 120, 80
- Salzer, J. J., Gronwall, C., Lipovetsky, V. A., et al. 2001, AJ, 121, 66
- Salzer, J. J., Gronwall, C., Sarajedini, V. L., et al. 2002, AJ, 123, 1292
- Salzer, J. J., Jangren, A., Gronwall, C., et al. 2005, AJ, 130, 2584
- Saunders, W., Rowan-Robinson, M., Lawrence, A., et al. 1990, MNRAS, 242, 318.
doi:10.1093/mnras/242.3.318
- Schechter, P. 1976, ApJ, 203, 297
- Stevans, M. L., Finkelstein, S. L., Wold, I., et al. 2018, ApJ, 863, 63

Symeonidis, M., & Page, M. J. 2019, MNRAS, 485, L11

Teplitz, H. I., Collins, N. R., Gardner, J. P., et al. 2003, ApJ, 589, 704.
doi:10.1086/374659

Van Sistine, A., Salzer, J. J., Sugden, A., et al. 2016, ApJ, 824, 25

Virtanen, Pauli and Contributors, 2020, Nature Methods, 17, 261-272

Wegner, G., Salzer, J. J., Jangren, A., et al. 2003, AJ, 125, 2373

Westra, E., Geller, M. J., Kurtz, M. J., et al. 2010, ApJ, 708, 534. doi:10.1088/0004-637X/708/1/534

Chapter 6

Star-Formation Rates with SFACT

6.1 Introduction

The thesis would seem incomplete without an examination of the star-formation rate density (SFRD) as a function of redshift in our sample. However, due to circumstances which reduced our observation time significantly, the results presented in this chapter are regrettably incomplete. We nevertheless present our preliminary results.

The focus of our SFRD calculations is with the three primary emission lines detected by SFACT: H α , [O III], and [O III]. As mentioned in Chapter 2, SFACT is not the only survey to make use of emission lines when studying SFRs, nor is it the only survey to take a multi-wavelength approach. However, the scope of our project provides a valuable collection of galaxies which were detected via the same methodology at a wide range of redshifts.

In this chapter, we make use of the thesis catalog of SFACT which was introduced in Chapter 2. This includes 12 Fall fields for which the follow-up spectroscopy is at least 40% complete. The thesis sample includes 1684 targets, 1134 of which have follow-up spectroscopy. Of these, 938 star-forming galaxies were detected via one of our primary emission-lines and are used in this analysis.

6.2 Flux Corrections

Before we calculate the SFRDs, there are multiple corrections which we apply to the flux measurements. Some of these corrections depend on the survey data themselves, and will be improved and refined as the survey becomes more complete. Here we discuss the corrections we use in the order of application¹¹.

6.2.1 Nearby Line Corrections

Since we measure the emission-line flux using photometry, our H α flux measurement is sometimes tainted by [N II] flux that falls within our filters. However, we can use our follow-up spectra to accurately correct for the contribution of [N II] flux using line ratios. This is performed on a galaxy by galaxy basis. Depending on the redshift of the galaxy, either one or both of the nitrogen lines will also fall within our narrow-band (NB) filter.

Because we have spectra for all of our galaxies, we are able to directly measure the [N II]/H α flux ratio for most of our low-redshift galaxies. For those which we cannot, we utilize a statistical correction. Following the example of Van Sistine et al. (2016), we use a sample of 803 galaxies from KISS (Salzer et al. 2000, 2001; Gronwall et al. 2004; Jangren et al. 2005) that are confirmed star-forming galaxies with high quality follow-up spectra (Wegner et al. 2003; Gronwall et al. 2004; Jangren et al. 2005; Salzer et al. 2005). Van Sistine et al. (2016) develops the following relationship

¹¹The SFRD scripts are listed in the thesis appendix.

between R magnitudes and the [N II]/H α flux ratio which we adopt for SFACT:

$$\log\left(\frac{f_{[N \text{ II}]\lambda 6584}}{f_{H\alpha}}\right) = \begin{cases} -0.279M_R - 6.231 & \text{if } M_R > -18.5 \\ 0.010 \times M_R^3 + 0.556 \times M_R^2 + & \\ 10.002 \times M_R + 57.068 & \text{if } -21.6 \leq M_R \leq -18.5 \\ -0.462 & \text{if } M_R < -21.6 \end{cases} \quad (6.1)$$

Following Van Sistine et al. (2016), we use an error of 0.24, corresponding to the rms scatter of their cubic fit when measured line ratios, and their corresponding uncertainties, are not available.

Because we know the redshift for each of our galaxies, we can compute the locations of the emission lines relative to the filter transmission curves. Hence, we are able to then determine the total [N II] to H α flux ratio for all relevant galaxies:

$$\frac{f_{[N \text{ II}]\lambda\lambda 6584,6548}}{f_{H\alpha}} = \frac{f_{[N \text{ II}]\lambda 6584}}{f_{H\alpha}} \frac{T_{\lambda 6584}}{T_{H\alpha}} + \frac{1}{3} \frac{f_{[N \text{ II}]\lambda 6584}}{f_{H\alpha}} \frac{T_{\lambda 6548}}{T_{H\alpha}}, \quad (6.2)$$

where $T_{H\alpha}$, $T_{\lambda 6548}$, and $T_{\lambda 6584}$ are the filter transmissions at the observed wavelength of the [N II] and H α lines, and $\frac{f_{[N \text{ II}]\lambda 6584}}{f_{H\alpha}}$ comes either from the measured values in the spectra or from Equation 6.1. We also assume that the [N II] $\lambda 6548$ line is 1/3 the strength of the [N II] $\lambda 6584$ line; this is in proportion to the ratio of their collision strengths (Osterbrock & Ferland 2006). The [N II] doublet-corrected flux for all H α -detected galaxies is then given by:

$$f_{H\alpha,corr} = \frac{f_{H\alpha+[N \text{ II}]}}{\left(1 + \frac{f_{[N \text{ II}]\lambda\lambda 6584,6548}}{f_{H\alpha}}\right)}, \quad (6.3)$$

where $f_{H\alpha+[N \text{ II}]}$ is measured from our NB images.

Using a similar method, we must also make a correction based on the [O III]

doublet. Because the $\lambda 4959$ and $\lambda 5007$ lines are so close together, we often have both lines in our NB filter. Similar to excluding the contribution from [N II], we wish to exclude the contribution from $\lambda 4959$. We use a flux strength ratio of 0.34 (based upon the average ratio from high-quality spectra) and the filter transmissions at the corresponding wavelengths to compute $\frac{f_{\lambda 4959}}{f_{\lambda 5007}}$, from which we derive $f_{\lambda 5007}$.

We treat the [O II] doublet as a single line. Because there are no other prominent lines close to [O II], no corrections for extra line flux within the NB filters need be performed.

6.2.2 Filter Transmission Correction

Once the NB fluxes have been corrected for unwanted contributions from nearby emission lines in the NB filters, we can scale by the transmission of the NB filter at the location of the primary emission line. This scales our flux so that we are using the flux we would've measured if the filter transmission was uniformly 100%. This correction has little impact if the object was detected near the center wavelength of the filter, but detections in the wings necessitate larger adjustments (see Figure 3.1 for the filter transmission curves).

For example, the $\lambda 5007$ emission line from SFF02-NB3-A7815 was detected on the edge of the NB3 filter, where the transmission was only 23%. It might not have been detected at all except for the $\lambda 4959$ emission in the center of the filter, boosting the total flux in our NB filter. After correcting for the flux of the nearby line, we then correct for the transmission of our NB filter. A flux of 0.066×10^{-14} erg s $^{-1}$ cm $^{-2}$ was scaled to 0.281×10^{-14} erg s $^{-1}$ cm $^{-2}$, or the flux we would've measured if the $\lambda 5007$ line had been in the center of the filter.

6.2.3 Dust Correction

We also correct for the internal absorption due to the dust in the observed galaxy. In some cases we are able to directly compute $c_{H\beta}$ by using the $f_{H\alpha}/f_{H\beta}$ or $f_{H\gamma}/f_{H\beta}$ ratio from the H α and [O III] detections, respectively. If possible, we use our measured ratio of Balmer lines to determine the optical depth along our line of sight. We have measured flux ratios for 66% of the H α -detected galaxies, and for 12% of the [O III]-detected galaxies.

For all remaining galaxies we once again follow Van Sistine et al. (2016) and use a statistical correction based on KISS galaxies a minor adjustment. For these galaxies we use a polynomial fit based on the absolute R magnitude:

$$c_{H\beta} = \begin{cases} 0.014M_R^2 + 0.430M_R + 3.133 & \text{if } M_R \geq -18 \\ 0.05 & \text{if } M_R < -18, \end{cases} \quad (6.4)$$

where galaxies less luminous than $M_R = -18$ are all treated as if $M_R = -18$.

Our galaxies, especially the high-redshift [O II] galaxies, are expected to have a lower metallicity than the KISS galaxies. As such, they will be less affected by dust and are predicted to have a lower $c_{H\beta}$ value than the original Van Sistine et al. (2016) equation was producing. Since the [O II] detections are highly dependent on the dust correction, we have decreased the computed $c_{H\beta}$ by 0.10 from the Van Sistine et al. (2016) curve in order to better approximate the SFACT data. The adjustment amount was set so that the computed $c_{H\beta}$ value for a galaxy with $M_R = -21$ is equal to the median measured $c_{H\beta}$ value of H α and [O III] galaxies at $-22 < M_R < -20$.

We expect to determine more exact values for all galaxies without measured $c_{H\beta}$ values when we have a larger sample of SFACT sources and we can derive a new statistical correction based upon our own data. For now, we adopt an uncertainty of 0.05 on all computed $c_{H\beta}$ values. We also currently use an uncertainty of 0.03 for all

measured flux ratios from H α detections, and 0.05 for all measured flux ratios from [O III] detections.

To apply the reddening correction, we assume an $R_v = 3.1$ absorption law and use reddening function values from Table 7.1 in Osterbrock & Ferland (2006) resulting in a flux correction

$$f_{H\alpha, gcorr} = f_{H\alpha} 10^{0.818c_{H\beta}} \quad (6.5)$$

$$f_{[O\ III], gcorr} = f_{[O\ III]} 10^{1.120c_{H\beta}} \quad (6.6)$$

$$f_{[O\ II], gcorr} = f_{[O\ II]} 10^{1.854c_{H\beta}} \quad (6.7)$$

based upon which emission-line triggered the detection.

6.3 Survey Depth Correction

Flux-limited astronomical surveys will always be limited by the brightness of their targets. As we look out at greater distances, we miss more of the low-luminosity targets which appear too dim for our telescope to detect. These missing galaxies must be accounted for when drawing conclusions about the wider universe based upon our survey sample (Postman & Geller 1984). The missing galaxies are especially important when they are at or below L* luminosities. Without galaxies at these luminosities, the calculated SFRD will be drastically under-estimated compared to reality.

In order to correct for this missing luminosity, we start by generating a fiducial estimate of the total line luminosity present in a typical volume of space. To do this, we adopt a luminosity function (LF) that we believe is representative of our sample of emission-line galaxies (ELGs) at all redshifts. Then we integrate this LF from the highest luminosities expected in the sample down to the lowest luminosities detected in the nearest redshift window. For our purposes, we use the KISSR H α LF discussed

in Chapter 5 since we expect the LF of SFACT to look similar.

We then integrate the same LF, but use different lower-luminosity limits. These alternate luminosity limits represent the limiting luminosities of each redshift window. For a more distant redshift window the limiting luminosity will be higher than the value used for the fiducial calculation, and the LF integral will represent a lower total luminosity. By comparing these total integrated luminosities to the fiducial, we are able to understand how much of the total luminosity we are missing. At each distance, a correction factor is computed based on the ratio of the two total luminosities. A function fit to these ratios gives us an equation by which we determine a correction factor based on the distance. This correction factor is then applied to the total luminosity of our galaxies within a given redshift window.

In the future, the LFs used in this correction will be based upon LFs derived from the SFACT data. For now, the same H α LF is used to compute the correction factor which is used in each redshift window. Because of this, we further adjust the [O III]-selected galaxies by the ratio of the KISSR and KISSB SFRDs. This partly accounts for the distinct shape of the [O III] LFs. Using the ratio of these two computed SFRDs (see Table 5.3), we estimate the amount of luminosity further missed due to the metallicity-dependence in [O III] detections. As discussed in Chapter 5.5, more luminous galaxies are likely to be missed when using [O III] as the selection method.

Since these are preliminary survey depth corrections, we have adopted a relative uncertainty in the computed correction factor. We have assumed a 10% uncertainty in the H α redshift windows, a 15% uncertainty in the [O III] windows, and a 20% uncertainty for our highest redshift [O II] windows. These uncertainties are conservative estimates and we expect the true uncertainties to be smaller when we refine this correction.

The corrections described in this and the previous section have a major impact on the final SFRD. In Figure 6.1 we show the impact of these two sets of changes. Red

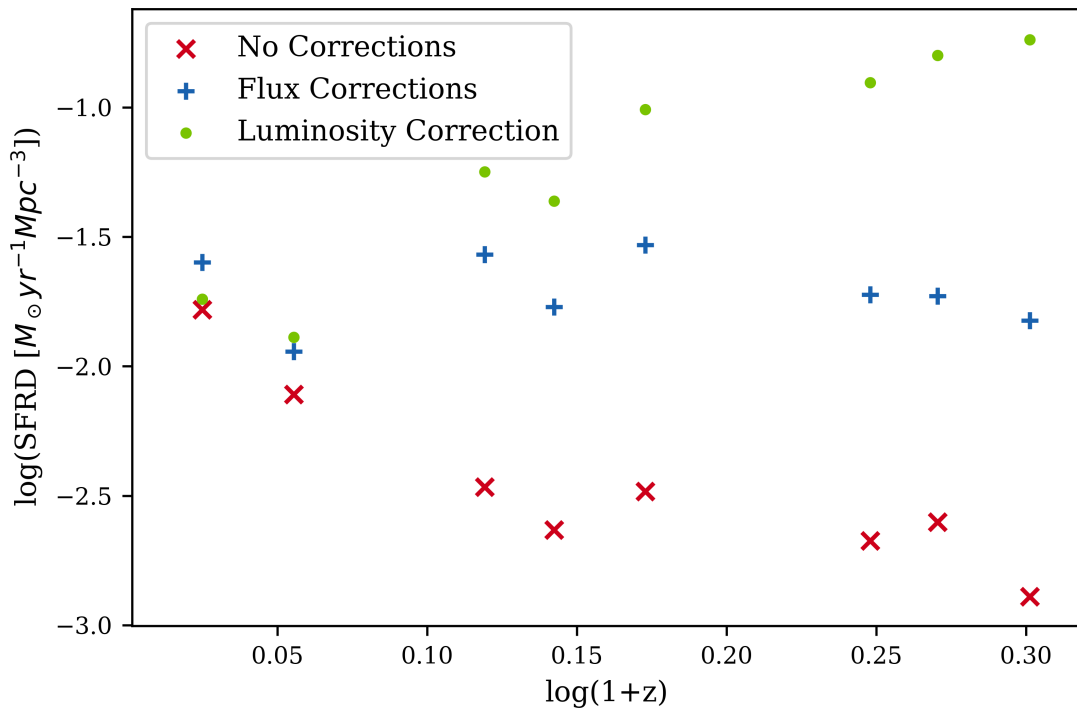


Figure 6.1 Here we present our SFRD measurements after different sets of corrections. Red crosses indicate the SFRD with no corrections applied. Blue plus signs show the SFRD when flux corrections are applied. Green dots show the final SFRD measurements when luminosity corrections are applied.

crosses show the SFRD as determined from the original measured fluxes. Blue plus signs are the results after only performing the corrections in Section 6.2. The green dots show the final SFRD measurement after the corrections in this section have been applied. It can be seen that accurate reckonings of the corrections applied to our data can have a substantial impact on the final SFRD measurement. For this reason, we discuss further improvements to our correction methodology in Section 6.6.

6.4 Star-Formation Rate Calculations

By using the redshift derived from the spectroscopy, we are able to determine the recessional velocity of each object. This includes a correction for the Local Group velocity. We can then convert this velocity to the distance of each object. Using these distances, we are able to determine the line flux luminosity of our sources using

$$L_X = 4\pi D^2 f_{X,corr}, \quad (6.8)$$

where D is the distance of each object as described above and $f_{X,corr}$ is the final flux after all flux corrections have been applied, regardless of the detection line.

We are also able to determine the total, co-moving volume surveyed for each redshift window. This volume is limited by both the area of the field, but also the redshift limits of the NB filter in which the object was detected. As listed in Table 2.1, there is a redshift limit at which we are able to detect each emission line. However, this limit is not quite as strict as the table implies since the transmission curves of the filter do not have straight sides (Figure 3.1). Because of this, we calculate the minimum and maximum distance of each redshift window by using the minimum and maximum distance of the objects detected in each redshift window.

In the following subsections we describe how we calculate the star-formation rates using each of our primary emission lines.

6.4.1 H α Star-Formation Rates

Recombination lines are a valuable way to measure the star formation of a galaxy. They are a direct and sensitive probe for studying young massive stellar populations. This is because only stars with masses of $>10 M_{\odot}$ and lifetimes of <20 Myr contribute significantly to the ionizing flux used in the evolutionary synthesis models. Like many other surveys, we make use of the H α emission line when calculating SFRs.

We use the calibration in Kennicutt (1998) to convert our H α luminosity measurements to SFRs:

$$SFR(M_{\odot} \text{ year}^{-1}) = 7.9 \times 10^{-42} L(H\alpha)(\text{ergs s}^{-1}). \quad (6.9)$$

As suggested in Ferguson et al. (1996), $L(H\alpha)$ includes the diffuse H α emission as well as the flux of the strong line we detected. We measure the H α emission using the photometry rather than the spectroscopy, and, as such, are able to include the entire galaxy in our measurement. This is especially important for the nearby, extended galaxies which subtend more than $2''$ and thus extend beyond the size of the Hydra fiber used for spectroscopy.

6.4.2 [O III] Star-Formation Rates

Since it is common for optical spectroscopy to be set up such that both H α and [O III] emission lines are covered, many ELG surveys compute SFR using the H α emission even if they select via [O III] line emission. Since we measure NB flux from our NB images, we are computing SFR from the [O III] $\lambda 5007$ line emission. The luminosities of the [O III] emission lines are not directly tied to ionizing luminosity, and their excitation is sensitive to the metal abundance and ionization state of the surrounding gas, but it can still be calibrated and used as a SFR tracer.

In order to calculate the [O III] SFR, we use a relationship from Khostovan et al.

(2020). This assumes a Salpeter IMF.

$$SFR(M_{\odot} \text{ year}^{-1}) = 7.35 \times 10^{-42} L([O \text{ III}]) (\text{ergs s}^{-1}) \quad (6.10)$$

6.4.3 [O II] Star-Formation Rates

The strongest emission feature in the blue region of the optical spectrum is the [O II] $\lambda 3727$ forbidden-line doublet. The caveats mentioned above regarding using [O III] emission as a SFR indicator also apply to the [O II] line, although to a lesser extent.

Calibration studies have been carried out by Gallagher et al. (1989) and Kennicutt (1992), and their results have been averaged to arrive at the current standard conversion:

$$SFR(M_{\odot} \text{ year}^{-1}) = 1.4 \times 10^{-41} L([O \text{ II}]) (\text{ergs s}^{-1}). \quad (6.11)$$

6.4.4 Completeness Correction

After calculating the SFR, we implement a final completeness correction. This is a correction which accounts for the fact that not all of the spectroscopic follow-up is complete. This correction is made on a field by field basis using the percentage of our targets in a field for which we have a processed spectrum. For each field we divide the average SFR by the percentage of the field which has spectroscopic follow-up.

6.5 Results

For the 12 thesis sample fields, there are 1109 galaxies which are confirmed ELG galaxies. We focus our SFR studies on the 938 star-forming galaxies which have been detected via H α , [O III], or [O II]. For each of these galaxies, we have performed the necessary corrections mentioned above and determined the star formation rate. We

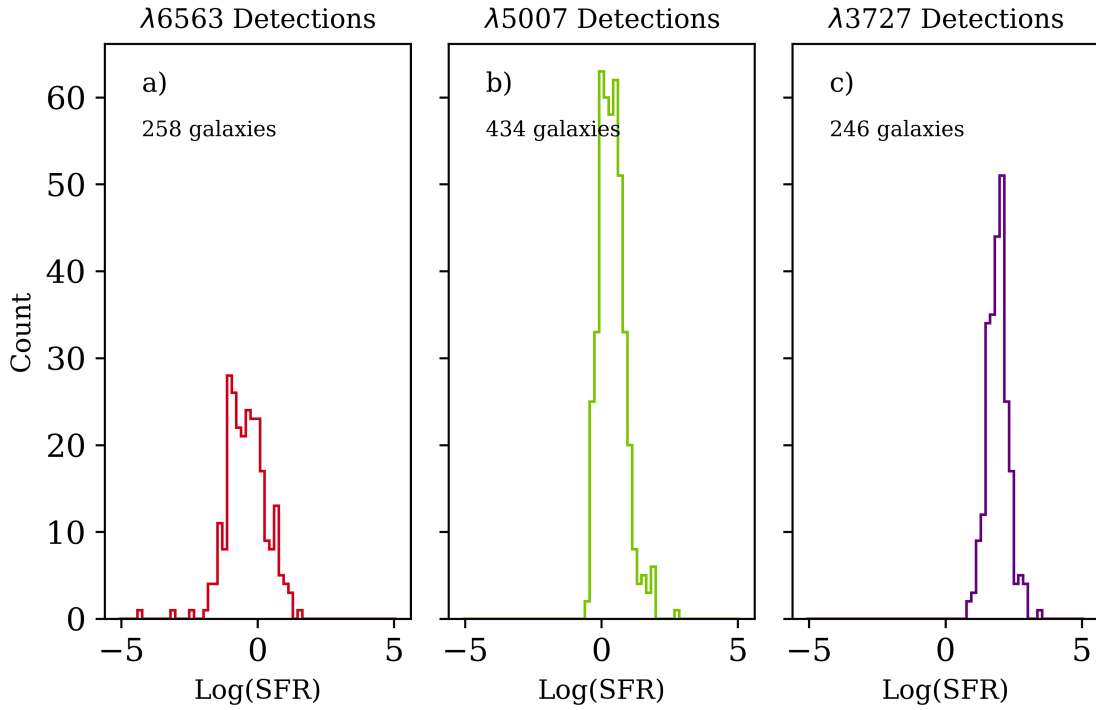


Figure 6.2 Histograms showing the log(SFR) of the thesis sample broken down by which emission line was detected in our filter. a) shows the galaxies detected via $\lambda 6563$, b) shows the galaxies detected via $\lambda 5007$, and c) shows the galaxies detected via $\lambda 3727$.

have also performed a completeness correction in order to account for the incomplete spectroscopic follow-up.

6.5.1 Star-Formation Rates

In Figure 6.2 we present the range of SFRs present in each of our emission-line samples. Each of the three histograms are plotted on the same scale to better visualize the differences in each emission-line sample. In the figure, the galaxies with the lowest SFR are clearly visible in the H α detections, as expected since only the redshift windows reached via H α are going to contain dwarf galaxies with small amounts of star formation. The individual galaxies with the highest SFRs were found via their [O II] detections. The median log(SFR) is highest for [O II] with $1.92 (M_{\odot} \text{ year}^{-1})$.

$\text{H}\alpha$ and $[\text{O III}]$ have median $\log(\text{SFRs})$ of -0.42 and 0.40 ($M_{\odot} \text{ year}^{-1}$), respectively. There are 258 objects detected via $\text{H}\alpha$ emission, 434 objects detected via $[\text{O III}]$ emission, and 246 objects detected via $[\text{O II}]$ emission. The relative numbers of galaxies detected in these three groups are the same as in the pilot-study fields and we expect it to remain as such for the complete SFACT catalog.

For a discrete redshift window breakdown, we turn to Figure 6.3. From left to right, top to bottom, we show our nine redshift windows. Galaxies detected via the same emission line are in the same row and use the same color; galaxies detected in the same NB filter are in the same column. For each subplot, the width of the SFR range displayed is the same. Subplot a) spans $-5.5 < \log(SFR) < -0.3$, subplots b) and c) span $-3.0 < \log(SFR) < 2.2$, and the others span $-1.0 < \log(SFR) < 4.2$.

The galaxies found in NB2 via their $\text{H}\alpha$ emission — subplot a) — are in our lowest redshift window and thus we are able to detect the least active galaxies. There are also only four galaxies in this redshift window, much lower than the next smallest window — NB3 $[\text{O II}]$ detections in subplot i) — which contains 50 galaxies.

In this figure, we can see that there is a general trend toward higher SFRs in galaxies at higher redshifts. This is a reflection of the fact that for a given flux level, more distant objects will be more luminous. More active, and therefore luminous, galaxies are more likely to be detected by our survey at higher redshifts. This is true even though we are selecting galaxies via their line emission. Furthermore, our lower redshift bins survey a smaller volume. This means the more rare galaxies, like starburst galaxies, are less likely to be included in our catalog at lower redshifts.

6.5.2 Preliminary Star-Formation Rate Densities

Although we have noted that there are still minor corrections which need to be more precisely applied to our data — we will discuss these in Section 6.6 — and more data in the processing stages, we still wanted to calculate a preliminary set of the

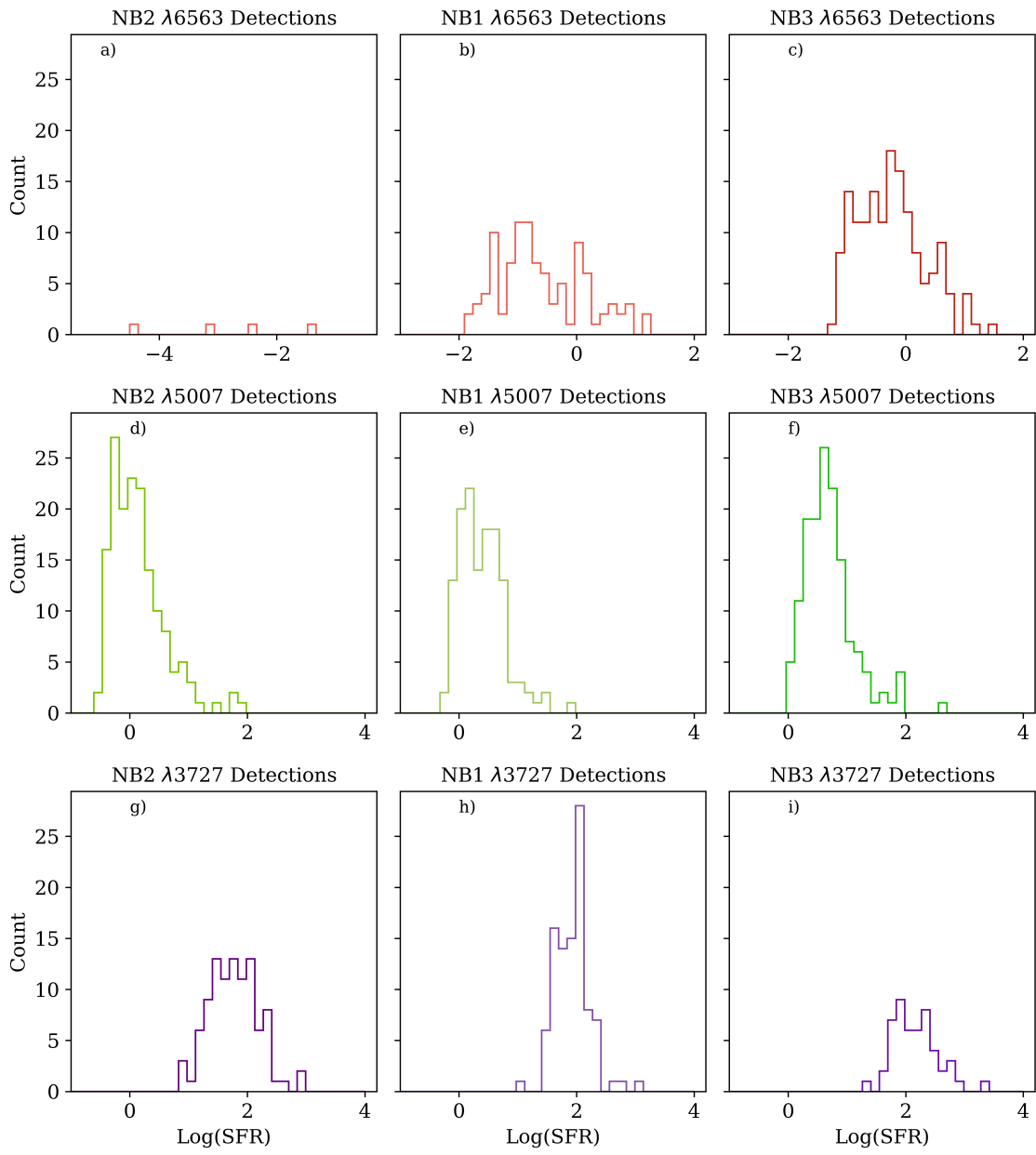


Figure 6.3 Histograms showing the $\log(\text{SFR})$ of the thesis sample broken down by which emission line was detected in which filter. There is one histogram for each of the nine main redshift windows. The galaxies detected via the same emission line are in the same row, and the galaxies detected in the same filter are in the same column. Redshift increases from left to right, then top to bottom. Subplots d) through i) have the same x range.

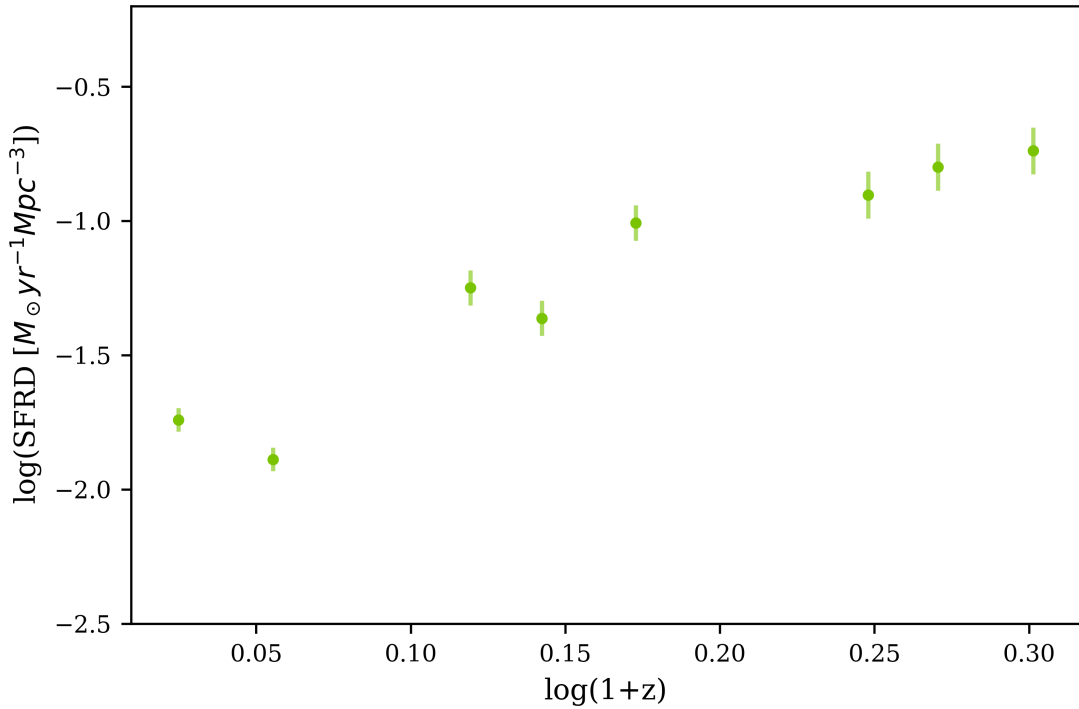


Figure 6.4 Here we present our SFRD measurements. We have plotted the logarithmic SFRD values against the redshift in a way that matches the axes of the familiar Madau plot. Each point represents the SFRD in a single redshift window, as defined by a single detection line in a single filter.

star-formation rate densities for our thesis sample. Figure 6.4 presents the current status of our SFRD measurements.

Each of the green dots in this plot represents the total SFR of the star-forming galaxies in a single redshift window, divided by the total volume surveyed within that redshift window. We have not displayed the lowest redshift window since there are only four galaxies and this is not sufficient for a robust measurement.

For the purposes of this thesis, we have determined approximate uncertainties for each redshift window. In the future, these uncertainties will be robustly determined based upon measured quantities from a larger data sample. The largest uncertainties currently are from the absorption correction, the survey depth correction, and our

volume calculation. The relative uncertainty in the survey depth correction is the dominate term the final uncertainties illustrated in Figure 6.4.

Our SFRDs plotted in Figure 6.4 resemble the familiar Madau plot (Madau et al. 1998) with a rising SFRD toward higher redshifts. Yet, there are still some differences. We point out that the overall trend is such that a higher redshift results in a higher SFRD, yet the [O II] NB1 window and the H α NB3 have lower SFRDs than the next lowest redshift windows. It is too early to tell which of these redshift windows may be wrong, and why it deviates from the overall trend. This might be due to cosmic variance in our still small sample size. The total SFR varies greatly between the 12 fields and although we ultimately want to view our results in the context of our redshift windows, we still see some lingering effects of the number variations within each redshift window. As we increase our sample size, the average of all our fields will be much more representative of the universe as a whole.

We also note that our [O II]-detections are showing a higher SFRD than commonly cited values in the literature (see below). These values are still expected to change as we better account for how the shape of the [O II] LF affects the survey depth corrections. Since SFACT is biased toward higher-luminosity galaxies, our calculated SFRD is likely to skew higher with only preliminary corrections.

6.5.3 Comparison with Literature

Despite the adjustments still to be applied to our results, it is worth comparing our preliminary results against the literature. Table 6.1 presents our SFRD values as well as values given by other emission-line selected surveys. The table is sorted according to redshift. These comparison points can also be seen in Figure 6.5 where the measurements from the same line have the same color.

The AHA project (Van Sistine et al. 2016), as discussed in Chapter 5, detected objects via H I emission and measured the H α emission to determine the SFRD. They

Table 6.1. SFRD Literature Comparison

Survey (1)	Measured line λ (2)	z (3)	log(SFRD) $M_{\odot} \text{ yr}^{-1} \text{ Mpc}^{-3}$ (4)
AHA	6563	0.01	-1.747±0.018
SFACT	6563	0.059	-1.740±0.043
Ly 2007	6563	0.07, 0.09	-1.87
SFACT	6563	0.136	-1.888±0.043
Sullivan 2000	6563	0.15 ± 0.150	-1.86 ± 0.06
SFACT	5007	0.316	-1.249±0.065
SFACT	5007	0.388	-1.362±0.065
HiZELS	6563	0.40	-1.52
LAGER	6563	0.47	-1.63±0.04
SFACT	5007	0.489	-1.007±0.065
DAWN	6563	0.62	-1.37
SFACT	3727	0.769	-0.903±0.087
Ly 2007	3727	0.83	-1.3
HiZELS	6563	0.84	-1.0
SFACT	3727	0.864	-0.800±0.087
LAGER	5007	0.93	-1.07±0.06
SFACT	3727	1.001	-0.738±0.087
HiZELS	6563	1.47	-0.88
HiZELS	3727	1.47	-0.77
LAGER	3727	1.59	-0.90±0.10

Notes. — The other surveys can be found in Ly et al. 2007, Sullivan et al. 2000, Khostovan et al. 2020 (LAGER), Coughlin et al. 2018 (DAWN), Van Sistine et al. 2016 (AHA), and Sobral et al. 2013 (HiZELS)

found a local SFRD of $\log(\text{SFRD}) = -1.747 \pm 0.018$. This closely aligns to the SFRD in our lowest redshift window.

The HiZELS survey (Sobral et al. 2013) used images to detect ELGs similar to SFACT, searching specifically for H α and [O II] emission. They were able to detect galaxies at a fainter flux limit because they made use of a 4 meter telescope (for the H α detections) and an 8 meter telescope (for the [O II] detections). However, unlike SFACT, they do not collect their own follow-up spectroscopy, instead using spectra found elsewhere in the literature. The initial H α HiZELS SFRD values are reported in (Sobral et al. 2013). HiZELS also searched higher redshifts than SFACT currently is able to reach. In the future we may have the opportunity to overlap at $z = 1.47$ and more directly compare our results.

The LAGER survey (Khostovan et al. 2020) is an in-progress survey also searching for ELGs and covering a similar footprint to the final SFACT survey. By using the Blanco 4-meter telescope, they discover galaxies via our three primary lines, in addition to Ly α at high redshifts. While their redshift windows are slightly different than ours due to different NB filters, a comparable detection methodology means they are a valuable survey to compare ourselves against. Of particular interest is a more detailed comparison between the LAGER $\lambda 6563$ $z = 0.47$ $\log(\text{SFRD})$ of -1.63 and the SFACT $\lambda 5007$ $z = 0.489$ $\log(\text{SFRD})$ of -1.01 . This is a wider discrepancy than expected, even though the SFRD measurements used different emission lines. When we have the additional NB filter allowing us to detected galaxies at the same redshift via $\lambda 6563$ and $\lambda 5007$, we may better understand the impact of the selection function on the final SFRD measurement.

The DAWN survey (Coughlin et al. 2018) has the most similar methodology to SFACT: they use NB imaging to detect ELGs and take their own follow-up spectroscopy to confirm their results. Again, their NB filters mean they survey a slightly different redshift range, but when we construct SFACT LFs, this survey which focuses

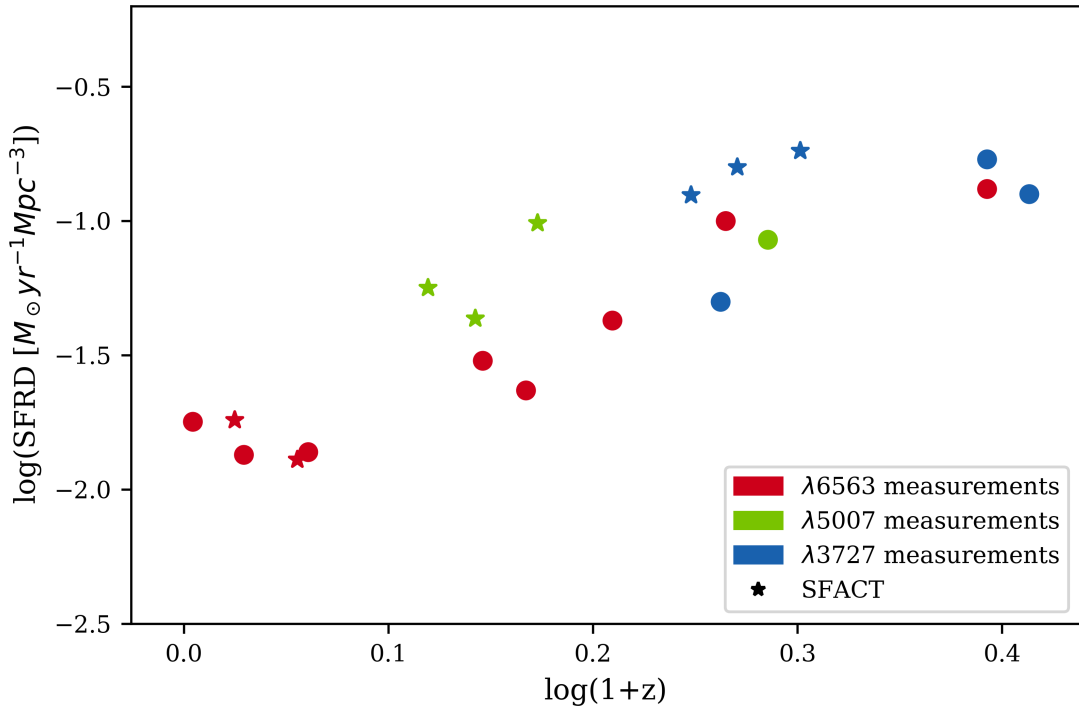


Figure 6.5 Here we present our SFRD measurements in comparison with other similar surveys (Table 6.1). Measurements from H α are rendered in red, measurements from [O III] are rendered in green, and measurements from [O II] are rendered in blue. In all cases, stars mark the SFACT data.

on H α -based LFs will be a valuable resource to compare against.

Figure 6.5 illustrates our comparison with other SFRD measurements in the literature. The color of each data point is chosen to illustrate the line used to measure the SFR of the sample. Measurements from H α are rendered in red, measurements from [O III] are rendered in green, and measurements from [O II] are rendered in blue. All SFACT data points are marked as stars. At the lowest two redshift windows, our SFACT values are consistent with other published values. This lends credibility to our SFRD measurements at these redshifts. At higher redshifts, our [O III] and [O II] SFRD measurements are noticeably higher than other surveys. We stress that we consider our measurements to be preliminary; future improvements in our correction

methodology may change our values (see below). Further investigation into the differences in SFRD measurements at higher redshifts will occur when we have a larger sample of SFACT galaxies.

6.6 Improvements

The results presented in this Chapter are preliminary and are likely to be refined in the near future. Some corrections we still need to perform include:

1. Our current volume calculations are based on the total area of each field. However, to be accurate, we should not be including the masked areas of the image since we didn't search those areas of the field. A script to correctly, and precisely, calculate the volume of each field is in development. This will be especially needed when we start working with a larger catalog size. For each field, the unmasked area needs to be determined on a quadrant by quadrant basis, while also not double counting the overlap regions.
2. As discussed in Section 6.2.3, we plan on improving our $c_{H\beta}$ determination for galaxies which lack the necessary line ratios. With a greater sample of SFACT galaxies, we plan to create our own statistical correction based upon our own sample, rather than a sample of KISS galaxies selected at a different redshift, with a different flux limit. Although we have currently made an adjustment to account for the different metallicity of the KISS galaxies compared to SFACT galaxies, we anticipate that a more accurately determined value of $c_{H\beta}$ for our high-redshift galaxies will improve the precision of our final result.
3. We have already performed a correction for survey depth in our redshift windows (Section 6.3). However, when we have a larger catalog of galaxies to work with, we will refine this correction using LFs based upon SFACT galaxies, rather

than using the galaxies in another survey. This will not only allow us to make a more accurate correction based on the data in this survey, but we will then also be able to provide a more accurate correction for the galaxies detected via oxygen-emission lines. As discussed in Chapter 5, the shape of the LF differs starkly depending on if the sample was detected via H α or [O III] line emission. We expect that the [O II] LF shape will be similar to that of H α LF, but a confirmation of this is desirable.

4. Improved corrections accounting for differences in the survey selection method also need to be created. In the future, we anticipate using our spectra to derive a relationship between the strength of our oxygen lines, to put the [O II] emission on an [O III] scale, and from there onto an H α scale.

We do not anticipate any of these changes to have a huge impact on the calculated SFRDs, but we plan on performing these prior to publication.

After making these improvements, we will also be able to better compare our SFACT results against the results in Chapter 5.

6.7 Conclusion

These are still early days for SFACT. We expect to double the SFR sample in the next ten months through new follow-up observations and spectral processing. In addition to new data, adding the processed Spring sample will add 580 spectra to our total sample.

Work to address the improvements mentioned in the previous section is ongoing. Our focus is currently geared toward the incorporation of the Spring fields to double our sample size.

References

- Coughlin, A., Rhoads, J. E., Malhotra, S., et al. 2018, ApJ, 858, 96. doi:10.3847/1538-4357/aab620
- Ferguson, A. M. N., Wyse, R. F. G., Gallagher, J. S., et al. 1996, AJ, 111, 2265. doi:10.1086/117961
- Gallagher, J. S., Bushouse, H., & Hunter, D. A. 1989, AJ, 97, 700. doi:10.1086/115015
- Gronwall, C., Salzer, J. J., Sarajedini, V. L., et al. 2004, AJ, 127, 1943
- Gronwall, C., Jangren, A., Salzer, J. J., et al. 2004, AJ, 128, 644
- Jangren, A., Salzer, J. J., Sarajedini, V. L., et al. 2005, AJ, 130, 2571
- Jangren, A., Wegner, G., Salzer, J. J., et al. 2005, AJ, 130, 496
- Kennicutt, R. C. 1992, ApJ, 388, 310. doi:10.1086/171154
- Kennicutt, R. C. 1998, ARA&A, 36, 189. doi:10.1146/annurev.astro.36.1.189
- Khostovan, A. A., Malhotra, S., Rhoads, J. E., et al. 2020, MNRAS, 493, 3966. doi:10.1093/mnras/staa175
- Khostovan, A. A., Malhotra, S., Rhoads, J. E., et al. 2020, MNRAS, 493, 3966. doi:10.1093/mnras/staa175
- Ly, C., Malkan, M. A., Kashikawa, N., et al. 2007, ApJ, 657, 738. doi:10.1086/510828
- Madau, P., Pozzetti, L., & Dickinson, M. 1998, ApJ, 498, 106. doi:10.1086/305523
- Osterbrock, D. E. & Ferland, G. J. 2006, Astrophysics of gaseous nebulae and active galactic nuclei, 2nd. ed. by D.E.
- Postman, M. & Geller, M. J. 1984, ApJ, 281, 95. doi:10.1086/162078 Osterbrock and G.J. Ferland. Sausalito, CA: University Science Books, 2006

Salzer, J. J., Gronwall, C., Lipovetsky, V. A., et al. 2000, AJ, 120, 80.
doi:10.1086/301418

Salzer, J. J., Gronwall, C., Lipovetsky, V. A., et al. 2001, AJ, 121, 66.
doi:10.1086/318040

Salzer, J. J., Jangren, A., Gronwall, C., et al. 2005, AJ, 130, 2584

Sobral, D., Smail, I., Best, P. N., et al. 2013, MNRAS, 428, 1128.
doi:10.1093/mnras/sts096

Sullivan, M., Treyer, M. A., Ellis, R. S., et al. 2000, MNRAS, 312, 442.
doi:10.1046/j.1365-8711.2000.03140.x

Van Sistine, A., Salzer, J. J., Sugden, A., et al. 2016, ApJ, 824, 25

Wegner, G., Salzer, J. J., Jangren, A., et al. 2003, AJ, 125, 2373

Chapter 7

Summary and Future Work

7.1 Summary

The SFACT survey uses narrow-band (NB) images to identify star-forming galaxies at $z \leq 1$ and create a substantial catalog that can be used to carry out star-formation rate density (SFRD) studies. By using NB filters, we create redshift windows to search for star-forming galaxies at a range of different redshifts using different emission lines. In this thesis we have examined the pilot-study sample (three fields and 533 targets) and the extended thesis sample (12 fields and 1684 targets).

We have used the WIYN 3.5m telescope at Kitt Peak National Observatory with both ODI and Hydra to obtain our imaging and spectroscopic data. Each field was observed through three broad-band (BB) filters (gri) and three custom NB filters. This potent combination of a large telescope and long total integration times allows us to detect galaxies at a wide range of line fluxes ($-13 < \log(\text{NB Flux}) [\text{erg s}^{-1} \text{cm}^{-2}] < -16$). We are able to sample emission-line galaxies (ELGs) with varying levels of emission-line strengths and with both faint and bright continuum magnitudes.

We have written custom programs to process and analyze our images. This includes identifying candidates with excess flux in the NB images, while discarding image artifacts or other non-ELG objects. Based on the pilot-study fields, we achieve a 91.9% success rate for correctly identifying ELGs. We have also written scripts to measure the emission-line flux using the NB images. We confirm that we cover

a wide range of luminosities and the colors seen in our catalog are consistent with active galaxies dominated by emission lines.

By using data from the previous KISS and AHA projects, an analysis of the derived SFRs using samples selected in different ways has been carried out. We find that H α -selected ELG surveys have the potential to miss 87% of the total H α luminosity in their survey volume. Surveys selecting via [O III] may result in missing 98% of the total star formation.

We also wrote scripts to compute the SFR of our star-forming galaxies. These incorporate corrections based on nearby emission lines, reddening effects, and completion corrections due to incomplete spectroscopic follow-up observations. Our preliminary SFR measures show that we are finding star-forming galaxies with varying levels of activity across our redshift windows. We have computed preliminary SFRD values for our SFACT sample, using the adjustments suggested by our previous analysis, but there are still minor adjustments to be made.

7.2 Future Work

7.2.1 Current Catalog

As mentioned previously, the SFACT survey is not complete. The largest sample used in this thesis includes only 12 fields. Our current catalog includes 41 fields for which the imaging observations are complete. Of these, spectroscopy is at least 40% complete for 27 fields, with many nearing 70% completeness.

Tables 7.1 and 7.2 present the SFACT fields with complete imaging observations. Included are the central positions of each field and the dates when the imaging observations were finished. Often multiple observing runs are needed to complete all necessary imaging for a single field (see Chapter 3 for observing details). The tables also present the total number of SFACT targets found by our software, and the

Table 7.1. Fall SFACT Fields Catalog

Field (1)	α (J2000) (2)	δ (J2000) (3)	Completion Date (4)	Targets (5)	Spectra (6)
SFF01*†	21:42:42	19:59:28	09/2018	132	101
SFF02*	22:00:00	20:00:00	11/2020	92	39
SFF03*	22:15:50	20:00:00	11/2018	92	50
SFF04	22:20:10	24:27:09	11/2018	122	44
SFF05	22:21:09	24:45:02	11/2018	166	8
SFF06*	23:19:46	24:51:56	11/2018	213	147
SFF07*	00:11:44	26:24:30	11/2018	208	114
SFF08*	00:43:00	25:51:25	10/2019	149	95
SFF09	01:23:46	28:03:01	11/2018	110	27
SFF10*†	01:44:20	27:54:23	09/2018	216	189
SFF11	02:00:29	02:00:29	10/2019	80	25
SFF12*	02:00:37	24:06:59	10/2019	100	52
SFF13	02:30:30	26:28:00	11/2018	127	47
SFF14*	02:34:34	27:16:54	09/2018	86	57
SFF15*†	02:38:52	27:51:43	09/2018	185	129
SFF16*	22:00:16	27:27:36	11/2020	64	43
SFF17*	01:47:12	28:01:34	11/2020	147	118
SFF18	02:47:40	20:20:00	11/2020	74	
SFF19	22:30:00	19:50:00	11/2021		
SFF20	22:59:30	20:00:00	11/2021		
SFF21	01:43:00	19:20:00	11/2021		
SFF22	02:01:30	20:00:00	01/2022		
SFF23	03:01:10	20:00:00	11/2021		
SFF24	03:14:00	19:29:00	01/2022		

Notes. — The three fields marked with † are our pilot-study fields. A * denotes a field which is part of the thesis sample. Fields without targets have been imaged but not processed. The number of spectra only reflects the number of spectra processed.

Table 7.2. Spring SFACT Fields Catalog

Field (1)	α (J2000) (2)	δ (J2000) (3)	Completion Date (4)	Targets (5)	Spectra (6)
SFS01	08:40:36	13:42:44	03/2021	78	58
SFS02	08:47:41	13:27:27	11/2020	160	114
SFS03	08:49:30	19:54:00	03/2021	50	36
SFS04	08:59:30	04:56:00	03/2021	101	
SFS05	09:18:30	13:46:11	11/2020	184	97
SFS06	11:59:00	42:42:00	04/2019	102	79
SFS07	12:22:24	43:11:22	03/2021	108	20
SFS08	13:10:09	29:17:43	03/2021	142	
SFS09	13:14:41	43:43:26	04/2019	149	81
SFS10	13:15:49	43:34:30	03/2021	134	
SFS11	14:20:38	43:43:31	03/2021	108	
SFS12	14:29:40	43:54:08	03/2021	135	13
SFS13	14:36:20	43:53:01	04/2021	105	61
SFS14	15:42:46	43:53:57	04/2019	82	61
SFS17	15:43:55	29:27:50	04/2021	70	
SFS20	09:41:53	12:12:18	11/2021	282	
SFS21	09:48:07	15:45:17	04/2021	75	

Notes. — Fields without targets have been imaged but not processed.
The number of spectra only reflects the number of spectra processed.

number of objects for which there is currently follow-up spectroscopy. Fields with no numbers in column 5 have not yet been processed.

7.2.2 Next Steps

In addition to improvements to the process of SFACT analysis (Section 6.6), we still have larger scale next steps. This includes taking more follow-up spectroscopy and processing the existing spectra. This would expand the total catalog of galaxies and the area of sky coverage. As demonstrated in Tables 7.1 and 7.2, there are many fields for which there exist targets awaiting confirmation.

At this time next year, we expect to increase the size of our star formation sample enough to produce and publish a robust SFRD analysis. We expect to have a sample of at least 30 fields, yielding a predicted \sim 4200 star-forming galaxies. A larger proportion of the fields will also have follow-up spectroscopic measurements which would be included in this analysis.

There is also more imaging work to be completed. The full SFACT survey is designed to include 50-60 fields and we currently have only 41 complete fields. If our proposed additional filters are commissioned, all of our fields would need additional imaging and subsequent follow-up spectroscopy to investigate newly discovered targets, including some out to $z=1.5$.

Since this project began, there have been other surveys which have done similar work at different redshifts. One of our goals in the future is to better compare our results with surveys such as HiZELS (Matthee et al. 2017) and LAGER (Khstovyan et al. 2020), which use similar methods to our own. We hope that by adding our final results to theirs, a more precise reckoning of the SFRD across cosmic time can be understood.

SFACT has proved itself as a successful narrow-band survey. As of this writing, we are only just beginning to demonstrate the full power of SFACT. There are thousands

of sources waiting in the wings for processing to expand the coverage of the survey and proceed with the planned science. We look forward to realizing the true potential of this complete survey.

7.3 Acknowledgements

The authors are honored to be permitted to conduct astronomical research on Iolkam Du'ag (Kitt Peak), a mountain with particular significance to the Tohono O'odham.

We gratefully acknowledge the long term financial support provided by the College of Arts and Sciences at Indiana University for the operation of the WIYN Observatory. Additional funds have been provided by the Department of Astronomy and the Office of the Vice Provost for Research at Indiana University to help support this project. The SFACT team wishes to thank the entire staff of the WIYN Observatory, whose dedication and hard work have made this survey possible. In particular, we acknowledge the contributions of Daniel Harbeck, Wilson Liu, Susan Ridgeway, and Jayadev Rajagopal. We also thank Ralf Kotulla (U. Wisconsin) for his development and continued support of the ODI image processing software (QuickReduce), and Arvid Gopu and Michael Young (Indiana U) for their support of the ODI Pipeline, Portal & Archive. And we wish to thank the WIYN telescope operators without whom there would be no data. Finally, we acknowledge the contributions made at various stages of this project by students in the Department of Astronomy at Indiana University who assisted with the data processing: Bryce Cousins, Anjali Dziarski, Sean Strunk, and John Theising.

Funding for the SDSS and SDSS-II has been provided by the Alfred P. Sloan Foundation, the Participating Institutions, the National Science Foundation, the U.S. Department of Energy, the National Aeronautics and Space Administration, the Japanese Monbukagakusho, the Max Planck Society, and the Higher Education Funding Council for England. The SDSS Web Site is <http://www.sdss.org/>.

The SDSS is managed by the Astrophysical Research Consortium for the Participating Institutions. The Participating Institutions are the American Museum of Natural History, Astrophysical Institute Potsdam, University of Basel, University of Cambridge, Case Western Reserve University, University of Chicago, Drexel University, Fermilab, the Institute for Advanced Study, the Japan Participation Group, Johns Hopkins University, the Joint Institute for Nuclear Astrophysics, the Kavli Institute for Particle Astrophysics and Cosmology, the Korean Scientist Group, the Chinese Academy of Sciences (LAMOST), Los Alamos National Laboratory, the Max-Planck-Institute for Astronomy (MPIA), the Max-Planck-Institute for Astrophysics (MPA), New Mexico State University, Ohio State University, University of Pittsburgh, University of Portsmouth, Princeton University, the United States Naval Observatory, and the University of Washington.

References

Matthee, J., Sobral, D., Best, P., et al. 2017, MNRAS, 471, 629.
doi:10.1093/mnras/stx1569

Khostovan, A. A., Malhotra, S., Rhoads, J. E., et al. 2020, MNRAS, 493, 3966.
doi:10.1093/mnras/staa175

Appendix A

Software Written for the SFACT Project

Here we present a list of the scripts we have written to facilitate the processing and analysis of SFACT data. All .cl scripts are IRAF tasks, and all .py scripts are Python scripts. These scripts are also being made available at
<https://github.com/JSieben7/SFACT>.

Scripts dealing with field processing and target selection were primarily collaborations between all three SFACT members. Scripts dealing with spectroscopy were primarily written by David Carr. Script dealing with photometry and star-formation rate density were primarily written by Jennifer Sieben.

A.1 Field Processing

This collection of scripts is used to process each field and identify objects

- `sfact1.cl` – This is the wrapper script for field processing
- `dotstart.cl` – This script initialised the IRAF database table
- `dotmult.cl` – This script identified objects in the field
- `dotdel.cl` – This script deleted duplication of identified objects
- `dotdel_py.py` – This script deleted duplication of identified objects more efficiently

- `dotadd.cl` – This script displays all candidates and gives the option for adding others
- `dotastrom.cl` – This script performs astrometry
- `sdss_fetch.py` – This script queries SDSS for matches to our catalog
- `sdssmerge.cl` – This script merges the results of the query with our database
- `satdisp.cl` – This script marks saturated stars
- `regionmask.cl` – This script allows the user to mark regions of the image which are of poor quality
- `regionflag.cl` – This script removes objects from the table if they are within a marked region

A.2 Target Selection

This collection of scripts works to identify any ELG candidates for a given filter

- `sfact2.cl` – This is the wrapper script for target selection
- `dotrestart.cl` – Re-initialization
- `dotphot.cl` – This script performs preliminary photometry on the continuum and NB image
- `dotselect.cl` – This script selects ELG candidates
- `dotsatdel.cl` – This script removes objects from consideration if they are too close to a saturated star to accurately measure
- `dotartifactdel.cl` – This script removes objects from consideration if they have artifact-like properties

- `dotmark.cl` – This script displays all ELG candidates, denoting which have received which flag to remove them from further consideration
- `classify.cl` – This is the script which displays all remaining candidates for user verification
- `reconcile.cl` – This script facilitates quality control via the comparison of each user’s classifications

A.3 Photometry

This collection of scripts performs photometric measurements and calibrations

- `sfactBB.cl` – This is the wrapper script for the broadband photometry
- `sfact4.cl` – This is the wrapper script for the narrowband photometry
- `photcalib.cl` – This script performs photometry on a list of SDSS stars using the full frame broadband images and the master table.
- `photcalibNB.cl` – This script performs photometry on a list of SDSS stars using the full frame narrowband images and the master table.
- `photdups.cl` – This script removes any duplicate calibration stars due to the merging of quadrants
- `BroadPhotPlots.py` – This script narrows the list of calibration stars and calculates the ZPCs to use in calibration
- `NarrowPhotPlots.py` – This script narrows the list of calibration stars and calculates the ZPCs to use in calibration
- `cutouts.cl` – This script creates cutouts of the SFACT targets from the master and BB images and saves them as one tiled image

- `cutoutsNB.cl` – This script creates cutouts of the SFACT targets from the master and NB images and saves them as one tiled image
- `photcog.cl` – This script performs repeated photometric measurements at different apertures in order to facilitate a curve of growth analysis
- `photcogNB.cl` – This script performs repeated photometric measurements at different apertures in order to facilitate a curve of growth analysis
- `CurveOfGrowth.py` – This script performs a curve of growth analysis in order to determine the best photometric aperture to use for each target
- `CurveOfGrowthNB.py` – This script performs a curve of growth analysis in order to determine the best photometric aperture to use for each target
- `Interloper.py` – This script flags targets which have another object nearby which might interfere with the photometry
- `photbyhand.cl` – This script prompts the user to check worrisome apertures and set the aperture for objects for which the curve of growth did not converge
- `photbyhandNB.cl` – This script prompts the user to check worrisome apertures and set the aperture for objects for which the curve of growth did not converge
- `photbb.cl` – This script performs the final broadband photometry and applies the relevant calibrations
- `photNB.cl` – This script performs the final narrowband photometry and applies the relevant calibrations
- `COGdisplay.py` – This script allows the user to display the curve of growth and the cutouts for any given object for inspection purposes

A.4 Spectroscopy

This collection of scripts performs spectroscopic measurements

- `fixskyms.cl` – This script masks sky lines in the processed multi-spec image
- `sortspec.cl` – This script separates the SFACT targets from the SDSS field galaxies in the multi-spec image
- `WRALF.py` – This script operates on the final multi-spec images and uses a user identified line, and the associated redshift, to automatically measure detected emission lines in the rest of the spectrum for all the spectra in the multi-spec image
- `remeasureN2.cl` – This script re-examines the final data tables for objects with H α emission lines but that are missing emission lines, and the user measures the missing line
- `remeasureHB.cl` – This script re-examines the final data tables for objects with [O III] emission lines but that are missing emission lines, and the user measures the missing line
- `remeasureO2.cl` – This script re-examines the final data tables for objects with [O III] emission lines but that are missing [O II] emission lines, and the user measures the missing line
- `remeasureQSO.cl` – This script re-examines the final data tables for objects with the QSO ELGTYPE designation so the broad emission lines can be measured

A.5 Star-Formation Rate Density

This collection of scripts facilitates the SFR and SFRD calculations

- `TableDownload.cl` – This script downloads the IRAF table to a python-readable format and includes only the relevant columns
- `SFR_pre.py` – This script collects the image size dimensions and converts redshift to a co-moving distance
- `Lumcorrs.py` – This script performs flux calibrations such as accounting for other emission lines in the filter and the transmission of the filter
- `LFcorr.py` – This script is responsible for the variable survey depth calculation
- `SFR_HA.py` – This script calculates the volume for the relevant redshift windows and converts NB flux to SFR
- `SFR_OIII.py` – This script calculates the volume for the relevant redshift windows and converts NB flux to SFR
- `SFR_OII.py` – This script calculates the volume for the relevant redshift windows and converts NB flux to SFR
- `SFACTplottingallSFR.py` – This script applies corrections based on the spectroscopic coverage of each field and plots SFR histograms
- `SFACT_SFRD.py` – This script computes the SFRD and creates an SFACT Madau plot

JENNIFER C. SIEBEN

Email: JSieben@iu.edu * Website: <https://jsieben7.github.io/>
Indiana University Department of Astronomy, 727 East 3rd Street,
Swain West Hall, Bloomington, Indiana 47405-7105

EDUCATION

Indiana University Ph.D., Astronomy Title: Star Formation Across Cosmic Time Advisor: Dr John Salzer Minor: Scientific Computing	<i>December 2022</i>
M.A., Astronomy	<i>March 2019</i>
Illinois Wesleyan University B.A., Physics	<i>May 2016</i>

RESEARCH INTERESTS

Star Formation History

I am interested in studying the long term history of the universe through the lens of star formation and galaxy evolution. I am particularly interested in medium-scale surveys to investigate global trends at different epochs.

RESEARCH EXPERIENCE

Graduate Research Assistant , Indiana University Star Formation Across Cosmic Time Advisor: John Salzer We are carrying out a narrow-band survey using the wide-field imager on the WIYN 3.5m telescope to discover emission line galaxies. This survey uses a combination of broad-band and narrow-band images to discover emission-line sources. Follow-up spectroscopy is then used to confirm the targets. Using nine redshift windows, we study galaxies up to $z = 1$. I have conducted observations and written pipelines to process the data as well as to measure the photometric properties of the galaxies. We have completed imaging of 41 fields, each with ~ 200 emission-line sources.	<i>2016—Present</i>
Independent Research , Illinois Wesleyan University Advisor: Linda French Observations of Delta Scuti stars with small telescope to determine rotation periods.	<i>2016</i>
Undergraduate Research Assistant , Illinois Wesleyan University Advisor: Linda French Observations of Trojan asteroids with the Cerro Tololo 0.9m telescope to determine rotation periods in order to discover a spin barrier and a limit of the density for comparison with cometary nuclei.	<i>Summer 2014</i>

OUTREACH

Astronomy Public Outreach, Indiana University *2016—Present*

Led public observing tours at IU's Kirkwood Observatory, led astronomy sessions at local public school events, volunteered at campus wide Science Fest

ScIU *2017—Present*

<https://sciu.indiana.edu/>

Writer and Editor-at-large for peer-edited, campus science blog, aimed at communicating science to an undergraduate audience. Also organized three annual science communication symposia for the wider public community and participated in various outreach oriented events around Southern Indiana.

Astronomy Department Outreach Coordinator, Indiana University *2019—2020*

Organized new outreach events, coordinated volunteers for public open house nights, led department participation in Science Fest - a full day of hands-on outreach activities from all science departments geared toward elementary to high school age public. Also revitalized the department twitter account.

Astronomy Public Outreach *2015—2016*

Regularly led public observing at IWU's Mark Evans Observatory and hosted a Lunar eclipse party attended by ~100 people.

Intern at Adler Planetarium *Summers 2013, 2015, 2016, Spring 2017*

Led public tours at Adler Planetarium's Doane Observatory with solar observing, and monthly nighttime observing sessions with short presentations about astronomy, also assisted in Space Visualization Lab

TEACHING EXPERIENCE

Instructor of Record, Indiana University *Summer 2018, 2021*

Taught A107: The Art of Astronomy (online course), an introductory science class for non-astronomy majors focusing on understanding astronomical images. Updated course structure and material in preparation for 2021 course.

Instructor

Co-Instructor for "Communicating Science in a Digital Age", *December 2020*
co-taught with Ruck, L., Holden, C.

Designed and taught a three-week online course covering science communication basics and how to promote your material online.

Science Communication Workshops

Day-long workshop given at ScIU Blogging Workshop Day, *May 2019*
co-led with Ruck, L., Moussa-Tooks, A.

Workshop given at ScIU: Conversations in Science at Indiana University 3rd Annual Science Communication Symposium, "Diving into SciComm", co-led with Ruck, L. *November 2019*

Workshop given at IU Journal of Undergraduate Research 3rd Annual Research Day, "Diving into SciComm", co-led with Ruck, L. *November 2019*

Associate Instructor, Indiana University *2016—2018, 2021—2022*

Discussion leader and grader for A107: The Art of Astronomy, A221/A222: General Astronomy

I/II, A103: The Search for Life in the Universe, and A100: The Solar System. 200 level courses were majors courses.

Undergraduate Teaching Assistant, Illinois Wesleyan University *2015–2016*
Facilitated lab activities and graded for A101: Introduction to Astronomy

PROFESSIONAL SOCIETIES

American Astronomical Society *Member*
SPIE - International Society of Optics and Photonics *Member, 2014–2016*

PROFESSIONAL SKILLS

WIYN 3.5M telescope (Kitt Peak, Az)	50+ nights, ODI and Hydra
CTIO 0.9m telescope (Cerro Tololo, Chile)	10 nights
Computer Languages	Python, IRAF, HTML, CSS, and SQL
Computer Software Knowledge	Google Drive Suite, MS Office Suite, Adobe Creative Suite, L ^A T _E X, Pinnacle Studios Video Editing, Audacity, <i>Mathematica</i> , <i>Canopus</i> , and IgorPro

AWARDS

Frank & Margaret Edmondson Prize for Teaching	<i>April 2021</i>
College of Arts and Sciences Dissertation Research Fellowship \$ 20,000	<i>2020—2021</i>
IUB Provost's Travel Award for Women in Science	<i>Fall 2018, Fall 2019, Fall 2021</i>
College of Arts and Sciences Travel Award	<i>Fall 2019</i>
Indiana Space Grant PhD Fellowship \$ 12,000	<i>2018—2019, 2019—2020</i>
Goethe Link Prize for Outreach and Public Education in Astronomy	<i>May 2019, April 2020</i>

INVITED TALKS

1. “Oven Baked Galaxies”
Public Science Symposium 2021
Indiana University, IN *June 2021*
 2. “Reaching Beyond the Stars”
Bays Mountain StarFest
Bays Mountain Park, TN *October 2018*

REFEREED PUBLICATIONS

- French, L. M., Stephens, R. D., Coley, D., Wasserman, L. H., and Sieben, J., "Rotation lightcurves of small jovian Trojan asteroids", *Icarus*, vol. 254, pp. 1–17, 2015.

2. Salzer, J. J., Carr, D. J., **Sieben, J.**, et al., “The Star Formation Across Cosmic Time (SFACT) Survey. I. Survey Description and Early Results from a New Narrow-Band Emission-Line Galaxy Survey”, ApJ, 2022 (in review)
3. **Sieben, J.**, Carr, D. J., Salzer, J. J., et al., “The Star Formation Across Cosmic Time (SFACT) Survey. II. The First Catalog of Targets from a New Narrow-Band Survey for Emission-Line Objects”, ApJS, 2022 (in review)
4. Carr, D. J., **Sieben, J.**, Salzer, J. J., et al., “The Star Formation Across Cosmic Time (SFACT) Survey. III. Spectroscopy of the Initial Catalog of Emission-Line Objects”, ApJS, 2022 (in review)

CONFERENCE POSTERS

1. Brucker, M. J., Nault, K. A., Hambergren, M., **Sieben, J.**, Gyuk, G., Solontoi, M. R. 2015. Preliminary Light Curve Results of NEOs from the Characterization and Astrometric Follow-Up Program at Adler Planetarium. AAS/Division for Planetary Sciences Meeting Abstracts #47 307.07.
2. **Sieben, J.**, Salzer, J., Carr, D. J. 2019. The SFACT Survey - Star Formation Across Cosmic Time. American Astronomical Society Meeting Abstracts #233, 144.04.
3. **Sieben, J.**, Salzer, J., Van Sistine, A., Gronwall, C. 2020. Luminosity Functions Derived from Three Distinct Emission Line Selected Galaxy Samples. American Astronomical Society Meeting Abstracts #235, 208.06.

SCIENCE COMMUNICATION WRITING

[ScIU](#), Author page
[Eclipses and Solar System Geometry](#)
[Science with Nemo: Ethics of Care in Animal Research](#)
[The Science Behind Meteor Showers in Animal Crossing](#)
[30 Years of Hubble: Images and Discoveries that Shaped Astronomy](#)
[Science without a Degree: What is Citizen Science and How to Get Involved](#)
[Global Collaboration in Science](#)
[The Quest for Alien Swimming Pools](#)
['Oumuamua: What's in a Name?](#)
[Why You Should Attend Conferences](#)
[The Metallic Age of Stars](#)
[An Astronomer's Sleep Schedule](#)
[+12 more](#)

MEDIA

Siegel, E. Interviewee. “#57 - The Universe’s Newborn Stars” Starts With a Bang. 2020 June.
Last updated: November 28, 2022